



IntechOpen

Novel Metal Electrodeposition and the Recent Application

Edited by Masato Sone and Kazuya Masu



Novel Metal Electrodeposition and the Recent Application

Edited by Masato Sone and Kazuya Masu

Published in London, United Kingdom



IntechOpen





Supporting open minds since 2005



Novel Metal Electrodeposition and the Recent Application

<http://dx.doi.org/10.5772/intechopen.73382>

Edited by Masato Sone and Kazuya Masu

Contributors

Brij Mohan Mundotiya, Wahdat Ullah, Takashi Nagoshi, Tso-Fu Mark Chang, Chiu Wan-Ting, Tomoko Hashimoto, Chun-Yi Chen, Hiromichi Kurosu, Haochun Tang, Daisuke Yamane, Toshifumi Konishi, Katsuyuki Machida, Eiichi Kondoh, Masaharu Yoshiba, Hiroyuki Ito, Hiroshi Toshiyoshi, Masatsugu Fujishige, Susumu Arai

© The Editor(s) and the Author(s) 2019

The rights of the editor(s) and the author(s) have been asserted in accordance with the Copyright, Designs and Patents Act 1988. All rights to the book as a whole are reserved by INTECHOPEN LIMITED. The book as a whole (compilation) cannot be reproduced, distributed or used for commercial or non-commercial purposes without INTECHOPEN LIMITED's written permission. Enquiries concerning the use of the book should be directed to INTECHOPEN LIMITED rights and permissions department (permissions@intechopen.com).

Violations are liable to prosecution under the governing Copyright Law.



Individual chapters of this publication are distributed under the terms of the Creative Commons Attribution 3.0 Unported License which permits commercial use, distribution and reproduction of the individual chapters, provided the original author(s) and source publication are appropriately acknowledged. If so indicated, certain images may not be included under the Creative Commons license. In such cases users will need to obtain permission from the license holder to reproduce the material. More details and guidelines concerning content reuse and adaptation can be found at <http://www.intechopen.com/copyright-policy.html>.

Notice

Statements and opinions expressed in the chapters are those of the individual contributors and not necessarily those of the editors or publisher. No responsibility is accepted for the accuracy of information contained in the published chapters. The publisher assumes no responsibility for any damage or injury to persons or property arising out of the use of any materials, instructions, methods or ideas contained in the book.

First published in London, United Kingdom, 2019 by IntechOpen

eBook (PDF) Published by IntechOpen, 2019

IntechOpen is the global imprint of INTECHOPEN LIMITED, registered in England and Wales,

registration number: 11086078, The Shard, 25th floor, 32 London Bridge Street

London, SE19SG – United Kingdom

Printed in Croatia

British Library Cataloguing-in-Publication Data

A catalogue record for this book is available from the British Library

Additional hard and PDF copies can be obtained from orders@intechopen.com

Novel Metal Electrodeposition and the Recent Application

Edited by Masato Sone and Kazuya Masu

p. cm.

Print ISBN 978-1-78985-295-0

Online ISBN 978-1-78985-296-7

eBook (PDF) ISBN 978-1-83962-063-8

We are IntechOpen, the world's leading publisher of Open Access books Built by scientists, for scientists

4,000+

Open access books available

116,000+

International authors and editors

120M+

Downloads

151

Countries delivered to

Our authors are among the
Top 1%

most cited scientists

12.2%

Contributors from top 500 universities



WEB OF SCIENCE™

Selection of our books indexed in the Book Citation Index
in Web of Science™ Core Collection (BKCI)

Interested in publishing with us?
Contact book.department@intechopen.com

Numbers displayed above are based on latest data collected.
For more information visit www.intechopen.com



Meet the editors



Prof. Masato Sone completed his doctor degree in engineering at the age of 28 at Tokyo Institute of Technology. He worked as a researcher in the Nippon Oil Company from 1996 to 2000. He was an assistant professor and then a research associate professor at Tokyo University of Agriculture and Technology from 2000 to 2005. He attained his current position of associate professor and full professor at Tokyo Institute of Technology in 2005. He has published more than 170 papers in scientific journals. His interests are microelectronics, metallurgy, surface finishing, chemical engineering, and liquid crystal and polymer science. His recent topic of interest is material design and the evaluation of electroplated gold alloys for high-sensitivity CMOS-MEMS accelerometers.



Prof. Kazuya Masu received his BE, ME, and PhD degrees in Electronics Engineering from Tokyo Institute of Technology (Tokyo Tech). He was an assistant professor and an associate professor at Tohoku University from 1982. In 2000, he was a professor and Director-General of the Institute of Innovative Research, Tokyo Tech, until March 2018. He was a visiting professor at the Georgia Institute of Technology in 2002 and 2005. He is currently President of Tokyo Tech. He has published more than 225 papers in scientific journals. He received an IEICE Electronics Society Award in 2004, IEICE Achievement Award in 2013, and IEEJ Outstanding Achievement Award in 2014. He served as Vice President of JSAP in 2014–2015. He is a JSAP Fellow, IEEJ Fellow, and IEICE Fellow.

Contents

Preface	XIII
Section 1 Evaluation Method of Electrodeposited Metal	1
Chapter 1 Evaluation Methods of Mechanical Properties of Micro-Sized Specimens <i>by Takashi Nagoshi, Tso-Fu Mark Chang</i>	3
Section 2 Electrodeposition of Pure Noble Metal	19
Chapter 2 Morphology Controlled Synthesis of the Nanostructured Gold by Electrodeposition Techniques <i>by Brij Mohan Mundotiya and Wahdat Ullah</i>	21
Chapter 3 Cu Wiring Fabrication by Supercritical Fluid Deposition for MEMS Devices <i>by Eiichi Kondoh</i>	39
Chapter 4 Pulse-Current Electrodeposition of Gold <i>by Chun-Yi Chen, Masaharu Yoshiba, Haochun Tang, Tso-Fu Mark Chang, Takashi Nagoshi, Daisuke Yamane, Toshifumi Konishi and Katsuyuki Machida</i>	55
Section 3 Alloy and Composite of Electrodeposited Noble Metal	69
Chapter 5 Electrodeposition of Gold Alloys and the Mechanical Properties <i>by Haochun Tang, Tso-Fu Mark Chang, Chun-Yi Chen, Takashi Nagoshi, Daisuke Yamane, Toshifumi Konishi and Katsuyuki Machida</i>	71
Chapter 6 Hard Pure-Gold and Gold-CNT Composite Plating Using Electrodeposition Technique with Environmentally Friendly Sulfite Bath <i>by Masatsugu Fujishige and Susumu Arai</i>	93

Chapter 7

Electrodeposition of High-Functional Metal Oxide on Noble Metal for
MEMS Devices

*by Wan-Ting Chiu, Chun-Yi Chen, Tso-Fu Mark Chang, Tomoko Hashimoto
and Hiromichi Kurosu*

111

Chapter 8

Multi-Physics Simulation Platform and Multi-Layer Metal Technology
for CMOS-MEMS Accelerometer with Gold Proof Mass

*by Katsuyuki Machida, Toshifumi Konishi, Daisuke Yamane, Hiroshi Toshiyoshi
and Hiroyuki Ito*

133

Preface

The history of metallic materials is thought to have begun about 11,000 years ago because of their brilliant beautiful features. The noble metals, especially gold, are often used as components in electronic devices because of their high electrical conductivity, chemical stability, corrosion resistance, and high density.

In the field of microelectromechanical system (MEMS) devices, continuous miniaturization, while maintaining high sensitivity, is always a challenge. Especially for MEMS accelerometers, sensitivity is highly affected by Brownian noise, and structures with sufficient mass in the device are needed to suppress this noise. Because of the requirement of overall mass of the components, it is difficult to reduce the dimensions of components to allow further miniaturization of the MEMS device.

This book presents recent progress in noble metal electrodeposition and the application of gold materials in the realization of highly sensitive complementary metal-oxide semiconductor-microelectromechanical systems (CMOS-MEMS) accelerometers. A feature of the CMOS-MEMS accelerometer is the use of gold proofmass. The high density of gold enables sensitivity enhancement by reducing thermomechanical noise, which is inversely proportional to overall mass of the proofmass. The developed CMOS-MEMS multiphysics design environment is also presented. An equivalent circuit of a MEMS accelerometer has been designed to simultaneously clarify both mechanical and electrical behaviors. One of the potential applications of the highly sensitive accelerometer is also discussed by focusing on early-stage diagnosis of Parkinson's disease.

Dr. Masato Sone and Dr. Kazuya Masu
Tokyo Institute of Technology, Japan

Section 1

Evaluation Method of
Electrodeposited Metal

Evaluation Methods of Mechanical Properties of Micro-Sized Specimens

Takashi Nagoshi, Tso-Fu Mark Chang

Abstract

Micro-sized components have been widely used to microelectromechanical systems (MEMSs) and medical apparatus in recent years. Measurement methodologies of the mechanical property of small materials need to be improved for structural designing of these devices because of their component size reduced to micro- or nano-regime where sample size effects emerge. Mechanical properties and deformation behavior could be very different with their dimensions and geometries especially for small materials. Our experiments on the micro-specimen tested in different dimensions and loading directions are suitable for the evaluations of materials for MEMS components. In this chapter, recent studies on micro-testing of bending, compression, and tension with micro-sized samples will be presented including fabrication methods of non-tapered micro-sized specimens.

Keywords: micro-testing, strength, anisotropy, microstructure, electrodeposition

1. Introduction

1.1 Micro-testing

Micro-sized components have been used in microelectromechanical systems (MEMSs). Recent developments of MEMS are outstandingly fast and need improved performance, reliable Device lifetime, and Miniaturization. MEMSs are often made up of components below 10 μm in size. For example, MEMS-based accelerometers or gyroscopes were widely used in smartphones, gaming consoles, and location-based devices. Some more examples shown in **Figure 1** are optical switch (a), gyro sensor (b), and micro-windmill (c) [1]. Micro-components used in MEMS such as micro-spring, bending beams, and structural support of MEMS suffer from mechanical straining and need suitable mechanical properties. However, at these size scales, the classical physics are not always useful. Sample size effect, which will be described in later section, emerges. Thus, the micro-testing method with specimen whose sample size is in the same scales with actual MEMS components is needed.

Besides testing methods for small materials, micro-sized testing of each representative elementary volume in heterogeneous materials is of great interest. According to the Japanese Industrial Standards, material mechanical property evaluation requires samples with gauge length larger than the 10 mm for tensile, bend, and compression testing. These samples could include all representative

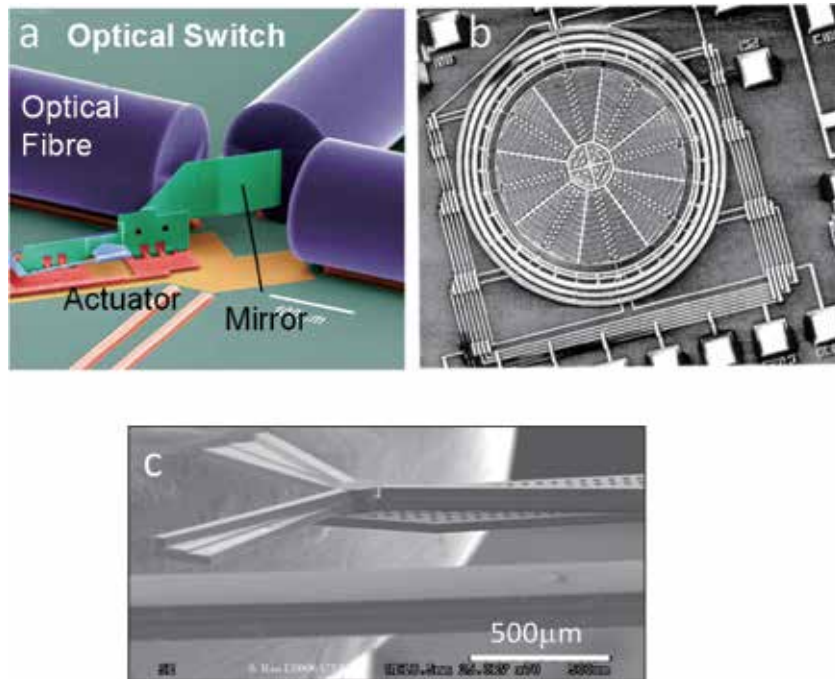


Figure 1.
Examples of MEMS devices: (a) optical switch, (b) gyro sensor, and (c) micro-windmill.

volume elements of materials, and thus the measurement results represent average properties of the material. On the other hand, micro-sized testing using micro-sized specimen can evaluate local mechanical properties such as second phase, locally damaged materials, and the interface or transition area among them.

1.2 Sample size effect

Mechanical property evaluations of small materials such as deposited film, heavily deformed metals, treated surface layer, etc. had been frequently conducted with indentation method because the size of the specimen can be very small and can easily conduct multiple tests for averaging. Hardness obtained from the indentation that repeatedly shows increase with decreasing indentation depth demonstrates a strong size effect [2–4]. Materials under the sharp indenter suffered from severe plastic flow from an early stage of indentation; thus, the deformations via dislocation and expansion of stacking faults are complicated, and strains had gradients from indentation site. The strain gradient under the indenter is supposed to be the main reason of indentation size effect as explained by strain gradient plasticity, which also justifies size effect on bending or torsional strength [4]. In an evolution of geometrical necessary dislocations with the presence of strain gradient, these formations induce an additional dislocations and cause material hardening, as supposed by Ashby [5]. Testing through compression or tension where strain gradients are absent had been conducted. Non-tapered pillar, i.e., no strain gradient inside, was fabricated and observed a generally unexpected size-dependent compression strength by Dimiduk et al. [6]. The following researches consistently showed size-dependent strength for tension and compression on various single-crystalline metals [7–11]. Size-dependent mechanisms on single-crystalline metals can be explained by the movement or evolution of dislocations in a limited volume of the small sample. Two commonly accepted models, dislocation starvation and source truncation, were proposed [12–14]. Dislocation starved condition observed by in-situ TEM

straining where new dislocation source nucleation needed with high stress [12, 15]. Truncated dislocations are observed as single-arm source where one end of the dislocation was pinned inside the specimens, and the other runs on the surface to attain strains [16]. These dislocation dynamics had been simulated using 3D discrete dislocation dynamics [17]. Size effects in single crystals had been well clarified based on the aforementioned dislocation mechanisms. However, size effects for the other deformations without dislocation motion such as grain boundary sliding and shear banding, which are frequently observed in nanocrystalline materials [18], are not yet been commonly understood. Rinaldi et al. [19] and Jang and Greer [20] have investigated the sample size effect on nickel nanocrystalline nano-pillars. They got different results: Jang and Greer observed a “smaller is weaker” dependence with the exponent smaller than one for single-crystalline metals, while Rinaldi et al. got very scattered result, which exhibits the slight increase in strength with decreasing sample size. Thus, sample size effect on nanocrystalline materials is inconclusive so far. Sample size effect on polycrystalline pillar has great interest in industries owing to miniaturization of MEMS devices reaching to its component scales at submicron or nano-regime.

1.3 Fabrications of MEMS

Metallic film formations are important processes for MEMS fabrication. There are two large classifications for film formation: one is the dry process and the other is the wet process. Dry process utilizes gas or metallic vapor for depositing metallic films on the surface of interest. Although it is a simple process, deposition rate is only sub-nm to several nm in a second [21, 22] and not suitable for industrial applications. On the other hand, one of the wet processes, electroplating, has been used for industrial fabrications of MEMS including components that require mechanical support thanks to fast deposition rate and controllable mechanical properties [23, 24].

The miniaturization of MEMS and IC goes into the nanoscale regime, the so-called nanotechnology. Each component size or wire width reaches several tens of nanometers. For the fabrication of such nanomaterials, gaps with an inversed geometry are filled with metals by deposition. In the gap filling, some problems happen as schematically shown in **Figure 2**. A liquid solution with surface tension and bad wettability to substrate do sometimes not fill the gaps or hydrogen gas bubbles evolved in the reaction. The areas without electrolyte were left unfilled during deposition leaving voids and pinholes [25]. We have developed a novel electroplating method with supercritical CO₂ emulsion (ESCE) to accomplish a successful metal gap fill [26, 27]. Emulsified

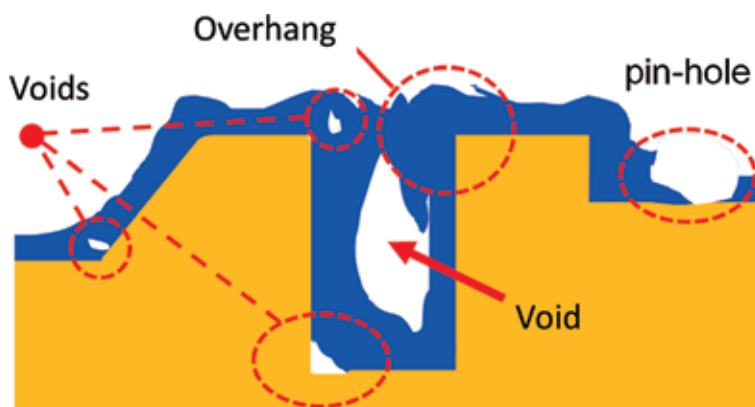


Figure 2.
Typical failures found in filling of gaps with electrodeposition.

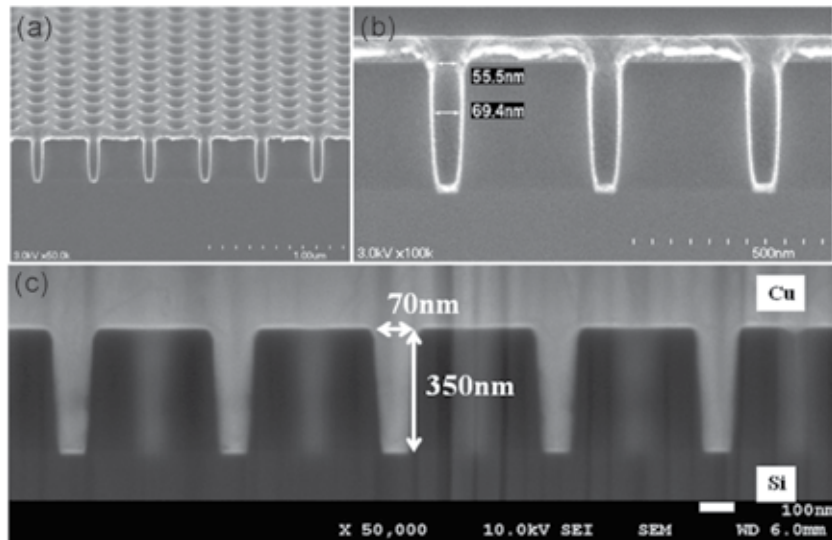


Figure 3. Cross-sectional SEM images of (a) substrate with holes of 70 nm in diameter with aspect ratio of 5, (b) expanded image of (a), and (c) substrate filled with Cu electroplated in ESCE.

supercritical CO₂ with surfactant forms micelles which continuously bounce on the surface of cathode. Evolved hydrogen bubbles and unfilled gaps are removed by the micelles, and the deposition stopped at the bounced area. The deposition resumed with refreshed electrolyte which enhances local plating rate. These plating mechanisms are called periodic plating characteristics (PPC) [28, 29]. The efficient hole filling was observed in the Cu filling to the hole with 70 nm in diameter and 350 nm in depth as shown in **Figure 3** [30, 31]. PPC also contributes to the film strengthening via grain refinement. Strengthening of MEMS components is essential for further miniaturization and high reliability of the devices. However, the size effect discussed in the last section is aggressively studied for single-crystalline metals and only few researches on structured materials such as nanocrystalline metals.

2. Micro-pillar compression testing

2.1 Pillar fabrications

Compressions of fabricated pillar could be the most frequently employed testing method for small materials. Starting from a notable work by Uchic et al. [32] who first probe the size effect without stress gradient, numerous works had been done by micro-compression. Uchic et al. fabricated fascinating cylindrical micro-pillars by focused ion beam (FIB) from single-crystal Ni. Automated fabrications by a series of side-wall milling and rotation for tilted pillars enabled non-tapered cylindrical pillar fabrication, while most of the FIB fabrication uses single-direction milling; thus, pillar tapered inheriting a tilted milling wall in a FIB fabrication. We have proposed novel method to fabricate non-tapered pillars using conventional FIB only. Schematic images of fabrication process are shown in **Figure 4**. Multidirectional ion beam irradiation was utilized to eliminate tapering. The fabrication can be divided in three parts: (1) coarse milling, (2) tilted milling, and (3) finishing. Before FIB milling, samples were thinned down to approximately 50 mm and mounted with projected part on the sample holder. In (1) coarse milling, the tip of projected part milled to form a rectangle pillar with specimen thickness on

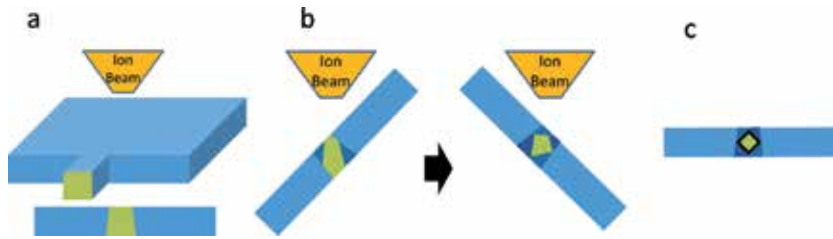


Figure 4. Schematic images of process for compression pillar fabrication: (a) coarse milling, (b) tilted milling, and (c) finishing.

side length. Following (2) tilted milling, specimen tilted to $\pm 45^\circ$; as more practically, sample rotated to 180° with tilting of 45° . The pillar size was reduced to a desired dimension leaving margins for finish milling. Tilted milling wall in FIB for this fabrication method results in a diamond-shaped cross section, which will be further modified in (3) finish milling. Using small current ion beam to minimize ion bombardment damage, the sample was milled from additional $\pm 2.3^\circ$ for each side of the pillar, i.e., ± 47.3 and ± 42.7 for four sides. SEM image of the fabricated pillar is shown in **Figure 5**. Uniform, non-tapered pillar is essential for the small-scale testing to reduce error in measurement. Finite element method indicates the tapering with the value of 20:1 (i.e., the angle between the post wall and the post axis is $\sim 2.86^\circ$) results in the increase of yield strength and observed work hardening even the perfectly plastically deformed model used [33].

2.2 Compression test of electrodeposited nickel

Electrodeposition of metals can be used as fabrications of mechanical support of MEMS devices which will suffer from bending, compression, and tension from any directions. The anisotropic features of deposited metals arising from the

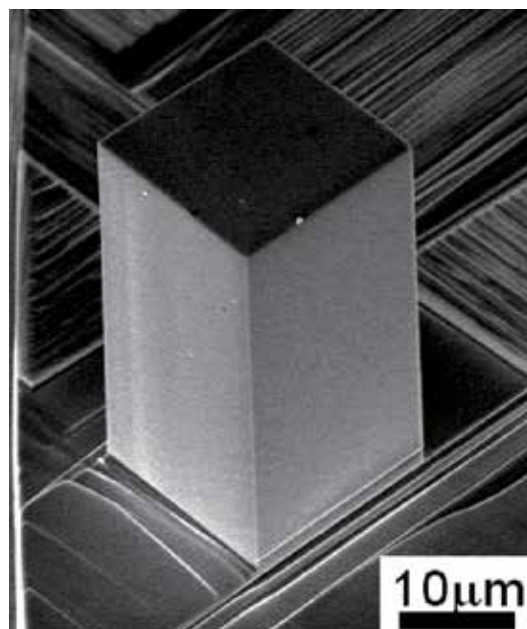


Figure 5. Fabricated compression pillar made from single-crystalline nickel.

microstructures and orientations could strongly effect on the mechanical properties of the components. To evaluate the anisotropic characteristics and resulting reliability of MEMS devices, compression test on electrodeposited nickel was conducted.

Microstructures of Ni electrodeposited by additive-free Watt's bath are investigated. The substrate was film of pure Cu annealed at 673 K for 1 h in vacuum. The film's cross section was evaluated by the scanning electron microscope (SEM) equipped with an electron backscatter diffraction (EBSD) pattern detector. Orientation map overlaid with grain boundary map where $\Sigma 3$ boundaries are colored yellow shown in **Figure 6** indicates fine columnar grains with diameter of around 100–200 nm grown toward film surface. Most of the columnar grain walls are $\Sigma 3$ boundaries, corresponding to twin boundaries, although the stacking fault energy of Ni is relatively high [34]. High density of twins, 42% among high-angle grain boundaries observed in this film, which commonly observed in various kinds of electrodeposited metals [35–37].

Mechanical properties of Ni film electrodeposited in conventional Watt's bath were evaluated using micro-compression. Compression pillars were fabricated by the FIB milling method mentioned in the previous section. Two pillars with $20 \times 20 \times 40 \mu\text{m}$ were fabricated with pillar axis parallel and perpendicular to growth direction as shown in **Figure 7**. The compression test was conducted by indenting the pillar using flat-ended diamond indenter. Stress-strain curve in **Figure 8** shows increase in compressive stress of the parallel pillar. However, in the cantilever bending test of same material indicate maximum stress of 2080 and 1582 MPa for the parallel and perpendicular cantilever with respect to the growth direction [38], i.e., the strength increased when the load direction vertical to the growth direction of the electrodeposited film which is the opposite result than the compression test. This is related to the stress gradient present in bending test where the stress maximizes at a fixed end and decreases along beam direction or neutralizes at the center of beam. These results that imply the mechanical properties of the small component are very sensitive to geometries, and hence, it is important to test them properly in their actual dimensions and geometries.

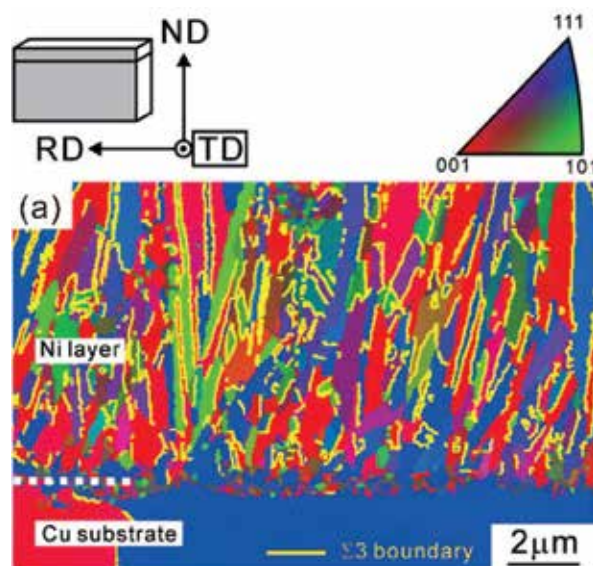


Figure 6. Cross-sectional orientation map of nickel film. Yellow line delineates the $\Sigma 3$ boundaries.

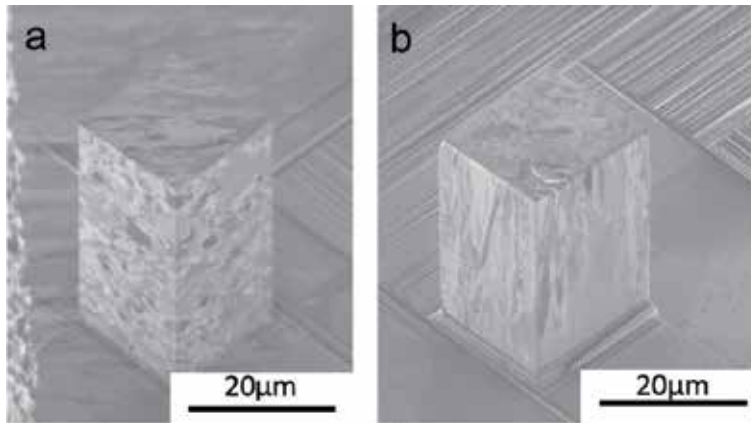


Figure 7. Scanning ion microscopy images of fabricated compression pillar with growth direction (a) vertical and (b) parallel to the pillar axis.

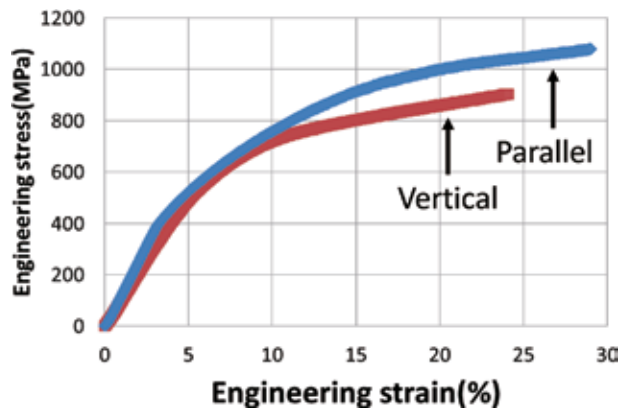


Figure 8. Stress-strain curves of micro-compressions of vertical and parallel pillar.

2.3 Sample size effect on nanocrystalline nickel

The size effect known as the mechanical property changes by the varying sample size below; several tens of microns had been extensively studied as summarized in the introduction. However, the sample size effect on the nanocrystalline metals had been under controversy including the existence of it. On the other hand, nanocrystalline materials are very important for MEMS components, while the aforementioned structural or orientation anisotropy is usually not involved even in submicron-sized samples. Microcompressions of nanocrystalline nickel with a different sample size are conducted to evaluate sample size effect on nanocrystalline materials [39].

Nanocrystalline nickel was electrodeposited with the ESCE mentioned in the introduction, which was developed in our group. Emulsions were formed by stirring the electrolyte with polyoxyethylene lauryl ether ($C_{12}H_{25}(OCH_2CH_2)_{15}OH$) under high pressure (15 MPa) of supercritical carbon dioxide. Plated nanocrystalline nickel (NCNi) and single-crystal nickel (SCNi) purchased from Nilaco Inc. were used to fabricate compression pillars. Square cross-sectional pillars with side length ranging from 5 to 30 μm are fabricated. Micro-compression testing was conducted by custom-made testing machine with flat-ended diamond indenter with a strain rate of 2.5×10^{-3} .

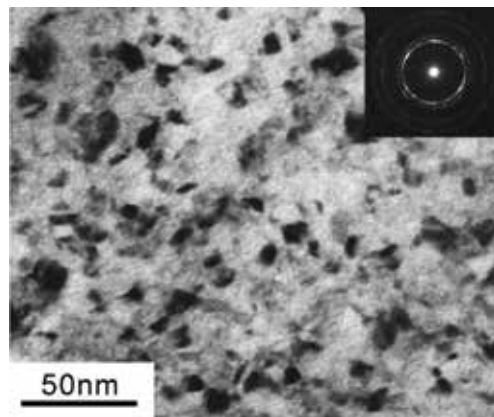


Figure 9.
TEM bright-field image of ESCE nickel viewed from film plane.

Deposited nanocrystalline nickel had 7.7 nm of average grain size measured by using TEM as shown in **Figure 9**. Pillars of SCNi with compression axis along $\langle 789 \rangle$ crystal orientation as analyzed by EBSD and NCNi were compression tested, and the results are shown in **Figure 10**. SCNi has a very low yield stress of 10–20 MPa which agrees well with the reported critical resolved shear stress of nickel. After yielding, large work hardening is due to the cross slip of dislocations, while several slip systems can be operative in compressions of near $[111]$ orientation. And finally work is softened by the macroscopic shear formation. Compression tests of NCNi were shown in true plastic strain starting from 0.2% offset stress as yield stress, which is more than ten times higher than that of SCNi. The deformation process is believed to be a grain boundary process, such as grain boundary sliding or grain rotation.

1% flow stress and yield strength of NCNi and peak stress of SCNi, were plotted against the sample size in double logarithmic scale in **Figure 11**. The stress dependence on sample size was negative, which means the smaller one is stronger in both single crystal and nanocrystalline materials. Although the scaling exponent of -0.125 for NCNi was very small compared with SCNi, strength increased from 2.5 to 3.1 GPa when the pillar size was decreased from 30 to 5 μm . The size effect in the present NCNi can be considered as a result of grain boundary sliding, which is reported to involve several grains in formation of micro shear band along the grain boundaries known as cooperative grain boundary sliding (CGBS) [40]. CGBS events could initiate from flat segment of grain boundaries, and the number of these segments decreased when sample size becomes smaller. Increase in strength with decreased sample size is the consequence of decreased shear areas in the operation of CGBS.

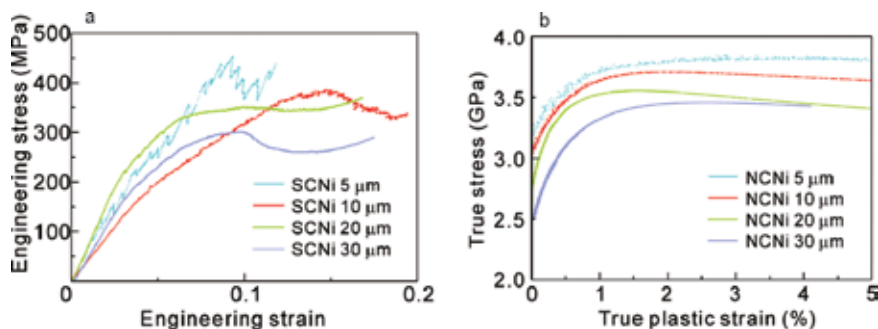


Figure 10.
Results of micro-compression test of sample with different sample sizes: (a) SCNi and (b) NCNi.

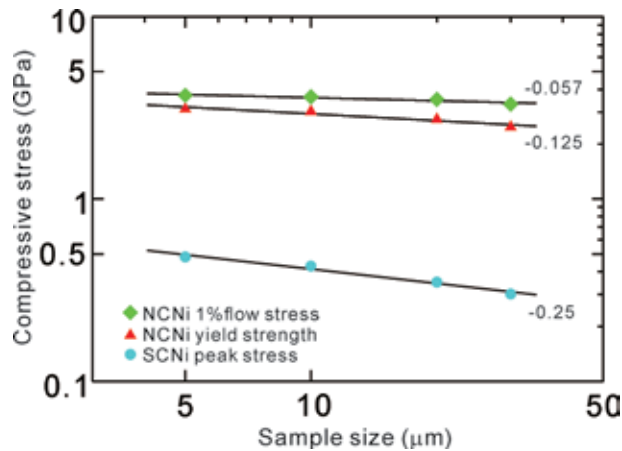


Figure 11.
Sample size dependence of compressive stresses.

3. Micro-tensile tests

3.1 Testing methods

Evaluating mechanical properties, such as fracture strength and elongation, of the materials in microscale is important to determine reliability of the micro-components used in MEMS. Although micro-compressions or micro-bending tests can provide some mechanical properties, these properties cannot be provided directly. For bulk materials, tensile tests are often used to evaluate mechanical properties including fracture strength and elongation and fracture behavior. Therefore, a tensile test in the microscale is needed to evaluate the properties of the micro-specimens. In the microscales, gripping the specimen and aligning the equipment for the tensile test are very difficult when comparing with micro-compression or bending tests; thus, there are only a few reports on micro-tensile test [41, 42]. The fabrication method of compression pillar shown in the previous section uses ion beam irradiation from vertical to pillar axis; thus, in a fabrication of tensile test specimen, the head of the sample and gauge part are separately fabricated as shown in **Figure 12**. At first, the thin sample was milled roughly by FIB, as shown in **Figure 12a**. Second, the grip part and gauge part were milled to a shape as shown in **Figure 12b**. Finally, the gauge part of the micro-tensile specimen was milled by the same way of the fabrication of compression pillar. The final shape of tensile specimen is shown in **Figure 12c**. High strength and stiffness of diamond are suitable materials for the micro-gripper to be used in micro-tensile test. Thus, the micro-gripper fabricated from the diamond-tip indenter can be used to evaluate mechanical property of high-strength materials.



Figure 12.
Schematics of tensile specimen fabrication. (a) Rough milling, (b) fabrication of grip part, and (c) SEM image of tensile specimen after gauge part milling by non-tapered pillar fabrication procedures.

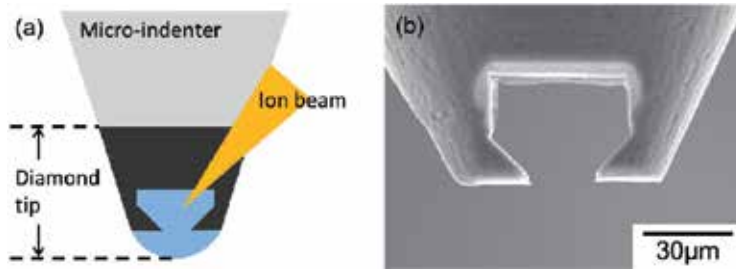


Figure 13. Schematic image showing fabrication method of the micro-gripper for the micro-tensile test and (b) SEM image of the fabricated micro-gripper.

Using same FIB equipment for fabrications of grip part and sample gripper enables the completely inverted-shaped combination of them feasible for aligned grip in tensile test. The grip part of the micro-gripper was fabricated by removing away the blue region by FIB milling as shown in **Figure 13a**. **Figure 13b** shows SEM image of fabricated micro-gripper taken along the direction of FIB irradiation.

3.2 Tensile test of single-crystal nickel

Aside from the structural anisotropy on polycrystalline metals shown in the previous section, single-crystal metals have strong anisotropy to mechanical properties. We have conducted tensile test of SCNi with different orientations of $\langle 111 \rangle$ and $\langle 223 \rangle$ along loading axis [43]. The difference in the stress-strain curves shown in **Figure 14** is an evidence of the effect of crystal anisotropy on the deformation behavior. In particular, stress-strain curve of the $\langle 223 \rangle$ oriented specimen can be divided into three hardening stages as shown in dashed line in **Figure 14**. The three-stage hardening for $\langle 223 \rangle$ specimen is typically observed in single-crystal bulk metals with fcc structure [44]. The regions divided by the dashed lines are named stages 1, 2, and 3 from left to right, respectively. In stage 1, single slip system having a high Schmid factor easily glides at a low tensile strength. In stage 2, a multiple slip events occurred due to other glides in slip systems with lower Schmid factor than the one already worked in stage 1. Thus, the work hardening rate increased due to cutting and tangling of dislocation lines. In stage 3, the dislocation multiplication is limited due to the saturation of dislocations. Work hardening rate is decreased. However, the three-stage deformation behavior observed in $\langle 223 \rangle$ specimen was not observed in the $\langle 111 \rangle$ specimen. For the $\langle 111 \rangle$ specimen, a multiple slip phenomenon occurred at the initial region of plastic deformation, which is same as observed in stage 2 for the $\langle 223 \rangle$ specimen. The difference comes from that there is no slip system having a Schmid factor that is much larger than the others as the case in the $\langle 223 \rangle$ specimen. In addition, four slip systems had similar high Schmid factor which indicates they can move at similar stress on the contrary to $\langle 223 \rangle$ specimen. The behavior observed in the true-stress-true-strain curve for the $\langle 111 \rangle$ specimen is also similar to the stress-strain curve of bulk single-crystal metal composed of fcc crystal structure having multiple slip [44, 45]. Strength and deformation behavior of single-crystal metals are highly dependent on the loading directions even in the microscale tensile testing.

3.3 Tensile test of nanocrystalline nickel

The high strength and sample size effect on NCNi deposited by our developed method ESCE were evaluated by the micro-compression test. However,

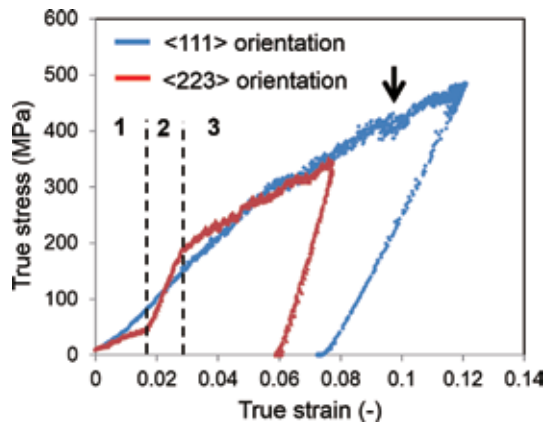


Figure 14.
Stress-strain curves of micro-tensile test conducted for single-crystal nickel oriented $\langle 111 \rangle$ and $\langle 223 \rangle$ to loading axis.

micro-compression testing does not provide fracture strength and elongation to failure. The aim of tensile test conducted is to obtain these mechanical properties and to clarify underlying deformation mechanisms of nanocrystalline nickel [46].

Figure 15 shows engineering stress-strain curves of NCNi tested in micro-tensile test, sample A tensile loaded until fracture and sample B unloaded after maximum tensile stress was reached. Both samples had worked softening after plastic strains of 1% indicating almost no work hardening capacity. Observations of sample A and B are shown in **Figure 16**. In sample B, a notable necking was observed at the gauge part as shown in a magnified view in **Figure 16a**, and the rest of the portions was left undeformed. For nanocrystalline or ultrafine-grained materials with grain size smaller than 1 μm , these low work hardening capacities and the absence of uniform elongations are observed in tensile test using bulk specimen [47, 48]. The metals with small grains have no space for multiplication of dislocations during deformation; thus, dislocations immediately relaxed or sank in grain boundaries, and no dislocation hardening was attained. However, the fracture surface had shear lips at the edge of the specimen and dimples as shown in **Figure 16a** and **b** indicating the ductile nature of deformation. Testing by the different loading conditions reveals underlying the nature of deformation behavior important for the mechanical property analysis.

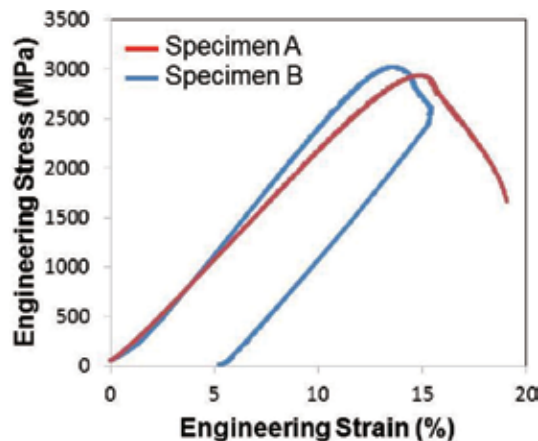


Figure 15.
Stress-strain curves of micro-tensile test conducted for ESCE nickel.

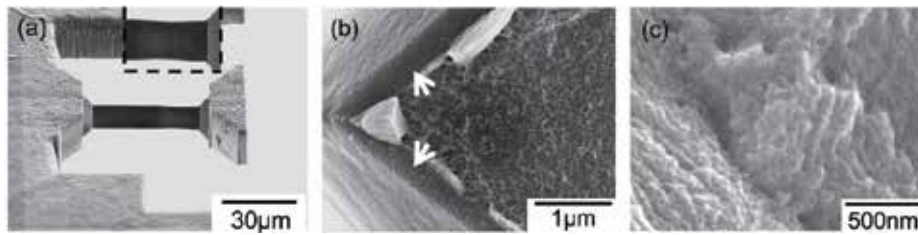


Figure 16. SEM images of the specimen after micro-tensile test. (a) Specimen B, (b) shear lip observed on fractured surface of specimen A, and (c) dimple patterns on the center of fractured surface.

4. Conclusion

The present chapter describes a variety of micro-testing suitable for evaluations of mechanical properties of deposited films. Different geometries and loading directions are essential for the practical evaluations of mechanical properties of materials to be used in MEMS components. The sample preparation for micro-testing, our proposed fabrication method of microscale samples for compression and tension tests, demonstrated the anisotropic deformation behavior of electrodeposited metals.

Compression test conducted on nickel film deposited by conventional method, which has structural anisotropy as columnar grains grow along the deposition direction. The strength of the film is varied due to both geometry and loading directions indicating the importance of micro-testing the MEMS components with their actual dimensions.

Micro-compression and tensile test reveal very high strength and peculiar deformation behavior of nanocrystalline nickel deposited in ESCE. And more importantly, the size effect on nanocrystalline materials has been observed and concluded to be due to the decreased shear areas of CGBS in small samples.

Author details


Takashi Nagoshi^{1*}, Tso-Fu Mark Chang²

¹ National Institute of Advanced Industrial Science and Technology, Tsukuba, Japan

² Tokyo Institute of Technology, Yokohama, Japan

*Address all correspondence to: nagoshi-t@aist.go.jp

IntechOpen

© 2018 The Author(s). Licensee IntechOpen. This chapter is distributed under the terms of the Creative Commons Attribution License (<http://creativecommons.org/licenses/by/3.0>), which permits unrestricted use, distribution, and reproduction in any medium, provided the original work is properly cited. 

References

- [1] Giomi E, Fanucci L, Rocchi A. Analog-CMDA based interfaces for MEMS gyroscopes. *Microelectronics Journal*. 2014;**43**:78-88
- [2] Oliver WC, Pharr GM. Improved technique for determining hardness and elastic modulus using loading and displacement sensing indentation. *Journal of Materials Research*. 1992;**7**:1564-1580
- [3] Ma Q, Clarke DR. Size dependent hardness in silver single crystals. *Journal of Materials Research*. 1995;**10**:853-863
- [4] Nix WD, Gao H. Indentation size effects in crystalline materials: A law for strain gradient plasticity. *Journal of the Mechanics and Physics of Solids*. 1998;**46**:411-425
- [5] Ashby MF. The deformation of plastically non-homogeneous materials. *Philosophical Magazine*. 1970;**21**:399-424
- [6] Dimiduk DM, Uchic MD, Parthasarathy TA. Size-affected single-slip behavior of pure nickel microcrystals. *Acta Materialia*. 2005;**53**:4065
- [7] Frick CP, Clark BG, Orso S, Schneider AS, Arzt E. Size effect on strength and strain hardening of small-scale [1 1 1] nickel compression pillars. *Materials Science and Engineering A*. 2008;**489**:319
- [8] Greer JR, Oliver WC, Nix WD. Size dependence of mechanical properties of gold at the micron scale in the absence of strain gradients. *Acta Materialia*. 2005;**53**:1821
- [9] Volkert CA, Lilleodden ET. Size effects in the deformation of sub-micron Au columns. *Philosophical Magazine*. 2006;**86**:5567
- [10] Kiener D, Motz C, Dehm G. Micro-compression testing: A critical discussion of experimental constraints. *Materials Science and Engineering A*. 2009;**505**:79
- [11] Ng KS, Ngan AHW. Deformation of micron-sized aluminium bi-crystal pillars. *Acta Materialia*. 2008;**56**:1712
- [12] Greer JR, Nix WD. Nanoscale gold pillars strengthened through dislocation starvation. *Physical Review B*. 2006;**73**:245410
- [13] Parthasarathy TA, Rao SI, Dimiduk DM, Uchic MD, Trinkle DR. Contribution to size effect of yield strength from the stochasticity of dislocation source lengths in finite samples. *Scripta Materialia*. 2007;**56**:313-316
- [14] Beanland R. Dislocation multiplication mechanisms in low-misfit strained epitaxial layers. *Journal of Applied Physics*. 1995;**77**:6217-6222
- [15] Hemker KJ, Nix WD. Nanoscale deformation: Seeing is believing. *Nature Materials*. 2008;**7**:97-98
- [16] Oh SH, Legros M, Kiener D, Dehm G. In situ observation of dislocation nucleation and escape in a submicrometre aluminium single crystal. *Nature Materials*. 2009;**8**:95-100
- [17] Cui YN, Lin P, Liu ZL, Zhuang Z. Theoretical and numerical investigations of single arm dislocation source controlled plastic flow in FCC micropillars. *International Journal of Plasticity*. 2014;**55**:279-292
- [18] Schiøtz J, Tolla FDD, Jacobsen KW. Softening of nanocrystalline metals at very small grain sizes. *Nature*. 1998;**391**:561
- [19] Rinaldi A, Peralta P, Friesen C, Sieradzki K. Sample size-effects in the yield behavior of nanocrystalline Ni. *Acta Materialia*. 2008;**56**:511

- [20] Jang D, Greer JR. Size-induced weakening and grain boundary-assisted deformation in 60 nm grained Ni nanopillars. *Scripta Materialia*. 2011;**64**:77-80
- [21] Sun Y, Miyasato T, Wigmore JK, Sonoda N, Watari Y. Characterization of 3C-SiC films grown on monocrystalline Si by reactive hydrogen plasma sputtering. *Journal of Applied Physics*. 1997;**82**:2334
- [22] Yoshida T, Tani T, Nishimura H, Akashi K. Characterization of a hybrid plasma and its application to a chemical synthesis. *Journal of Applied Physics*. 1983;**54**:640
- [23] Gad-el-Hak M. *The MEMS Handbook*. Boca Raton, FL: CRC, Taylor & Francis; 2006
- [24] Schultze JW, Bressel A. Principles of electrochemical micro- and nano-system technologies. *Electrochimica Acta*. 2001;**47**:3
- [25] Tsai WL, Hsu PC, Hwu Y, Chen CH, Chang LW, Je JH, et al. Electrochemistry: Building on bubbles in metal electrodeposition. *Nature*. 2002;**417**:139
- [26] Yoshida H, Sone M, Wakabayashi H, Yan H, Abe K, Tao XT, et al. New electroplating method of nickel in emulsion of supercritical carbon dioxide and electrolyte solution to enhance uniformity and hardness of plated film. *Thin Solid Films*. 2004;**446**:194
- [27] Yan H, Sone M, Sato N, Ichihara S, Miyata S. The effects of dense carbon dioxide on nickel plating using emulsion of carbon dioxide in electroplating solution. *Surface and Coating Technology*. 2004;**182**:329
- [28] Yoshida H, Sone M, Mizushima A, Yan H, Wakabayashi H, Abe K, et al. Application of emulsion of dense carbon dioxide in electroplating solution with nonionic surfactants for nickel electroplating. *Surface and Coating Technology*. 2003;**173**:285
- [29] Chang TFM, Sone M, Shibata A, Ishiyama C, Higo Y. Bright nickel deposited by supercritical carbon dioxide emulsion using additive-free Watts bath. *Electrochimica Acta*. 2010;**55**:6469
- [30] Shinoda N, Shimizu T, Chang TFM, Shibata A, Sone M. Filling of nanoscale holes with high aspect ratio by Cu electroplating using suspension of supercritical carbon dioxide in electrolyte with Cu particles. *Microelectronic Engineering*. 2012;**97C**:126
- [31] Shimizu T, Ishimoto Y, Chang TFM, Kinashi H, Nagoshi T, Sato T, et al. Cu wiring into nano-scale holes by electrodeposition in supercritical carbon dioxide emulsified electrolyte with a continuous flow reaction system. *Journal of Supercritical Fluids*. 2014;**60**:60
- [32] Uchic MD, Dimiduk DM, Florando JN, Nix WD. Sample dimensions influence strength and crystal plasticity. *Science*. 2004;**305**:986-989
- [33] Zhang H, Schuster BE, Wei Q, Ramesh KT. The design of accurate micro-compression experiments. *Scripta Materialia*. 2006;**54**:181-186
- [34] Humphreys FJ, Hartherly M. *Recrystallization and Related Annealing Phenomena*. 2nd ed. Amsterdam: Elsevier; 2004
- [35] Nakahara S. Growth twins and development of polycrystallinity in electrodeposits. *Journal of Crystal Growth*. 1981;**55**:281
- [36] Bastos A, Zaefferer S, Raabe D, Schuh C. Characterization of the microstructure and texture of

- nanostructured electrodeposited NiCo using electron backscatter diffraction (EBSD). *Acta Materialia*. 2006;**54**:2451
- [37] Shinada E, Nagoshi T, Chang TFM, Sone M. Crystallographic study on self-annealing of electroplated copper at room temperature. *Materials Science in Semiconductor Processing*. 2013;**16**:633
- [38] Imamura H, Nagoshi T, Yoshida A, Chang TFM, Onaka S, Sone M. Evaluation of anisotropic structure in electrodeposited Ni film using micro-sized cantilever. *Microelectronic Engineering*. 2012;**100**:25
- [39] Nagoshi T, Mutoh M, Chang TFM, Sato T, Sone M. Sample size effect of electrodeposited nickel with sub-10 nm grain size. *Materials Letters*. 2014;**117**:256-259
- [40] Zelin MG, Mukherjee AK. Cooperative phenomena at grain boundaries during superplastic flow. *Acta Metallurgica et Materialia*. 1995;**43**:2359
- [41] Haque MA, Saif MTA. A review of MEMS-based microscale and nanoscale tensile and bending testing. *Experimental Mechanics*. 2003;**43**:248
- [42] Kiener D, Grosinger W, Dehm G, Pippan R. A further step towards an understanding of size-dependent crystal plasticity: In situ tension experiments of miniaturized single-crystal copper samples. *Acta Materialia*. 2008;**56**:580-592
- [43] Kihara Y, Nagoshi T, Chang TFM, Hosoda H, Sato T, Sone M. Tensile behavior of micro-sized specimen made of single crystalline nickel. *Materials Letters*. 2015;**153**:36-39
- [44] Honeycombe RWK. *The Plastic Deformation of Metals*. 2nd ed. London: Butler & Tanner Ltd; 1984
- [45] Cottrell AH. *Dislocations and Plastic Flow in Crystals*. Oxford: Clarendon Press; 1953
- [46] Kihara Y, Nagoshi T, Chang TFM, Hosoda H, Sato T, Sone M. Tensile behavior of micro-sized specimen fabricated from nanocrystalline nickel film. *Microelectronic Engineering*. 2015;**141**:17-20
- [47] Wang YM, Ma E. Three strategies to achieve uniform tensile deformation in a nanostructured metal. *Acta Materialia*. 2004;**52**:1699-1709
- [48] Torre FD, Swygenhoven HV, Victoria M. Nanocrystalline electrodeposited Ni: Microstructure and tensile properties. *Acta Materialia*. 2002;**50**:3957-3970

Section 2

Electrodeposition of Pure Noble Metal

Morphology Controlled Synthesis of the Nanostructured Gold by Electrodeposition Techniques

Brij Mohan Mundotiya and Wahdat Ullah

Abstract

The gold nanostructures find several technological applications in MEMS, optoelectronics, and electronics industries. To enhance the applicability and suitability of the gold nanostructures in these fields, modification of the morphology of the deposited nanostructure is required. In recent years, the electrodeposition method has emerged as a widely known method for the deposition of the nanostructures of different dimensions and morphologies due to its time efficiency, cost-effectiveness, and absence of vacuum technology. In this method, the morphology of the deposited gold nanostructure can also be easily controlled by tuning the electrodeposition process parameters such as electrolyte concentration, electrolyte temperature, current density, deposition time, etc. This chapter gives a detailed overview of the crucial electrodeposition parameters affecting the morphology of the gold nanostructures deposits.

Keywords: deposition parameters, electrodeposition, electrolyte, morphology, nanostructured gold, stability

1. Introduction

The origin of the word gold comes from the old English Anglo-Saxon word for geolo meaning “yellow”, while the symbol ‘Au’ of gold is originated from the Latin word aurum, meaning ‘shining dawn’ [1]. Gold is a precious element and has an atomic number 79. In nature, it exists in a pure form. It is lustrous, slightly reddish yellow in color, soft, has high density, high corrosion resistance, highly malleable and ductile. Due to these properties, it has a long history in playing a very important role in the development of human societies since ancient time to till date. It was used by Chinese and Egyptians in ancient time (in the fifth or fourth century B.C). Gold is used in both bulk and nanostructure forms. In bulk form, gold is used in making jewelry, coins, statues, decorative objects, etc. Nanostructured gold materials are not new materials for mankind. Gold materials with nanostructures were used by mankind since a long time, but due to unavailability of characterizing tools for nanostructure (like high-resolution transmission electron microscopy (HRTEM), atomic force microscopy (AFM), X-ray diffractometer (XRD), etc.) their structures were unrevealed. Nanostructured gold is used in the microelectromechanical system (MEMS) due to its properties of high electrical conductivity, excellent corrosion resistance, solderability, thermal conductivity, and bondability.

For applications of nanostructured gold coating in MEMS, the coating must have some essential basic properties which are as follows [2]: (a) Conductivity of coating should be high; (b) Adhesion should be strong between coating and substrate to prevent cracking, delamination and spallation; (c) Residual stress in the coating should be minimum; (d) Coating should be stable within a wide range of temperature; and (e) Coating should also be resistant to surface wears, corrosion, and oxidation. Gold has also a good combination of high electrical conductivity and corrosion resistance; therefore, it is widely used as a standard material for interconnections, bond pads, contacts, as well as conductors, electrodes, and other passive components [3]. For the electrical connectors and contacts, deposit of gold has high hardness and good wear resistant [4]. Nanostructured gold also used in a variable capacitor, chemical and biological sensors, optical detectors, etc. [2].

Electrodeposition technique is a well-established versatile technique to synthesize nanostructured gold on the conducting substrate. The earliest reference to the gold coating by the electrodeposition process can be found in 1805 [1]. Relative to other deposition techniques like sputtering [5], evaporation [6] and molecular beam epitaxy [7], electrodeposition technique has many advantages such as time efficiency, low cost, high deposition rate, relatively inexpensive equipment due to absence of vacuum technology, thickness and uniformity controllable of the layers of the deposited coatings, etc. The properties of the deposited nanostructured gold coating are simply controlled by tuning its morphology. And, the morphology of the deposited gold can be tuned by changing the electrodeposition process parameters; mainly in the composition and pH of the electrolyte, the magnitude of the applied current density, temperature of electrolyte and substrate. Moreover, it is also found that the addition of some suitable additive in the electrolyte and a pre-treatment of the conductive substrate can also modify the morphology of deposited gold [8]. It is also reported by Tian et al. [9] that the variation in the applied potential to the electrodes and concentration of the precursor gold in the electrolyte plays a very crucial role in modification of the geometries and morphologies of the gold deposits. On the variation of applied potential to the electrodes, they obtained pyramidal, rod-like, and spherical morphologies of nanostructured gold in a pre-treated substrate.

In this chapter, an overview of the information related to effects of process parameters in the morphologies of nanostructured gold deposits is provided in detail.

2. Electrodeposition of gold

Schematic of the electrodeposition process is shown in **Figure 1**. For the electrodeposition process, an electrolytic cell, an electrolyte, electrodes (an anode and a cathode), and a power supply source are required. The electrolyte is the electrochemical solution of metal or alloy salts that is/are required to deposit at cathode (conductive substrate) surface during electrolysis. When a power source is connected to the terminals of electrodes, the current flows through them. As a result of this, the cations (the metal ions (M^{Z+})) are attracted to the cathode and deposited on it. The continuous deposition of metal ions on the cathode surface forms a uniform layer of metal on it through the reduction process. During the electrodeposition process, following chemical reactions (Eqs. (1) and (2)) take place at cathode and anode:



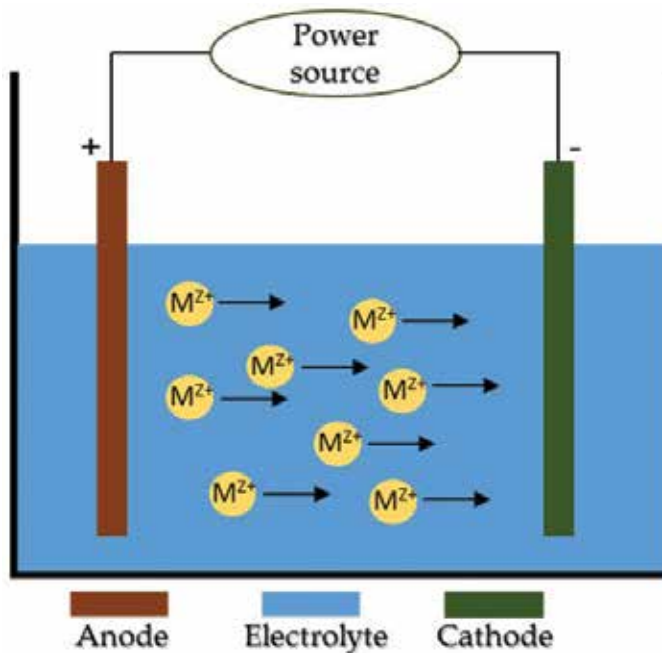


Figure 1.
Schematic of an electrodeposition process.

In electrodeposition of metal or metal alloy, according to requirement one can use two types of anodes: (a) sacrificial anode and (b) permanent anode. The sacrificial anode is a dissolvable anode and it is made up of metal being deposited on the cathode. During electrodeposition process, sacrificial anode sacrifices itself and provides the metal ions to the electrolyte. On the other hand, permanent anode or inert anode is generally made of platinum and carbon. This type of anode is employed only to complete the electrical circuit. It does not give any metal ions to the electrolyte during electrodeposition process. The cathode is the substrate on that deposition is carried out.

Electrolytes used for deposition of gold nanostructures are generally cyanide and noncyanide based. Gold is present in these electrolytes primarily in the oxidation states like +1 and +3. The $[\text{Au}(\text{CN})_2]^-$ is the most commonly used gold complex for the deposition of gold. This complex has the stability constant of 10^{39} and the oxidation state of +1. One more frequently used gold complex is anionic chlorocomplex $[\text{AuCl}_4]^-$ in hydrochloric solution which exists in the +3 oxidation state. The other popular complexes of gold are gold sulfite $[\text{Au}(\text{SO}_3)_2]^{-3}$ and gold thiosulfate $[\text{Au}(\text{S}_2\text{O}_3)_2]^{-3}$. Stability constant of gold sulfite and gold thiosulfate are 10^{10} and 10^{28} , respectively [1].

Most of the electrodeposited gold coatings have some degree of compressive/tensile residual stresses. The residual stress of gold coating is unwanted for its application in the MEMS. Because the residual stresses create curvatures in the coating which provide the most prone sites for creation of nano/microcracks. Also, chances of delamination of the coating from the substrate increases due to the presence of residual stresses on it. Presence of high level of residual stresses in the gold coatings also leads the risk of breakage of the wafer during handling. Therefore, minimization of residual stresses in the electrodeposited coating is an essential requirement for its application in the fabrication of coating based devices. It is found that the residual stresses in deposited coatings can be controlled by changing the electrodeposition process parameters. It has been reported in scientific literature that the

developed residual stresses in electrodeposited coatings are the function of current density [10–12], electrolyte temperature [12], coating thickness [10], cathode agitation [4], and brighteners [12]. The developed stress in the deposited coatings can be calculated by using the Stoney's formula for thin film. For this purpose, the wafer curvature before and after the deposition is measured by using a profilometer. The load and scanning speed is kept fixed during the curvature measurement. Stress in the film is expressed by Stoney's formula given in Eq. (3) [13]:

$$\sigma_f = \frac{E_s h_s^2 k}{6 h_f (1 - \nu_s)} \quad (3)$$

where σ_f is the stress in the coating, h_f is the thickness of the coating, h_s thickness of the substrate, E_s is Young's modulus of the substrate, k is the curvature difference between the coating and substrate, and ν_s is the Poisson's ratio.

Normally, two types of electrodeposition methods for deposition of gold nanostructures, namely: (a) DC electrodeposition and (b) pulse electrodeposition. In this chapter, we will be focused on DC electrodeposition method for deposition of gold nanostructures.

3. Gold electrodeposition solution

As the gold is one of the costliest metal, therefore, it is necessary to identify the best and suitable electrolyte solution to reduce the deposition cost of the desirable gold nanostructures by electrodeposition. The first trace of deposition of gold onto the silver substrate by the electrodeposition process can be found in work of Italian chemist Luigi Brugnatelli in 1805 [1]. A wide range of suitable electrolytes for deposition of gold with nanostructures have been identified by researchers so far (see **Table 1**). For the deposition of nanostructured gold, the electrolyte baths have been classified into different classes such as cyanide-based and noncyanide-based electrolytes. Cyanide-based electrolyte could be operated at acidic (pH value less than 7), neutral (pH value equal to 7), or alkaline (pH more than 7) pH's. The deposited nanostructured gold from this electrolyte can be soft or hard. On the other hand, noncyanide-based electrolytes could be operated only at neutral or alkaline pHs. And, deposited gold by these electrolytes is soft [18]. The hardening of deposited gold occurs due to the co-deposition of gold with metals such as nickel, cobalt, and iron. The co-deposited metals such as nickel, cobalt, and iron are known as hardening agents.

Traditionally, classical cyanide-based electrolyte bath is most frequently used for the deposition of nanostructured gold. From this electrolyte bath, the deposited gold coating is either pure or may contain an impurity of some other metals such as silver, nickel, cobalt, and copper. Co-deposition of these metals in the deposited gold could alter its color. Furthermore, the cyanide-based electrolyte is highly toxic. The other problem associated with electrodeposition of gold using cyanide-based electrolytes is that they often incompatible with positive photoresist [17]. The electrolyte attacks the interface between the resist film and the substrate which leads to change in the geometry of pattern of the desired component in MEMS that created in the photoresist. The component has a different shape and size after the electrodeposition. Therefore, researchers and scientist are looking to develop an electrolyte bath that is nontoxic and compatible with microdevice manufacture such as the conventional photoresist used to delineate bump pattern.

A sulfite-based electrolyte bath is alternatively used for the deposition of the nanostructured gold in MEMS applications. Sulfite based electrolyte has been

Type	Composition	pH	Temperature (°C)	Current density (mA/cm ²)	Substrate
Dicyanoaurate bath [14]	KAu(CN) ₂ : 12 g/L Citric acid: 40 g/L NH ₄ -citrate: 40 g/L	–	Room temperature	<0.25	Cu
Sulfite bath [4]	Commercially solution: Metalor ECF 60	9.5	22–60	1–5	A seed layer of Au on Si-wafer
Cyanide bath [2]	Commercial solution: ATOTECH™ gold potassium cyanide	–	45–75	1–7	Seed layer of Cr/Au on Si-wafer
Cyanide bath [8]	K[Au(CN) ₂]: 10 g/L KH ₂ PO ₄ : 100 g/L	–	55	–	Transparent conductive oxide glass (glass/SnO ₂ :F)
Sulfite bath [15]	Na ₃ Au(SO ₃) ₂ : 0.080 mol/L Na ₂ SO ₃ : 0.32 mol/L Ti ₂ SO ₄ : 1 mmol/L	9	23	1.5	Seed layer of Au on Si-wafer
Chloride bath [16]	HAuCl ₄ : 0.02–0.20 mmol/L	7	30	–	ITO glass
Chloride bath [9]	HClO ₄ : 0.1 M HAuCl ₄ : 4–40 mM	–	–	–	ITO glass
Sulfite bath [17]	Technigold 25E	6.5	35	1–4	Copper beryllium alloy strip

Table 1.
Electrolyte solution and some parameters of Au-electrodeposition.

known since 1842. This bath consists of gold(I) sulfite complex ($[\text{Au}(\text{SO}_3)_2]^{3-}$). However, the major issues associated with sulfite-based electrolytes are its solution solubility and instability under neutral or slightly acidic conditions necessary for optimum resist compatibility [19, 20]. Sulfite-based electrolyte bath without stabilizing agents suffers instability due to low solubility constant (10^{10}) as compared to cyanide complex, $[\text{Au}(\text{CN})_2]^-$ which has a relatively higher stability constant, 10^{39} [1, 18]. When alkaline soluble positive resists are used in an alkaline condition (pH 8.5–10), another problem of mixing of a significant amount of contamination of organic compound in gold coatings arises. Because, in alkaline condition, the positive photoresist dissolves with a slow rate, as a result of this, contamination of organic compound is mixed with deposited gold [21]. To solve this issue, the sulfite-based electrolyte is operated preferably in the neutral or acidic medium. Stabilizing additives such as the polyamine aromatic nitro compound and 2,2'-bipyridine are used to stabilize the electrolytic bath in the neutral or acidic medium [18, 21]. The polyamine such as ethylenediamine helps to operate the electrolyte at lower pH range of 5–8. With a combination of ethylenediamine and nitrobenzene, the electrolyte bath could be operated at pH value as low as 4.0–6.5 [18].

Many cyanide and noncyanide-based electrolytes are now commercially available and actually being in the industry to synthesize nanostructure gold deposits with desired properties.

4. Electrodeposition of zero-dimensional gold nanostructures

The gold nanoparticles are used in photo-electrical accessories, biochemical sensors, electrocatalytic activity, etc. By variation of the size and density of the nanoparticles, the performance of these devices can be altered. Dolati et al. [22] produced the gold nanoparticles by using the electrolyte of chloride solution (1 mM HAuCl_4 , 0.5 M H_2SO_4) of with cysteine additives. Cysteine (2-amino-3-mercaptopropanoic acid) is a complexing agent which provide helps to deposit the gold particles on the surface of cathode separately. Cysteine also acts as a grain refining agent in the gold nanoparticle deposition. Gold nanoparticles can also be produced by using an electrolyte of chloride solution, as reported by Zhu et al. [23]. They deposited gold nanoparticles on NH_2 -reduced graphene oxide (rGo-NH_2). This modified electrode is used for the determination of adenosine triphosphate. The determination limit of these electrodeposited gold nanoparticles on rGo-NH_2 shows a range from 10 pM to 100 nM.

The morphologies of the deposited gold nanoparticles can be controlled by the deposition parameters. Zhang et al. [24] explored the influences of current densities on the sizes of the deposited gold nanoparticles. They deposited arrays of gold nanoparticles on an indium tin oxide (ITO) glass, as shown in **Figure 2**. It was observed that the particle size decreases with increasing applied current densities. Moreover, the particle densities were found to increase with increasing current density. At the current density of 5.92 mA/cm^2 , the mean size of particles was about 18 nm with broader size distribution and low particle density. When the current density was decreased to 0.75 mA/cm^2 , the particle size was increased with broader size distribution. At the current density to 0.3 mA/cm^2 , only very few big particles were obtained (see **Figure 2(b)**). These results suggest that the overpotential at cathode would decrease with a decrease in the current density, as a result of this, the rate of nucleation become slower. Therefore, the current density is an important factor to control the particle size and density distribution.

The morphology and the particle size of the gold nanoparticles can also be modified by changing the electrodeposition time. El-Said and Fouad [25] deposited the gold nanoparticles on the ITO substrate by using electrolyte of an aqueous solution of 1 mM HAuCl_4 . The authors observed that the particle size of the deposited gold nanoparticles increases with increasing the deposition time from 5 to 15 s, however, the morphology remains unchanged. On further increase of the deposition time to 20 s, a change in the morphology from nanospheres to the nanostars was observed. Again, the morphology of the nanostars remain unchanged for the deposition time

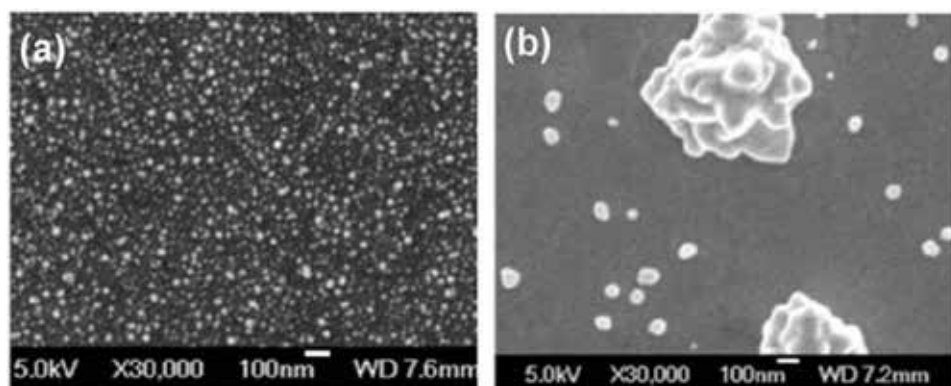


Figure 2. SEM micrographs of gold nanoparticles deposited on the ITO glass substrate at (a) 11 mA/cm^2 and (b) 0.3 mA/cm^2 [24].

25 and 30 s, however, a slight increment in their diameters was observed. A similar type of variation in sizes of gold nanoparticles with respect to deposition time also reported by Sakai et al. [26]. Dependence of particle size on the deposition time can be explained as follows: (a) During the electrodeposition process, formation of nanoparticles starts by nucleation of nuclei on the substrate; (b) The rate of nucleation is faster at the beginning of electrodeposition process; (c) As electrodeposition process proceeds, growth of these nuclei take place; (d) After prolonged deposition time, the whole surface of the substrate is covered by gold nuclei, the rate of nucleation of new nuclei decreases at this stage; (e) After filling of the substrate surface from the nuclei, the growth of nuclei takes by the diffusion process.

5. Electrodeposition of one-dimensional gold nanostructures

Recently, one-dimensional metallic nanostructures such as nanorods, nanotubes, nanowires have received the considerable attention of material scientists due to their unique properties and exciting applications in the field of magnetic storages devices, optoelectronic, cooling system, etc. [27]. One-dimensional gold nanostructures can be synthesized by photolithography and template-based electrodeposition techniques. The photolithography technique is costly due to the high equipment cost, photoresist and developer consumption, high mask cost, etc. For the production of nanorods and nanotubes of different sizes, different masks are required which increase production cost. Despite high production cost, the photolithography technique has emerged as a widely known technique for the production of different sizes of one-dimensional nanostructures such as nanorods and nanotubes. Unlike of the photolithography technique, template-based electrodeposition technique is a simple approach to produce one-dimensional nanostructures in relatively lesser production cost. The porous aluminum oxide (AAO) membranes are most widely used as templates to produce nanostructures. The structure of AAO membrane is regular hexagonal arrays. **Figure 3** shows schematics of the formation of gold nanotubes in AAO membrane. As, it is clear from the schematic diagrams that the morphology of the nanotubes progressively changes from hollow nanotubes to the solid nanotubes with progress in deposition time. The change in the morphology of the nanostructures strongly depends on the electrodeposition process parameters. Template-based electrodeposition technique provides a good control over dimensions of the target, and it can be used to produce a wide range of materials with aligned structure [27].

In template-based electrodeposition technique, before starting the electrodeposition in the template, the template is pre-processed. A thin layer of the conductive layer is sputtered on the bottom side of the template. This conductive layer makes a bridge over the pores and pores remain open. After that, the template is soaked in the deionized water for a certain period by ultrasonication. After ultrasonication of the template, electrodeposition is performed on it.

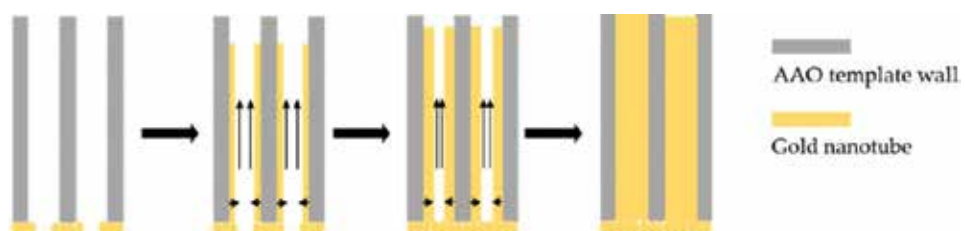


Figure 3.
A schematic diagram of the formation of gold nanotubes from hollow morphology to the solid morphology.

A lot of research has been dedicated to produce the gold nanotubes and nanorods. Wang et al. [27] produced the gold nanowires with tubular-rod structure by the electrodeposition process using the AAO membrane as a template. The average diameter of gold nanowires was about 180 nm and the average height was about 60 μm . The average diameter of the gold nanowires was found to be the same diameter as the average diameter of the pores of the template. To produce this nanostructure, a layer of the platinum on the bottom side of the AAO membrane template was deposited by the sputtering. The sputtering current was 45 mA and the deposition time was 150 s. For the electrodeposition of gold nanowires, chloride solution (5 g/L $\text{HauCl}_4 \cdot 3\text{H}_2\text{O}$, 2 g/L EDTA, 65 g/L Na_2SO_3 , 12.5 g/L K_2HPO_4) was used and the deposition current density was 4.5 mA/cm^2 . EDTA is a polyamino carboxylic acid and it acts as a chelating agent. Polycarbonate templates can also use for the production of gold nanotubes. Mollamahalle et al. [28] successfully electrodeposited gold nanotubes in polycarbonate templates with different lengths even as long as the template thickness (see **Figure 4**). But, for the electrodeposition of long gold nanostructures, the major problem found to be associated with polycarbonate template was the occurrence of blockage of the pores. To eliminate this problem, a coupling agent was used. The coupling agent 3-aminopropyltriethoxysilane (APS) was used to functionalize the pore walls of the template. By the ethoxy groups, the APS molecules are easily attached to the hydrophilic pore walls, while amino groups are faced in the electrolyte. Amino groups have a strong tendency to attract the gold ions which enhance the growth of deposit in the vertical direction of the pores by suppressing growth in the radial direction. A cyanide-based electrolyte was used for the deposition of these gold nanotubes. After electrodeposition of the gold nanotubes, the template was cleaned by using the deionized water to remove any residual impurities on the surface of it. Finally, the template was dissolved in a CH_2Cl_2 solution for 30 minutes to obtain gold nanotube for further characterization.

The length of the gold nanotubes can be controlled by the electrodeposition parameters such as the deposition time, deposition potential, deposition current density, and the electrolyte concentration. Yang et al. [29] studied the effect of the deposition potential and time on the morphology of gold nanotubes which was electrodeposited by using chloride solution in the AAO templates. Growth directions of the gold nanotubes were both along the length as well as along the thickness. However, the preferred growth direction was the thickness of gold nanotubes (see **Figure 3**). The morphology of the gold nanotubes was changed from hollow to solid nanotubes when the electrodeposition time proceeded. Tian et al. [9] reported the electrodeposition of rod-like gold nanostructures from a chloride solution (0.1 M HClO_4 , 4–40 mM HAuCl_4) without using the template. The rod-like nanostructures (100 nm wide and 200–300 nm long) were obtained by applying the negative

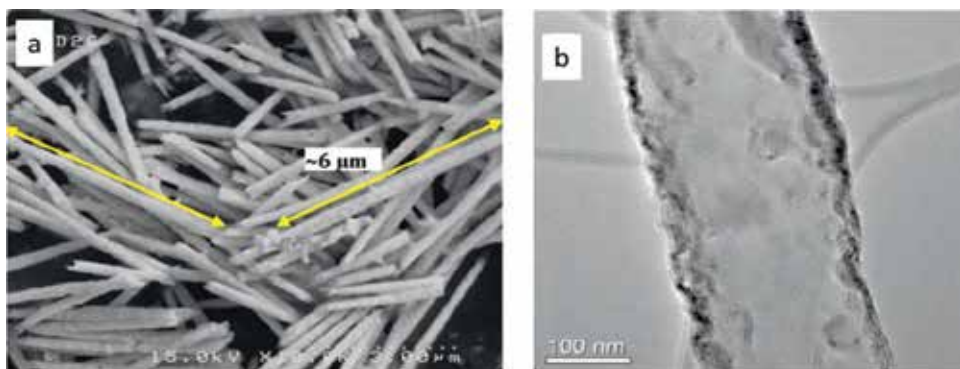


Figure 4. (a) SEM micrograph of gold nanotubes and (b) TEM micrograph of individual gold nanotube [28].

potential of -0.08 V versus Ag/AgCl. The authors observed a change in morphology of rod-like nanostructure of the gold in changing the electrodeposition parameters such as electrolyte concentration and potential. The rod-like morphology was changed to nanopyramidal nanostructures (50–200 nm edge length at the bottom and several hundreds of nanometer in height) when the concentration of HAuCl_4 was increased from 4 mM to 40 mM. On the other hand, spherical nanostructure morphology (70–100 nm in diameter) was obtained when the potential increased from -8 to -2 V keeping the concentration of the HAuCl_4 at 40 mM.

6. Electrodeposition of two-dimensional gold nanostructures

In recent years, gold thin films have finds several technological applications in MEMS, optoelectronics, and electronics industries. To enhance the applicability and suitability of gold nanostructure films in the above-mentioned fields, modification of morphology of deposited nanostructure is required to achieve desired properties. Nowadays, there are wide varieties of a thin film of gold deposition methods based on high vacuum, such as sputtering [5], evaporation [6], molecular ion beam [7], and without vacuum such as electrodeposition [2, 4, 14], electroless deposition [30]. Among these methods, electrodeposition method has grown rapidly in recent years due to its time efficiency, cost-effectiveness, and absence of vacuum technology. In this method, the morphology of the deposited gold nanostructure film can also be easily controlled by varying the electrodeposition process parameters. Some of the crucial process parameters influencing the morphology of gold nanostructures films are discussed in given below sub-sections.

6.1 Cathode agitation

During the electrodeposition, the vicinity of mass in the electrolyte near the cathode surface takes place with deposition time. The vicinity of mass leads the poor quality of coating such as (a) phase change, (b) composition variation in coating across the thickness, (c) influence of the stress [12]. The mass transport in the electrodeposition process influences the properties of the coated films or layer [31]. This transport phenomenon could be controlled by the cathode agitation or electrolyte agitation. The cathode agitation can be achieved by the slider-crank mechanism while the electrolyte agitation is achieved by a magnetic stirrer. If the instantaneous linear velocity of the cathode agitation is sinusoidal, then the root mean square velocity of the crank is given by Eq. (4) [4].

$$v_{rms} \approx \frac{r\omega}{\sqrt{2}} \quad (4)$$

where v_{rms} is the root square velocity of the crank, r and ω are the radius and angular velocity of the crank, respectively. The cathode agitation affects the intrinsic stress in the coated gold film. Intrinsic stress decreases with increasing the agitation speed (v_{rms}) [4]. Therefore, cathode agitation could be used as a parameter to control the stress in the gold film.

6.2 Current density

Current density also plays a crucial role in the creation of stresses in the deposited gold film during the electrodeposition process. Pu et al. [4] studied the effect of the current densities on the stresses generated on the deposited gold film during the

electrodeposition process. They investigated this, at the range of current densities from 1.0 to 5.0 mA/cm². The electrolyte temperature and the film thickness were maintained at 55°C and 0.7 μm, respectively for each value of current density. The observed effects of current densities on the generated stresses of the deposited films are shown in **Figure 5**. The results showed that the deposited gold films have compressive stresses of range – 35 to 103 MPa within the range of deposition current densities from 1.0 to 5.0 mA/cm².

It is also reported in the scientific literature [32, 33] that the current density plays a very important role in the occurrence of a transition in growth mode of deposited nano-structured film. Furthermore, the generation of compressive stresses on the deposited gold film can also be evaluated on the basis of its growth mode and incorporation of impurities on it during the electrodeposition process [34, 35]. The adatom insertion into the grain boundaries and inclusion of impurities in the deposited film during the electrodeposition process together are the main suspected sources of generation of compressive stresses on it. However, the relative contribution of these two factors on the generation of compressive stresses on the deposited films is difficult to calculate.

In another study, reported by Kal et al. [2], it was observed that the deposited gold films have tensile stresses when the cyanide-based electrolyte is used. They studied the effect of current densities on the stresses of the deposited films at different annealing temperatures. The results obtained are shown in **Figure 6**. It is interesting to note that the observed trends in stresses with current densities are similar in natures at different annealing temperatures. However, the stresses are sufficiently high at relatively higher annealing temperatures. The result shows that at low current density, the tensile stress value is low and it increases with an increase in the current density till 4 mA/cm², after that it starts to decrease in the further increase in current density at different annealing temperatures. At higher annealing temperature, the grains of the deposited film re-arrange themselves with considerable growth in their sizes. While coming back to room temperature after the annealing, the film structure relaxes. As the thermal coefficient of expansion of the film and substrate is different, the substrate and the film cool down with a different rate that leads to the creation of tensile stresses in the film [36].

In both the results (**Figures 5 and 6**), the behavior of the observed stress with current densities are similar, but, the type of stresses generated in the films are different due to differences in employed electrolytes. Therefore, the nature of the

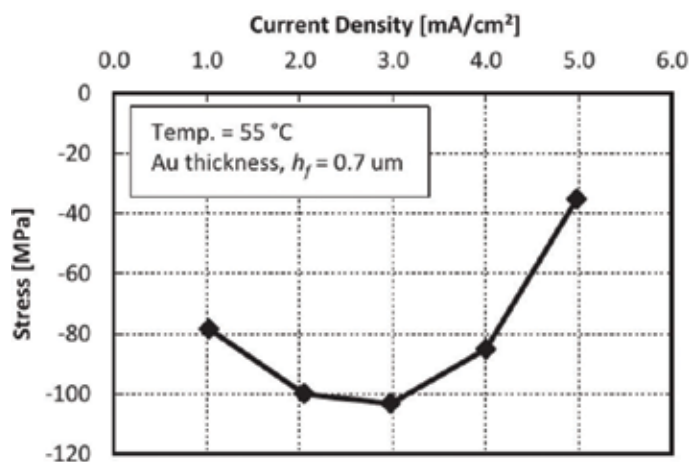


Figure 5. Effect of current density on the stress of the Au-coated film [4].

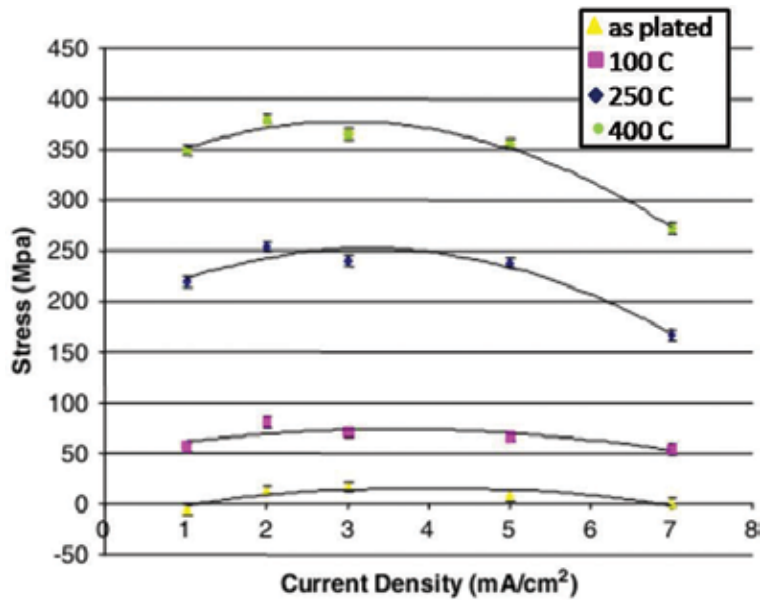


Figure 6.
Stress variation with current density at different annealing temperature [2].

generated stresses on the deposited films can be controlled by changing the current density and electrolyte.

The magnitude of generated residual stress in the gold film can also be controlled by adding the suitable stress-relieving additives in the electrolyte bath. Kelly et al. [17] studied the behaviors of stresses generated in the deposited films with and without adding stress-relieving additives in the electrolyte bath. It was observed that the films deposited without additives in the electrolyte bath had high tensile stresses within the range of 50–80 MPa at the current densities of the range of 1–4 mA/cm². However, with the addition of stress-relieving additive of 25 ppm arsenic ions in the electrolyte bath, the values of stresses in the deposited films were found to decrease with increasing current densities. In this case, at the current densities of the range of 1 to 4 mA/cm², the values of stresses generated in the films were within the range of –10 to –40 MPa,

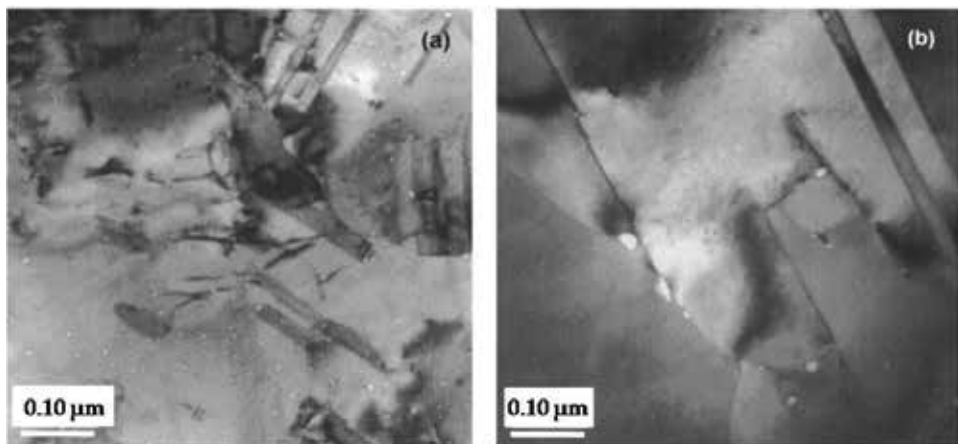


Figure 7.
Plan-view TEM-BF micrographs of gold films deposited at a current density value of 2 mA/cm². Micrographs (a) arsenic-free film and (b) 25 ppm arsenic-containing gold film [2].

respectively. **Figure 7** shows representative the bright field TEM micrographs of the gold film deposited at the current density 2 mA/cm^2 with and without arsenic content. As it is obvious from the TEM micrograph that the arsenic-free film reveals the presence of a high level of porosity (white tinny spots of nanometer range are believed to be nano-pores), twins, and dislocations with moderate (111) orientation. On the other side, the TEM micrograph of the arsenic-containing gold film reveals strong preferred (111) orientation with the relatively lower level of twins, dislocations, and pores. These results indicate that the observed microstructural change in the deposited gold films with and without stress-relieving additives in the electrolytic baths occurred due to their different growth modes which generate different levels of stresses in the final product.

6.3 Electrolyte temperature

The temperature of the electrolyte is also a very important parameter that influences the morphology of the deposited gold film. de Sá et al. [37] studied the effect of electrolytic temperature on the microstructural (morphological) evolution in the deposited gold films at a constant applied potential (-1 V) and a deposition time (1500 s). They employed pyrrolidinium-based ionic liquid electrolyte for the experiments. **Figure 8** shows SEM micrographs of deposited gold films that obtained at different temperatures (293, 333, and 353 K) of the electrolytes and a constant applied potential (-1 V) and deposition time (1500 s). As it is revealed by the micrographs that the continuity and the particle size in the deposited films increase with increasing temperatures of the electrolyte. At relatively higher electrolyte temperatures (333 and 353 K) the particles of deposited gold films were continuous,

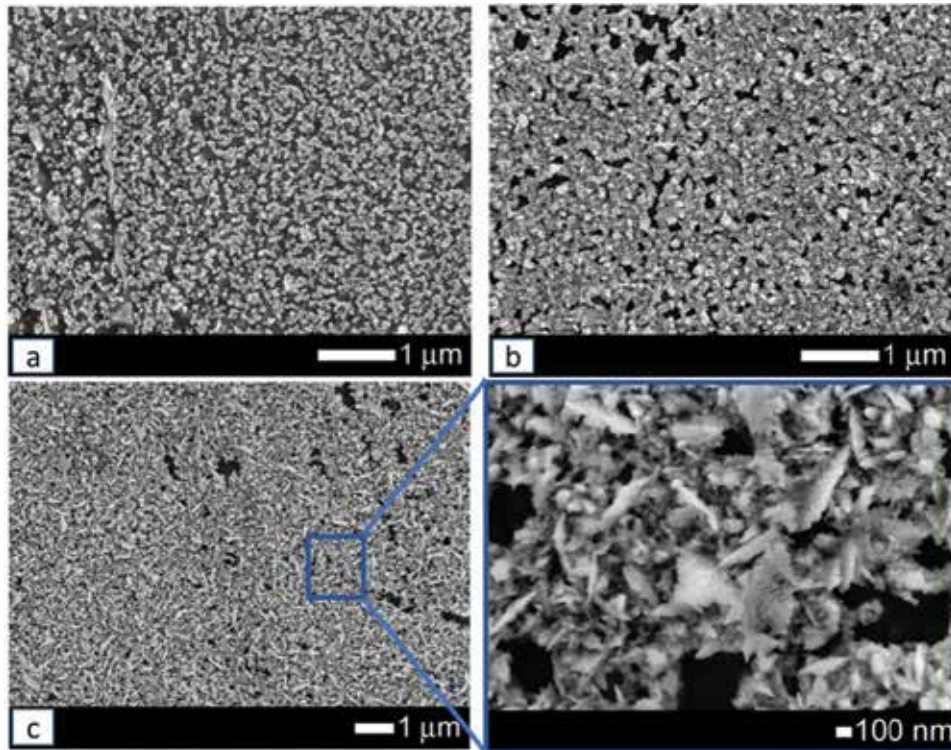


Figure 8. SEM micrograph of gold films deposited at the potential of -1 V during 1500 s at different temperatures of (a) 293 K, (b) 333 K, and (c) 353 K [37].

while at a relatively lower temperature (293 K), the particles in the obtained gold film were discontinuous and poorly adherent with each other. Deposited films have acicular particles with a dendritic kind of morphology on the top surface of the globular film. At a relatively higher temperature of the electrolyte, the deposited film has large dendritic particles with well-developed primary and the secondary arms (see **Figure 8(c)**). The primary arms of the dendrites develop in $\langle 100 \rangle$ direction while the secondary arms in $\langle 111 \rangle$ directions [37, 38].

A similar type of morphology of the particles in the deposited film is also reported by Oyama et al. [39]. They deposited gold film by using an electrolyte solution of NaAuCl₄/EMI-BF₄, the deposition potential of -1 V, and the deposition time of 1000 s. The dendritic gold nanostructure could be grown by increasing the deposition time. The formation of dendritic morphology of the gold nanostructure could be attributed to the prolonged deposition time. The formation mechanism of dendritic nanostructures can be explained by the anisotropic crystal growth and diffusion-limited aggregation (DLA) model [40, 41]. This model says that in the electrodeposition process of the gold nanostructure films on the substrate, initially Au³⁺ ions in the electrolyte rapidly reduces and forms the gold adatom. As deposition proceeds, a large number of gold nuclei accumulates on the surface of the substrate and further grow to form nanoparticles of the gold. These gold nanoparticles hit and stick to each other and form a growth core. The gold nanoparticles accumulate continuously on the growth core and form a backbone of the dendrites after sufficiently large deposition time. As the deposition time becomes prolonged, the concentration of gold salt in the electrolyte decreases. This leads to the formation of new gold nanoparticles which attaches to the surfaces of the dendritic backbone. This oriented attachment of gold nanoparticles in the dendritic backbone looks like new shorter branches [42].

7. Conclusions

In this chapter, an overview of the morphology controlled synthesis of zero-dimensional, one-dimensional, and two-dimensional gold nanostructures by electrodeposition techniques are discussed and presented. Furthermore, the information related to effects of the electrodeposition process parameters (such as current density, deposition time, concentration and nature of electrolyte) in the morphologies of nanostructured gold deposits are provided in detail. Based on the observations of above discussed experimental works of the electrodeposition of the nanostructured gold reported by different groups of researcher the following general conclusions can be drawn.

1. The properties of the electrodeposited nanostructured gold can be simply controlled by tuning its morphology. And, the morphology of the deposited gold can be tuned by changing the electrodeposition process parameters (such as current density, composition, and pH of the electrolyte, addition of suitable additives in the electrolyte, temperature of electrolyte, etc.).
2. The morphologies of the nanostructures gold strongly depend on the nature of the electrolytes used for the electrodeposition process. A cyanide and a noncyanide based electrolyte are found to be suitable for the deposition of the nanostructured gold of different morphologies. The problem associated with the cyanide-based electrolyte is its toxicity and incompatibility with positive photoresist. These problems can be eliminated by replacing cyanide-based electrolyte with an alternative noncyanide-based electrolyte.
3. The morphology and the size of the electrodeposited gold nanoparticles can be controlled by the applied current density and the electrodeposition time.

The particle size of the deposited gold decreases and their density increases with increasing the current density. The particle size of the deposited film also increased with increasing the temperature of the electrolyte. At relatively prolonged deposition time, the growth of the well-developed dendritic kind of morphology in the deposited gold nanostructured film is favored. The lengths and morphologies of the one-dimensional gold deposit such as nanotubes can also be controlled by the deposition time. The length of the nanotubes increases with increasing deposition time. At prolonged electrodeposition time, the morphology of the gold nanotubes changes from hollow to solid nanotubes. The morphology of the one-dimensional nanotubes also changes with changing the concentration of the electrolyte.

4. The stress generated in the gold deposit is unwanted for their application. The generated stresses in the gold deposit can be controlled by the applied current density, nature of the used electrolyte, cathode or electrolyte agitation and post-deposition annealing treatments. The internal stresses increase with increasing the current density, and above the certain current density, the internal stresses start to decrease. The internal stresses in the deposited structures can be minimized by the application of agitation of the electrolyte. The internal stresses reduce with increasing the speed of agitation of the electrolyte by a magnetic stirrer. Also, the stresses in the deposited film can be decreased by post-deposition annealing of the film at a relatively lower temperature. Furthermore, the stresses in the deposit can also be minimized by adding some suitable additives such as arsenic ions in the electrolyte.

Author details


Brij Mohan Mundotiya^{1*} and Wahdat Ullah²

1 National Institute of Technology (NIT), Hamirpur, Himachal Pradesh, India

2 Malaviya National Institute of Technology (MNIT), Jaipur, Rajasthan, India

*Address all correspondence to: brij2010iitrke@gmail.com

IntechOpen

© 2018 The Author(s). Licensee IntechOpen. This chapter is distributed under the terms of the Creative Commons Attribution License (<http://creativecommons.org/licenses/by/3.0>), which permits unrestricted use, distribution, and reproduction in any medium, provided the original work is properly cited. 

References

- [1] Kohl PA. Electrodeposition of gold. In: Schlesinger M, Paunovic M, editors. *Modern Electroplating*. 5th ed. New Jersey: Wiley; 2011. pp. 115-130. DOI: 10.1002/9780470602638
- [2] Kal S, Bagolini A, Margesin B, Zen M. Stress and resistivity analysis of electrodeposited gold films for MEMS application. *Microelectronics Journal*. 2006;**37**:1329-1334. DOI: 10.1016/j.mejo.2006.07.006
- [3] Dimitrijević S, Rajčić-Vujasinović M, Alagić S, Grekulović V, Trujić V. Formulation and characterization of electrolyte for decorative gold plating based on mercaptotriazole. *Electrochimica Acta*. 2013;**104**:330-336. DOI: 10.1016/j.electacta.2013.04.123
- [4] Pu SH, Holmes AS, Yeatman EM. Stress in electroplated gold on silicon substrates and its dependence on cathode agitation. *Microelectronic Engineering*. 2013;**112**:21-26. DOI: 10.1016/j.mee.2013.05.019
- [5] Andersen HH, Bay HL. Heavy-ion sputtering yields of gold: Further evidence of nonlinear effects. *Journal of Applied Physics*. 1975;**46**:2416-2422. DOI: 10.1063/1.321910
- [6] Fan H, Yang K, Boye DM, Sigmon T, Malloy KJ, Xu H, et al. Self-assembly of ordered, robust, three-dimensional gold nanocrystal/silica arrays. *Science*. 2004;**304**:567-571. DOI: 10.1126/science.1095140
- [7] Wu ZH, Mei XY, Kim D, Blumin M, Ruda HE. Growth of Au-catalyzed ordered GaAs nanowire arrays by molecular-beam epitaxy. *Applied Physics Letters*. 2002;**81**(27):5177-5179. DOI: 10.1063/1.1532772
- [8] Elias J, Gizowska M, Brodard P, Widmer R, de Hazan Y, Graule T, Michler J, Philippe L. Electrodeposition of gold thin films with controlled morphologies and their applications in electrocatalysis and SERS. *Nanotechnology* 2012;**23**:255705 (7 pp). DOI: 10.1088/0957-4484/23/25/255705
- [9] Tian Y, Liu H, Zhao G, Tatsuma T. Shape-controlled electrodeposition of gold nanostructures. *Journal of Physical Chemistry B*. 2006;**110**:23478-23481. DOI: 10.1021/jp065292q
- [10] Chu W, Schattenburg ML, Smith HI. Low-stress gold electroplating for X-ray masks. *Microelectronic Engineering*. 1992;**17**(1-4):223-226. DOI: 10.1016/0167-9317(92)90046-T
- [11] Chiu SL A. Electrodeposition of low stress gold for X-ray mask. *Journal of Vacuum Science & Technology B: Microelectronic Processing and Phenomena*. 1990;**8**(6):1589-1594. DOI: 10.1116/1.585121
- [12] Dauksher WJ, Resnick DJ, Johnson WA, Yanof AW. A new operating regime for electroplating the gold absorber on X-ray masks. *Microelectronic Engineering*. 1994;**23**(1-4):235-238. DOI: 10.1016/0167-9317(94)90145-7
- [13] Feng X, Huang Y, Rosakis AJ. On the Stoney formula for thin film/substrate system with nonuniform substrate thickness. *Transactions of the ASME*. 2007;**74**:1276-1281. DOI: 10.1115/1.2745392
- [14] Bozzini B, Giovannelli G, Natali S, Fanigliulo A, Cavallotti PL. Crystallographic structure of gold films electrodeposited at low current densities. *Journal of Materials Science*. 2002;**37**:3903-3913. DOI: 10.1023/A:1019655522750
- [15] Josell D, Levin I, Moffat TP. Morphological transitions during au

- electrodeposition: From porous films to compact films and nanowires. *Journal of the Electrochemical Society*. 2015;**162**(12):D556-D567. DOI: 10.1149/2.0221512jes
- [16] Du J, Di J. Electrodeposition of blue gold thin film onto indium tin oxide coated glass. *Advanced Materials Research*. 2011;**287-290**:2271-2274. DOI: 10.4028/www.scientific.net/AMR.287-290.2271
- [17] Kelly JJ, Yang N, Headley T, Hachman J. Experimental study of the microstructure and stress of electroplated gold for microsystem applications. *Journal of The Electrochemical Society*. 2003;**150**(6):C445-C450. DOI: 10.1149/1.1573197
- [18] Kato M, Okinaka Y. Some recent developments in non-cyanide gold plating for electronics applications. *Gold Bulletin*. 2004;**37**(1-2):37-44. DOI: 10.1007/BF03215515
- [19] Sadyrbaeva T. Electrolysis system for electrodeposition of gold from non-cyanide solutions. *Scientific Journal of Riga Technical University: Material Science and Applied Chemistry*. 2011;**23**:13-16
- [20] Green TA. Gold electrodeposition for microelectronic, optoelectronic and microsystem applications. *Gold Bulletin*. 2007;**40**(2):105-114. DOI: 10.1007/BF03215566
- [21] Green TA, Roy S. Speciation analysis of Au(I) electroplating baths containing sulfite and thiosulfate. *Journal of the Electrochemical Society*. 2006;**153**(3):C157-C163, 10.1149/1.2164724
- [22] Dolati A, Imanieh I, Salehi F, Farahani M. The effect of cysteine on electrodeposition of gold nanoparticle. *Materials Science and Engineering B*. 2011;**176**:1307-1312. DOI: 10.1016/j.mseb.2011.07.008
- [23] Zhu L, Liu Y, Yang P, Liu B. Label-free aptasensor based on electrodeposition of gold nanoparticles on graphene and its application in the quantification of adenosine triphosphate. *Electrochimica Acta*. 2015;**172**:88-93. DOI: 10.1016/j.electacta.2015.04.100
- [24] Zhang K, Wei J, Zhu H, Ma F, Wang S. Electrodeposition of gold nanoparticle arrays on ITO glass as electrode with high electrocatalytic activity. *Materials Research Bulletin*. 2013;**48**:1338-1341. DOI: 10.1016/j.materresbull.2012.12.029
- [25] El-Said WA, Fouad DM. Size and morphological controlled of gold nanoparticles based on deposition time. *Trends in Nanotechnology & Material Science*. 2015;**1**:1-5
- [26] Sakai N, Fujiwara Y, Arai M, Yu K, Tatsuma T. Electrodeposition of gold nanoparticles on ITO: Control of morphology and plasmon resonance-based absorption and scattering. *Journal of Electroanalytical Chemistry*. 2009;**628**:7-15. DOI: 10.1016/j.elechem.2008.12.008
- [27] Wang H, Zou C, Yang B, Lu H, Tian C, Yang H, et al. Electrodeposition of tubular-rod structure gold nanowires using nanoporous anodic alumina oxide as template. *Electrochemistry Communications*. 2009;**11**:2019-2022. DOI: 10.1016/j.elecom.2009.08.042
- [28] Mollamahalle YB, Ghorbani M, Dolati A. Electrodeposition of long gold nanotubes in polycarbonate templates as highly sensitive 3D nanoelectrode ensembles. *Electrochimica Acta*. 2012;**75**:157-163. DOI: 10.1016/j.electacta.2012.04.119
- [29] Yang G, Li L, Jiang J, Yang Y. Direct electrodeposition of gold nanotube arrays of rough and porous wall by cyclic voltammetry and its applications of simultaneous determination of ascorbic acid and uric acid.

Materials Science and Engineering C. 2012;**32**:1323-1330. DOI: 10.1016/j.msec.2012.04.004

[30] Whelan JC, Karawdeniya BI, Nuwan YM, Bandara DY, Velleco BD, Masterson CM, et al. Electroless plating of thin gold films directly onto silicon nitride thin films and into micropores. *ACS Applied Materials & Interfaces*. 2014;**6**:10952-10957. DOI: 10.1021/am501971n

[31] Datta M, Landolt D. Fundamental aspects and applications of electrochemical microfabrication. *Electrochimica Acta*. 2000;**45** (15-16):2535-2558. DOI: 10.1016/S0013-4686(00)00350-9

[32] Floro JA, Chason E, Cammarata RC, Srolovitz DJ. Physical origins of intrinsic stresses in Volmer-Weber thin films. *MRS Bulletin*. 2002;**27**(1):19-25. DOI: 10.1557/mrs2002.15

[33] Weil R. The structures of electrodeposits and the properties that depend on them. *Annual Review of Materials Science*. 1989;**19**:165-182. DOI: 10.1146/annurev.ms.19.080189.001121

[34] Angerer H, Ibl N. On the electrodeposition of hard gold. *Journal of Applied Electrochemistry*. 1979;**9**(2):219-232. DOI: 10.1007/BF00616092

[35] Rehrig DL, Mandich NV. Stress determination in pulse electroplated gold deposits. *Transactions of the IMF*. 2001;**79**(5):160-162. DOI: 10.1080/00202967.2001.11871387

[36] Margesin B, Bagolini A, Guarnieri V, Giacomozzi F, Faes A, Pal R, et al. Stress characterization of electroplated gold layers for low temperature surface micromachining. In: *DTIP for MEMS and MOEMS*; May 5-7, 2003. Cannes, France: IEEE; 2003. pp. 402-405

[37] de Sá AI, Eugénio S, Quaresma S, Rangel CM, Vilar R. Electrodeposition of gold thin films from 1-butyl-1-methylpyrrolidiniumdicyanamide Au³⁺ solutions. *Thin Solid Films*. 2011;**519**:6278-6283. DOI: 10.1016/j.tsf.2011.03.135

[38] Zhou P, Dai Z, Fang M, Huang X, Bao J. Novel dendritic palladium nanostructure and its application in biosensing. *Journal of Physical Chemistry C*. 2007;**111**(34):12609-12616. DOI: 10.1021/jp072898l

[39] Oyama T, Okajima T, Ohsaka T. Electrodeposition of gold at glassy carbon electrodes in room-temperature ionic liquids. *Journal of The Electrochemical Society*. 2007;**154**(6):D322-D327. DOI: 10.1149/1.2724706

[40] Witten TA, Sander LM. Diffusion-limited aggregation, a kinetic critical phenomenon. *Physical Review Letters*. 1981;**47**(19):1400-1403. DOI: 10.1103/PhysRevLett.47.1400

[41] Wang S, Xin H. Fractal and dendritic growth of metallic Ag aggregated from different kinds of γ -irradiated solutions. *Journal of Physical Chemistry B*. 2000;**104**(24):5681-5685. DOI: 10.1021/jp000225w

[42] Du X, Zhang Z, Miao Z, Ma M, Zhang Y, Zhang C, et al. One step electrodeposition of dendritic gold nanostructures on β -lactoglobulin-functionalized reduced graphene oxide for glucose sensing. *Talanta*. 2015;**144**:823-829. DOI: 10.1016/j.talanta.2015.07.034

Cu Wiring Fabrication by Supercritical Fluid Deposition for MEMS Devices

Eiichi Kondoh

Abstract

Process technologies that use supercritical CO₂ fluids to fabricate high-aspect-ratio three-dimensional nano- and micro-components are described. Supercritical CO₂ is a state of CO₂ above the critical point. Supercritical CO₂ fluids are used as alternatives to common media (gases and liquids) in MEMS device fabrication to both overcome the drawbacks of these materials and to realize a superior three-dimensional process opportunity. Supercritical fluids behave as both gases and liquids, offer many of the advantages of both, and have zero surface tension. Supercritical fluids are an ideal medium for fabricating very high-aspect-ratio features owing to their superior capability of diffusion transport. As MEMSs have complex and high-aspect-ratio structures, using a supercritical fluid as a process medium in MEMS fabrication provides ideal performance in film coating, plug filling of concave features, and the etching/cleaning of residues. In this chapter, the physicochemical properties of supercritical fluids are first described in terms of MEMS processing, but from a different point of view than that of the common literature on supercritical chemical processing. Next, various applications to thin film processing are described with a focus on interconnect/wiring fabrication of MEMS devices.

Keywords: supercritical fluid, carbon dioxide, electroplating, thin film deposition, interconnect, wiring, electrode

1. Introduction

In MEMS devices, high-aspect-ratio three-dimensional components are employed, and their sizes vary from the nm-scale to the mm-scale. Interconnects and conductor wiring/electrodes are not exceptions.

Si micromachining is a key MEMS technology. Si micromachining has been developed and expanded based on Si integrated circuit fabrication technologies. The step that applies electrically-conductive components to a non-conductive surface is called “metallization”. In Si processing, metallization refers to process steps that place wiring or interconnects on the Si device surface. Vacuum evaporation was employed in the early era of the Noyes patent [1]. Sputtering was soon introduced, and is now the most commonly used metallization process. The progress of Si large-scale integrated circuit (LSI) technology was accomplished in large part by the advancement of vacuum and dry process technologies.

This paradigm changed drastically in 1987 when IBM released Cu metallization technology for ultra-large-scale integrated circuit (ULSI) fabrication. As the dry etching of Cu is not straightforward, Cu is electroplated into trenches or vias—a via is a vertical hole that connects upper and lower layers of horizontal wiring—and the excess Cu is removed by chemical mechanical polishing (CMP). The significance of this is that wet technologies, which were used only for cleaning in advanced ULSI manufacturing, were introduced to metallization. ULSI interconnect metals other than Cu, such as Co and Ru, are now deposited by electrochemical deposition, but vacuum processes are also commonly used in ULSI metallization.

Process scientists and engineers have long used gas, vacuum, and wet technologies in ULSI metallization, utilizing their advantages and minimizing their drawbacks. But what comes next? If vacuum or wet processes impose limitations, what can be done?

MEMSs have more various and complicated structures than LSIs, as their dimensions, operating principles, and functions vary enormously. Wiring that interconnects sensors, actuators, and electronic components takes on different dimensions and shapes, and substrate materials also vary from semiconductors, ceramics, and glasses to polymers. This diversity sometimes challenges the limitations of existing wet and dry processes.

Fortunately, the use of supercritical CO₂ fluid can help to solve some of these issues. Supercritical CO₂ is a fluidic medium that is neither a gas nor a liquid. It has solvent capability and zero surface tension. The application of supercritical CO₂ to LSI processing was attempted for drying [2] and cleaning [3] in the 1990s. Moreover, supercritical CO₂ was commonly used for sticking-/stiction-free drying, which was the simplest application of supercritical CO₂ because no additional chemicals or gases must be added to the CO₂ and the operation temperature is not very high.

This section describes the use of supercritical CO₂ in metal deposition. Cu and related metal deposition is reviewed along with data regarding the fabrication of wiring and interconnects.

2. What is supercritical CO₂ fluid?

Figure 1 shows a phase diagram of CO₂ and depicts the motion of CO₂ molecules. The phases (liquid, gas, solid) of a substance are uniquely defined as a function of pressure and temperature. The phase diagram maps the regions of the phases, and the borders between the phases are called equilibrium lines. The gas-liquid equilibrium line dead-ends at the upper-right, and this point is called the critical point. Above the critical point, the substance behaves as a homogeneous and continuous fluid, neither as a gas nor as a liquid, and this fluid is called a supercritical fluid. The critical point of CO₂ is 7.38 MPa and 31.1°C [4]. CO₂ has a lower critical pressure and temperature than most other industrially-used supercritical fluids such as H₂O.

Supercritical CO₂ fluid has the following superior characteristics: (1) nano-penetration capability comparable to that of a gas, (2) solvent and cleaning capability comparable to a liquid, (3) inert, stable, and safe, (4) zero surface tension, and (5) recyclability. It has been used industrially for the extraction of caffeine, edible oils, essential oils, and aromatic substances. Supercritical CO₂ has also been widely used in electron microscopy to dehydrate biological tissues. This technique is called “critical point drying” and is an essential technique used to prevent the shrinkage of tissues during drying. **Table 1** lists several important properties of gas, liquid, and supercritical CO₂ fluids.

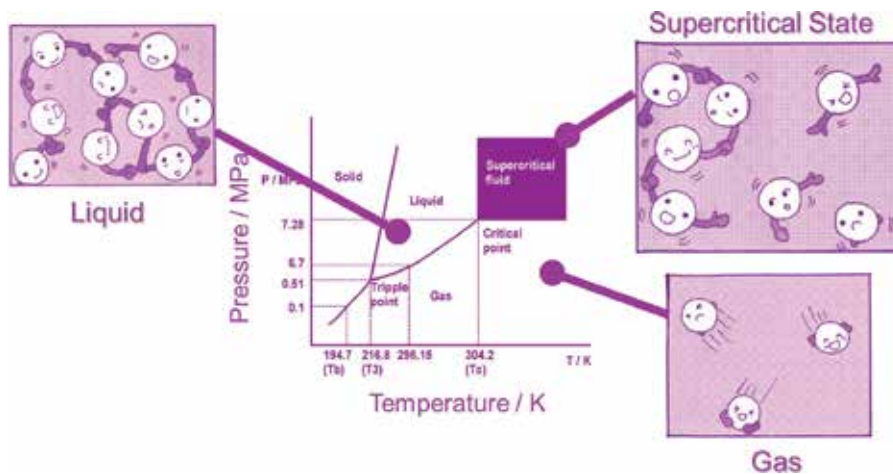


Figure 1. Conceptual phase diagram of CO₂ and a depiction of the motion of molecules.

	Density (kg/m ³)	Viscosity (kg/m/s)	Thermal conductivity (W/m/K)	Diffusion constant (m ² /s)
Liquid	1000	10 ⁻³	0.6	10 ⁻⁹
Supercritical fluid	100	3 × 10 ⁻⁵	0.1	10 ⁻⁷
Gas	0.7	1 × 10 ⁻⁵	0.03	10 ⁻⁵

Table 1. Properties of gas, liquid, and supercritical carbon dioxide fluids.

Several uses of supercritical CO₂ in microelectronics manufacturing have been proposed, such as wafer cleaning and high-aspect-ratio photoresist drying, as mentioned above. In metallization or wire formation, the deposition of highly-conductive metals is of concern. Besides vacuum technology, there are two other commonly used categories of technology for the chemical deposition of metals. One is electrochemical deposition; in our case, electrodeposition (electroplating), in which a thin metal film is formed from metal cations. The other is chemical deposition, in which a thin metal film is formed from metal-containing molecules. Furthermore, electroless deposition can be employed, and will also be discussed.

3. Electrochemical deposition

3.1 Catalyst seeding for electroless plating

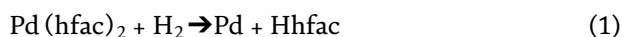
Electroless plating is a series of non-galvanic reactions proceeding thermo-chemically in an aqueous solution. A noble metal catalyst is necessary to start the reactions, in which metal cations are reduced to zero-valence metal atoms by a reduction reagent added to the electrolyte. One very strong advantage of electroless plating is its ability to metallize non-conductive substances such as polymers and glasses. In MEMS devices, electroless plating has a large advantage in fabricating actuators and flexible devices that use polymers as a supporting component.

The adhesion of metals to polymers has been a serious issue in polymer metal-ization, as the attractive forces between metals and polymers are generally weak.

Moreover, the difference in thermal expansion coefficients between metals and polymer is large, which can induce significant internal shear stress at the interface. Metal-polymer delamination can easily occur by either effect between the polymer and the electroless-plated metal or between the polymer and the seeded noble metal catalyst. When the components are large, such as in the automobile industry or in commodity manufacturing, the polymer surface can be roughened by chromic or manganese acids, greatly enhancing adhesion. This is frequently referred to as the “anchor effect”. However, in MEMS and/or microelectronic applications, nanometer precision is required, and such brute force methods cannot be employed.

The use of supercritical CO₂ to catalyze the polymer surface has been proposed. Supercritical CO₂ has a high-diffusivity as well as a low viscosity. It is a non-polar hydrophobic fluid and functions as a plasticizer for hydrophobic polymers [5, 6]. In addition to these characteristics, supercritical CO₂ is a solvent that can dissolve hydrophobic organic compounds, including organometallic complexes. Organometallic complexes that have ligands containing a large alkyl group or a fluorinated group have a higher solubility in supercritical CO₂. For instance, dimethyl(cyclooctadiene)platinum II and hexafluoroacetylacetonatepalladium (Pd(hfac)₂) are known to have high solubility [7]. These dissolved compounds will diffuse towards the free volume of a polymer that has been swelled in supercritical CO₂.

Noble metal complexes can function as catalysts for electroless plating; however, as free metals offer superior catalytic performance, these organometallic compounds are thermally decomposed or reduced by a reduction reagent. One example of this type of reaction is:



Byproducts of this type of reaction dissolve better than the organometallic compounds, therefore, they do not reside in the polymer. Free metal atoms form clusters and/or nanoparticles that are dispersed in the polymer matrix [8].

When a polymer treated in this manner is placed in a plating bath, an electroless deposition reaction starts at the metal catalyst surfaces that are exposed to the bath solution. As the catalyst metal particles are embedded in the polymer, the adhesion between the polymer and the plated metal is improved. Dispersion of the catalyst particles influences the adhesion significantly. The dispersion density and dispersion thickness are tailored by adjusting the conditions of the injection of the complexes, such as the concentration, temperature, and CO₂ pressure. Mixtures of organometallic complexes can also be used.

In this chapter, the application of supercritical CO₂ fluids for electroless plating is described. The fluids are used as a medium to provide a catalyst to a non-conductive surface. The fabrication of Cu-coated aramid fibers [8], liquid crystal polymers [9], and polyimide sheets [10] has been reported. The topic in this chapter does not include a plating process itself, electroless plating in a supercritical CO₂-based fluid was also reported. The design concept of an electroless plating bath is similar to the electroplating described hereinafter.

3.2 Electroplating

In electroplating, an external electric potential is applied to a conductive workpiece in an electrolyte, and a metal film is deposited through electrochemical reactions. Metal ions (cations) are reduced by the electrons injected from the surface of the conductive workpiece. Electroplating offers a high current efficiency,

a large deposition rate, cost effectiveness, low temperature (room temperature) process capability, and the ability to fabricate three-dimensionally complicated components, which is called electrocasting. For these reasons, electroplating has been widely used in various industries to manufacture automobiles, appliances, machine elements, tools and jewelry. In MEMS fabrication processes, electroplating is a commonly used technique for metallization, electrode/wiring formation, and metal component fabrication. LSI Cu metallization and the fabrication of inductors in the pickup heads of magnetic disks are well known nanotech applications of electroplating.

Supercritical CO₂ itself is not electrically conductive or polar, and is not miscible with electrolytes, and Silvestri concluded that supercritical CO₂ is not appropriate as a medium for electrochemical reactions [11]. One way of solving this serious issue is to add a supporting electrolyte to the CO₂, and the synthesis of conductive polymer [12] and Cu plating [13] have been reported.

Sone et al. proposed the use of a supercritical CO₂-aqueous electrolyte emulsion as a medium for electrochemical reactions. Such an emulsion can be formed by adding a surfactant, such as poly(ethylene oxide)alkyl ethers and stirring this mixture above the critical point of CO₂ [14, 15]. Before stirring, the CO₂ and electrolyte are separated, and an apparently single-phase mixture solution, or emulsion is formed when the mixture is stirred intensively. Interestingly, this emulsion is electrically conductive. That is, current paths that connect the anode and cathode exist, and thus electroplating reactions can occur. Sone named this process “supercritical nanoplating,” abbreviated SNP hereinafter (**Figure 2**).

Figure 3 compares the surfaces of electroplated Ni films. The film obtained by SNP using a usual plating solution (Watts bath) as an electrolyte had a smoother surface. On the other hand, the film obtained using the Watts bath alone exhibited pinholes and scratches/grooves. The pinholes originated from H₂ bubbles at the cathode surface and the scratches and grooves reflect the surface roughness of the workpiece. This superior surface smoothness of the SNP sample was thought to be due to good miscibility between H₂ and supercritical CO₂. The H₂ bubbles dissolve in the supercritical CO₂, suppressing the formation of pinholes and improving the surface levelness. The critical role of the supercritical CO₂ in the SNP was confirmed by comparing these results with those of another experiment that used a hexane-electrolyte emulsion—supercritical CO₂ has a similar solvent capability as hexane and hexane is also nonconductive—, and the surface topography of that deposited film was much worse than that shown in **Figure 3** [16].

These advantages of SNP are quite attractive for MEMS component production. Many MEMS components have complicated three-dimensional topography,

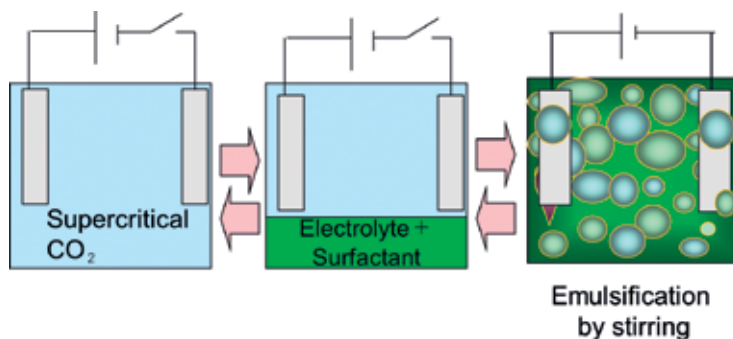


Figure 2. Supercritical nanoplating (SNP). Courtesy of Prof. Masato Sone.

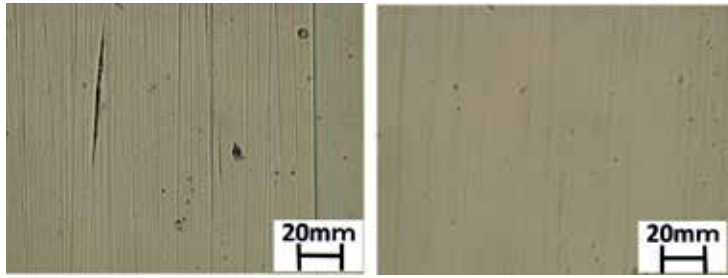


Figure 3. Surfaces of Ni films deposited using a usual Ni plating solution (Watts bath, left) and SNP (right). Courtesy of Prof. Masato Sone.

and this makes it difficult to employ conventional electroplating. The electrolysis reaction competing with the plating reaction produces gaseous H_2 , and the resulting H_2 gas bubbles cause pinholes and voids. Void formation is a serious issue in wiring/interconnect formation, especially for via filling. More H_2 bubbles or voids appear when the plating time is longer or the current density is higher. The sizes of MEMS components are diverse, and a long time and/or a high current density plating process is needed to fabricate large components, which tends to lead to void formation. SNP does not generate bubbles, and Ni micro pillars 50–120 μm in diameter have been successfully formed by electroplating Ni in holes opened in an SU-8 film [17].

SNP of Cu has also been demonstrated. Cu nanoparticles were co-added to a plating emulsion to tailor the distribution of the electric field in the emulsion. **Figure 4** shows cross-sectional transmission electron microscope (TEM) images of Cu-filled LSI test vias 60 nm in diameter and 120 nm in depth. No voids or fill flaws were observed [18]. The Cu grew from the via bottom, so a bottom-up fill was performed, and the via consisted of a single grain texture (111). SNP allows the control of crystallinity by tuning the plating conditions. One difference from ordinary electroplating is that the current path in an SNP bath is generated through the percolation of micelles of the electrolyte. Electrochemical reactions can occur when a chain of micelles is incidentally generated and connects the cathode and anode. This percolation chain is instantly severed, realizing pulse-like electroplating and leading to improved crystallinity and growth rate. The application of supercritical CO_2 fluids to Cu through-Si vias (TSVs) was also reported [19], demonstrating the versatility of this method.

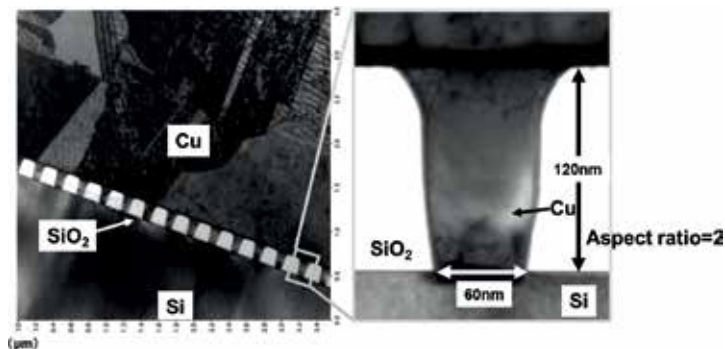


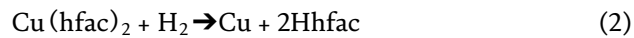
Figure 4. Cross-sectional transmission electron microscope (TEM) images of a Cu via. Courtesy of Prof. M. Sone.

4. Supercritical fluid chemical deposition

4.1 Principle and features

In supercritical fluid chemical deposition, abbreviated SFCD or SCFD, the deposition reactions proceed thermochemically. The precursor is dissolved in the supercritical fluid, and the fluid functions as a reaction medium and is not usually involved in the deposition reaction. This is similar to thermal CVD or metal organic CVD (MOCVD) using an inert gas as a carrier of the precursor. The precursor used in CVD is a gas, at least when supplied to the reaction chamber, and therefore should be volatile. Most metal organic compounds are not very volatile and are mostly solid, as their molecular weight is large, which often leads to difficulty in process design and control and in ensuring safety and cleanliness. However, in SFCD, the precursors are dissolved in the supercritical CO₂ fluid (CO₂ is commonly used) and the good diffusivity of the fluid enables conformal deposition and/or nanofilling, which are crucial for MEMS device fabrication.

For example, a deposition reaction can be stated as:



for the case of Cu deposition [20], where hfac = a hexafluoroacetylacetonate ligand. The byproduct Hhfac (hexafluoroacetylacetonone) has a higher solubility in supercritical CO₂, which means that this reaction preferentially proceeds to the right, the deposition temperature is lower than for the same reaction in the gas, and the deposited Cu contains less impurities. Other noble and near-noble metals such as Ni [21, 22], Co [21], Pd [23], Pt [24], and Ru [25] can be deposited using similar chemistry. Typical temperatures and pressures for Cu deposition are 50–250°C, and 10–20 MPa. These temperatures are higher than those used for supercritical CO₂ drying and cleaning; reactive metals are generally not deposited as they react with the CO₂. Oxides can also be deposited in a similar manner through thermochemical reactions in the fluid that dissolve the precursors. RuO_x [25], TiO₂ [26], SiO₂ [27], ZnO [28], Al₂O₃ [29], Y₂O₃ [30], Bi₂O₃ [31], SrO [32], and other oxides and mixed oxides that are deposited by CVD can also be deposited by SFCD. **Figure 5** illustrates the principles of SFCD for high-aspect-ratio feature filling, and this will be discussed below.

4.2 Film deposition and nano filling

SFCD exhibits superior conformal deposition. The example shown here is the metallization of glass fibers. A few-mm-thick glass fiber textile was immersed in

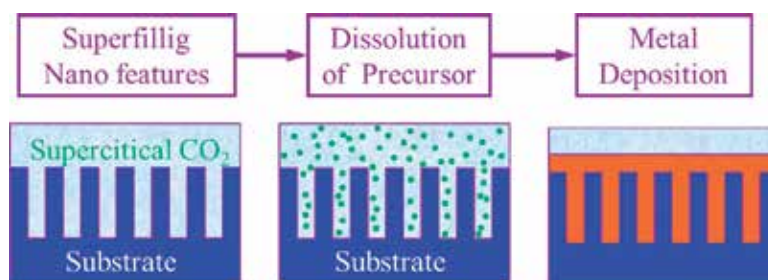


Figure 5.
Principles of metal filling into small features by SFCD.

a supercritical CO₂ solution and Cu deposition was carried out. **Figure 6** shows a cut cross-section after the Cu deposition. Due to good diffusivity and penetrability of the supercritical CO₂, even the deep interior of the textile was successfully metallized.

Supercritical CO₂ is hydrophobic. This means that it can wet deep into complicated structures that have a hydrophobic surface that would repel an electroplating electrolyte. **Figure 7** shows MEMS needles designed for electric bio-tweezers. The needles are made by filling Cu into a PDMS mother die, fabricated by an ordinary MEMS pattern transfer process. One challenge in forming this structure is the coating and filling of Cu into the PDMS while maintaining a sharp tip. One serious issue in Cu metallization is the formation of a seed (electrode) Cu layer directly on the needles. Sputtering is not very useful due to the poor conformability of sputtering. Moreover, overheating and deterioration of the PDMS occurred due to the incidence of energetic ions, as PDMS is thermally insulative. Electroless plating was thought to be a promising alternative technology, but the poor wettability of the electrolyte was a serious issue preventing good film conformability. Cu CVD requires a high temperature and poor nucleation due to weak Cu-PDMS chemical interaction was also problematic. Cu SFCD can avoid all of the above issues. The surface of the PDMS needles was coated with a thin Cu film by SFCD, and then Cu was electroplated using the SFCD Cu layer as a seed layer to thicken the Cu film. The PDMS mother die was detached and self-standing Cu needles remained (**Figure 7**).

Figures 8 and 9 shows electron micrographs of Cu filled into test structures of LSI interconnects (vias and trenches). Nanostructures with aspect ratios of 10–40 were successfully filled. The superior filling capability of SFCD was demonstrated by completely filling 2 nm hydrophobic pores (in a porous low-dielectric constant

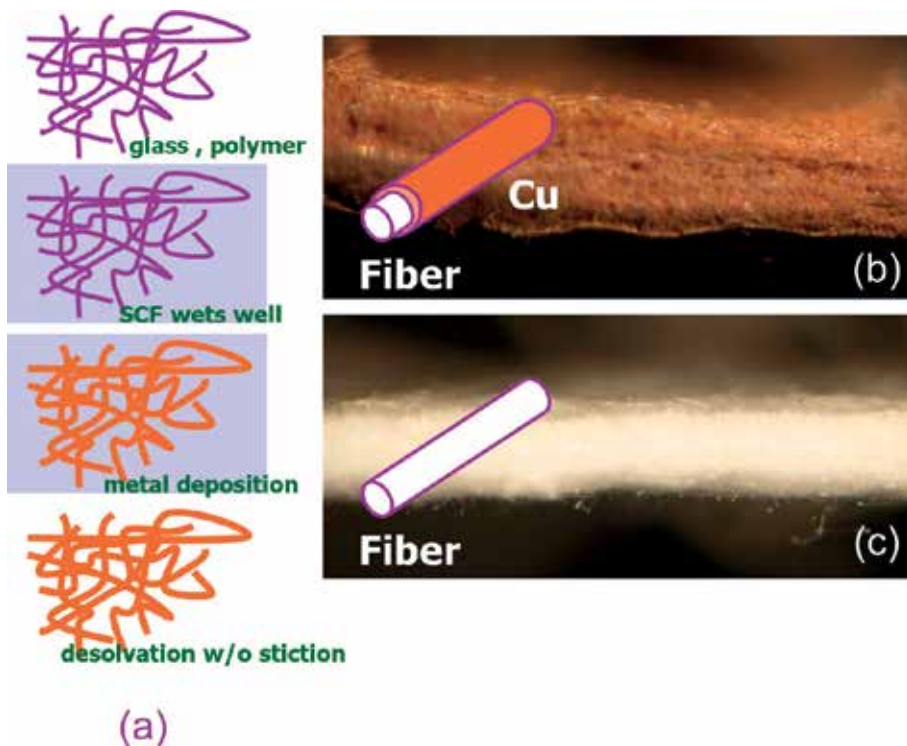


Figure 6. Metallization of glass fibers. Illustrated principle (a), cut cross-sections after (b) and before (c) metallization.

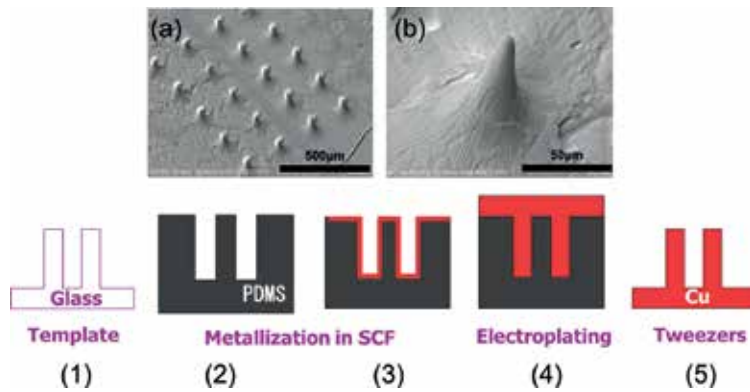


Figure 7. SEM images of Cu bio-tweezers (a, b) and process steps. (1) glass template, (2) pattern transfer to PDMS, (3) seed Cu layer formation by SFCD, (4) Cu electroplating, and (5) detachment of PDMS.

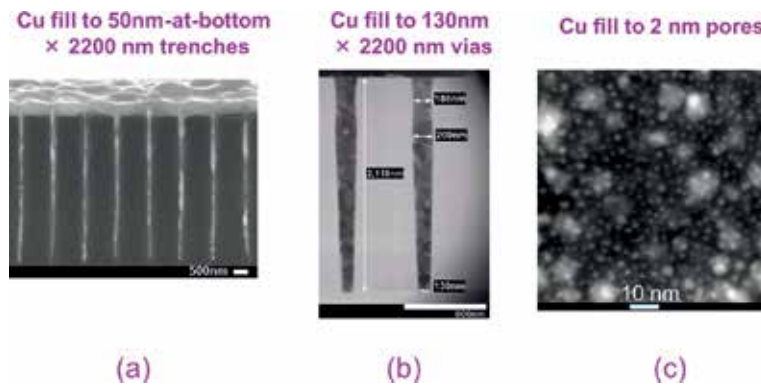


Figure 8. Cu filling into nanoscale features for LSI. (a) Cross-sectional SEM image of 50-nm-wide trenches, (b) cross-sectional TEM image of 130-nm-diameter vias, (c) Cu fill into 5 nm pores.

film) with Cu [33]. Similar outstanding filling capabilities have been repeatedly reported [34, 35]. Other LSI metallization materials such as Ni and Co demonstrate comparable superior filling capabilities [22]. The dimensions of LSI interconnects and wiring are continuously shrinking, while the aspect ratio of the interconnects is increasing; therefore, SFCD is a very attractive technology for LSI interconnect fabrication.

SFCD metallization has also been applied to MEMS-based LSI packaging (Jisso) technologies. One example is the metallization of Si through-vias (Si TSVs) or glass through-vias (TGVs) [36, 37], where high aspect-ratio vias opened by engraving an Si or glass wafer using micromachining technology were metallized with Cu. **Figure 10** shows a cross-sectional optical micrograph of Cu-metallized bent TGVs in a glass interposer. The interposer is a small circuit board that provides interconnects between Si chips attached to it and provides electrical connections to the printed circuit board on which the interposer is mounted. Si and glass are promising next-generation materials, and if the vias can be bended and pass through the interposer, the through-vias will form a faster and shorter electrical circuit inside the interposer body. The aspect ratios of such through-vias are extremely high, and it is a serious issue that there is no practical method to fill the vias or coat the via interior with a diameter of 15 µm and a length of 2 mm (aspect ratio = 130).

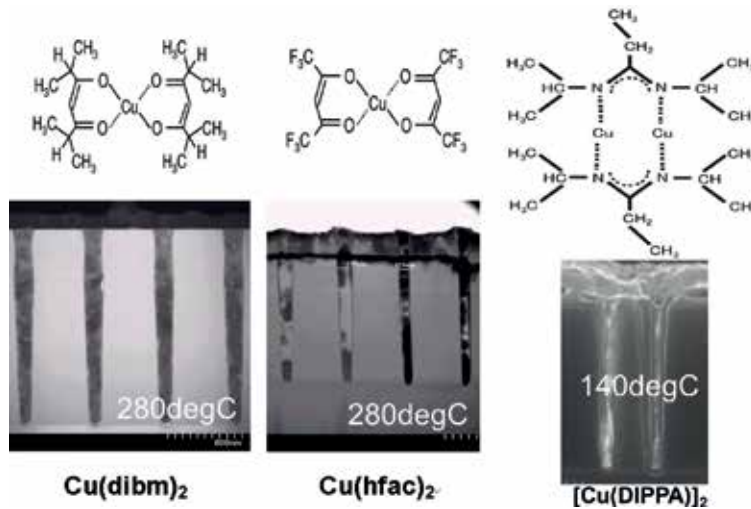


Figure 9. Cu filling into deep nanoscale features using different precursors. Dibm = diisobutyrylmethane, hfac = hexafluoroacetylacetonone, dippa = diisopropylpropion-amidinate.

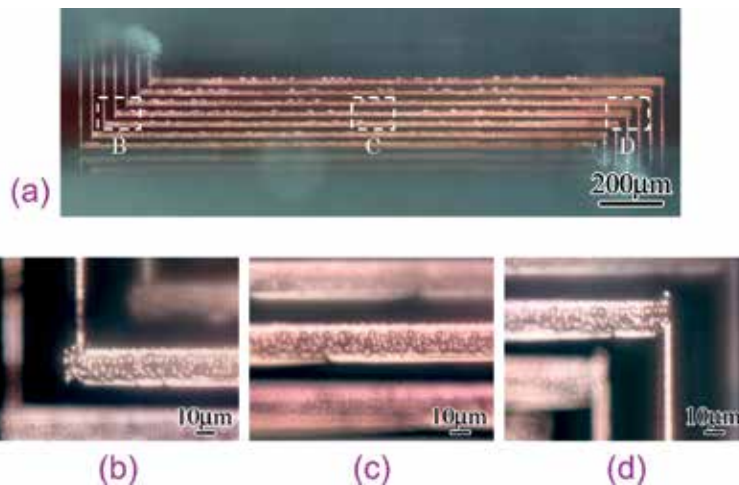


Figure 10. Cu coating inside TGVs with an aspect ratio of 130. (a) Cross-sectional optical micrograph of a glass interposer, and (b), (c), and (d) show enlarged views of regions B, C, and D in (a).

5. Advantages of using supercritical fluids

The general advantages of supercritical fluids have already been described above. Here, we discuss specific advantages over other media (gases and liquids).

First, a supercritical fluid is the best medium for the transport of chemical precursors by diffusion. Many publications on supercritical fluid processing have stated that supercritical fluids have a density as high as that of a liquid and a diffusivity as high as that of a gas. However, as shown in **Table 1**, the density and diffusivity of supercritical CO_2 both have intermediate values, between that of the gas and the liquid. In contrast, the ability to transport a dissolving substance by diffusion, or diffusion flux, becomes the highest, as the diffusion flux is a product of diffusivity and density (see **Figure 11**).

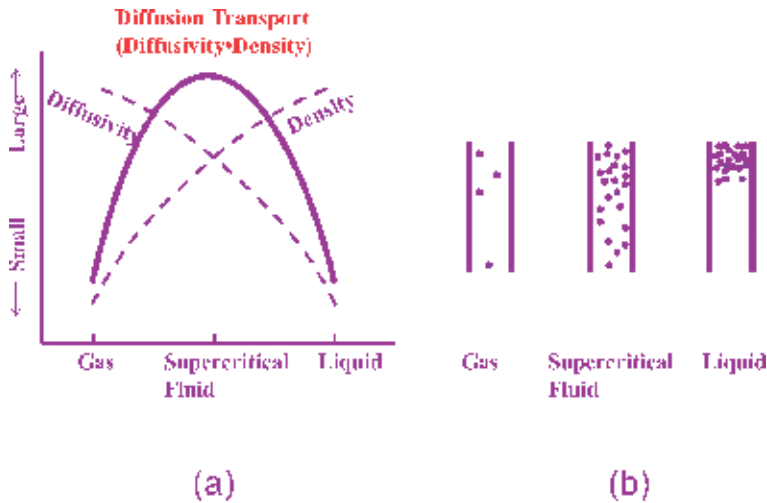


Figure 11. Diffusion flux (a) and molecular motions in small features (b) of gas, liquid, and supercritical fluids.

This is analogous to transport on motorways. In a suburban area, the speed of cars (diffusivity) is high but the number of cars (density) is low, so the overall transportation volume is low. In big cities like Tokyo, Moscow, New York, and Paris, the motorways are heavily backed up (high density), and the cars move slowly (low diffusivity). As a result, the net transportation volume is small. On inter-city motorways, cars run at a moderate speed (medium diffusivity) keeping a moderate inter-vehicle distance (medium density), and therefore the transport volume per a unit time is the highest (**Figure 12**).

Inside high-aspect-ratio features, diffusion transport is the governing transportation mechanism; other transport mechanisms such as advection are negligible especially, inside nanoscale features. Therefore, the supercritical fluid has the best ability to transport chemical precursors deep into small high-aspect-ratio features.

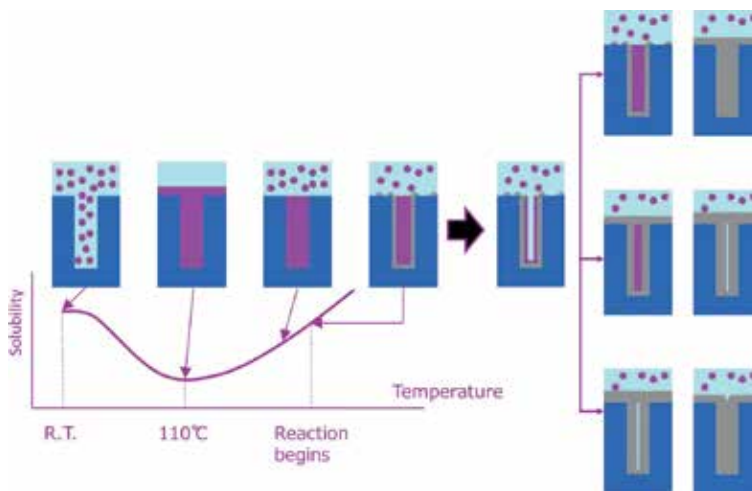


Figure 12. Condensation/precipitation of precursor inside nanoscale features upon temperature change in supercritical medium.

The second distinct feature of the supercritical fluid is its complicated solubility behavior. The solubility of a substance in supercritical CO₂ fluid is a function of temperature and pressure. At high temperatures, the vapor pressure of the solute increases, increasing the solubility, whereas the decrease in the fluid density leads to the decrease in the solvent capability of the fluid, decreasing the solubility. At higher pressures, the fluid density increases and the solvent capability increases, although the high pressure can influence molecular interaction and decrease the solubility. During actual processing, the temperature of the specimen/wafer/workpiece and the pressure of the fluid inevitably change. Such changes can lead to precipitation, liquefaction, condensation, and even re-dissolution of the precursor. Condensation and precipitation occur preferentially in concave nanofeatures, and once the condensation occurs, the condensed phase will not easily re-dissolve into the supercritical CO₂. The condensed phase finally converts to a solid under proper reaction chemistry, resulting in nano-filling.

It should be noted that the above phenomena are unique and distinct characteristics of supercritical CO₂ and do not occur in gas or liquid processes. These characteristics can be observed in terms of nano-deposition and are not obvious or common, even to researchers who work with supercritical fluids. Unique physico-chemical properties of supercritical fluids open possibilities of completely novel nanofabrication technologies.

6. Summary

This chapter described the leading principles of the formation of high quality, high aspect ratio, and three-dimensional wiring and interconnects for MEMS and LSI applications using supercritical CO₂. The unique characteristics of supercritical CO₂ allow it to meet future requirements for increased complexity, miniaturization, and scale divergence of MEMS components.


Common sense as applied in semiconductor wet and dry processes is not applicable in designing supercritical CO₂ processes. There is a lot of room for the development of true novel processes and processors. The future development of supercritical fluid processing must involve rethinking the pros and cons of existing dry and wet processes.

Author details

Eiichi Kondoh
University of Yamanashi, Kofu, Japan

*Address all correspondence to: kondoh@yamanashi.ac.jp

IntechOpen

© 2018 The Author(s). Licensee IntechOpen. This chapter is distributed under the terms of the Creative Commons Attribution License (<http://creativecommons.org/licenses/by/3.0>), which permits unrestricted use, distribution, and reproduction in any medium, provided the original work is properly cited. 

References

- [1] Noyce R. Semiconductor device-and-lead structure. U.S. Patent 2,981,877; 1964
- [2] Namatsu H. Dimensional limitations of silicon nanolines resulting from pattern distortion due to surface tension of rinse water. *Applied Physics Letters*. 1995;**66**:2655-2657. DOI: 10.1063/1.113115
- [3] Saga K, Hattori T. Wafer cleaning using supercritical CO₂ in semiconductor and nanoelectronic device fabrication. *Solid State Phenomena*. 2008;**134**:97-103. DOI: 10.4028/www.scientific.net/SSP.134.97
- [4] Span R, Wagner W. A new equation of state for carbon dioxide covering the fluid region from the triple-point temperature to 1100 K at pressures up to 800 MPa. *Journal of Physical and Chemical Reference Data*. 1996;**25**: 1509-1596. DOI: 10.1063/1.555991
- [5] Watkins JJ, McCarthy TJ. Polymerization in supercritical fluid-swollen polymers: A new route to polymer blends. *Macromolecules*. 1994;**27**:4845-4847. DOI: 10.1021/ma00095a031
- [6] Hirogaki K, Tabata I, Hisada K, Hori T. An investigation of the interaction of supercritical carbon dioxide with poly(ethylene terephthalate) and the effects of some additive modifiers on the interaction. *The Journal of Supercritical Fluids*. 2005;**36**:166-172. DOI: 10.1016/j.supflu.2005.05.004
- [7] Darr JA, Poliakoff M. New directions in inorganic and metal-organic coordination chemistry in supercritical fluids. *Chemical Reviews*. 1999;**99**: 495-542. DOI: 10.1021/cr970036i
- [8] Zhao X, Hirogaki K, Tabata I, Okubayashi S, Hori T. A new method of producing conductive aramid fibers using supercritical carbon dioxide. *Surface and Coating Technology*. 2006;**201**:628-636. DOI: 10.1016/j.surfcoat.2005.12.021
- [9] Ohnuki H, Si S, Takaku S, Hori T. Increased peel strength of copper plating using supercritical fluid methods for epoxy printed circuit boards. *Fiber*. 2011;**67**:245-252. DOI: 10.2115/fiber.67.245
- [10] Rosolovsky J, Boggess RK, Rubira AF, Taylor LT, Stoakley DM, St. Clair AK. Supercritical fluid infusion of silver into polyimide films of varying chemical composition. *Journal of Materials Research*. 1997;**12**:3127-3133. DOI: 10.1557/JMR.1997.0408
- [11] Silvestri G, Gambino S, Filardo G, Cuccia G, Guarino E. Electrochemical processes in supercritical phases. *Angewandte Chemie, International Edition*. 1981;**20**:101-102. DOI: 10.1002/anie.198101011
- [12] Yan H, Sato T, Komago D, Yamaguchi A, Oyaizu K, Yuasa M, et al. Electrochemical synthesis of a polypyrrole thin film with supercritical carbon dioxide as a solvent. *Langmuir*. 2005;**21**:12303-12308. DOI: 10.1021/la050806i
- [13] Ke J, Su W, Howdle SM, George MW, Cook D, Perdjon-Abel M, et al. Electrodeposition of metals from supercritical fluids. *Proceedings of the National Academy of Sciences of the United States of America*. 2009;**106**: 14768-14772. DOI: 10.1073/pnas.0901986106
- [14] Yoshida H, Sone M, Mizushima A, Abe K, Tao XT, Ichihara S, et al. Electroplating of nanostructured nickel in emulsion of supercritical carbon dioxide in electrolyte solution. *Chemistry Letters*. 2002;**11**:1086-1087. DOI: 10.1246/cl.2002.1086

- [15] Yoshida H, Sone M, Mizushima A, Yan H, Wakabayashi H, Abe K, et al. Application of emulsion of dense carbon dioxide in electroplating solution with nonionic surfactants for nickel electroplating. *Surface and Coatings Technology*. 2003;**173**:295-292. DOI: 10.1016/S0257-8972(03)00734-5
- [16] Yan H, Sone M, Sato N, Ichihara S, Miyata S. The effects of dense carbon dioxide on nickel plating using emulsion of carbon dioxide in electroplating solution. *Surface and Coating Technology*. 2004;**182**:329-334. DOI: 10.1016/j.surfcoat.2003.07.006
- [17] Chang T-FM, Tasaki T, Ishiyama C, Sone M. Defect-free nickel micropillars fabricated at a high current density by application of a supercritical carbon dioxide emulsion. *Industrial and Engineering Chemistry Research*. 2011;**50**:8080-8085. DOI: 10.1021/ie200469e
- [18] Shinoda N, Shimizu T, Chang T-FM, Shibata A, Sone M. Cu electroplating using suspension of supercritical carbon dioxide in copper-sulfate-based electrolyte with Cu particles. *Thin Solid Films*. 2013;**529**:29-33. DOI: 10.1016/j.tsf.2012.03.089
- [19] Chuang H-C, Lai W-H, Sanchez S. An investigation of supercritical-CO₂ copper electroplating parameters for application in TSV chips. *Journal of Micromechanics and Microengineering*. 2015;**25**(015004):1-11. DOI: 10.1088/0960-1317/25/1/015004
- [20] Kondoh E, Kato H. Characteristics of copper deposition in a supercritical CO₂ fluid. *Microelectronic Engineering*. 2002;**64**:495-499. DOI: 10.1016/S0167-9317(02)00826-2
- [21] Hunde ET, Watkins JJ. Reactive deposition of cobalt and nickel films from their metallocenes in supercritical carbon dioxide solution. *Chemistry of Materials*. 2004;**16**:498-503. DOI: 10.1021/cm0344433n
- [22] Watanabe M, Osada K, Kondoh E, Okubo S, Hikata T, Nakayama A. Nickel filling in nanofeatures using supercritical fluid and its application to fabricating a novel catalyst structure for continuous growth of nanocarbon fibers. *APL Materials*. 2014;**2**(100701):1-5. DOI: 10.1063/1.4897962
- [23] Fernandes NE, Fisher SM, Poshusta JC, Vlachos DG, Tsapatsis M, Watkins JJ. Reactive deposition of metal thin films within porous supports from supercritical fluids. *Chemistry of Materials*. 2001;**13**:2023-2031. DOI: 10.1021/cm000837t
- [24] Watanabe M, Akimoto T, Kondoh E. Synthesis of platinum-ruthenium alloy nanoparticles on carbon using supercritical fluid deposition. *ECS Journal of Solid State Science and Technology*. 2013;**2**:M9-M12. DOI: 10.1149/2.020301jss
- [25] Kondoh E. Deposition of Ru thin films from supercritical carbon dioxide fluids. *Japanese Journal of Applied Physics*. 2005;**44**:5799-5802. DOI: 10.1143/JJAP.44.5799
- [26] Uchida H, Otsubo A, Itatani A, Koda S. Low-temperature deposition of polycrystalline titanium oxide thin film on Si substrate using supercritical carbon dioxide fluid. *Japanese Journal of Applied Physics*. 2005;**44**:1901-1906. DOI: 10.1143/jjap.44.1901
- [27] Lee H-B-R, Hwang I, Kim J-M, Kim H. Supercritical fluid deposition of SiO₂ thin films: Growth characteristics and film properties. *Journal of the Electrochemical Society*. 2012;**159**:D46-D49. DOI: 10.1149/2.031202jes
- [28] Kondoh E, Sasaki K, Nabetani Y. Deposition of zinc oxide thin films in supercritical carbon dioxide

solutions. *Applied Physics Express*. 2008;**1**(061201):1-3. DOI: 10.1143/apex.1.061201

[29] Barua D, Gougousi T, Young ED, Parsons GN. Supercritical-carbon dioxide-assisted cyclic deposition of metal oxide and metal thin films. *Applied Physics Letters*. 2006;**88**(092904):1-3. DOI: 10.1063/1.2181651

[30] Gougousi T, Chen Z. Deposition of yttrium oxide thin films in supercritical carbon dioxide. *Thin Solid Films*. 2008;**516**:6197-6204. DOI: 10.1016/j.tsf.2007.11.104

[31] Zhao Y, Jung K, Shimoyama Y, Shimogaki Y, Momose T. Conformal bismuth titanate formation using supercritical fluid deposition. *ECS Journal of Solid State Science and Technology*. 2017;**6**:P483-P488. DOI: 10.1149/2.0011708jss

[32] Lee JH, Son JY, Lee H-B-R, Lee SH, Ma D-J, Lee C-S, et al. Supercritical fluid deposition of conformal SrTiO₃ films with composition uniformity in nanocontact holes. *Electrochemical and Solid-State Letters*. 2009;**12**:D45-D47. DOI: 10.1149/1.3092891

[33] Kondoh E, Tamegai Y, Watanabe M, Jin L. Selective Cu filling of nanopores using supercritical carbon dioxide. *Japanese Journal of Applied Physics*. 2015;**54**(05EA02):1-4. DOI: 10.7567/jjap.54.05ea02

[34] Momose T, Sugiyama M, Kondoh E, Shimogaki Y. Conformal deposition and gap-filling of copper into ultranarrow patterns by supercritical fluid deposition. *Applied Physics Express*. 2008;**1**:1-3. DOI: 10.1143/apex.1.097002

[35] Ye X-R, Lin Y, Wang C, Engelhard MH, Wang Y, Wai CM. Supercritical fluid synthesis and characterization of catalytic metal nanoparticles on carbon nanotubes. *Journal of Materials*

Chemistry. 2004;**14**:908-913. DOI: 10.1039/B308124A

[36] Watanabe M, Takeuchi Y, Ueno T, Kondoh E, Yamamoto S, Kikukawa N, et al. Cu coating inside small (15 μm) and ultrahigh-aspect-ratio (>130) through-holes using supercritical CO₂ fluid. *Japanese Journal of Applied Physics*. 2014;**53**(05GA08):1-7. DOI: 10.7567/JJAP.53.05GA08

[37] Matsubara M, Kondoh E. Coverage of copper thin films deposited on the sidewall of through-silicon vias using supercritical fluids. *Hyomen Gijutsu/ Journal of the Surface Finishing Society of Japan*. 2009;**60**:533-539. DOI: 10.4139/sfj.60.533

Pulse-Current Electrodeposition of Gold

*Chun-Yi Chen, Masaharu Yoshiba, Haochun Tang,
Tso-Fu Mark Chang, Takashi Nagoshi, Daisuke Yamane,
Toshifumi Konishi and Katsuyuki Machida*

Abstract

Pulse-current electrodeposition and a sulfite-based electrolyte were used in fabrication of pure gold films. Surface of the pulse-electrodeposited gold film possessed less defect, lower roughness, smaller grain size, and denser texture when compared with the gold film prepared by constant-current electrodeposition. Microstructures and compressive yield strength of the electrodeposited gold could be controlled by regulating the pulse on-time and off-time intervals in pulse-current electrodeposition. The gold film prepared under the optimum conditions showed an average grain size at 10.4 nm, and the compressive yield strength reached 800 MPa for a pillar-type micro-specimen having dimensions of $10\ \mu\text{m} \times 10\ \mu\text{m} \times 20\ \mu\text{m}$ fabricated from the pulse-electrodeposited gold film. Average grain size of the pulse-electrodeposited gold film was much smaller, and the compressive yield strength was much higher than the values reported in other studies. The high strength is due to the grain boundary strengthening mechanism known as the Hall-Petch relationship. In general, the pulse-electrodeposited gold films showed yield strength ranging from 400 to 673 MPa when the average grain size varied by adjusting the pulse-electrodeposition parameters.

Keywords: pulse-current electrodeposition, gold material, micro-mechanical property, micro-compression test, Hall-Petch relationship

1. Introduction

Gold materials fabricated by electrodeposition are commonly used as contact materials in printed circuit boards, electrical connectors, relays, and micro- and nanoscale electronic components for many decades because of the high electrical conductivity, chemical stability, corrosion resistance, and ductility [1–5]. In recent years, gold has become a promising material as movable structures and proof masses in micro-electrical-mechanical system (MEMS) accelerometer devices, because of the high density ($19.3 \times 10^3\ \text{kg/m}^3$ at 298 K), which is about ten times higher than that of silicon ($2.33 \times 10^3\ \text{kg/m}^3$ at 298 K) [6]. However, gold is known to be a soft metallic material. The mechanical strength becomes a concern in further miniaturization of the MEMS device. The yield strength of bulk gold is reported to be 55–200 MPa [7], and the strength can be increased to 550 MPa when using specimens having sub-micro-dimensions because of the size effect [8]. Decreasing

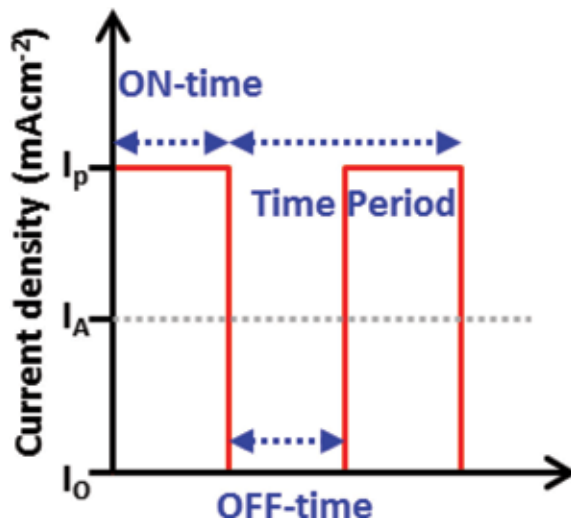


Figure 1.
Illustration of typical pulse-current waveform.

grain size of the gold materials is expected to allow further enhancement of the mechanical properties according to the Hall-Petch relationship [9, 10].

Pulse-current electrodeposition (PCE) has been reported to be effective in fabrication of gold materials with finer grains, higher uniformity, and lower porosity [11, 12] when compared with constant-current electrodeposition (CCE). Also, it is possible to control the microstructure and the film thickness by regulating the pulse-current amplitude (on-time current density and off-time current density) and the width (on-time and off-time interval), as shown in **Figure 1**. Most importantly, an increase in the nuclei density could be achieved to deposit films with finer grains. On the other hand, for evaluating mechanical properties of the deposited films, Vickers microhardness test is the most popular method. However, the hardness characteristics are often affected by the substrate. Vickers microhardness test cannot show the real strength of deposited films, especially for films having thickness in micro-/nanoscale. Therefore, it is necessary to characterize mechanical strength of the electrodeposited gold film by micro-mechanical testing method for practical applications in miniaturized devices.

In this chapter, gold films prepared by the PCE with a sulfite-based electrolyte showed less defect, lower surface roughness, finer grain size, and denser texture when compared with gold films prepared by the conventional CCE. Micro-mechanical properties of gold micro-specimens fabricated from the gold films prepared by the PCE and CCE were evaluated by micro-compression tests. To the best of our knowledge, this is the first report on micro-mechanical characterization of pure gold materials fabricated by PCE. Also, the electrodeposited pure gold film prepared by the PCE showed an ultrahigh strength of 800 MPa, which is the highest value reported for pure gold when compared with values reported in the literature.

2. Electrodeposition of gold

The gold electrolyte used in this study was a commercially available sulfite-based electrolyte provided by Matex Japan. The electrolyte contained 10 g/L of gold with pH of 8.0 and 5% sodium gluconate as the additive. Cu plates and Pt plates were used as the cathode and anode, respectively. For the PCE, the on-time current density (I_{on}) was 10 mA/cm², and the off-time current density (I_{off}) was 0 mA/cm².

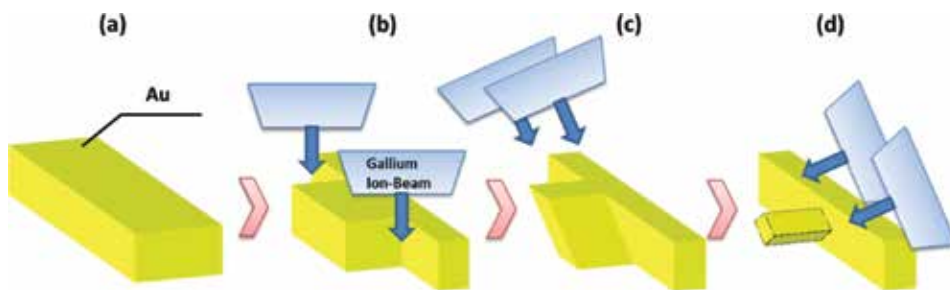


Figure 2. Schematic images showing flow of the pillar-type micro-specimen fabrication steps. (a) Polished electrodeposited gold. (b) Size reduction of the specimen. (c) and (d) Finishing with a low intensity beam at a tilt angle of $45 \pm 1.7^\circ$.

The on-time interval (T_{on}) and the off-time interval (T_{off}) varied from 1 to 10 ms to study the effect on properties of the deposited gold film. The reaction temperature was 60°C for both PCE and CCE. For the CCE, the current density was fixed at 5 mA/cm^2 , which is the same as the average current density of the PCE. A gold film was electrodeposited using a cyanide-based electrolyte containing 20 g/L of gold with pH of 5.0 to be used as the comparison reference specimen. The gold film was electrodeposited on a Pt substrate. The current density was 4 mA/cm^2 , and the temperature was 60°C .

Morphology of the gold films was examined by an atomic force microscope (AFM, XE-100, Park System). The crystallographic structures of the films were investigated by an X-ray diffractometer (XRD, Ultima IV, Rigaku) at a glancing angle of 1.0° . The X-ray was generated by a Cu target operated at 40 kV and 40 mA. Average grain size was calculated using the Scherrer equation.

After the electrodeposition step, pillar-type micro-specimens were fabricated from the gold films by focused ion beam (FIB, FB2100, Hitachi) milling. Details of the fabrication process are shown in **Figure 2**. In order to minimize the tapering effect often observed in the FIB milling, instead of the conventional top-down milling process using irradiation along the pillar axis, the ion beam was irradiated from one side of the pillar at a tilt angle of $45 \pm 1.7^\circ$ as shown in **Figure 2(c)** and **(d)**. Therefore, the tapering effect can be minimized.

Dimensions of the fabricated micro-specimens had a square cross section with $10 \mu\text{m}$ in each side and a height of $20 \mu\text{m}$. The compression tests were carried out using a test machine modified from a micro-indentation machine, which was specially designed for the micro-sized specimens and the compression test. The test machine was equipped with a flat-end diamond indenter and a piezoelectric actuator to control the displacement speed at $0.1 \mu\text{m/s}$. The load resolution was $10 \mu\text{N}$. Observation of the micro-specimens before and after the compression test was conducted using a scanning ion microscope (SIM) equipped within the FIB.

3. Pulse-current electrodeposition of ultrafine nanocrystalline gold

3.1 Properties of the electrodeposited gold film

Figure 3 shows the AFM micrographs of the gold films. The gold film electrodeposited with the cyanide-based electrolyte had hill-like bump morphology and a rough surface as shown in **Figure 3(a)**. The surface roughness (R_a) was 117.1 nm . The gold film prepared by the CCE with the sulfite-based electrolyte showed irregular small dome-shaped bumps having a height of ca. $0.2\text{--}0.25 \mu\text{m}$ as shown in **Figure 3(b)**. On

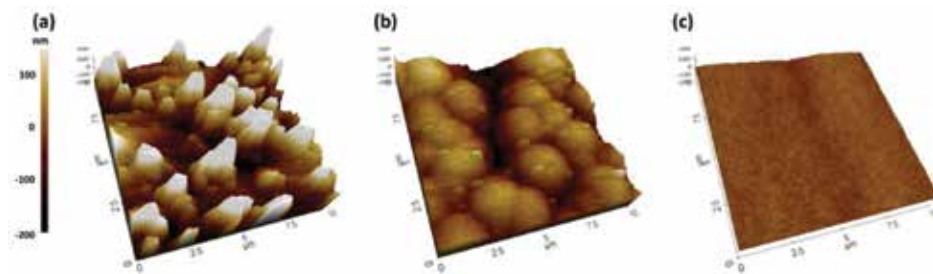


Figure 3. AFM micrographs of (a) the gold film surface prepared by the CCE with the cyanide-based electrolyte, (b) the gold film surface prepared by the CCE, and (c) the PCE with the sulfite-based electrolyte.

the other hand, the gold film fabricated by the PCE with the sulfite-based electrolyte had a smooth and defect-free surface as shown in **Figure 3(c)**. For the CCE with the sulfite-based electrolyte, the surface roughness was 32.5 nm, whereas it was only 10.7 nm for the PCE with the sulfite-based electrolyte. The smooth surface achieved by the PCE is attributed to the enhanced desorption of the hydrogen gas bubbles during the off-time interval of the PCE, because the defects are suggested to be mainly caused by the hydrogen gas bubbles formed along with reduction of the gold ions.

Figure 4 shows XRD patterns of the gold films. All XRD patterns exhibited four peaks corresponding to the (111), (200), (220), and (311) planes of metallic face-centered cubic (FCC) gold (JCPDS No. 04-0784). The XRD results were similar to

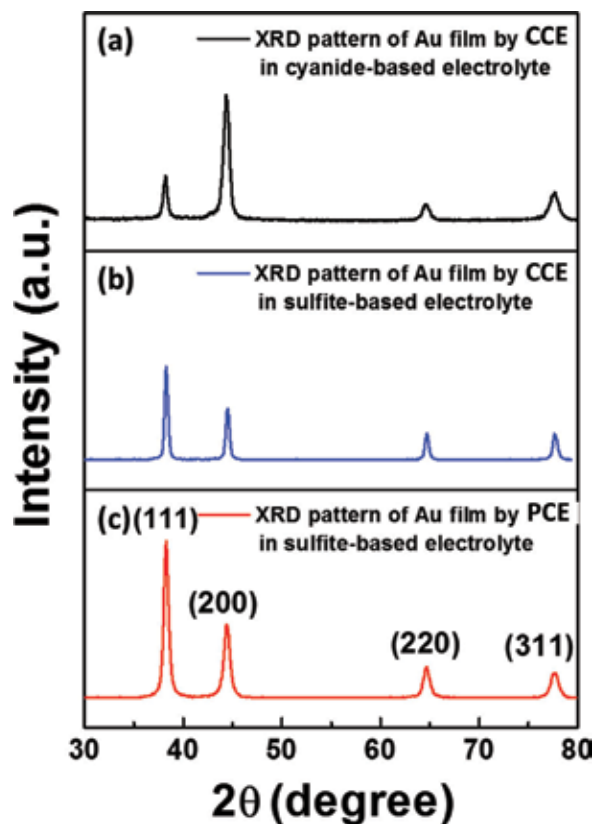


Figure 4. X-ray diffraction patterns of (a) the gold film prepared by the CCE with the cyanide-based electrolyte, (b) the gold film prepared by the CCE, and (c) the PCE with the sulfite-based electrolyte.

the work reported by Bozzini et al. [13]. Unlike the reference gold film prepared with the cyanide-based electrolyte, the gold films fabricated with the sulfite-based electrolyte showed intense (111) orientation. It was reported that the surface energy of the (111) crystal growth orientation is the lowest when compared with the other crystal orientation for FCC metals, such as the (100) and the (110) planes [14]. Moreover, XRD peaks of gold films prepared by the PCE with the sulfite-based electrolyte were broader than those by the CCE. The estimated grain size of the gold film prepared by the PCE was 10.5 nm, which was much smaller than the grain size of 22.8 and 17.6 for the CCE with the sulfite-based electrolyte and the cyanide-based electrolyte, respectively. The grain refinement effect is attributed to the high on-time current density, which results in high nucleation rate during the on-time interval.

In summary, the AFM micrographs and XRD patterns indicate that smooth and defect-free gold film with ultrafine grain size of 10.5 nm can be achieved by the optimized parameters of the PCE. The grain size is smaller than the values reported in previous studies [15–17]. For the optimized PCE parameters, the pulse current is 10 mA/cm² and the off-time current is 0 mA/cm². On-time and off-time of the PCE are both 10 ms.

3.2 Mechanical properties of the gold micro-specimen

Microstructure of the micro-specimens before and after the compression test and the deformation behaviors was observed from the SIM images shown in **Figure 5**.

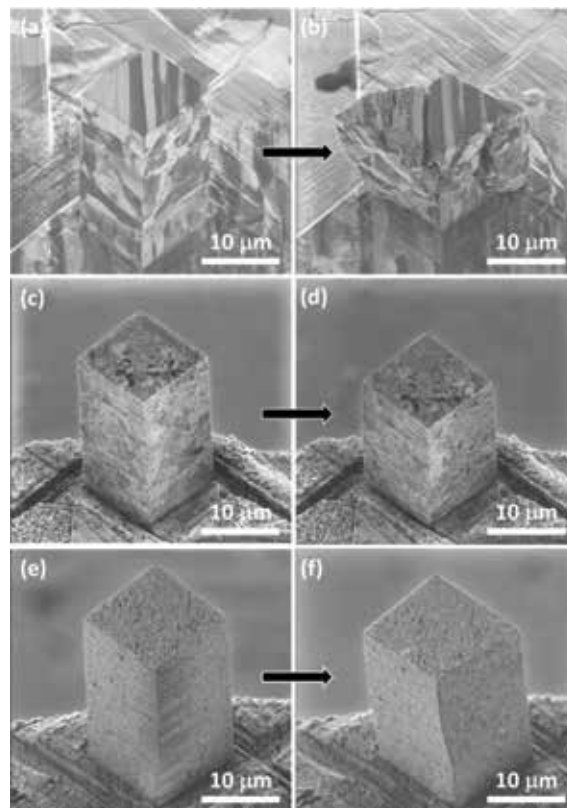


Figure 5. SIM images of the (a) as-fabricated and (b) deformed gold micro-specimens fabricated from the CCE with the cyanide-based electrolyte, (c) the as-fabricated and (d) deformed gold micro-specimens fabricated from the CCE with the sulfite-based electrolyte, and the (e) as-fabricated and (f) deformed gold micro-specimens fabricated from the PCE with the sulfite-based electrolyte.

The ion channeling contrast shown in the SIM images indicates orientation changes of the textures on the sample surface. A gold micro-specimen was fabricated from the cyanide-based electrolyte to act as a comparison, and the results are shown in **Figure 5(a)** and **(b)**. White and gray irregular strip patterns in several μm orders were observed on both the top and sidewall surfaces, and these patterns are attributed to the columnar textures having a direction of perpendicular to the substrate/electrolyte interface. Cracks shown in **Figure 5(b)** indicate brittle fractures along the texture boundary, which suggest the brittle nature of the texture boundary. The grain size obtained from XRD was 17.6 nm, which is far smaller than the size of the patterns observed in the SIM image. While the contrast of the SIM image represents the crystal orientation against the beam direction, the boundaries observed in **Figure 5(a)** and **(b)** should be texture boundaries instead of grain boundaries. Camouflage pattern of the grain/structure was observed on surfaces of the gold micro-specimen prepared from the sulfite-based electrolyte, as shown in the SIM image in **Figure 5(c)**. The gold micro-specimen exhibited broad shear crossing from the top front to the bottom after ca. 10% of deformation, as shown in **Figure 5(d)**, which is similar to the deformation of electrodeposited nanocrystalline Ni [18]. In **Figure 5(e)**, there is no obvious grain/texture boundary on the surface of the gold micro-specimen, which is consistent with the XRD results that fine grains of 10.5 nm were results of the PCE since the SIM could not identify boundaries finer than ca. 1 μm . The ductile deformation shown in **Figure 5(f)** was attributed to the intrinsic property of ultrafine or nanocrystalline materials during the compressive deformation [19]. Although the grain size was different between the gold micro-specimens fabricated from gold films by the CCE and PCE with the sulfite-based electrolyte, the deformation behaviors were similar as shown in **Figure 5(d)** and **(f)**.

Figure 6(a) shows compressive engineering stress-strain curves generated from compression tests of the gold micro-specimens. Deformation behaviors of the micro-specimens prepared from the cyanide-based electrolyte were different from the micro-specimens prepared from the CCE and the PCE with the sulfite-based electrolyte. Yield drops observed in the stress-strain curve generated from compression test of the micro-specimen prepared from the cyanide-based electrolyte may correspond to the cracks observed in **Figure 5(b)**. The cracks are suggested to be caused by the impurities derived from the cyanide-based bath, which lead to a decrease in the adhesion between the textures. The micro-specimens prepared from the sulfite-based electrolyte by the CCE and PCE both showed parabolic hardening generally observed in polycrystalline samples. Notable work hardening observed in the micro-specimen prepared from the PCE with the sulfite-based electrolyte could be a consequence of the reduction in defects by the PCE. A summary of the strengths obtained from this work and from the literatures is shown in **Figure 6(b)**. The strengths obtained in this work followed the Hall-Petch relationships well and reached 800 MPa. To the best of our knowledge, a compressive strength of 800 MPa is the highest value reported for electrodeposited pure gold [7, 8, 20, 21]. Also, the gold film prepared by the PCE showed large work hardening which indicates high ductility and malleability of the material.

3.3 Effects of the on-time and off-time intervals

The T_{on} and T_{off} varied from 1 to 10 ms to study the effect on the microstructure. Detailed information of the PCE parameters is given in **Figure 7**. SIM images of the three micro-specimens fabricated from the gold films pulse electrodeposited with three different on- and off-time combinations are shown in **Figure 8**. **Figure 8(d)–(f)** shows a side view of the micro-specimens A, B, and C, respectively. The contrast observed in the SIM images represents the grain/texture boundaries. Two types of

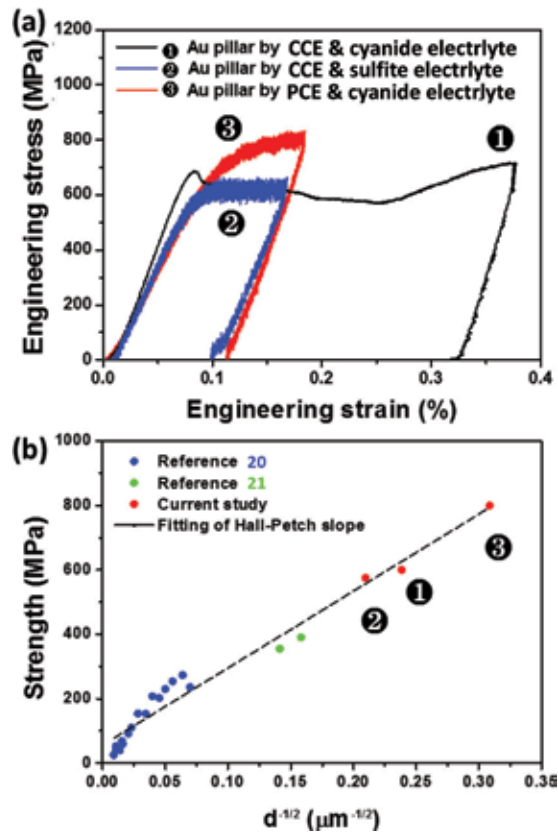


Figure 6.
Engineering stress-strain curves obtained from the micro-compression test of the gold micro-specimens and (b) Hall-Petch plot of polycrystalline gold micro-specimens.

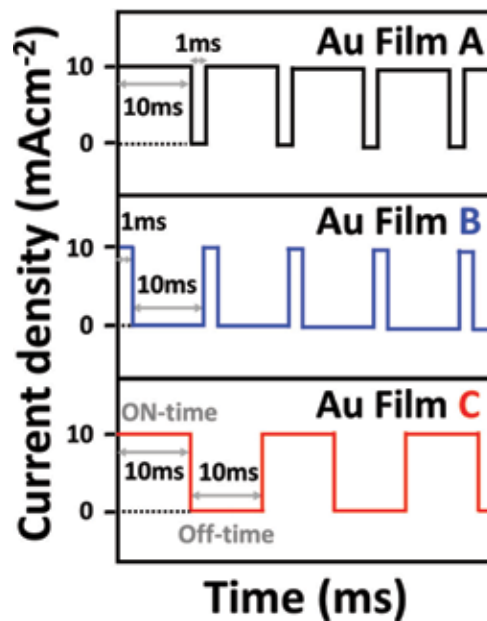


Figure 7.
Parameters of pulse-current waveform used in the PCE-fabricated gold films A, B, and C.

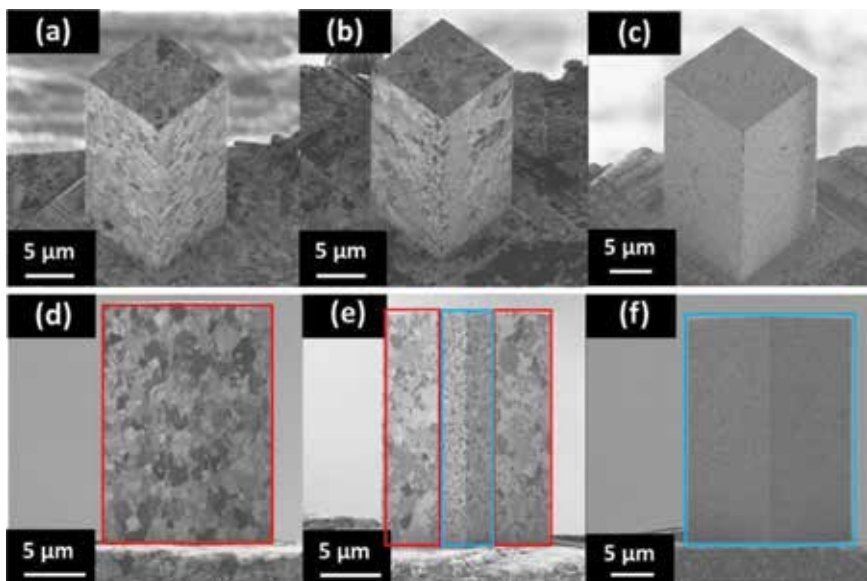


Figure 8.

SIM images of the as-fabricated micro-specimens A (a), B (b), and C (c) and side views of the as-fabricated micro-specimens A (d), B (e), and C (f). In the area surrounded by red full line, grains of several hundred nanometers (shown as red-dotted line) and heterogeneous pattern were observed. In the area surrounded by red full line, no obvious grain/texture boundary was observed.

grain structures were observed between **Figure 8(d)** and **(f)**. For micro-specimen A (**Figure 8(a)** and **(d)**), most of the grains were in micrometer order. Only a few grains having sizes less than 1 μm were observed. One of the relatively large grains is clearly shown in the enlarged image surrounded by red-dotted line in **Figure 8(d)**. The grain structure of micro-specimen A was considered to be composed of non-homogeneous mixture of micro-grains and nano-grains. For the second type shown in micro-specimen C (**Figure 8(c)** and **(f)**), there were no obvious grain/texture boundaries observed from the SIM image. The film was considered to be composed of homogeneous nano-grains, in which details of the boundaries were beyond the detection limit of the SIM. Micro-specimen B (**Figure 8(b)** and **(e)**) showed a mixture of the two grain structure types. The nano-grains similar to those in micro-specimen C were located in the front corner as shown in **Figure 8(b)**.

It could be concluded that intervals of 10 ms for both the T_{on} and T_{off} were the optimized conditions to achieve uniform nano-grains; in such PCE conditions, the grain nucleation dominated in the gold reduction reaction rather than grain growth of the already-existing grains. During the T_{off} interval, the depleted surface concentration of gold ions on the cathode can be replenished by the diffusion of gold ions from the bulk electrolyte, and as-formed by-products during the reaction would diffuse away from the cathode surface. New nuclei are more likely to form because of the high-surface concentration of gold ions during the T_{on} interval. In the case of micro-specimen A, the T_{off} of 1 ms was too short, and it was insufficient for the gold ion replenishment. The low-surface gold ion concentration led to the large grain growth. Also, the short T_{off} promoted continuous growth of the already-existing grains. Therefore, the electrodeposition condition became similar to the CCE, which leads to similar grain structures with the CCE. The results suggest that the T_{on} should be short enough to confirm the gold ion consumed in each T_{on} period, which could be sufficiently replenished during the T_{off} period. When the T_{on} is too long, the electrodeposition condition would be close to the CCE conditions and leads to large grains and occurrence of side reactions. On the other hand, T_{on} cannot be too

short. It should be long enough to allow full charge of the electrical double layer. Otherwise, the reduction reaction cannot be initiated properly. For micro-specimen B, T_{on} of 1 ms may be too short to fully charge the double layer. Moreover, Molina et al. reported that the calculated critical radius of the nuclei of nickel film became much larger, when T_{on} of 1 ms was applied. Also, the nucleation rate is much lower when too short T_{on} was used [22]. The result of micro-specimen B was in agreement with results reported by Molina et al., in which the short T_{on} of 1 ms used in micro-specimen B led to the large grain growth due to the low nucleation rate and large critical size of nuclei.

SEM images of micro-specimens A, B, and C before and after the compression test are shown in **Figure 9**. All the gold micro-specimens showed broad shear crossing from top to bottom of the micro-specimens, and protrusions on sidewalls of the micro-specimen were observed after the deformation. Formation of the protrusions was attributed to the grain boundary slip occurred during the compression test, because the micro-specimens in this study were composed of polycrystals.

Yield strengths of the micro-specimens were determined from the engineering stress-strain curves given in **Figure 10**. By assuming volume conservation during the plastic deformation, the engineering stress σ is defined in the following equation:

$$\sigma = P/S \quad (1)$$

where P is the measured force and S is the cross-sectional area. The engineering strain ε can be calculated as the following equation:

$$\varepsilon = \Delta L/L_0 \quad (2)$$

where ΔL is the applied displacement and L_0 is the initial length of the micro-specimen. Both of the P and the ΔL were acquired by the test machine. The S and the L_0 were both obtained from SEM observations. The flow stresses of micro-specimen A and micro-specimen B were 440 and 600 MPa, respectively. Micro-specimen C showed the highest flow stress of 800 MPa. These differences of flow

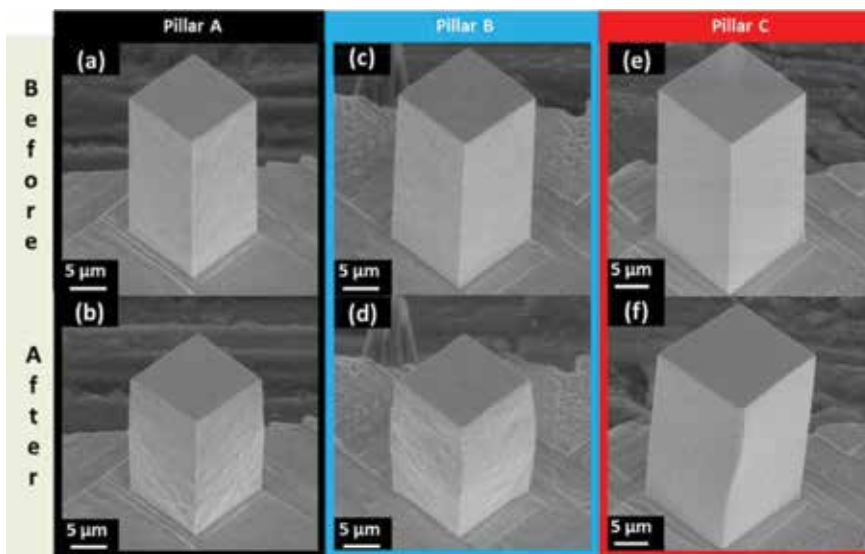


Figure 9. SEM images of the (a) as-fabricated and (b) deformed micro-specimen A, the (c) as-fabricated and (d) deformed micro-specimen B, and the (e) as-fabricated and (f) deformed micro-specimen C.

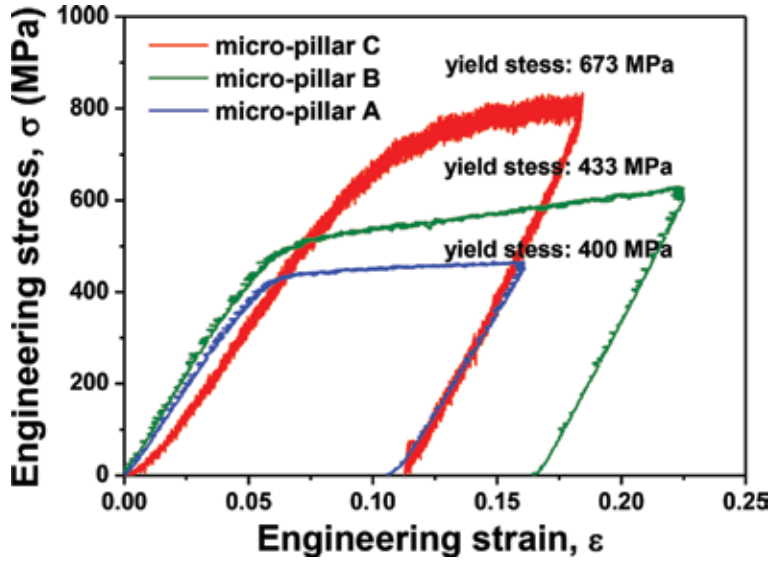


Figure 10. Engineering stress-strain curves obtained from the micro-compression tests of the gold micro-specimens.

stress are due to structural differences, i.e., grain size. As the grain size becomes smaller, the strength becomes higher due to the grain boundary strengthening mechanism or well expressed as the Hall-Petch effect [20]. Hall and Petch had concluded that the yield strength can be expressed as.

$$\sigma = \sigma_0 + k_y d^{-1/2} \quad (3)$$

where σ is the yield strength, σ_0 is a material constant for the starting stress for dislocation movement (or the resistance of the lattice to dislocation motion), k_y is the strengthening coefficient (a constant specific to each material), and d is the average grain diameter. To confirm if the Hall-Petch relationship holds in this work, we measured yield strength and grain size of the films. **Figure 9** shows the yield strength measured at a plastic strain of 0.2%. For micro-specimens A, B, and C, the yield strengths were 400, 433, and 673 MPa (compressive strength of 800 MPa), respectively. Although the yield strength was only slightly higher for micro-specimen A when compared with micro-specimen B, the enhanced work hardening demonstrates the effect of the partially nano-grained region in micro-specimen B. In addition, SEM observation shown in **Figure 8(d)** shows smooth deformation morphology at the front corner of micro-specimen B, which indicates a resistance to the deformation by the nano-grained region. The fully nano-grained micro-specimen C had a yield strength of 673 MPa, which is the highest value for pure gold reported when compared with the literature within our reach [7, 20, 23]. XRD diffraction patterns and the Scherrer equation were used to estimate the grain size of the film C. The Scherrer equation was given in the following equation:

$$g = \frac{\lambda}{\beta \cos\theta} \quad (4)$$

where g , λ , β , and θ are the average grain size, X-ray wavelength (0.15418 nm), full width at half maximum in radians, and Bragg angle, respectively. The estimated grain size was 10.4 nm. The nano-scale grain size agrees well with the outstandingly high strength observed in this work.

In summary, it can be deduced that the T_{on} of 10 ms and T_{off} of 10 ms are the optimum parameters for the PCE of gold with a sulfite-based electrolyte, because the grain size reached ca. 10 nm and the compressive strength of 800 MPa (yield strength of 673 MPa) was much higher than the other micro-specimens evaluated in this study. These results demonstrate that the PCE is promising for MEMS applications since it demonstrates a simple method to control the grain size and the mechanical strength of gold micro-components by regulating the PCE T_{on} and T_{off} intervals.

4. Conclusion

Pulse-current electrodeposition and a non-cyanide sulfite-based electrolyte were used in fabrication of gold films toward fabrication of MEMS components. The pulse-current electrodeposition with different combinations of the T_{on} and T_{off} were investigated to evaluate the influence on the film properties and the micro-mechanical properties. Surface of the PCE gold films possessed less defect, lower roughness, smaller grain size, and denser texture than the gold film prepared by the constant-current electrodeposition. Micro-mechanical properties of the pulse-current plated gold films were evaluated by micro-compression tests using pillar-type micro-specimens fabricated from the gold films by FIB milling. For both the T_{on} and the T_{off} , 10 ms was concluded to be the optimum condition to achieve uniform nano-grained films. The finest grain size reached 10.4 nm for the PCE gold film. The compressive strength was 800 MPa (yield strength of 673 MPa) for the specimen having dimensions of $10\ \mu\text{m} \times 10\ \mu\text{m} \times 20\ \mu\text{m}$ fabricated from the PCE gold film. For the deformation behavior, all the micro-specimens showed promoted surface relief phenomenon after the compression tests. All of the gold micro-specimens had a yield strength higher than 400 MPa, which was much higher than that of the bulk gold. The grain size was much smaller, and the compressive strength obtained was much higher than the values reported in other studies. The high strength is suggested to be due to the grain boundary strengthening mechanism known as the Hall-Petch effect. The results demonstrate that the PCE method with the sulfite-based electrolyte is effective to control the microstructure and enhance the mechanical strength of gold materials for applications in miniaturized electronic devices.

Acknowledgements

This work was supported by JST CREST Grant Number JPMJCR1433 and by the Grants-in-Aid for Scientific Research (S) (JSPS KAKENHI Grant Number 26220907).

Conflict of interest

We have no conflict of interest to declare.

Author details

Chun-Yi Chen^{1*}, Masaharu Yoshiba¹, Haochun Tang¹, Tso-Fu Mark Chang¹, Takashi Nagoshi², Daisuke Yamane¹, Toshifumi Konishi³ and Katsuyuki Machida¹

1 Institute of Innovative Research, Tokyo Institute of Technology, Yokohama, Japan

2 National Institute of Advanced Industrial Science and Technology (AIST), Ibaraki, Japan

3 NTT Advanced Technology Corporation, Atsugi, Kanagawa, Japan

*Address all correspondence to: chen.c.ac@m.titech.ac.jp

IntechOpen

© 2018 The Author(s). Licensee IntechOpen. This chapter is distributed under the terms of the Creative Commons Attribution License (<http://creativecommons.org/licenses/by/3.0>), which permits unrestricted use, distribution, and reproduction in any medium, provided the original work is properly cited. 

References

- [1] Togasaki N, Okinaka Y, Homma T, Osaka T. Preparation and characterization of electroplated amorphous gold-nickel alloy from electrical contact applications. *Electrochimica Acta*. 2005;**51**:882-887. DOI: 10.1016/j.electacta.2005.04.057
- [2] Kato M, Senda K, Musha Y, Sasano J, Okinaka Y, Osaka T. Electrodeposition of amorphous gold alloy films. *Electrochimica Acta*. 2007;**53**:11-15. DOI: 10.1016/j.electacta.2007.01.045
- [3] Yamachika N, Musha Y, Sasano J, Senda K, Kato M, Okinaka Y, et al. Electrodeposition of amorphous Au-Ni alloy film. *Electrochimica Acta*. 2008;**53**:4520-4527. DOI: 10.1016/j.electacta.2008.01.018
- [4] Brun E, Durut F, Botrel R, Theobald M, Legaie O, Popa I, et al. Influence of the electrochemical parameters on the properties of electroplated Au-Cu alloys. *Journal of the Electrochemical Society*. 2011;**158**:D223-D227. DOI: 10.1149/1.3554727
- [5] Homma H. Plating technology for electronics packaging. *Electrochimica Acta*. 2001;**47**:75-84. DOI: 10.1016/S0013-4686(01)00591-6
- [6] Yamane D, Konishi T, Matsushima T, Machida K, Toshiyoshi H, Masu K. Design of sub-1g microelectromechanical systems accelerometers. *Applied Physics Letters*. 2014;**104**:074102-1-074102-4. DOI: 10.1063/1.4865377
- [7] Greer JR, Oliver WC, Nix WD. Size dependence of mechanical properties of gold at the micron scale in the absence of strain gradients. *Acta Materialia*. 2005;**53**:1821-1830. DOI: 10.1016/j.actamat.2004.12.031
- [8] Espinosa HD, Prorok BC, Peng B. Plasticity size effects in free-standing submicron polycrystalline FCC films subjected to pure tension. *Journal of the Mechanics and Physics of Solids*. 2004;**52**:667-689. DOI: 10.1016/j.jmps.2003.07.001
- [9] Hall EO. The deformation and ageing of mild steel: II characteristics of the Lüders deformation. *Proceedings of the Physical Society. Section B*. 1951;**64**:747-753
- [10] Petch NJ. The cleavage strength of polycrystals. *Journal of the Iron and Steel Institute*. 1953;**174**:25-28
- [11] Horkens J, Romankiw LT. Pulsed potentiostatic deposition of gold from solutions of the Au (I) sulfite complex. *Journal of the Electrochemical Society*. 1977;**124**:1499-1505
- [12] Ruffoni A, Landolt D. Pulse-plating of Au-Cu-Cd alloys: II. Theoretical modelling of alloy composition. *Electrochimica Acta*. 1988;**33**:1281-1289. DOI: 10.1016/0013-4686(88)80116-6
- [13] Bozzini B, Fanigliulo A, Serra M. Electrodeposition of star-shaped gold crystallites. *Journal of Crystal Growth*. 2001;**231**:589-598. DOI: 10.1016/S0022-0248(01)01513-5
- [14] Udler D, Seidman DN. Grain boundary and surface energies of fcc metals. *Physical Review B*. 1996;**54**:R11133-R11136
- [15] Lee Y, Ahn SK, Roh Y. Comparison of nanometer-scale gold structures electrodeposited on Au and Pt seed electrode. *Surface and Coating Technology*. 1995;**193**:137-141. DOI: 10.1016/j.surfcoat.2004.07.055
- [16] Chandrasekar MS, Pushpavanam M. Pulse and pulse reverse plating

conceptual, advantages and applications. *Electrochimica Acta*. 2008;**53**:3313-3322. DOI: 10.1016/j.electacta.2007.11.054

[17] Yevtushenko O, Natter H, Hempelmann R. Grain-growth kinetics of nanostructured gold. *Thin Solid Films*. 2006;**515**:353-356. DOI: 10.1016/j.tsf.2005.12.098

[18] Nagoshi T, Mutoh M, Chang T-FM, Sato T, Sone M. Sample size effect of electrodeposited nickel with sub-10 nm grain size. *Materials Letters*. 2014;**117**:256-259. DOI: 10.1016/j.matlet.2013.12.017

[19] Jia D, Ramesh KT, Ma E. Effects of nanocrystalline and ultrafine grain sizes on constitutive behavior and shear bands in iron. *Acta Materialia*. 2003;**51**:3495-3509. DOI: 10.1016/S1359-6454(03)00169-1

[20] Gan Z, He Y, Liu D, Zhang B, Shen L. Hall–Petch effect and strain gradient effect in the torsion of thin gold wires. *Scripta Materialia*. 2014;**87**:41-44. DOI: 10.1016/j.scriptamat.2014.05.011

[21] Emery RD, Povirk GL. Tensile behavior of free-standing gold films. Part II. Fine-grained films. *Acta Materialia*. 2003;**51**:2079-2087. DOI: 10.1016/S1359-6454(03)00007-7

[22] Molina J, Hoyos BA. Modeling of grain size and hardness for pulse current electroplating. *Electrochimica Acta*. 2009;**54**:1784-1790. DOI: 10.1016/j.electacta.2008.10.002

[23] Emery RD, Povirk GL. Tensile behavior of free-standing gold films. Part I. Coarse-grained films. *Acta Materialia*. 2003;**51**:2067-2079. DOI: 10.1016/S1359-6454(03)00006-5

Section 3

Alloy and Composite of
Electrodeposited Noble
Metal

Electrodeposition of Gold Alloys and the Mechanical Properties

*Haochun Tang, Tso-Fu Mark Chang, Chun-Yi Chen,
Takashi Nagoshi, Daisuke Yamane, Toshifumi Konishi
and Katsuyuki Machida*

Abstract

Strengthening of electrodeposited gold-based materials is achieved by alloying with copper according to the solid solution strengthening mechanism. Composition of the Au–Cu alloys is affected by the applied current density. The mechanical properties are evaluated by micro-compression tests to evaluate the mechanical properties in microscale to take consideration of the sample size effect for applications as microcomponents in MEMS devices. The yield strength reaches 1.15 GPa for the micropillar fabricated from constant current electrodeposited Au–Cu film, and the film is composed of 30.3 at% Cu with an average grain size of 5.3 nm. The yield strength further increases to 1.50 GPa when pulse current electrodeposition method is applied, and the Cu concentration is 36.9 at% with the average grain size at 4.4 nm.

Keywords: electrodeposition, gold-based alloys, mechanical property, microcompression test, Hall-Petch relationship, solid solution strengthening

1. Introduction

1.1 Application of Au materials in MEMS devices

In recent years, microelectromechanical system (MEMS) capacitive accelerometers have been developed and used in a variety of consumer electronics for acceleration detection in a range of 1–5 G (1 G = 9.8 m/s²) [1–3]. For applications in medical and health care fields, accurate sensing with sub-1 G detection is necessary to monitor hardly detectable body motions [4, 5]. To detect such low acceleration in a compact sensor module, various types of MEMS accelerometers based on silicon (Si) bulk micromachining have been reported [6, 7]. In order to suppress the thermal-mechanical noise (i.e., Brownian noise (BN) [8]) for the highly sensitive detection, a large proof mass is required. Limited choices of materials for the proof mass and other movable components in a CMOS-MEMS accelerometer have been a major challenge to reduce the BN, which becomes more critical when the parasitic capacitance is reduced in miniaturized devices. Yamane et al. [9–11] propose a miniaturized MEMS accelerometer by using a post-CMOS process with electrodeposited Au in the main components, which enables further size reduction of the proof mass and the device footprint without compromising the sensitivity. With the application of electrodeposited Au in MEMS accelerometers [9–11], a wide range

of acceleration from 1 mG to 20 G can be achieved and are expected to be used in monitoring of hardly detectable body motions.

However, mechanical strengths of Au are much lower than the values of other commonly used materials in electronic devices. For instance, the yield strength of Au is 50–200 MPa in its bulk state [12], and the fracture strength of Si is 1–3 GPa [13], which is one order larger than the strength of Au. The low mechanical strength of Au raises concerns on the structure stability when employed as movable micro-components. In a study on long-term vibration test of microcantilever made of electrodeposited Au, an obvious tip deflection is reported after 10^7 cycles of the vibration [14]. Therefore, strengthening of the Au-based material is necessary to ensure high structure stability for applications in MEMS devices.

1.2 Strengthening mechanisms in electrodeposits

There are four strengthening mechanisms in metallic materials, including work (strain) hardening, grain boundary strengthening, precipitation strengthening, and solid solution strengthening. Except for the work hardening, the other strengthening methods are plausible in the electrodeposits by controlling the electrodeposition conditions. For example, Rashidi et al. [15, 16] report that a finer crystalline grain structure is obtained in the electrodeposited Ni by controlling the electrodeposition parameters such as current density, bath temperature, and additive amount in the aqueous electrolyte. Grain boundary strengthening of the electrodeposited gold is therefore applicable by the grain refinement effect. Classically, the mechanical strength is proportional to inverse square root of the average grain size according to the Hall-Petch Equation [17] given by.

$$\sigma = \sigma_0 + k \cdot d_g^{-0.5} \quad (1)$$

where σ_0 is the friction stress in the absence of grain boundaries, k is a constant, and d_g is the average grain size. In other words, the yield stress increases as the average grain size decreases because pileups in fine-grained materials contain fewer dislocations, and the stress at the tip of the pileup decreases. Thus, a larger applied stress is required to generate dislocations in the adjacent grain. When the average grain size becomes too small, this mechanism breaks down because the grains could not support the dislocation pileups. Typically, breakdown of the Hall-Petch relationship would occur when the average grain size reaches 10 nm in most metals.

Alloying is also one of the commonly applied methods to increase the mechanical strength in electrodeposits. Solid solution strengthening results from the interaction between dislocation and solute atoms can take place. The solute atoms affect the elastic energy of a dislocation due to both local size and modulus changes and act as obstacles to dislocation motions. The alloys could be electrodeposited from a mixed electrolyte containing different metal salts. Schuh et al. [18] reported that the hardness of Ni increased from 1 to 8 GPa by forming Ni–W alloys. Similar strengthening was also reported in Ni–Co [19, 20], Ni–P [21], and Ni–Mn [22] alloys. In addition, alloying of elements having a large difference in the atomic masses would exhibit pronounced strengthening as demonstrated in Cu-based alloys [23].

1.3 Electrodeposition of metallic materials

In metal electrodeposition, current density is often used to control the characteristics in electrodeposits, in particular, grain size. Metal electrodeposition generally follows Butler-Volmer Equation [24], which indicates the current density applied to the electrode is interrelated to the overpotential η :

$$j = j_0 \{ \exp(\alpha_a z F \eta / RT) - \exp(\alpha_c z F \eta / RT) \} \quad (2)$$

$$\eta = E - E_{eq} \quad (3)$$

where j is the current density, j_0 is the exchange current density, z is the number of electrons involved in the electrochemical reaction, F is the Faraday constant, R is the universal gas constant, T is the absolute temperature, α_a and α_c are the anodic and cathodic transfer coefficient, η is the overpotential, E is the electrode potential, and E_{eq} is the equilibrium potential. On the other hand, the nucleation rate (ν) of the metal deposited on the electrode is expressed by the following Equation [25]:

$$\nu = a \cdot \exp(-b \varepsilon^2 / q k_b T |\eta|) \quad (4)$$

where a is a proportionality constant, b is the geometrical factor, ε is the surface energy, and q is the required charges for formation of a monolayer. Combining Eqs. (2) and (4), the nucleation rate can be promoted by an increase in the current density, leading to electrodeposits having a finer-grained structure. In addition, electrodeposition can produce not only pure metals but also alloys with controlled compositions. Alloy electrodeposition can realize further enhancement of the mechanical strength based on the solid solution strengthening mechanism [26, 27].

Pulse electrodeposition is a versatile method that has been proven to produce nanocrystalline materials [28, 29]. Pulse electrodeposition parameters (current on-time, current off-time, and pulse current density) play important roles in controlling the electrodeposition process and hence the microstructure and properties of the electrodeposits [30, 31].

1.4 Mechanical properties of small-scale materials

Microcomponents used in MEMS such as microsprings, cantilevers, and structural support could suffer mechanical straining during employment, and mechanical property evaluation of the specimen in microscale is needed. Conventional indentation or wear tests are widely used to characterize mechanical properties of the electrodeposited metallic materials [32]. However, the obtained results are often affected by the substrate, which may not represent the real information of the microcomponents. Moreover, mechanical properties of materials in microscale are much different from those of bulk materials due to the sample size effect [33]. Since Uchic et al. [34] firstly introduced the uniaxial compression testing of micropillars, a new wave of studies of small-scale plasticity has been explored in numerous materials [35–41]. Therefore, micromechanical tests using specimens (i.e., micropillars [40], microcantilevers [42]) in microscale are recognized as the most reliable method to provide reliable information on the mechanical properties for design of MEMS microcomponents.

2. Electrodeposition of Au–Cu alloys from noncyanide electrolyte

Electrodeposition of Au-based alloys is reported for the uses of decorative jewelry, conductive materials in electronic devices, magnetic materials, or catalysts. For applications in MEMS accelerometers, it is particularly important to have properties such as high mechanical strength, high electrical conductivity, and high density. Au–Ni [43, 44] and Au–Co [45] alloys are reported to show improved

mechanical strength, but their magnetic properties may cause the undesired effects in the MEMS devices. Au–Sn alloys are reported to be soft materials and mainly used for soldering [46]. Among these solute elements, Cu has high electrical conductivity and is widely used in electronic devices. Besides the difference of atomic masses between Au and Cu is large, a pronounced effect of solid solution strengthening is expected. The Au–Cu alloys are usually electrodeposited from the alkaline cyanide electrolyte due to the electrolyte stability [47, 48]. However, such strong alkaline electrolyte cannot be used in the lithography process for fabrication of MEMS components, which would cause damage of the photoresists. In this chapter, we utilize the noncyanide electrolyte to electrodeposit Au–Cu alloys and characterize their properties.

2.1 Fabrication of Au–Cu alloys by constant current electrodeposition

The Au–Cu electrolyte used in this work is a commercially available electrolyte provided by MATEX Co., Japan, which contained 17.3 g/L of $X_3\text{Au}(\text{SO}_3)_2$ ($X = \text{Na}, \text{K}$), 1.26 g/L of CuSO_4 , and EDTA as the additive with pH of 7.5. A potentiostat (Solartron SI1287) is served for applying the constant current. The electrodeposition is carried out at 50 °C, and the current density is varied from 2 to 9 mA/cm². A piece of Pt plate and Cu plate with the same dimensions of 1 × 2 cm² is used as the anode and the cathode, respectively. Two thicknesses of the films are prepared for the characterization. Thin films with a thickness of ~3 μm are used for surface characterization, and thick films with a thickness of ~50 μm are used only for fabrication of the microcompression specimens.

Figure 1 shows surface morphology of the Au–Cu alloy films electrodeposited at various current density. The films deposited at lower current densities exhibited nodular-like structures as shown in **Figure 1(a)** and **(b)**. When a higher current density is used (4–7 mA/cm²), the surface morphology gradually changes to smooth surface condition as shown in **Figure 1(c)**–**(f)**. Large agglomerates of bump clusters are observed on the surface when the current density is higher than 8 mA/cm², as shown in **Figure 1(g)** and **(h)**. Similar morphology is reported for the Au-based alloys electrodeposited at high current density [48].

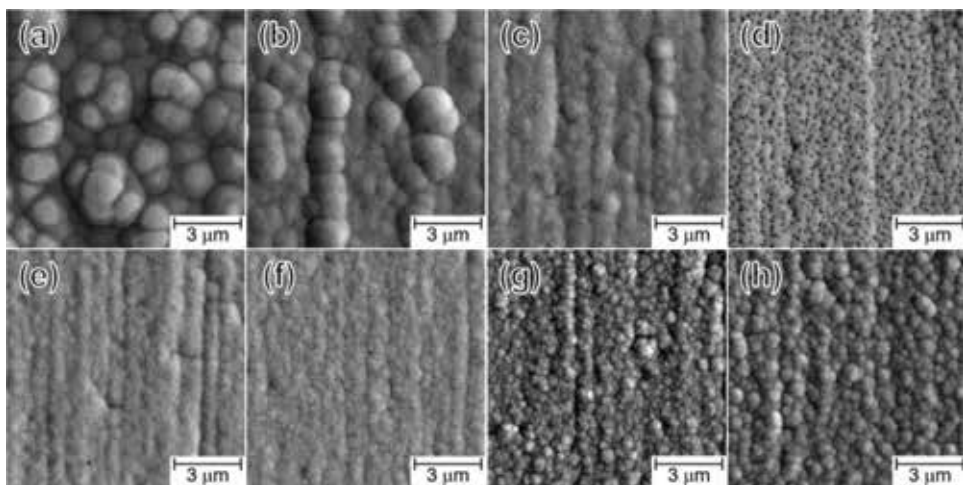


Figure 1. SEM micrographs of the Au–Cu alloy films electrodeposited at current density (a) 2, (b) 3, (c) 4, (d) 5, (e) 6, (f) 7, (g) 8, and (h) 9 mA/cm².

2.2 Crystalline structure and chemical composition of electrodeposited Au–Cu alloys

Figure 2 shows XRD patterns of the Au–Cu alloys electrodeposited at current densities ranging from 2 to 9 mA/cm². Both the (111) and (200) peaks shift continuously to a higher diffraction angle as the current density increases. For instance, the (111) peak shifts from $2\theta = 38.79^\circ$ at the current density 3 mA/cm² to $2\theta = 40.09^\circ$ at the current density 8 mA/cm². The peak shift is suggested to be a result of the increase in the Cu content since the lattice constants of Cu are larger than that of Au. No diffraction peaks from intermetallic nor other ordered phases are observed in the electrodeposited films. Relationships between the current density with average grain size, Cu concentration, and the lattice constant are summarized in **Figure 3**. The average grain sizes are estimated from the XRD results and the Scherrer equation. The grain size is reduced from 8.8 nm to a minimum value of 5.3 nm when the current density is increased from 2 to 6 mA/cm². Grain size of electrodeposited materials is highly dependent on the overpotential, in which grain refinement is observed as the overpotential increased [49]. Based on the Butler-Volmer equation, the overpotential is interrelated to the current density, in which the overpotential increases as the current density increases. Therefore, it is expected to see a reduction in the grain size as the current density increases.

On the other hand, an increased in the grain size is observed when the current density increases beyond 6 mA/cm². Increasing the current density also promotes side reaction(s), such as hydrogen evolution. Because of this, overpotential of the main reactions, which are reduction of Au and Cu in this study, would be lowered when the side reaction(s) is promoted [50]. This should be the cause of the grain

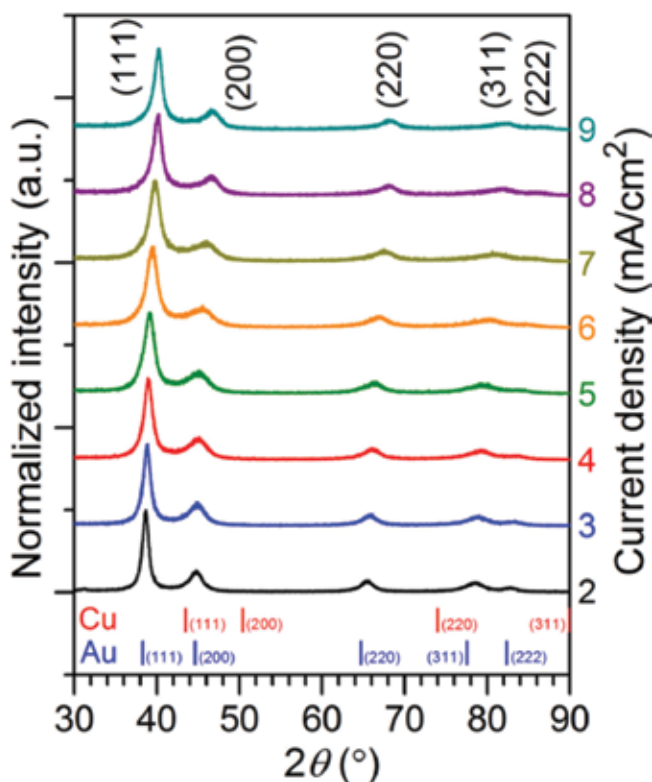


Figure 2. XRD patterns of the Au–Cu alloy films electrodeposited at varied current density.

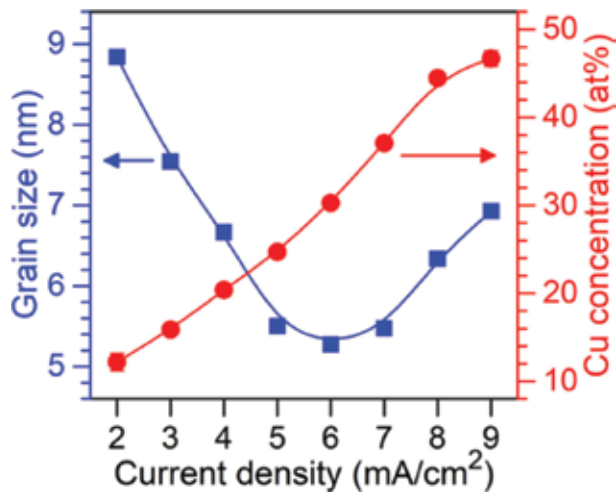


Figure 3.
Plots of the current density versus grain size and Cu concentration.

coarsening observed when the current density is higher than 6 mA/cm². Meanwhile, a sustained increase of the Cu concentration from 12.2 to 46.7 at% is observed when the current density is increased from 2 to 9 mA/cm². The results can be interpreted by the difference in the standard reduction potential between Au and Cu [51]. The standard reduction potential of Cu is more negative than that of Au. An increase in the cathodic current density would make the applied potential to be more negative; hence, reduction of Cu is gradually favored and leads to an increase in the Cu concentration.

2.3 Fabrication of Au–Cu micropillars and micromechanical properties

Micromechanical properties of the Au–Cu alloys are evaluated using micropillars fabricated from the thick Au–Cu films by focus ion beam (FIB, Hitachi FB2100). Fabrication process of micropillar is shown in **Figure 4**. The Au–Cu micropillars have square cross section of 10 × 10 μm² and height of 20 μm. The microcompression tests are conducted with a testing machine specially designed for microspecimens. The compression is conducted at a constant displacement rate of 0.1 μm/s using a piezoelectric actuator.

Figure 5 shows SIM images of the Au–Cu alloy micropillars fabricated from the thick Au–Cu alloy films before and after the microcompression tests. Barrel-shape deformations are observed in the micropillars fabricated from the films electrodeposited at current density 3, 5, and 6 mA/cm², which are typical deformation behaviors for polycrystalline metallic materials [52, 53]. When the current density is further increased to 8 mA/cm², brittle fractures indicated by the cracks along

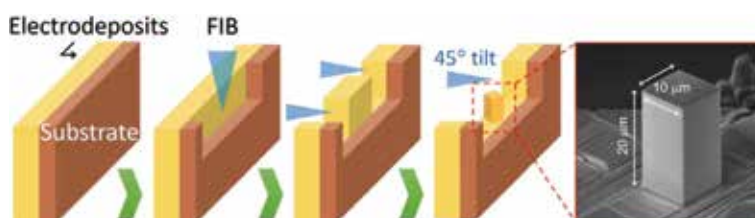


Figure 4.
Fabrication process of micropillars by FIB.

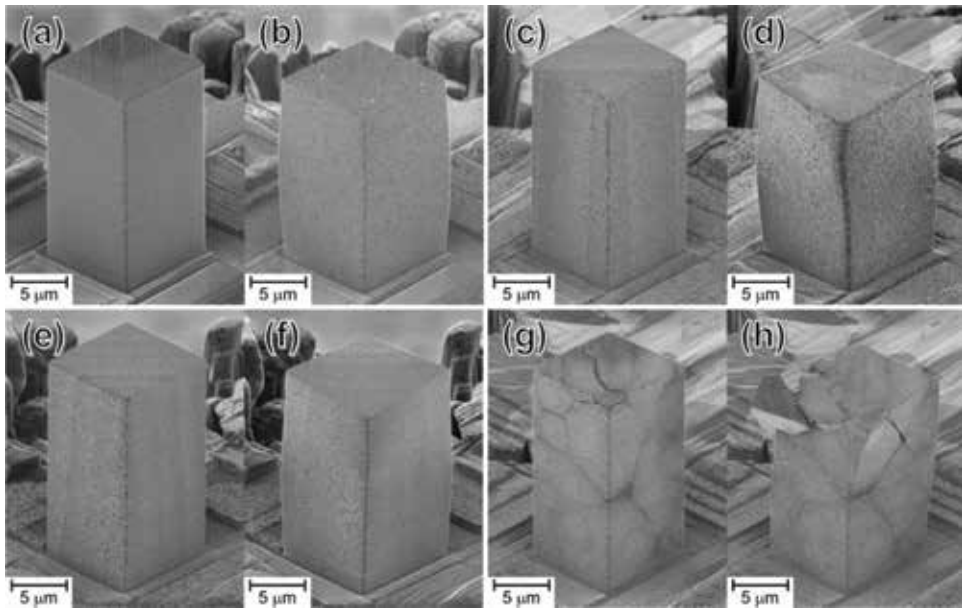


Figure 5. SIM images of the Au–Cu alloy micropillars fabricated from the films electrodeposited at current density (a,b) 3, (c,d) 5, (e,f) 6, and (g,h) 8 mA/cm². (a,c,e,g) Before and (b,d,f,h) after microcompression tests.

boundaries of the agglomerates are observed after the compression test. The Au–Cu alloy film electrodeposited at 8 mA/cm² is composed of nano-grains, which is similar to the film electrodeposited at lower current density of 3 mA/cm²; however, formation of the bump-clustered agglomerates at high current density might be the main cause of the brittle deformation. Au–Cu alloys are known to be highly ductile materials. To the best of our knowledge, this is the first report on brittle fracture of Au–Cu alloys, and this information is essential for the design of components used in MEMS devices.

Engineering strain–stress (SS) curves obtained from the microcompression tests are shown in **Figure 6**. Generally, all the pillars exhibit extremely high yield stress (σ_y , determined by the cross-point of the SS curve and 0.2% offset line of the elastic deformation region) ranged at 1.00–1.15 GPa, which are far larger than the yield

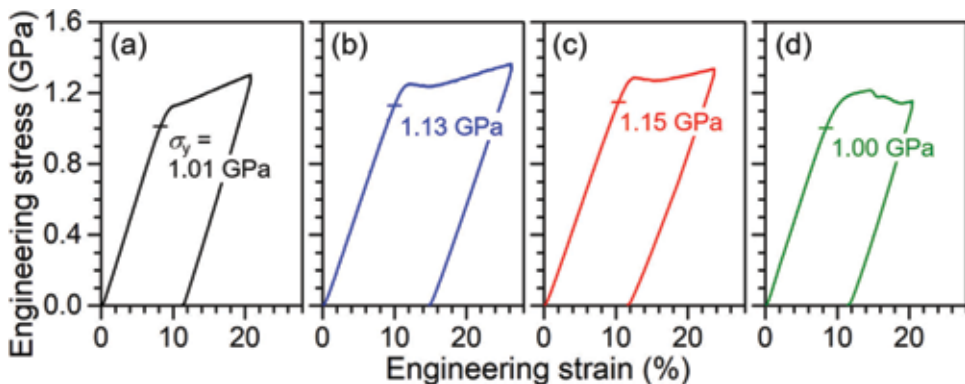


Figure 6. Engineering strain–stress curves of the micropillars fabricated from the films electrodeposited at current density of (a) 3 mA/cm², (b) 5 mA/cm², (c) 6 mA/cm², and (d) 8 mA/cm². The yield strength (σ_y) in each curve is marked by a horizontal bar.

stress obtained from micromechanical tests of pure Au and pure Cu reported in the literature [52, 54]. Flow stresses (σ_f) at 10% plastic strain of all the micropillars are higher than 1.3 GPa except for the micropillar prepared from the film electrodeposited at current density of 8 mA/cm², in which the crack-induced brittle fracture should be the reason of the lowered flow stress.

The enhanced yield stress in the Au–Cu alloys is mainly attributed by the following two mechanisms: (i) grain boundary strengthening [17] and (ii) solid solution strengthening [26, 27]. As shown in **Figure 3**, the grain refinement effect goes along with an increase in the Cu concentration as the current density increases. According to the grain boundary strengthening mechanism, the strength of metallic materials increases as the total amount of grain boundary in a specimen increases, which is also understood as a decrease in the average grain size. Moreover, the solid solution strengthening mechanism could restrict the dislocation movement due to interaction of the dislocations with the strained lattice surrounding the solute atoms, which then leads to a stacked strengthening beyond the grain boundary strengthening mechanism.

3. Pulse current electrodeposition of ultrahigh strength nanocrystalline Au–Cu alloys

3.1 Fabrication of Au–Cu alloys by pulse current electrodeposition

The Au–Cu alloys are electrodeposited on cold-rolled Cu substrates with a commercially available electrolyte (see Section 2.1). Temperature of the electrolyte is maintained at 50 ± 1°C using a water bath. The pulse current electrodeposition is carried out using a pulse power supply (plating electronic GmbH, type pe86CB-20-5-25-S/GD). For all experiments, the current on-time (t_{on}) is fixed at 10 ms, while the pulsed current density (J_p) and the current off-time (t_{off}) are varied. The parameters are summarized in **Table 1**. Thin Au–Cu alloy films with a thickness of 3–5 μm are used for characterization of the composition, grain size, and morphology. Thick films (thickness ~50 μm) are prepared for fabrication of the microcompression specimens.

3.2 Effects of the pulse current density

Figure 7(a) shows XRD patterns of the Au–Cu alloys electrodeposited at the J_p of 5–20 mA/cm² with the t_{on} and t_{off} both fixed at 10 ms. All electrodeposits show the same crystal structure, in which all of the peaks could be indexed to the face-centered cubic (fcc) reflection. With an increase in the J_p , the peaks shift to larger diffraction angles due to the lattice shrinkage caused by the increase in the Cu concentration. Effects of the J_p on the Cu concentration and grain size are plotted in **Figure 7(b)**. The copper concentration linearly increases from 15.3 to 41.2 at% as

Operating parameters	Range
Pulse current density (mA/cm ²)	5–60
Current on-time (ms)	10
Current off-time (ms)	5–600
Electrolyte temperature (°C)	50

Table 1. Parameters for pulse electrodeposition of Au–Cu alloy films.

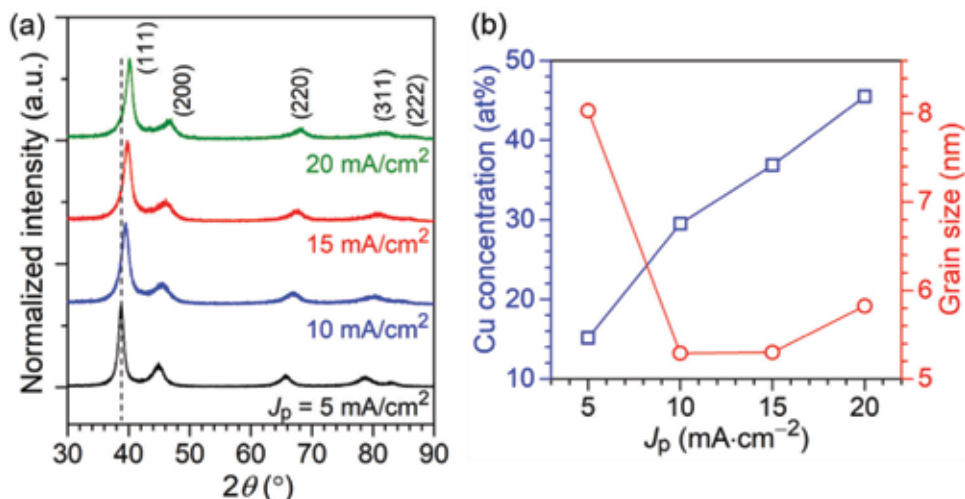


Figure 7. (a) XRD patterns of the Au–Cu alloys electrodeposited at the J_p varied from 5 to 20 mA/cm² with t_{on} and t_{off} both fixed at 10 ms. The straight dash line indicates the center of (111) diffraction peak in the J_p of 5 mA/cm² sample. (b) Plot of the J_p versus the grain size and Cu concentration.

the J_p increases from 5 to 20 mA/cm². These results are similar to the Au–Cu alloys prepared by the constant current electrodeposition, in which an increase in the J_p leads to a higher Cu concentration. The standard reduction potential of Cu²⁺ ions is more negative than that of Au⁺ ions [51]. An increase in the J_p makes the applied potential to be more negative; therefore, the reduction of Cu²⁺ is gradually favored and leads to an increase in the Cu concentration. In the meanwhile, the grain size decreases from 8.0 nm to a minimum value of 5.2 nm as the J_p increases from 5 to 10 mA/cm², which is attributed to the increase of the nucleation rate as the current density increases [49]. On the other hand, after reaching the minimum value, the grain size increases to 5.8 nm as the J_p increases to 20 mA/cm². The grain growth at high J_p could be attributed to the promoted side reactions (i.e., hydrogen evolution) as the applied potential becomes more negative, which then lowers overpotential of the main reaction(s) (reductions of Au⁺ and Cu²⁺ in this case). The grain size of electrodeposits is highly dependent on the overpotential, and the grain size increases when the overpotential is lowered [49].

3.3 Effects of current off-time

Effects of the t_{off} on crystal structure and alloy composition of the Au–Cu alloys are discussed in this section. **Figure 8** shows XRD patterns of the Au–Cu alloys electrodeposited at the J_p of 20 mA/cm² and the t_{off} varied from 20 to 120 ms. Similar to **Figures 3** and **7(a)**, all the XRD patterns show the fcc reflections, and no other diffraction peak is observed. The major (111) peak gradually shifts from $2\theta = 40.2^\circ$ to 38.8° when the t_{off} increases from 20 to 120 ms, which indicates a decrease in the Cu concentration. It is known that the t_{off} plays an important role in controlling the alloy composition due to the galvanic displacement reaction occurred on the substrate surface [55–58]. During of the off-time period, nobler metals continue to be deposited on the substrate surface, and less noble metals on the substrate surface would be oxidized and dissolved away. The displacement reaction leads to a decrease in concentration of the less noble component in the alloy. In the present Au–Cu system, the standard reaction potential of Au is more positive than Cu; hence, nobleness of Au is higher. Therefore, the displacement reaction occurred during the

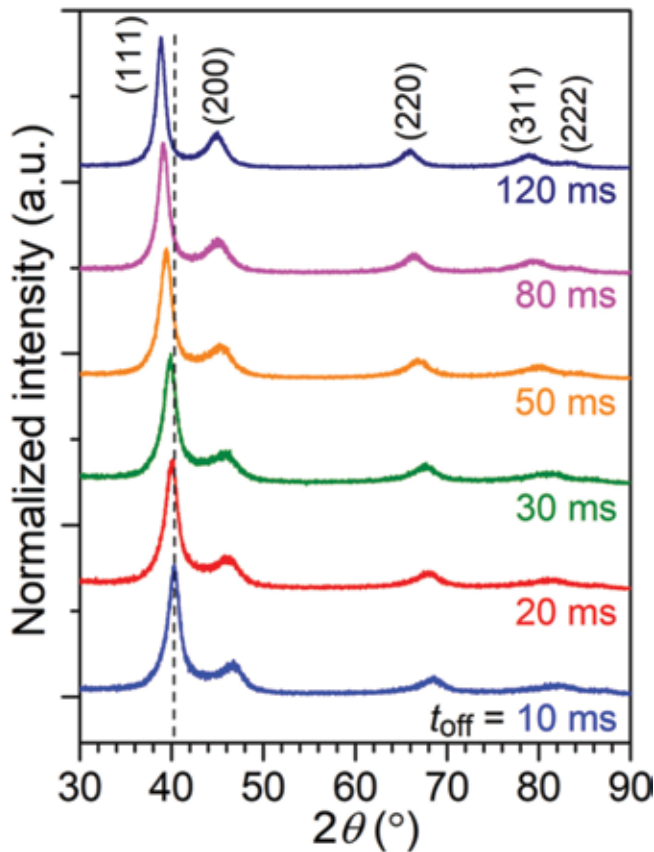


Figure 8.

XRD patterns of the Au–Cu alloys electrodeposited at the J_p of 20 mA/cm^2 with the t_{off} varied from 10 to 120 ms. The t_{on} was fixed at 10 ms. The straight dash line indicates center of the (111) diffraction peak in the t_{off} of 10 ms sample.

off-time period causes a decrease in copper concentration in the Au–Cu alloy, which is consistent with the lattice swelling observed from the XRD results.

Dependence of the Cu concentration and grain size on the t_{off} as the J_p varies from 10 to 60 mA/cm^2 is shown in **Figure 9**. Several trends are observed as the J_p and the t_{off} change. Firstly, a decrease in the Cu concentration is observed as the t_{off} increases at all of the J_p . The results correspond well with those observed from the XRD patterns, in which more Cu is replaced by Au as the t_{off} increases. Secondly, when the t_{off} increases, decreasing rate of the Cu concentration shows a transition from high to low as indicated by the change in slope of the curves in **Figure 4(a)**. The J_p of 50 mA/cm^2 curve indicates this point clearly. Cu concentration of the Au–Cu alloy shows a steep decrease from a short t_{off} to t_{off} of 240 ms, and the slope becomes less steep at t_{off} longer than 240 ms. The slope is suggested to be related to the displacement reaction or dissolution rate of Cu component in the Au–Cu alloy, in which a steep slope indicates a high Cu dissolution rate. Again, the result is expected since the Cu dissolution rate is directly related to concentration of Cu component at the surface of the film, and the Cu concentration is higher at the moment when the electrodeposition just entered the off-time period. Then the Cu concentration gradually decreases and leads to a lower Cu dissolution rate. Thirdly, the decreasing rate of Cu concentration is slowed down as the J_p increases. The evidence can be clearly seen in the J_p of 20 mA/cm^2 and J_p of 60 mA/cm^2 cases. The Cu concentration decreases from 36.9 to 18.4 at% when the t_{off} is increased from 30

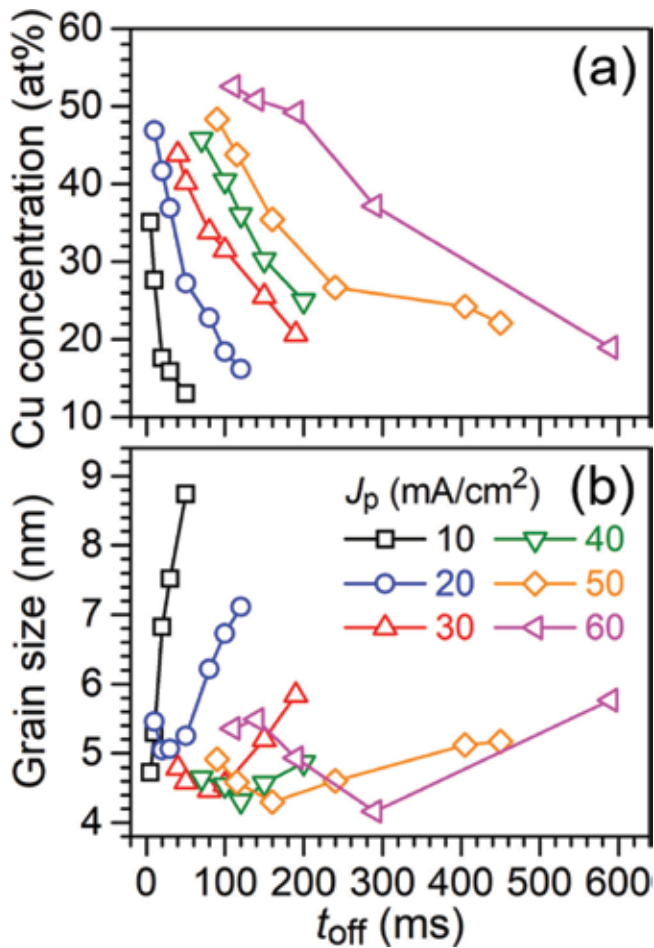


Figure 9.
 Plots of the t_{off} versus (a) grain size and (a) Cu concentration at varied J_p .

to 100 ms in the case of the J_p of 20 mA/cm². A much longer t_{off} is required, from 290 to 590 ms, for the Cu concentration to decrease from 37.1 to 18.9 at% in the case of the J_p of 60 mA/cm². The alloys electrodeposited at higher J_p contain higher Cu concentration. Although the dissolution rate is highly dependent on the Cu concentration, diffusion of Cu²⁺ away from surface of the substrate and Au⁺ from the bulk to the reaction site could also affect the dissolution rate. Hence, a longer t_{off} is needed to reach the same Cu concentration when the J_p is high.

Effects of the t_{off} on the grain size show similar trends at various J_p , in which the grain size initially decreases to a minimum value of ca. 4.40 nm and then the grain size reversely increases when the t_{off} increases. The displacement reaction occurred during the off-time period can initiate rearrangement of atoms in the alloy, which could induce nucleation or grain growth of the reduced metals in the alloy. The driving force of the rearrangement is dependent on the dissolution rate. When the driving force is high, the rearrangement is more vigorous, and nucleation is induced. As shown in **Figure 9(a)** and **(b)**, the grain size reduces with a decrease in the Cu concentration until reaching ca. 35 at%. On the other hand, the rearrangement is less vigorous, and grain growth is favored when the Cu concentration is low. This is why grain coarsening is observed when the Cu concentration is lower than ca. 35 at% as the t_{off} increases.

As a result, a wide Cu concentration ranging from 10.1 to 53.0 at% is attained by adjusting either or both the J_p and the t_{off} . In addition, the critical point observed

at the Cu concentration of ca. 35 at% indicates the grain size is interrelated to the alloy composition. **Figure 10** shows the grain size as a function of the Cu concentration. The Cu concentration and the grain size basically follow a monotonic relationship. Similar behavior is reported in other pulse current electrodeposited alloys [58, 59]. When compared to the constant current electrodeposited Au–Cu (square symbols), the constant current electrodeposited Au–Cu also shows the same monotonic relationship. Furthermore, the pulse current electrodeposition allows fabrication of Au–Cu alloys with a wider range of the Cu concentration and a much finer-grain size than those of the constant current electrodeposition, which are both advantageous for applications as movable microcomponents.

3.4 Morphology of pulse electrodeposited Au–Cu alloys

Effects of the pulse current electrodeposition parameters on morphology of the Au–Cu films are observed by the SEM as shown in **Figure 11**. The overview of the Au–Cu alloys electrodeposited at the J_p of 15 mA/cm² shows bright surfaces when the t_{off} is between 20 to 50 ms. From **Figure 11(a)**, the alloy film electrodeposited at the t_{off} of 20 ms shows pebble-like structures, and size of the pebble-like structures shrinks gradually as the t_{off} increases to 50 ms as shown in **Figure 11(b)** and (c). The surface becomes dull when the t_{off} increases to 100 ms, and the pebble-like structures are still observed as shown in **Figure 11(d)**. When a lower J_p at 5 mA/cm² is used, two alloy films deposited at the t_{off} of 30 and 100 ms both show dull surface. The size of the pebble-like structures increases as the t_{off} increases to 100 ms (**Figure 11(f)**). The surface condition becomes very rough when the J_p is increased to 20 mA/cm². As shown in **Figure 11(g)**, the alloy film deposited at the J_p of 20 mA/cm² and the t_{off} of 20 ms shows large agglomerates of colony-like clusters, and dull surface is observed. Then the surface becomes bright, and the size of the pebble-like structures decreases as the t_{off} increases to 50 ms, shown in **Figure 11(h)**. An interesting conclusion could be made here, in which Au–Cu alloys with similar surface morphology and similar Cu

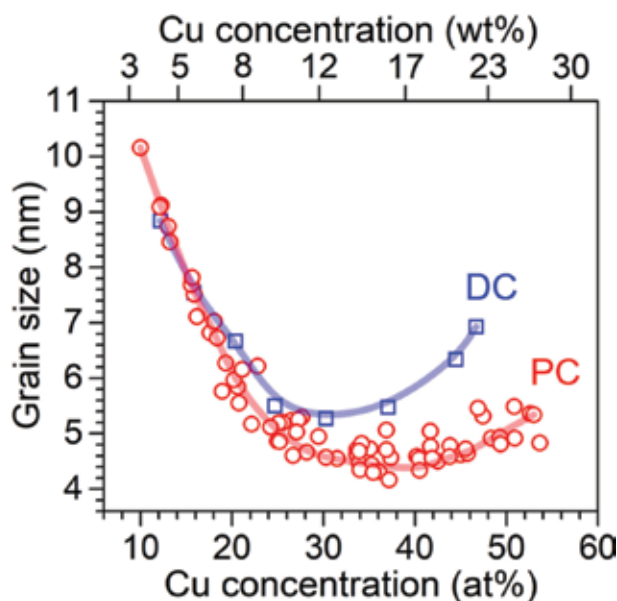


Figure 10. A plot of relationship between grain size and Cu concentration for Au–Cu alloys electrodeposited with varied J_p and t_{off} .

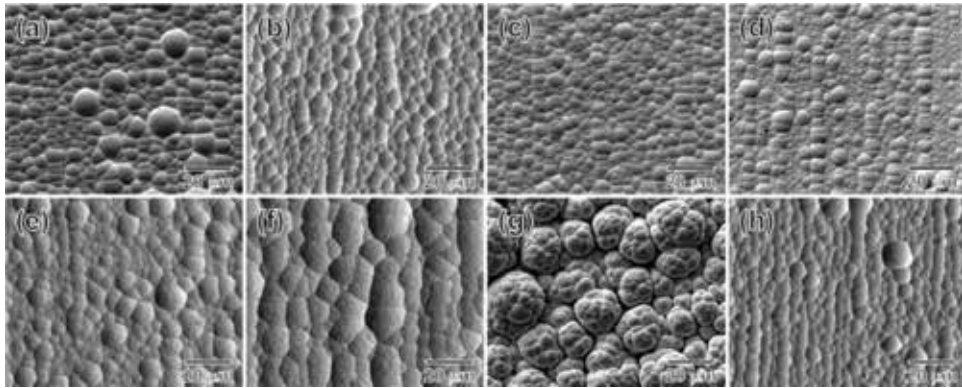


Figure 11. SEM micrographs of the Au–Cu alloy thick films. The alloys electrodeposited at the J_p of 15 mA/cm² with the t_{off} of (a) 20 ms, (b) 30 ms, (c) 50 ms, and (d) 100 ms; J_p of 5 mA/cm² with (e) 30 ms and (f) 100 ms; J_p of 20 mA/cm² with (g) 20 ms and (h) 50 ms. The t_{on} is fixed at 10 ms.

concentration could be fabricated using different pulse parameters (**Figure 11(b)**): $J_p = 15$ mA/cm², $t_{off} = 30$ ms; **Figure 11(h)**: $J_p = 20$ mA/cm², $t_{off} = 50$ ms). This result demonstrates that not only the grain size but also the surface morphology is interrelated to the Cu concentration. The morphology, composition, grain size, and electrodeposition parameters of the Au–Cu alloy thick films are summarized in **Table 2**.

Effects of the J_p and the t_{off} on the morphology and the Cu concentration are summarized and illustrated in **Figure 12**. In general, roughness of the surface is affected by the current density, and smoothness of the surface is related to the displacement reaction, i.e., dissolution of the Cu component in the Au–Cu alloy. In other words, an increase in the J_p leads to roughening of the surface, and promotion of the displacement reaction causes smoothing of the surface. For example, when a high J_p and a short t_{off} are applied, a rough surface would be formed during the on-time period because of the high J_p , and the smoothing effect caused by the displacement reaction would be insufficient because of the short t_{off} . In this case, a rough surface condition is obtained as shown in **Figure 11(g)**. When a high J_p and a long t_{off} are applied, although the high J_p would give a rough surface, but with a long enough t_{off} , the displacement reaction could cause enough smoothing effect to produce a smooth surface. On the other hand, when a low J_p is used, the surface

J_p , mA/cm ²	t_{off} , ms	[Cu], at%	d_g , nm	Morphology
20	20	46.4	4.8	Colony-like clusters and dull surface
	50	33.9	4.7	Pebble structure and bright surface
15	20	36.9	4.7	Pebble structure and bright surface
	30	34.2	4.8	Pebble structure and bright surface
	50	29.5	4.9	Pebble structure and bright surface
	100	21.2	6.2	Pebble structure and dull surface
5	30	18.0	7.0	Pebble structure and dull surface
	100	12.1	9.1	Pebble structure and dull surface

Table 2. A summary of pulse parameters, Cu concentration ([Cu]), grain size (d_g), and morphology of the Au–Cu alloys.

would be less rough than the one using high J_p . However, the Cu concentration is low when a low J_p is used, and this limits the displacement reaction, that is, the surface smoothing effect. As observed in the alloys electrodeposited at the $J_p = 5 \text{ mA/cm}^2$ in **Figure 11(e)** and **(f)**, the surface condition does not become smoother as the t_{off} increases from 30 to 100 ms.

3.5 Micromechanical properties of pulse electrodeposited Au–Cu alloys

Micromechanical properties of the pulse current electrodeposited Au–Cu alloys are evaluated by microcompression tests to demonstrate the potential for applications in microelectronic devices. The micropillars with the same dimensions of $10 \times 10 \times 20 \mu\text{m}^3$ are fabricated from the thick Au–Cu films by FIB. **Figure 13** shows SIM images of 6 Au–Cu micropillars with different alloy compositions after the micro-compression tests. Typical polycrystalline deformation (barrel-shape) is observed in the micropillars at the Cu concentration below $\sim 35\%$ (**Figure 13(a)–(d)**). As the Cu concentration increases to $\sim 37\%$, the deformation behaviors change into brittle fracture (**Figure 13(e)**). For the Cu concentration of 46.4 at% pillar (**Figure 13(f)**), the brittle fracture occurs from the crack boundaries originating from the large agglomerates as observed in **Figure 11(g)**. The large agglomerates and the brittle fracture are also observed in the constant current Au–Cu alloys electrodeposited using a high current density, in which the brittle fracture is observed when the Cu concentration is higher than 37 at% (**Figure 5(g)** and **(h)**).

Engineering strain–stress (SS) curves obtained from the microcompression tests are shown in **Figure 14**. The σ_y 's are estimated from the 0.2% offset line of the elastic deformation region. Similar to the constant current Au–Cu micropillars, the σ_y increases with an increase of Cu concentration and a decrease of grain size until the Cu concentration reaches $\sim 34\%$ (**Figure 14(a)–(d)**). For the Cu concentration of 37

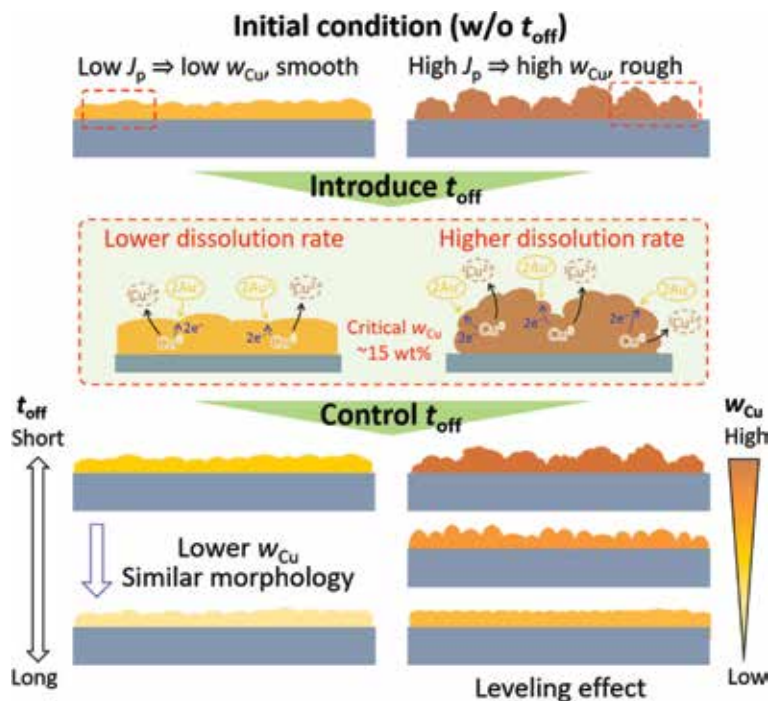


Figure 12. Illustration of the morphology change with the pulse electrodeposition parameters.

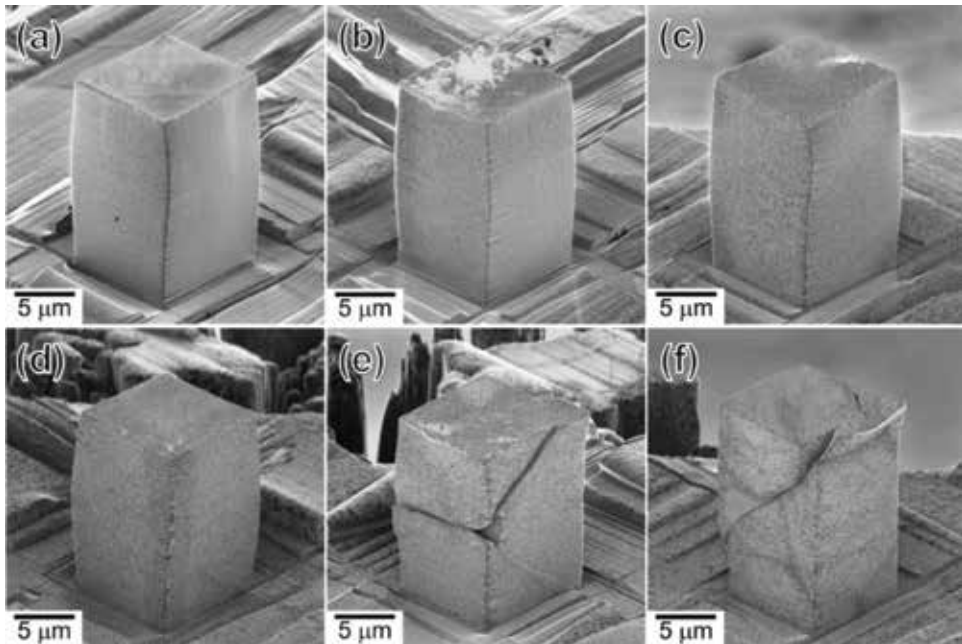


Figure 13. SIM micrographs of the pulse current Au–Cu micropillars after compression tests. The micropillars were fabricated from the thick Au–Cu with the Cu concentration of (a) 12.1 at%, (b) 15.6 at%, (c) 21.2 at%, (d) 34.2 at%, (e) 36.9 at%, and (f) 46.4 at%.

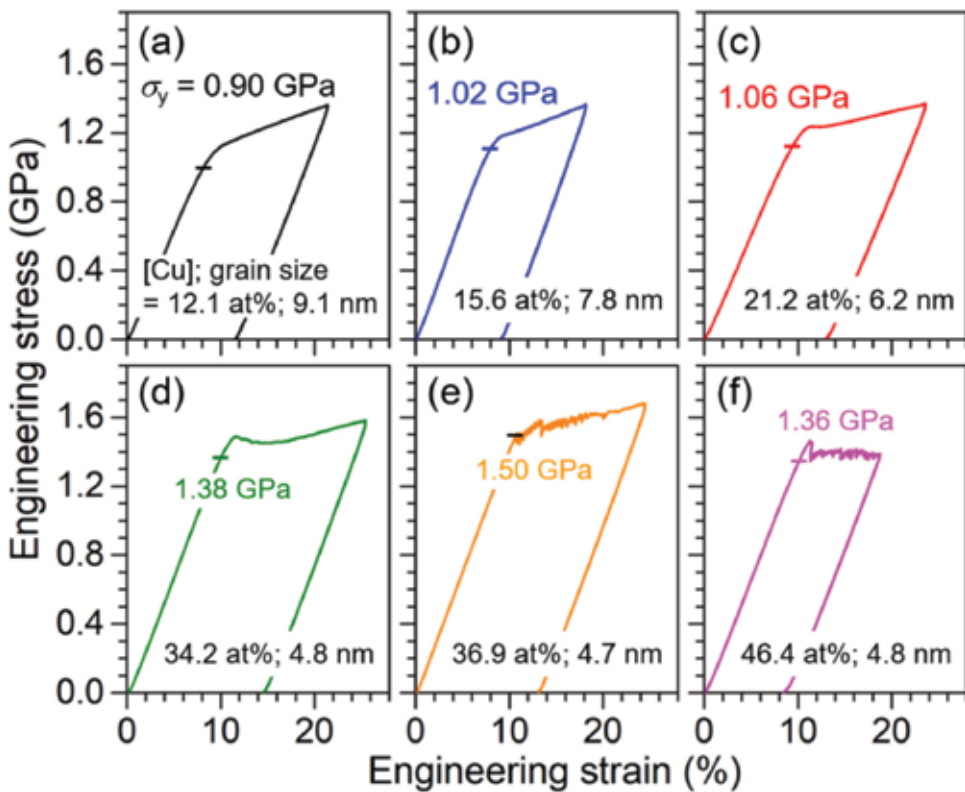


Figure 14. Engineering SS curves of the micropillars containing the Cu concentration of (a) 12.1 at%, (b) 15.6 at%, (c) 21.2 at%, (d) 34.2 at%, (e) 36.9 at%, and (f) 46.4 at%. The yield strength σ_y is marked by a horizontal bar.

at% micropillar, the σ_y reaches the highest value of 1.50 GPa. However, the subsequent flow stress behaviors are different with the lower Cu concentration micropillars, which are attributed to the difference in the deformation behaviors. The brittle fracture in the Cu concentration of 36.9 at% and 46.4 at% micropillar (**Figure 11(e)** and **(f)**) leads to the stagnant and trembling flow stress after the yielding points.

3.6 Strengthening mechanisms in electrodeposited Au–Cu alloys

The σ_y ranges from 0.90 to 1.50 GPa in the constant current- and pulse current electrodeposited Au–Cu micropillars, which can be understood as synergistic effects of the grain boundary strengthening [17] and the solid solution strengthening mechanisms [26, 27]. According to the grain boundary strengthening mechanism [17], the strength of metallic materials increases as total amount of grain boundary in a specimen increases, which is also understood as a decrease in the average grain size. Moreover, the solid solution strengthening mechanism [26, 27] is considered to restrict the dislocation movement due to interaction of the dislocations with the strained lattice surrounding the solute atoms, which then leads to a stacked strengthening beyond the grain boundary strengthening mechanism. In **Figure 15**, the grain boundary strengthening mechanism can be summarized as the Hall-Petch plots (σ_y vs. $(\text{grain size})^{-0.5}$) using the results presented in this study and the literature [47, 48, 60]. Due to lack of the literature on the yield stress of Au–Cu alloys, the results obtained from Vicker microhardness (HV) tests are adopted and converted to the yield stress by dividing the microhardness value to a Tabor coefficient of 4 ($\sigma_y = \text{HV}/4$ [61]) for the comparison.

Overall, the values reported in the literature all follow the Hall-Petch relationship. However, softening caused by the inverse Hall-Petch effect occurs when the grain size scales down to ~ 6 nm. The results presented in this work also follow the Hall-Petch relationship well. Most importantly, the results obtained in this study are much more reliable than those of Vicker microhardness tests since the hardness results are often

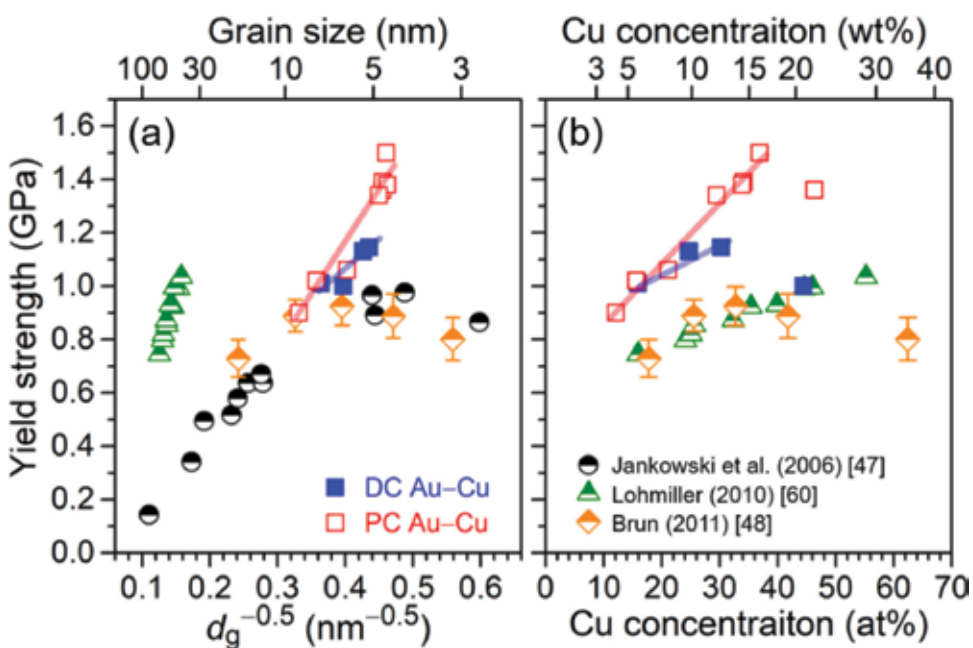


Figure 15. Plots of (a) inverse square root of the grain size (d_g) and (b) Cu concentration versus the σ_y .

affected by the substrate, which cannot reflect real strength of the electrodeposited films. A number of theories for solid solution strengthening have proposed that the strength is proportional to the solute concentration with order of 1/2 [Fleischer (1963)] or 2/3 [Labusch (1970)], which depends on the solute concentration. It is worth noticing that the highest σ_y at 1.38 GPa obtained in the pulse current electrodeposited Au–Cu micropillar is higher than that of constant current electrodeposited micropillar with the same Cu concentration ($\sigma_y = 1.15$ GPa), demonstrating the capability to further refine the grain size and enhance the strength by pulse current electrodeposition.

4. Conclusions

In the present study, high-strength Au–Cu alloys with nanocrystalline structure are successfully fabricated by electrodeposition techniques in order to be applied in fabrication of movable microcomponents in MEMS devices. The Au–Cu alloys are first fabricated by constant current electrodeposition. Surface morphology of the Au–Cu alloy films shows a wide variation from smooth surface to bump-clustered agglomerates as the current density varies from 2 to 9 mA/cm². A reduction in the grain size and an increase in the Cu content are observed with an increase in the current density. The film with the finest grain size at 5.3 nm is obtained when current density 6 mA/cm² is used. For the microcompression tests, the specimens evaluated are micropillars with dimensions of 10 × 10 × 20 μm³ fabricated from the electrodeposited Au–Cu alloys. The highest σ_y at 1.15 GPa is achieved for the Au–Cu micropillar having the grain size of 5.3 nm and the Cu concentration of ~30 at%. The yield strength is higher than the values reported in the literatures and suggested to be a synergistic effect of the grain boundary strengthening mechanism with the solid solution strengthening mechanism.

Furthermore, effects of the pulse current parameters on the alloy composition, grain size, surface morphology, and micromechanical property of the Au–Cu alloys are investigated. A wide Cu concentration in the Au–Cu alloys ranging from 10 to 54 at% is obtained. An increase in the Cu concentration is observed by using either or both of a high pulsed current density and a short current off-time. The smallest grain size of ca. 4.4 nm is achieved in films having the Cu concentration ranging from 30 to 40 at%. Grain refinement is achieved with a high J_p , and promoting the displacement reaction could also reduce the grain size. A high J_p results roughening of the surface, and enhancing the displacement reaction leads to a surface smoothing effect. Deformation behavior of the Au–Cu micropillar is affected by the Cu concentration, in which brittle fraction is observed when the copper concentration is higher than 37 at%. An ultrahigh yield strength of 1.50 GPa is obtained in the micropillar having the Cu concentration of 37 at% and the grain size of 4.7 nm. As a result, Au–Cu alloys developed in the present study are suggested to fulfill the requirements to fabricate more sensitive and miniaturized next-generation MEMS devices.

Acknowledgements

This work was supported by JST CREST Grant Number JPMJCR1433 and by the Grant-in-Aid for Scientific Research (S) (JSPS KAKENHI Grant number 26220907).

Conflict of interest

I confirm there are no conflicts of interest.

Author details

Haochun Tang¹, Tso-Fu Mark Chang^{1*}, Chun-Yi Chen¹, Takashi Nagoshi²,
Daisuke Yamane¹, Toshifumi Konishi³ and Katsuyuki Machida¹


1 Institute of Innovative Research, Tokyo Institute of Technology, Yokohama, Japan

2 National Institute of Advanced Industrial Science and Technology (AIST),
Ibaraki, Japan

3 NTT Advanced Technology Corporation, Atsugi Kanagawa, Japan

*Address all correspondence to: chang.m.aa@m.titech.ac.jp

IntechOpen

© 2018 The Author(s). Licensee IntechOpen. This chapter is distributed under the terms of the Creative Commons Attribution License (<http://creativecommons.org/licenses/by/3.0>), which permits unrestricted use, distribution, and reproduction in any medium, provided the original work is properly cited. 

References

- [1] Seidel H, Riedel H, Kolbeck R, Mück G, Kupke W, Königer M. Capacitive silicon accelerometer with highly symmetrical design. *Sensors and Actuators A*. 1990;**21**:312-315. DOI: 10.1016/0924-4247(92)80138-S
- [2] Ha B, Oh Y, Song C. A capacitive silicon microaccelerometer with force-balancing electrodes. *Japanese Journal of Applied Physics*. 1998;**37**:7052-7057. DOI: 10.1143/JJAP.37.7052
- [3] Okada H, Kobayashi T, Masuda T, Itoh T. Ultra-low power event-driven wireless sensor node using piezoelectric accelerometer for health monitoring. *Japanese Journal of Applied Physics*. 2009;**48**:070222. DOI: 10.1143/JJAP.48.070222
- [4] Mayagoitia RE, Nene AV, Veltink PH. Accelerometer and rate gyroscope measurement of kinematics: An inexpensive alternative to optical motion analysis systems. *Journal of Biomechanics*. 2002;**35**:537-542. DOI: 10.1016/S0021-9290(01)00231-7
- [5] Hong Y-J, Kim I-J, Ahn SC, Kim H-G. Mobile health monitoring system based on activity recognition using accelerometer. *Simulation Modelling Practice and Theory*. 2010;**35**:446-455. DOI: 10.1016/j.simpat.2009.09.002
- [6] Chae J, Kulah H, Najafi K. A monolithic three-axis micro-g micromachined silicon capacitive accelerometer. *IEEE Journal of Microelectromechanical Systems*. 2005;**14**:235-242. DOI: 10.1109/JMEMS.2004.839347
- [7] Abdolvand R, Amini BV, Ayazi F. Sub-micro-gravity in-plane accelerometers with reduced capacitive gaps and extra seismic mass. *IEEE Journal of Microelectromechanical Systems*. 2007;**16**:1036-1043. DOI: 10.1109/JMEMS.2007.900879
- [8] Lemkin M, Boser E. A three-axis micromachined accelerometer with a CMOS position-sense interface and digital offset-trim electronics. *IEEE Journal of Solid-State Circuits*. 1999;**34**:456-468. DOI: 10.1109/4.753678
- [9] Yamane D, Konishi T, Matsushima T, Machida K, Toshiyoshi H, Masu K. Design of sub-1g microelectromechanical systems accelerometers. *Applied Physics Letters*. 2014;**104**:074102. DOI: 10.1063/1.4865377
- [10] Machida K, Konishi T, Yamane D, Toshiyoshi H, Masu K. Integrated CMOS-MEMS technology and its applications. *ECS Transactions*. 2014;**61**:21-39. DOI: 10.1063/1.4865377
- [11] Yamane D, Matsushima T, Konishi T, Toshiyoshi H, Masu K, Machida K. A dual-axis MEMS capacitive inertial sensor with high-density proof mass. *Microsystem Technologies*. 2015;**22**:459-464. DOI: 10.1007/s00542-015-2539-y
- [12] Greer JR, Oliver WC, Nix WD. Size dependence of mechanical properties of gold at the micron scale in the absence of strain gradients. *Acta Materialia*. 2005;**53**:1821-1830. DOI: 10.1016/j.actamat.2004.12.031
- [13] Tsuchiya T, Tabata O, Sakata J, Taga Y. Size dependence of mechanical properties of gold at the micron scale in the absence of strain gradients. *Journal of Microelectromechanical Systems*. 1998;**7**:106-113. DOI: 10.1109/84.661392
- [14] Yamane D, Konishi T, Safu T, Tachibana K, Teranishi M, Chen C-T, et al. Long-term vibration characteristics of MEMS inertial sensors by multi-layer metal technology. In: *Proc. 19th International Conference on Solid-State Sensors, Kaohsiung, Taiwan*; 18 June-22 June 2017; DOI: 10.1109/TRANSDUCERS.2017.7994510

- [15] Rashidi AM, Amadeh A. The effect of current density on the grain size of electrodeposited nanocrystalline nickel coatings. *Surface and Coating Technology*. 2008;**202**:3772-3776. DOI: 10.1016/j.surfcoat.2008.01.018
- [16] Rashidi AM, Amadeh A. The effect of saccharin addition and bath temperature on the grain size of nanocrystalline nickel coatings. *Surface and Coating Technology*. 2009;**204**:353-358. DOI: 10.1016/j.surfcoat.2009.07.036
- [17] Petch NJ. The cleavage strength of polycrystals. *Journal of the Iron and Steel Institute*. 1953;**174**:25-28
- [18] Schuh CA, Nieh TG, Iwasaki H. The effect of solid solution W additions on the mechanical properties of nanocrystalline Ni. *Acta Materialia*. 2003;**51**:431-443. DOI: 10.1016/S1359-6454(02)00427-5
- [19] Li Y, Jiang H, Huang W, Tian H. Effects of peak current density on the mechanical properties of nanocrystalline Ni-Co alloys produced by pulse electrodeposition. *Applied Surface Science*. 2008;**254**:6865-6869. DOI: 10.1016/j.apsusc.2008.04.087
- [20] Chung CK, Chang WT. Effect of pulse frequency and current density on anomalous composition and nanomechanical property of electrodeposited Ni-Co films. *Thin Solid Films*. 2009;**517**:4800-4804. DOI: 10.1016/j.tsf.2009.03.087
- [21] Chang L, Kao PW, Chen C-H. Strengthening mechanisms in electrodeposited Ni-P alloys with nanocrystalline grains. *Scripta Materialia*. 2007;**56**:713-716. DOI: 10.1016/j.scriptamat.2006.12.036
- [22] Yang NYC, Headley TJ, Kelly JJ, Hruby JM. Metallurgy of high strength Ni-Mn microsystems fabricated by electrodeposition. *Scripta Materialia*. 2004;**51**:761-766. DOI: 10.1016/j.scriptamat.2003.11.001
- [23] Maki K, Ito Y, Matsunaga H, Mori H. Solid-solution copper alloys with high strength and high electrical conductivity. *Scripta Materialia*. 2013;**68**:777-780. DOI: 10.1016/j.scriptamat.2012.12.027
- [24] Erdey-Gruz T, Volmer M. Zur theorie der wasserstoff überspannung. *Zeitschrift für Physikalische Chemie*. 1930;**150**:203
- [25] Hamann CH, Vielstich W. *Elektrochemie II*. Weinheim: Verlag Chemie; 1981. DOI: 10.1002/bbpc.19820860826
- [26] Fleischer RL. Substitutional solution hardening. *Acta Materialia*. 1963;**11**:203-209. DOI: 10.1016/0001-6160(63)90213-X
- [27] Labusch R. A statistical theory of solid solution hardening. *Physica Status Solidi B: Basic Solid State Physics*. 1970;**41**:659-669. DOI: 10.1002/pssb.19700410221
- [28] Youssef MS, Koch CC, Fedkiw PS. Influence of additives and pulse electrodeposition parameters on production of nanocrystalline zinc from zinc chloride electrolytes. *Journal of the Electrochemical Society*. 2004;**151**:C103-C111. DOI: 10.1149/1.1636739
- [29] Youssef MS, Koch CC, Fedkiw PS. Influence of pulse plating parameters on the synthesis and preferred orientation of nanocrystalline zinc from zinc sulfate electrolytes. *Electrochimica Acta*. 2008;**54**:677-683. DOI: 10.1016/j.electacta.2008.07.048
- [30] Tury B, Lakatos-Varsanyi M, Roy S. Effect of pulse parameters on the passive layer formation on pulse plated Ni-Co alloys. *Applied Surface Science*. 2007;**253**:3103. DOI: j.apsusc.2006.06.063

- [31] Chang LM, An MZ, Guo HF, Shi SY. Microstructure and properties of Ni-Co/nano-Al₂O₃ composite coatings by pulse reversal current electrodeposition. *Applied Surface Science*. 2006;**253**:2132-2137. DOI: 10.1016/j.apsusc.2006.06.063
- [32] Cahoon JR, Broughton WH, Kutzak AR. The determination of yield strength from hardness measurements. *Metallurgical and Materials Transactions*. 1971;**2**:1979-1983. DOI: 10.1007/bf02913433
- [33] Arzt E. Size effects in materials due to microstructural and dimensional constraints: A comparative review. *Acta Materialia*. 1998;**46**:5611-5626. DOI: 10.1016/S1359-6454(98)00231-6
- [34] Uchic MD, Dimiduk DM, Florando JN, Nix WD. Sample dimensions influence strength and crystal plasticity. *Science*. 2004;**305**:986-989. DOI: 10.1126/science.1098993
- [35] Frick CP, Clark BG, Orso S, Schneider AS, Arzt E. Size effect on strength and strain hardening of small-scale [1 1 1] nickel compression pillars. *Materials Science and Engineering A*. 2008;**489**:319-329. DOI: 10.1016/j.msea.2007.12.038
- [36] Greer JR, Weinberger CR, Cai W. Comparing the strength of fcc and bcc sub-micrometer pillars: Compression experiments and dislocation dynamics simulations. *Materials Science and Engineering A*. 2008;**493**:21-25. DOI: 10.1016/j.msea.2007.08.093
- [37] Uchic MD, Shade PA, Dimiduk DM. Plasticity of micrometer-scale single crystals in compression. *Annual Review of Materials Research*. 2009;**39**:361-386. DOI: 10.1146/annurev-matsci-082908-145422
- [38] Greer JR, De Hosson JTM. Plasticity in small-sized metallic systems: Intrinsic versus extrinsic size effect. *Progress in Materials Science*. 2011;**56**:654-724. DOI: 10.1016/j.pmatsci.2011.01.005
- [39] Dietiker M, Buzzi S, Pigozzi G, Löffler JF, Spolenak R. Deformation behavior of gold nano-pillars prepared by nanoimprinting and focused ion-beam milling. *Acta Materialia*. 2011;**59**:2180-2192. DOI: 10.1016/j.actamat.2010.12.019
- [40] Nagoshi T, Chang T-FM, Tatsuo S, Sone M. Mechanical properties of nickel fabricated by electroplating with supercritical CO₂ emulsion evaluated by micro-compression test using non-tapered micro-sized pillar. *Microelectronic Engineering*. 2013;**110**:270-273. DOI: 10.1016/j.mee.2013.02.001
- [41] Hagen AB, Thaulow C. Low temperature in-situ micro-compression testing of iron pillars. *Materials Science and Engineering A*. 2016;**678**:355-364. DOI: 10.1016/j.msea.2016.09.110
- [42] Imamura H, Nagoshi T, Yoshida A, Chang T-FM, Onaka S, Sone M. Evaluation of anisotropic structure in electrodeposited Ni film using micro-sized cantilever. *Microelectronic Engineering*. 2012;**100**:25-27. DOI: 10.1016/j.mee.2012.07.118
- [43] Clinton JR, Tyler EH, Luo HL. Electrical and magnetic properties of Au-Ni alloys. *Journal of Physics F: Metal Physics*. 1974;**4**:1162-1169. DOI: 10.1088/0305-4608/4/8/012
- [44] Togasaki N, Okinaka Y, Homma T, Osaka T. Preparation and characterization of electroplated amorphous gold-nickel alloy film for electrical contact applications. *Electrochimica Acta*. 2005;**51**:882-887. DOI: 10.1016/j.electacta.2005.04.057
- [45] Raub CJ, Knödler A. The electrodeposition of gold by pulse plating. *Gold Bulletin*. 1977;**10**:38-44. DOI: 10.1007/bf03215426
- [46] Djurfors B, Ivey DG. Pulsed electrodeposition of the eutectic Au/

- Sn solder for optoelectronic packaging. *Journal of Electronic Materials*. 2001;**30**:1249-1254. DOI: 10.1007/s11664-001-0157-1
- [47] Jankowski AF, Saw CK, Harper JF, Vallier BF, Ferreira JL, Hayes JP. Nanocrystalline growth and grain-size effects in Au–Cu electrodeposits. *Thin Solid Films*. 2006;**494**:268-273. DOI: 10.1016/j.tsf.2005.08.149
- [48] Brun E, Durut F, Botrel R, Theobald M, Legaie O, Popa I, et al. Influence of the electrochemical parameters on the properties of electrodeposited Au–Cu Alloys. *Journal of the Electrochemical Society*. 2011;**158**:D223-D227. DOI: 10.1149/1.3554727
- [49] Budevski E, Staikov G, Lorenz WJ. Electrocrystallization: Nucleation and growth phenomena. *Electrochimica Acta*. 2000;**45**:2559-2574. DOI: 10.1016/S0013-4686(00)00353-4
- [50] Gabe DR. The role of hydrogen in metal electrodeposition processes. *Journal of Applied Electrochemistry*. 1997;**27**:908-915. DOI: 10.1023/a:1018497401365
- [51] Bard AJ, Parsons R, Jordan J. *Standard Potentials in Aqueous Solution*. New York: CRC Press; 1985. ISBN: 9781351414746
- [52] Zhang JY, Cui JC, Liu G, Sun J. Deformation crossover in nanocrystalline Zr micropillars: The strongest external size. *Scripta Materialia*. 2013;**68**:639-642. DOI: 10.1016/j.scriptamat.2012.12.024
- [53] Nagoshi T, Mutoh M, Chang T-FM, Sato T, Sone M. Sample size effect of electrodeposited nickel with sub-10 nm grain size. *Materials Letters*. 2014;**117**:256-259. DOI: 10.1016/j.matlet.2013.12.017
- [54] Meyers MA, Mishra A, Benson DJ. Mechanical properties of nanocrystalline materials. *Progress in Materials Science*. 2006;**51**:427-556. DOI: 10.1016/j.pmatsci.2005.08.003
- [55] Marlot A, Kern P, Landolt D. Pulse plating of Ni–Mo alloys from Ni-rich electrolytes. *Electrochimica Acta*. 2002;**48**:29-36. DOI: 10.1016/S0013-4686(02)00544-3
- [56] Roy S, Landolt D. Effect of off-time on the composition of pulse-plated Cu–Ni alloys. *Journal of the Electrochemical Society*. 1995;**142**:3021-3027. DOI: 10.1149/1.2048679
- [57] Bradley PE, Landolt D. A surface coverage model for pulse-plating of binary alloys exhibiting a displacement reaction. *Electrochimica Acta*. 1997;**42**:993-1003. DOI: 10.1016/S0013-4686(97)83305-1
- [58] Ghosh SK, Grover AK, Dey GK, Totlani MK. Nanocrystalline Ni–Cu alloy plating by pulse electrolysis. *Surface and Coating Technology*. 2000;**126**:48-63. DOI: 10.1016/S0257-8972(00)00520-X
- [59] Liu F, Kirchheim R. Nano-scale grain growth inhibited by reducing grain boundary energy through solute segregation. *Journal of Crystal Growth*. 2004;**264**:385-391. DOI: 10.1016/j.jcrysgr.2003.12.021
- [60] Lohmiller J, Woo NC, Spolenak R. Microstructure–property relationship in highly ductile Au–Cu thin films for flexible electronics. *Materials Science and Engineering A*. 2010;**527**:7731-7740. DOI: 10.1016/j.msea.2010.08.043
- [61] Tabor D. *The Hardness of Metals*. London: Oxford Univ. Press; 1951. ISBN: 9780198507765

Hard Pure-Gold and Gold-CNT Composite Plating Using Electrodeposition Technique with Environmentally Friendly Sulfite Bath

Masatsugu Fujishige and Susumu Arai

Abstract

Gold was used by Chinese and Egyptians of ancient times (at least ca 3000 BC). For many years, gold based materials have received great attention from people, due to the good conductor, high chemical stability, unique optical and processable properties. Electrodeposition technology is a long established technique for synthesizing metals on conductive substrates. Advances in equipment and creations of nanomaterials could carry out new technological progress, a large duty ratio with a pulse overvoltage became possible and new composite fillers (for example, carbon nanotubes: CNTs) appeared. Moreover, environmental considerations have become more important as Sustainable Development Goals (SDGs). SDGs were adopted at the United Nations Summit in September 2015 and are the goals set by the 193 member countries to achieve in the 15 years from 2016 to 2030. For the global environment and workers, friendly manufacturing methods have become more important. In this chapter, two nanostructured golds (hard pure-gold plating and gold-CNT composite plating) are discussed. They are a method of hardening the metal as pure-gold by pulsed electrodeposition and a method of combining CNT by controlling the zeta potential with additives, and their application as a contact material was investigated. Additionally, the synthesis and characteristics of electrostatic deposition films with properties using environmentally friendly sulfite bath are discussed.

Keywords: nanostructure, gold-plating, non-cyanide, Hall-Petch relation, contact resistance, CNT composite

1. Introduction

Richard P. Feynman spoke “There is Plenty of Room at the Bottom” [1]. This talk is given on 26 December 1959, at the annual meeting of the American Physical Society (APS) at the California Institute of Technology, reconsidered the importance and possibility of micro and nanotechnology in recent years. Microelectromechanical systems (MEMS) shows sensors and devices fabricated based on semiconductor microfabrication technology [2]. MEMS are usually used in pressure

sensors, inkjet printers, microfluidics, etc. In recent years, product integration has increased, various problems are occurring. Electric contacts are also no exception, and here we discuss new gold plating that provides a solution to the problem. It is widely used as a contact material.

Gold was used by Chinese and Egyptians of ancient times (at least ca 3000 BC) [3–5]. For many years, gold based materials have received great attention from people, due to the good conductor, high chemical stability, unique optical and processable properties [6]. Electrodeposition technology is a long established technique for synthesizing metals on conductive substrates. The properties of the deposited film are simply controlled by their morphologies (grain size, shape, roughness, brightness). Moreover, the deposited structure depends on process parameters such as the composition, temperature and pH of electrolyte, the magnitude of applied current densities, substrate. Advances in equipment and creations of nanomaterials could carry out new technological progress, a large duty ratio with a pulse overvoltage became possible and new composite fillers (for example, carbon nanotubes: CNTs) appeared. Moreover, environmental considerations have become more important as Sustainable Development Goals (SDGs). SDGs were adopted at the United Nations Summit in September 2015 and are the goals set by the 193 member countries to achieve in the 15 years from 2016 to 2030. For the global environment and workers, friendly manufacturing methods have become more important.

In this chapter, two nanostructured golds (hard pure-gold plating and gold-CNT composite plating) are discussed. Additionally, the synthesis and characteristics of electrostatic deposition films with properties using environmentally friendly sulfite bath are discussed.

2. Two kinds of new gold plating for contact material

2.1 Hard pure-gold plating

In recent years, there has been a demand for miniaturization to various parts due to an increase in degree of integration of electronic parts. Electric signal probes for inspecting semiconductor package parts have the same demand, and the terminal pitch is gradually narrowed. As a result, the mechanical contact pressure of the probe was lowered and its contact resistance increased. Technical problems have been occurred such as the device stability, and heat generation of the electrical contacts for inspecting the electronic parts. For example, at a contact pressure of about 0.5 N, the contact resistance of the probe is 30 m Ω , whereas at a contact pressure of about 0.15 N, the contact resistance reaches 100 m Ω . This Joule heating value is approximately three times as high as the original. Therefore, there is a demand for a new plating film on the probe surface which does not increase the contact resistance even with a low contact force, while maintaining the environment/durability equal to or higher than the conventional level.

Generally, the gold used as the contact point is a soft metal. However, gold plating for inspection probes has a moderate hardness and durability improved by adding trace amount of Co. In this conventional gold plating film, the specific resistance value is higher than that of pure gold, and the contact resistance associated with this value is also increased. Therefore, we focused on hard pure-gold plating technique without alloying [7]. There are reports [8–10] that can control the grain size toward small by pulse plating that repeats ON/OFF of current. The plating bath and the pulse electrodeposition method were devised to decrease the crystal size. In metals, according to Hall-Petch law [6, 11], metals are hardened by

reducing crystal size. The obtained hard pure-gold plating film was applied to the probe surface [12] and its electrical contact characteristics were evaluated. Furthermore, in consideration of recent SDGs correspondence, the non-cyanide base bath has been used for a friendly environmental society.

2.1.1 Material and method

There is a report [13] in which a sulfite complex is used for a non-cyanic plating bath. In this section, the base sulfite bath was used as a non-cyan gold plating bath. **Table 1** shows the composition of the plating bath and the plating conditions.

The condition of rectangular pulse current was optimized at the average current density of 50 A/m², the pulse period of 100 ms, and the duty ratio of 0.1. The Ni-P plated film was used as an experimental substrate (amorphous alloy as a base film) with thickness of about 3 μm on Cu plate. A plating bath manufactured by Meltex was used for plating the base film. The substrate used for the experiment was insulated with a masking tape excepting the deposition surface (10 mm × 20 mm), alkaline degreasing and acid treatment were carried out as plating pretreatment. Further, for comparison, a hard gold plating film with Co-content was similarly prepared, which was plated on the probe, used a commercially cyan bath (by Meltex: Auronal 44 BC). The characteristics of the plated films were evaluated in terms of surface morphology, Vickers hardness, X-ray diffraction (XRD), and specific resistance value, by a field emission scanning electron microscope (FE-SEM: S-4100, Hitachi), a dynamic indentation tester (DUH-201, SHIMADZU), X-ray diffractometer (RINT2200V, Rigaku), a four probe method, respectively.

2.1.2 Prototype probe

Figure 1 shows the photograph of the probe with both ends moved (spring movable stroke of 0.65 mm). A prototype was fabricated by plating the developed plating film on the movable part at both ends of the probe (Cu alloy, and the Ni-P plating as base) shown in **Figure 1**.

The repeated durability of the contact resistance was compared and evaluated for the prototype probes (using the same parts) of the current plating film and the developed plating film. Both gold plates were used for the contact resistance measurement of the probe, and a four-terminal method was used for the electric circuit

Sodium gold sulfite	0.05 M
Sodium sulfite	0.5 M
2,2'-bipyridyl	100 ppm
Additive	Small quantity
Bath temperature	60°C
Bath volume	100 ml
Average current density	50 A/m ²
Film thickness	5 μm (efficiency 100%)
Substrate	Amorphous Ni-P alloy film
Anode	Pt-plated Ti mesh
Agitation	Magnetic stirring

Table 1.
Sulfite gold plating bath composition and plating condition.

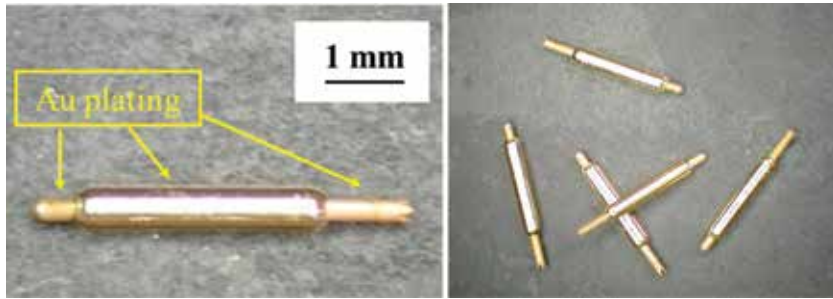


Figure 1.
Photograph of the probe with both ends moved (spring movable stroke of 0.65 mm).

measurement. Here, the measurement was performed at room temperature (RT, the temperature: 24°C, the humidity: 50% [14]) with the probe stroke of 0.65 mm, the load of about 0.24 N, and the measuring current of 10 mA.

2.1.3 Surface observation by FE-SEM

The three types of electrodeposited films, (a) a hard gold plating film with Co-containing (AuCo film) from a cyanide bath, (b) a direct current (DC) gold plating film (DC-Au film) from an original sulfite bath, (c) a pulsed current plating film from the same original sulfite bath (PC-Au film), were prepared and observed the surface morphology by FE-SEM are shown in **Figure 2**, respectively.

Compared with the surface morphology of AuCo film from **Figure 2(a)**, it can be confirmed that the DC-Au film has larger angular crystals (**Figure 2(b)**). The surface of PC-Au film (**Figure 2(c)**) shows the small crystals without corners by comparing with that of DC-Au film (**Figure 2(b)**).

2.1.4 Vickers hardness (H_v) measurement

Figure 3 shows the average value, the maximum value, and the minimum value of H_v obtained from three kinds of plated film surfaces by measuring 10 times at RT using a dynamic indentation tester. Here, the measurement conditions using a diamond indenter were carried out at the test load of 10 gf, the load speed of 0.675 gf/s, and the holding time of 20 s.

From this result, (c) PC-Au film is about twice as hard as (b) DC-Au film, which is harder. The H_v value is close to that of commercially available (a) AuCo film. It is presumed that the improved hardness of PC-Au film is due to the crystal size. Next, the crystal structure of the plating film was investigated by XRD.

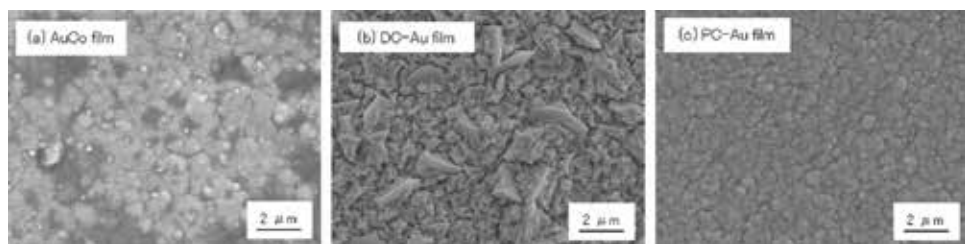


Figure 2.
Surface SEM images of various Au plating films, (a) AuCo film, (b) DC-Au film, (c) PC-Au film.

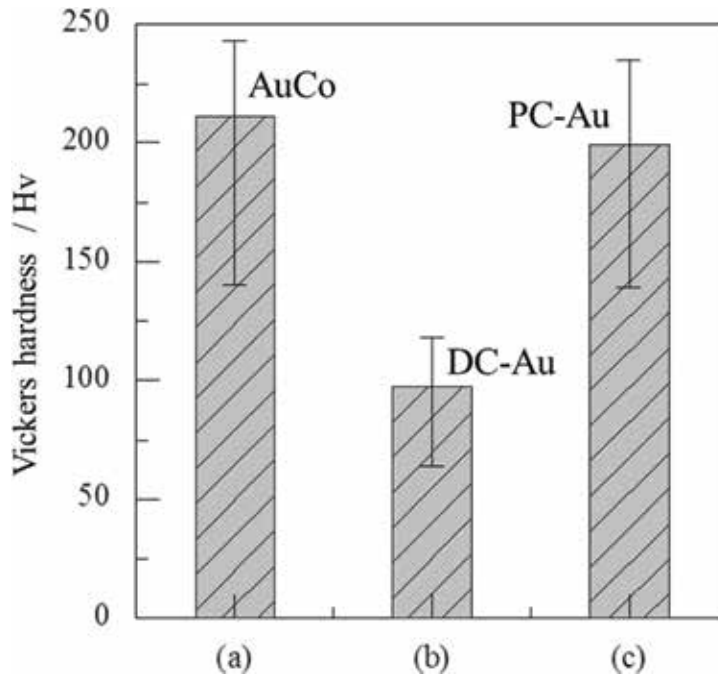


Figure 3. Vickers hardness (the average, maximum and minimum value) of various Au plating films; (a) AuCo film, (b) DC-Au film, (c) PC-Au film.

2.1.5 Relationship between crystallite size and Vickers hardness (Hv)

Figure 4 shows the results of XRD measurement of the three plating films, (a) AuCo film, (b) DC-Au film, and (c) PC-Au film, using Cu tube (CuK α 1: wavelength 1.5405 Å), at 40 kV and 20 mA.

From **Figure 4**, gold peaks of face-centered cubic (FCC) crystal were confirmed in all the samples. The crystallite size D_{hkl} of the (hkl) face (Miller Index) was calculated by the Scherrer equation of the following Eq. (1) [15].

$$D_{hkl} = \frac{K \cdot \lambda}{\beta \cdot \cos \theta} \quad (1)$$

The apparent crystallite size (D_a) was determined using a weighted average of the crystallite sizes from the XRD peaks on each face. In this calculation, the following Eq. (2) was used.

$$D_a = \frac{\sum_{hkl} D_{hkl} \cdot I_{hkl}}{\sum_{hkl} I_{hkl}} = \frac{D_{111} \cdot I_{111} + D_{200} \cdot I_{200} + D_{220} \cdot I_{220} + D_{311} \cdot I_{311}}{I_{111} + I_{200} + I_{220} + I_{311}} \quad (2)$$

As a result, the values of the crystallite size (D_a) from (a) AuCo, (b) DC-Au, and (c) PC-Au films were (a) 19.1 nm, (b) 28.9 nm, and (c) 17.0 nm, respectively. In the original bath, (c) PC-Au film obtained by the pulse electrodeposition has wider peak and smaller D_a than that of (b) DC-Au film obtained by the direct current electrodeposition. The reason for these results is related to the fact that the critical radius r_c of the crystal nucleus according to the following Eq. (3) is decreased by pulse electrodeposition with a large overvoltage (η) [16].

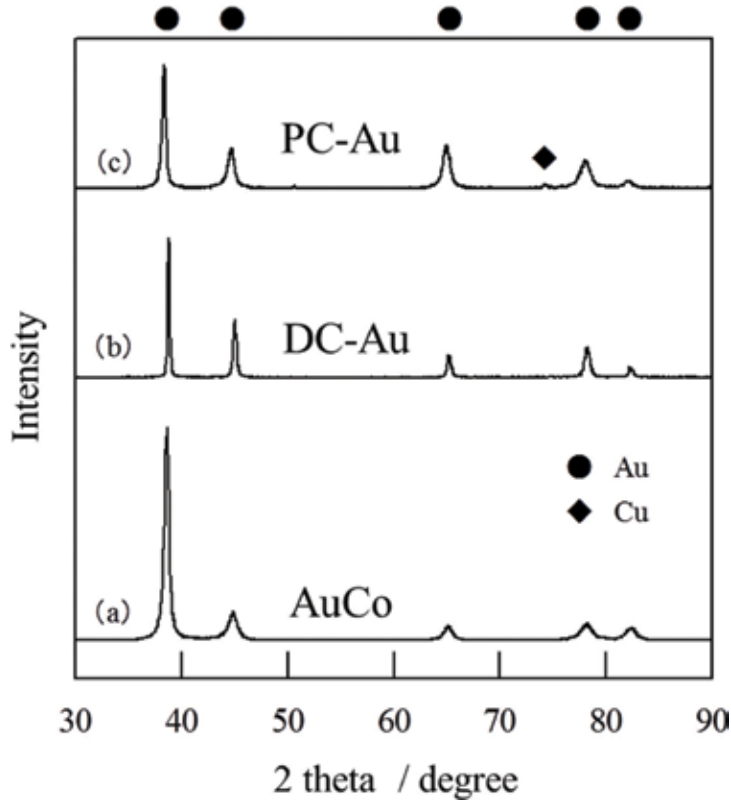


Figure 4. X-ray diffraction patterns of various Au films; (a) AuCo film, (b) DC-Au film, (c) PC-Au film.

$$r_c = \frac{\gamma \cdot V}{zF \cdot \eta} \quad (3)$$

It is possible to form small crystal nucleus in this case. Here, γ is the intrinsic surface energy, V is the atomic capacity (the volume occupied by 1 g atom in the solid state), z is the valence, F is the Faraday constant, and η is the overvoltage. In general, for metals, the Hall-Petch rule expressed by the following Eq. (4) is established with mechanical yield strength σ [6, 11].

$$\sigma = \sigma_0 + k \cdot d^{-\frac{1}{2}} \quad (4)$$

Here, σ_0 is the intrinsic yield strength (independent of crystal size), k is the constant depending on materials, and d is the crystal size. For the metal film, a proportional relationship is established between the yield strength and the hardness Hv. Paying attention to Eq. (4), the smaller the crystal size is, the harder the metal material is.

Various samples were prepared by changing pulse conditions in the same method, and the relationship between grain size (D_a) from XRD and Hv was as shown in **Figure 5** (Hall-Petch rule).

From the results in **Figure 5**, although the Hv of the pulsed electrodeposition film increases as the crystallite size decreases, the plot tends to decrease from around the critical point ($D_a^{-1/2} = 0.24$). The reason for this is presumed to be the result of the inverse Hall-Petch rule [17–19] that the self-weight collapse occurs in this gold electrodeposition film when the crystallite size becomes too small.

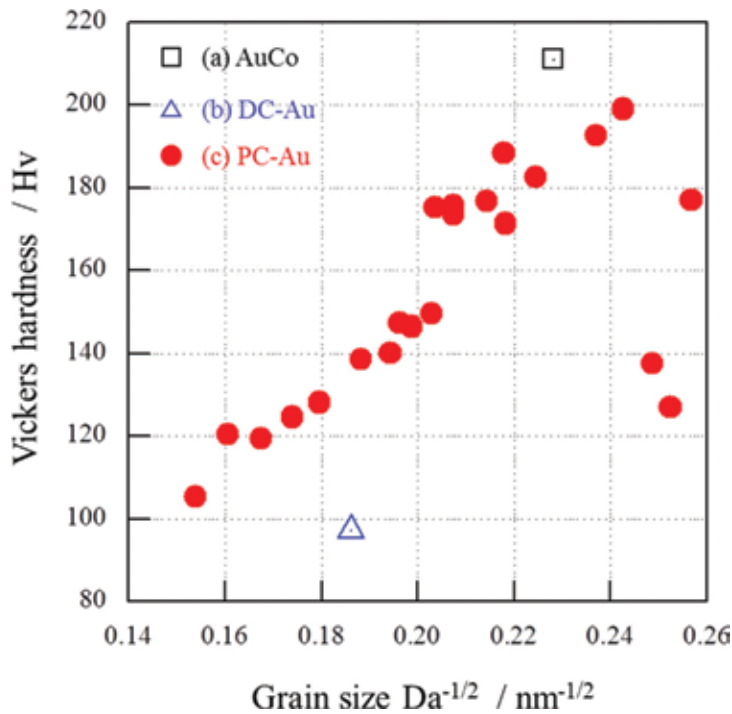


Figure 5. Relationship between crystallite size (grain size D_a) from XRD and Vickers hardness H_v ; (a) AuCo film, (b) DC-Au film, (c) PC-Au film.

Therefore, the condition around $D_a^{-1/2} = 0.22$ ($D = 20.7$ nm) was selected to form the plated film to obtain appropriate hardness for probe application.

2.1.6 Specific resistance value of plating film

In general, the four probe method of the following Eq. (5) is used as a standard method for measuring the resistivity ρ at RT [20]. Here, the variable t is the plating thickness, and the value (V/I) indicates the resistance value between the measuring terminals.

$$\rho = \frac{\pi t}{\ln 2} \cdot \left(\frac{V}{I} \right) \quad (5)$$

In order to measure the resistivity, the sample plated films were peeled. The resistivity ρ was calculated by the four probe method using the tungsten probe at intervals of 1 mm, and the results are shown in **Table 2** (reference description: crystallite size (D_a), average value of H_v). The plating thickness is obtained by averaging five points as measured by the fluorescent X-ray meter (SFT 3200, SII).

Compared to the resistivity of the commercially available (a) AuCo film, those of both (b) DC-Au film and (c) PC-Au film from the original pure gold plating bath were about 3×10^{-6} m Ω cm lower.

2.1.7 Prototype probe applied with gold plating

In a system in which elastic deformation is predominant, such as $0.1 \text{ N} < P < 100 \text{ N}$ (P is the contact load), the contact resistance R is expressed by the empirical formula of the following Eq. (6) [21, 22]. Here, ρ_1 and ρ_2 are the resistivity

	(a) AuCo	(b) DC-Au	(c) PC-Au
Average of measured resistance values (mΩ)	4.03	2.6	3.2
Deviation of measured resistance value (mΩ)	0.11	0.06	0.92
Average plating thickness (μm)	4.4	3.95	3.44
Specific resistivity ρ (10 ⁻⁶ mΩ cm)	8.04	4.65	4.98
Average value of Vickers hardness (Hv)	211	97	199
Apparent crystallite size Da (nm)	19.1	28.9	17

Table 2. Specific resistivity ρ of samples; (a) AuCo film, (b) DC-Au film, (c) PC-Au film (reference description: crystallite size Da, average value of Vickers hardness).

values of two materials in contact, H is the Brinell hardness, and P is the contact load.

$$R = 140 \cdot \frac{\rho_1 + \rho_2}{2} \cdot \sqrt{\frac{H}{P}} \quad (6)$$

It is suggested that the contact resistance can be lowered by the decrease of the resistivity proportional to its value. Utilizing this, the pulsed hard pure gold plating film was applied to the parts of the probe. Using two types of plated film probes, (a) AuCo film (conventional product) from commercial cyanide bath and (c) PC-Au film (fabricated product) from original bath, the results of the durability comparison during the contact resistance of 100,000 times are shown in **Figure 6**. In **Figure 6**, the vertical axis represents the contact resistance value [mΩ] of the probe; (a) AuCo plating and (c) PC-Au plating, and the horizontal axis represents every 1000 durability measurement times. The bar is maximum and minimum values at every 1000 times measurement, and the average values were plotted.

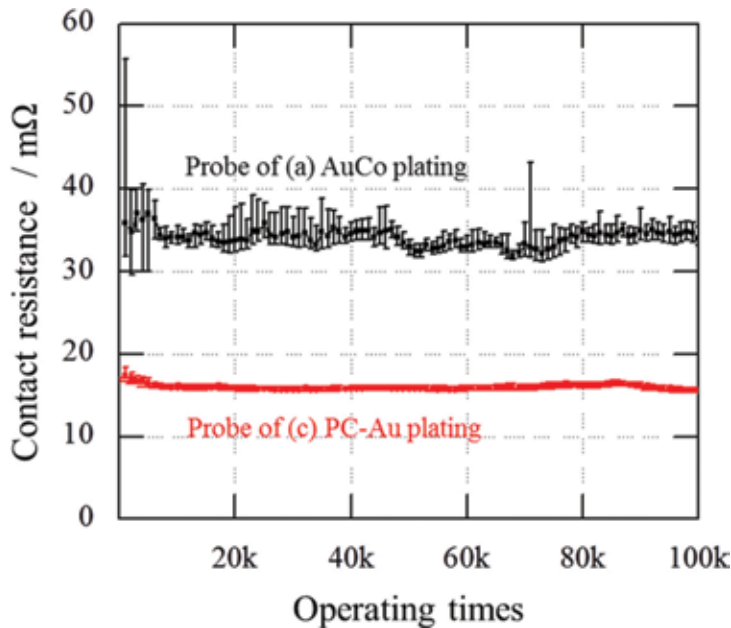


Figure 6. The durability about the contact resistance of 100,000 times; the probe of (a) AuCo plating and (c) PC-Au plating.

Calculating the average value of the contact resistance, (a) the resistance of the conventional product probe was 32.6 m Ω (deviation 2.07), and (c) that of the fabricated product probe was 21.6 m Ω (deviation 0.80). This fabricated probe has an advantage that the contact resistance value decreases by 11 m Ω and its variation is low, and improvement of electrical contact characteristics could be realized.

2.2 Gold-CNT composite plating

Carbon materials have attracted attention for a long time due to their characteristic structural, electronic, thermal, chemical, mechanical properties [23]. Since the discovery of carbon nanotube (CNT) [24, 25], great number of fundamental and technological research on CNT has been developed [26]. CNT is characterized by small diameter and high aspect ratio with outstanding mechanical strength, flexibility, high electrical conductivity and chemical stability [27].

For instance, material-CNT composites as a lightweight and high strength material have been actively studied [28–32]. Recently, CNT's application of seawater desalination has progressed in Shinshu University and has been drawing attention [33]. In general, the hydrophilic property at the interface and the difference in specific gravity between a metal matrix and filled CNTs make it difficult to fabricate a metal-CNT composite film with uniformly distributed CNTs and a good tribological behavior. Metal-CNT composite films have been fabricated [34–37], using various types of metals (Ni, Cu and Ag) by composite plating [38–44]. However, the pH levels of plating baths, being on the acidic side, are low. There are very few reports about the fabrication of a CNT composite plating film under the basic condition. Moreover, recently used industrial electric contacts, for example, a probe for inspecting parts of a semiconductor package, have encountered a drawback due to their adhesion and increase in resistivity after repeated use. Thus, a non-adhesive plating material for connector application is strongly required.

In this section, to develop a new composite material for next-generation electric contact applications, an Au-CNT composite plating film was fabricated by electrodeposition [40]. An effective additive was added into a non-cyanide CNT plating solution, affording the formation of an Au-CNT composite film in a basic solvent by an environmentally friendly method.

2.2.1 Carbon nanotube (CNT) and gold plating bath

A vapor-grown carbon fiber (VGCF; Showa Denko) which is one type of multiwalled CNTs, was used in this study. An Au-CNT plating bath was prepared by adding 0.05 M Na₃Au(SO₃)₂, 0.5 M Na₂SO₃, 100 pp. 2,2'-dipyridyl, and 0.2 g/l VGCF into ion-exchanged water. Moreover, 0.1 g/l trimethyl stearyl ammonium chloride (C₂₁H₄₆ClN) was added into the above solution. The mixture was stirred using an ultrasonic agitator (28 kHz) for 2 h. The volume of the plating bath was 100 cm³. The plating was performed at 60°C and pH 8 using a magnetic stirring agitator. The current density was 50 A/m² and a Pt-plated Ti mesh was used as the anode [8]. A copper (Cu) board with an exposed area of 200 mm² (10 × 20 mm²) was used as the substrate. The Cu substrate was plated using a Ni-P amorphous alloyed layer with a thickness of 3 mm. A Ni-P plating bath is a commercially available plating solution (Meltex). Before plating, the substrate was pretreated by alkali degreasing and acid treatment. For comparison, an Au plating film was prepared using an Au plating bath without adding CNTs. FE-SEM equipped with energy-dispersive X-ray spectroscopy (EDX; JED-2300F, JEOL) was used to study the surface morphology and CNT content of the fabricated plating films. Hv was measured using a dynamic hardness tester (DUH-201, Shimadzu). A diamond

indenter was vertically employed with a test load of 0.098 N, a load speed of 6.6 mN/s, and a hold time of 20 s at RT. The intrinsic resistance of the fabricated plating films was determined by a four-point probe method. Tungsten (W) probes were used with a probe spacing of 1 mm. Tribological properties were measured using a ball-on-plate-type reciprocating friction abrasion test machine (MMS-2419, Nissho-EW). A brass ball (8 mm in diameter) plated with 4.5 μm Ni-P and 1 μm hard-Au layers, was used as the counter surface. The test was repeatedly conducted in 50 cycles at a load of 0.5 N, a sliding length of 2 mm, a sliding speed of 0.5 mm/s at RT. The test was performed under ambient conditions without any lubricants. During the test, the friction coefficient was measured continuously using a load tester.

2.2.2 Gold-CNT composite plating film

The fabricated Au-CNT composite film appeared to be relatively black. **Figure 7 (a) and (b)** shows SEM images of the fabricated Au-CNT composite film and the Au film, respectively.

CNTs were tangled with the Au matrix and protruded from the matrix surface. The surface morphology of the Au-CNT composite film was relatively rough owing to the existence of many voids. It was previously reported that, in the composite film, metal is easily separated at the CNT apex and defects of CNTs. Before CNTs are entirely coated, the plating process is promoted at the apex or defects of CNTs, resulting in the formation of voids in the deposited film [34]. The result of EDX analysis indicated that the content of CNTs in the Au plating film was about 4 mass %. In the plating process, CNTs could not be homogeneously dissolved in the solution without $\text{C}_{21}\text{H}_{46}\text{ClN}$ even if it had been mechanically stirred for 48 h, and consequently, the plating bath could not be prepared. From the above results, $\text{C}_{21}\text{H}_{46}\text{ClN}$ was found to be an effective additive for Au-CNT composite film fabrication using a non-cyanide bath, which is an environmentally friendly method.

2.2.3 Gold plating bath and zeta potential

The mechanism of the eutectoid composition of the Au-CNT composite film is assumed to be based on the deposition of CNTs by electrophoresis. Normally, the zeta potential of CNTs decreases and easily becomes negative when the solution becomes basic [45, 46]. Although CNTs are modified by N-doping or heat treatment, their zeta potential becomes negative at a basic pH of 8 [47, 48]. Since the CNTs repulsed by the cathode during reduction react, it is difficult to combine CNTs in a basic solution. At this stage, although the role of the additive has not yet

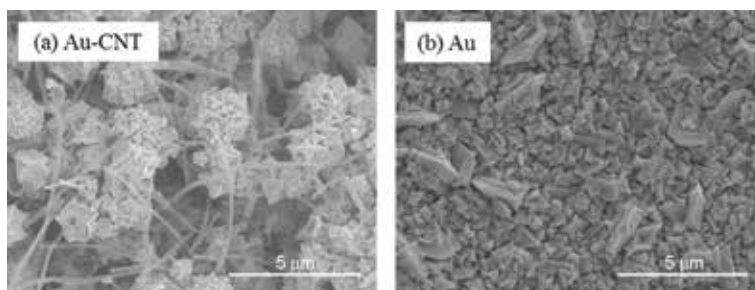


Figure 7. SEM images of the surface sample; (a) the fabricated Au-CNT composite film, (b) Au film.

been clearly elucidated, the results obtained in this study apparently show that the additive is important for Au-CNT composite film fabrication.

Figure 8 shows the VGCF zeta potential of 0.05 g/L under various potential of hydrogen (pH) in three solutions; (a) conventional dispersant of 0.5 mM in water, (b) fabricated dispersant (C₂₁H₄₆ClN) of 0.5 mM in water, (c) plating solution diluted 20 times.

The hydrophobicity of the additive is likely to effectively provide a positive zeta potential for CNTs. This was also evidenced in the plating process. The zeta potential of CNTs was found to be positive in the solution, and consequently, CNTs with a positive zeta potential were attracted toward the plating cathode.

2.2.4 Hardness and electrical properties of Au-CNT composite film

Table 3 shows the Hv and resistivity of the Au-CNT composite film and the Au film, respectively. The Hv is the average measured at 10 points. In general, to measure the Hv accurately, film thickness is required to be 10 times higher than the depth of the indenter pressed into the film. Thus, it should be noted that the measured value includes the substrate effect.

The Hv of the Au-CNT composite film and the Au film were Hv 133 and Hv 95, respectively. The fabricated Au-CNT composite film was harder than the Au film by 1.4 times.

For intrinsic resistance measurement, while the film thickness is sufficiently small compared with the probe spacing, the intrinsic resistivity ρ can be expressed by $\rho = (\pi t / \ln 2) / (V/I)$ [20], where value t is the average film thickness measured at

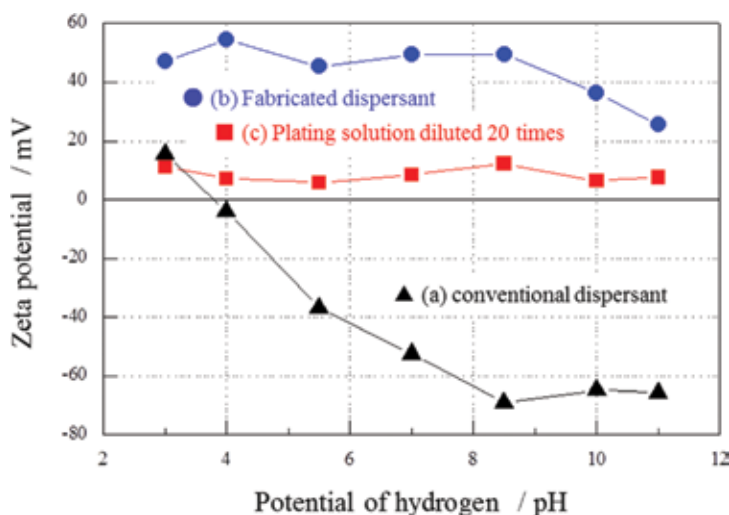


Figure 8. The VGCF zeta potential of 0.05 g/L under various potential of hydrogen (pH) in three solutions; (a) conventional dispersant of 0.0005 M in water, (b) fabricated dispersant (C₂₁H₄₆ClN) of 0.0005 M in water, and (c) plating solution diluted 20 times.

	Vickers hardness (Hv)	Resistivity (10 ⁻⁶ mΩ cm)
Au-CNT composite film	133	5.63
Au plating film	95	4.65

Table 3. The Vickers hardness and resistivity of the Au-CNT composite film and the Au film.

five points by X-ray fluorescence analysis (SFT3200, SII), and (V/I) is the average resistance of the thin film measured at three points. The resistivity of the Au-CNT composite film and the Au film were 5.6 and $4.7 \times 10^{-6} \text{ m}\Omega \text{ cm}$, respectively. The fabricated Au-CNT composite film showed a higher resistivity than the Au film by 1.2 times. The voids and the interface between Au and CNTs are likely attributed to the Vickers hardness and the resistivity.

2.2.5 Friction coefficients of the Au-CNT composite film

Figure 9 shows the friction coefficients of the Au-CNT composite film and the Au film, as a function of sliding length against Sn ball of 8 mm diameter.

In the case of the Au-CNT composite film, the friction coefficient gradually decreased toward the sliding length. After the test, at a total sliding length of 200 mm (50 repeated cycles), the friction coefficient was 0.28. On the other hand, in the case of the Au film, the friction coefficient increased to 0.58 and gradually decreased at a sliding length of 130 mm. The Au-CNT composite film showed a lower friction coefficient than the Au film.

Figure 10(a) and **(b)** shows SEM images of the Au-CNT composite film and the Au film after the wear test, respectively.

The worn area of **(b)** the Au film was relatively large compared with that of **(a)** the Au-CNT composite film. The track with a width of approximately 200 μm was

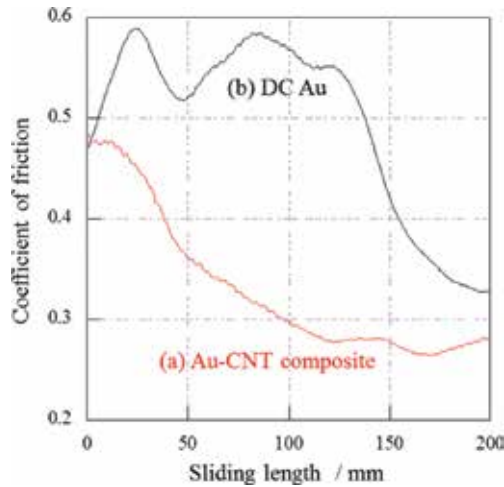


Figure 9. The friction coefficient of (a) the Au-CNT composite film and (b) the Au film, as a function of sliding length against Sn ball of 8 mm diameter.

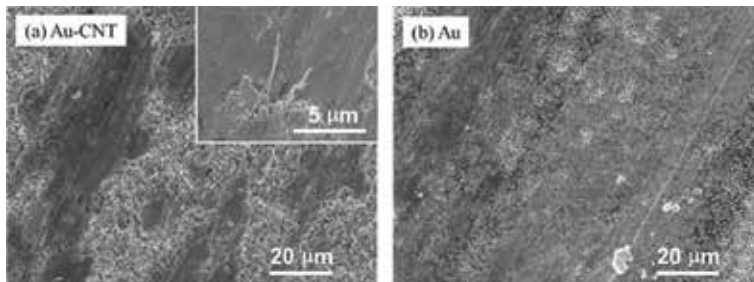


Figure 10. SEM images of (a) the Au-CNT composite film and (b) the Au film after the wear test.

found on the surface of the Au film. The entire surface of the worn area of the Au film was damaged, while that of the Au-CNT composite film was partly damaged. CNTs still remained in the worn area of the Au-CNT composite film, lying transversely [Figure 10(a) inset]. Adhesive wear is one of the friction phenomena. The smaller the surface area, the weaker the force of the adhesion shear [49]. The small contact area and transversely lying CNTs seem to contribute to the low friction coefficient.

3. Conclusions

To summarize, a pure-gold plated film with nano-order crystals was fabricated by devising a pulse electrolysis method using a non-cyanide bath. As a result of confirming their structure with FE-SEM or XRD, although refinement of this crystal showed an increase in hardness according to Hall-Petch rule, this law did not hold in the range smaller than around $D_a = 20$ nm, and on the contrary it showed a decrease in hardness. By controlling a crystallite size (around $D_a = 21$ nm) where the hardness does not decrease, the fabricated pure gold plating film without alloying maintains a moderate hardness ($H_v = 199$: $H_v = 210$ with AuCo film), its specific resistance (5×10^{-6} m Ω cm: 8×10^{-6} m Ω cm with AuCo film) than the conventional hard gold plating film. By applying the developed plating film to the probe, the contact resistance value of the repeated test could be reduced by about 11 m Ω , be achieving high performance with low variation. Conventionally, non-cyanic plating baths have lower life and stability compared to cyanide baths, and this is also a problem in the developed plating baths. However, compared to conventional AuCo plating, the fabricated hard pure gold plating has superiority in environmental and workability with non-cyan, reliability of electric contact (reduction in contact resistance, stability of repeated variation).

In summary of the second film, an Au-CNT composite plating film was fabricated by electrodeposition. A non-cyanide Au-CNT composite plating film was successfully formed by adding an effective additive, at alkaline environment. This was presumed to relate the zeta potential. The Au-CNT composite film is advantageous over the Au plating film in terms of a high hardness and a low friction coefficient. Thus, the Au-CNT composite film along with the desired method and the precise control of the content and orientation of CNTs are expected to make CNTs as promising material of sliding electric contacts, such as connectors.

In view of the application of contact materials used for MEMS, two methods of gold plating were introduced. In the society where miniaturization is advancing, the role of electrical contacts has also grown. Gold as a contact material will become more important. As described above, the advantage and potential of the new gold plating were confirmed, but there is still room for improvement in terms of performance. In addition, issues such as economical cost, safety of the use side, system construction for sustainable society formation (recycling) remain. Technological progress in the future is strongly expected.

Acknowledgements

This work was supported by MEXT Cluster brochure (Nagano Prefecture region). We express our appreciation to Prof. Morinobu Endo of Shinshu University for his great support and fruitful discussion. We also thank to Dr. Kenji Takeuchi and Dr. Noboru Akuzawa of Shinshu University, Dr. Winadda Wongwiriyapan of King Mongkut's Institute of Technology Ladkrabang, Prof. Feng Wang of Beijing University of Chemical Technology, for their kind advices.

Author details

Masatsugu Fujishige and Susumu Arai*
Shinshu University, Nagano, Japan

*Address all correspondence to: fshige@shinshu-u.ac.jp

IntechOpen

© 2018 The Author(s). Licensee IntechOpen. This chapter is distributed under the terms of the Creative Commons Attribution License (<http://creativecommons.org/licenses/by/3.0>), which permits unrestricted use, distribution, and reproduction in any medium, provided the original work is properly cited. 

References

- [1] Feynman RP. There's plenty of room at the bottom. *Journal of Microelectromechanical Systems*. 1992; **1**(1):60-66
- [2] Gardner JW, Varadan VK, Awadelkarim OO. *Microsensors, MEMS, and Smart Devices*. John Wiley & Sons, Ltd; 2001. p. 5. <https://www.wiley.com/en-us/Microsensors%2C+MEMS%2C+and+Smart+Devices-p-9780471861096>
- [3] Zhang R, Pian H, Santosh M, Zhang S. The history and economics of gold mining in China. *Ore Geology Reviews*. 2015; **65**:718-727
- [4] James TGH. Gold technology in ancient Egypt: Mastery of metalworking method. *Gold Bulletin*. 1972; **5**(2):38-42
- [5] Klemm D, Klemm R, Murr A. Gold of the Pharaohs—6000 years of gold mining in Egypt and Nubia. *African Earth Sciences*. 2001; **33**:643-659
- [6] Nishikawa S. *Gold, Grain Size and Yield Stress*, Shinban Kinzokukougaku Nyumon. Agune Gijyutsu Center; 2001. pp. 150-500 (in Japanese)
- [7] Fujishige M, Arai S, Wang F, Ushiyama M, Park KC, Takeuchi K, et al. Improvement of electric contact in probes by nanocrystallization-enhanced hardening of pure gold plating films. *IEICE Transactions C*. 2006; **J92-C**(6): 218-224
- [8] Hosokawa K. Application of pulse electrodeposition. *Kinzoku Hyomengijyutsu*. 1988; **39**(4):156-161 (in Japanese)
- [9] Choh HY. Electrodeposition of gold by pulsed current. *Journal of the Electrochemical Society*. 1971; **118**(4): 551-557
- [10] Lan LT, Ohno I, Haruyama S. Nucleation and growth in pulse plating. *Denki Kagaku*. 1983; **51**(1):167-168 (in Japanese)
- [11] Nieh TG, Wang JG. Hall-Petch relationship in nanocrystalline Ni and Be-B alloys. *Intermetallics*. 2005; **13**: 377-385
- [12] Fujishige M, Arai S, Wang F, Endo M, Ushiyama M, Makizaki S. Non-cyan hard Au plating for probe. In: Reports of the 114th Annual Meeting (Hokkaido University) of SFSJ. The Surface Finishing Society of Japan; 2006. pp. 58-59 (in Japanese)
- [13] Kagaya Y, Honma H. Gold plating from gold sulfite complex. *Journal of the Surface Finishing Society of Japan*. 1993; **44**(7):638-642 (in Japanese)
- [14] Tamai T. Effect of humidity in the atmosphere on electrical contact characteristics. *IEICE Technical Report*. 2006; **105**(604):13-18
- [15] Analysis Center in Rigaku Corporation. *X-ray Diffraction Guide*. Rigaku Corporation.; 1981. pp. 75-79. NCID: BA67145761 (in Japanese)
- [16] Haruyama S. Mechanism and speed of electrodeposition. In: *Electrochemistry for Surface Engineers*. Maruzen Co; 2005. pp. 132-134. ISBN: 4-621-07573-X C 3058 Printed in Japan
- [17] Takeuchi S. The mechanism of the inverse Hall-Petch relation of nanocrystals. *Scripta Materialia*. 2001; **44**:1483-1487
- [18] Fan GJ, Choo H, Liaw PK, Lavernia EJ. A model for the inverse Hall-Petch relation of nanocrystalline materials. *Materials Science and Engineering A*. 2005; **409**:243-248

- [19] Song HW, Guo SR, Hu ZQ. A coherent polycrystal model for the inverse Hall-Petch relation in nanocrystalline materials. *Nanostructured Materials*. 1999;**11**(2): 203-210
- [20] Okada T. Electron conduction and current magnetic effect. In: *Electrical Properties—Laboratory Physics Course*. Kyoritsu Shuppan Co., Ltd.; 1977. pp. 57-61. ISBN-10: 4320030710; ISBN-13: 978-4320030718
- [21] Holm R. *Stationary Contacts, Electric Contacts*. 4th ed. Springer-Verlag; 1967. pp. 40-47. ISBN: 9783662066881 3662066882 9783642057083 364205708X; OCLC No.: 652351662. <https://www.springer.com/la/book/9783540038757>
- [22] Tamai T. Friction and contact resistance through true contact interface. *IEICE Technical Report*. 2005; **105**(412):7-12
- [23] Dresselhaus MS, Dresselhaus G, Eklund PC. *Science of Fullerenes and Carbon Nanotubes*. New York: Academic Press, Inc; 1996
- [24] Oberlin A, Endo M, Koyama T. Filamentous growth of carbon through benzene decomposition. *Journal of Crystal Growth*. 1976;**32**:335-349
- [25] Iijima S. Helical microtubules of graphitic carbon. *Nature*. 1991;**354**: 56-58
- [26] Endo M, Hayashi T, Kim YA, Muramatsu H. Development and application of carbon nanotubes. *Japanese Journal of Applied Physics*. 2006;**45**(6A):4883-4892
- [27] Dresselhaus MS, Dresselhaus G, Avouris P. *Carbon Nanotubes; Synthesis, Structure, Properties and Application*. New York: Springer; 2001
- [28] Martinez-Sanchez R, Estrada-Guel I, Miki-Yoshida M, Antunez-Flores W, Santos-Beltran A, Barajas-Villaruel I. Novel composites aluminum-multi-walled carbon nano-tubes. *Microscopy and Microanalysis*. 2005;**11**:1738-1739
- [29] George R, Kashyap KT, Rahul R, Yamdagni S. Strengthening in carbon nanotubes/aluminium (CNT/Al) composites. *Scripta Materialia*. 2005;**53**: 1159-1163
- [30] Noguchi T, Magario A, Fukazawa S, Shimizu S, Beppu J, Seki M. Carbon nanotube/aluminium composites with uniform dispersion. *Materials Transactions*. 2004;**45**(2):602-604
- [31] Endo M, Noguchi T, Ito M, Takeuchi K, Hayashi T, Kim YA, et al. Extreme-performance rubber nanocomposites for probing and excavating deep oil resources using multi-walled carbon nanotubes. *Advanced Functional Materials*. 2008; **18**:3403-3409
- [32] Takeuchi K, Noguchi T, Ueki H, Niihara K, Sugiura T, Inukai S, et al. Improvement in characteristics of natural rubber nanocomposite by surface modification of multi-walled carbon nanotubes. *Journal of Physics and Chemistry of Solids*. 2015;**80**:84-90
- [33] Inukai S, Cruz-Silva R, Ortiz-Medina J, Morelos-Gomez A, Takeuchi K, Hayashi T, et al. High-performance multi-functional reverse osmosis membranes obtained by carbon nanotube-polyamide nanocomposite. *Scientific Reports*. 2015;**5**(13562):1-10
- [34] Guglielmi N. Kinetics of the deposition of inert particles from electrolytic baths. *Journal of the Electrochemical Society*. 1972;**119**:1009
- [35] Musiani M. Electrodeposition of composites: An expanding subject in electrochemical materials science.

- Electrochimica Acta. 2000;**45**:
3397-3402
- [36] Low CTJ, Wills RGA, Walsh FC. Electrodeposition of composite coatings containing nanoparticles in a metal deposit. *Surface and Coating Technology*. 2006;**201**(1–2):371-383
- [37] Hovestad A, Janssen LJJ. Electrochemical codeposition of inert particles in a metallic matrix. *Journal of Applied Electrochemistry*. 1995;**25**: 519-527
- [38] Arai S, Endo M. Various carbon nanofiber-copper composite films prepared by electrodeposition. *Electrochemistry Communications*. 2005;**7**:19-22
- [39] Arai S, Endo M, Kaneko N. Ni-deposited multi-walled carbon nanotubes by electrodeposition. *Carbon*. 2004;**42**:641-644
- [40] Arai S, Fujimori A, Murai M, Endo M. Excellent solid lubrication of electrodeposited nickel-multiwalled carbon nanotube composite films. *Materials Letters*. 2008;**62**:3545-3548
- [41] Fujishige M, Sekino M, Fujisawa K, Morimoto S, Takeuchi K, Arai S, et al. Electric contact characteristic under low load of silver-carbon nanotube composite plating film corroded using H₂S gas. *Applied Physics Express*. 2010; **3**:065801
- [42] Arai S, Osaki T, Hirota M, Uejima M. Fabrication of copper/single-walled carbon nanotube composite film with homogeneously dispersed nanotubes by electroless deposition. *Materials Today Communications*. 2016; **7**:101-107
- [43] Arai S, Kanazawa T. Electroless deposition of Cu/multiwalled carbon nanotube composite films with improved frictional properties. *Journal of Solid State Science and Technology*. 2014;**3**(6):201-206
- [44] Fujishige M, Wongwiriyapan W, Wang F, Park KC, Takeuchi K, Arai S, et al. Gold-carbon nanotube composite plating film deposited using non-cyanide bath. *Japanese Journal of Applied Physics*. 2009;**48**:070217
- [45] Lu C, Chiu H. Adsorption of zinc(II) from water with purified carbon nanotubes. *Chemical Engineering Science*. 2006;**61**:1138-1145
- [46] Yang K, Xing B. Adsorption of fulvic acid by carbon nanotubes from water. *Environmental Pollution*. 2009; **157**:1095-1100
- [47] Lu C, Su F. Adsorption of natural organic matter by carbon nanotubes. *Separation and Purification Technology*. 2007;**58**:113-121
- [48] Amadou J, Chizari K, Houille M, Janowska I, Ersen O, Begin D, et al. N-doped carbon nanotubes for liquid-phase CC bond hydrogenation. *Catalysis Today*. 2008;**138**:62-68
- [49] Kimura Y, Okabe H. *Tribology-gairon*. Tokyo: Yokendo; 1985. p. 34 (in Japanese)

Electrodeposition of High-Functional Metal Oxide on Noble Metal for MEMS Devices

*Wan-Ting Chiu, Chun-Yi Chen, Tso-Fu Mark Chang,
Tomoko Hashimoto and Hiromichi Kurosu*

Abstract

MEMS gas sensors could exert a significant impact on the automotive sector since future legislation is expected to stipulate the monitoring of NO_x and unburned fuel gases in vehicle exhausts. Among the materials, zinc oxide and TiO_2 are the most promising and extensively used materials for monitoring of NO_x gas since zinc oxide and TiO_2 show the high sensitivity, good stability, and fast response. Electrochemistry is a potential method to fabricate zinc oxide and TiO_2 for the applications since it is carried out at relatively low temperature and can cooperate with photolithography, which is an important process in MEMS. This study integrated zinc oxide/gold-layered structure and TiO_2/NiP hybrid structure on elastic fabrics, respectively, to realize an elastic gas sensor. Electroless plating (EP) and cathodic deposition were used to metallize and deposit metal oxides on elastic fabrics. Supercritical carbon dioxide (scCO_2) was further introduced into the electrochemical process to enhance the composite reliability.

Keywords: MEMS gas sensors, zinc oxide, TiO_2 , supercritical carbon dioxide, electroless plating

1. Introduction

The worldwide market of functional wearable devices (WD) is predicted to keep blossoming in the near future [1]. Meanwhile, WDs are differentiated into various functions such as gas sensor, and photocatalytic devices [2] due to different requirements in the next-generation technology. The combination of gas sensor materials and elastic substrate materials turns out to be the most crucial step in assembly of the component used in WDs. For instance, integration of gas sensor materials (i.e., zinc oxide and TiO_2), electrically conductive bases, and elastic substrate material is necessary to produce WDs-equipped gas sensing.

Elastic materials like cloth fabrics are mostly electrically insulator, and the elastic substrate material can be made electrically conductive by coating thin metallization layer on the electrically nonconductive substrate through electroless plating (EP) [3]. EP consists of a pretreatment procedure to clean the substrate material, a catalyzation (cat.) procedure to activate the substrate, and a metallization procedure to deposit metallization layer on the substrate material.

At (conventional) CONV cat. step, catalyst-included acidic aqueous solution is utilized to activate the substrate material by inlaying catalysts on substrates; meanwhile, the substrate morphology is often destroyed in this step. Due to polarity of the aqueous cat. solution and the high surface tension, the catalyst is merely deposited on the surface of the substrate bringing low adhesion between two materials. On the other hand, supercritical CO₂ (scCO₂) is introduced to the cat. procedure to improve the deposition characters [4, 5]. CO₂ turns into supercritical phase showing properties in the middle of gas phase and liquid phase as both the temperature and pressure are higher than its critical point [6]. scCO₂ is used as the solvent and a metal-organic complex was used as the catalyst. Due to the affinity to nonpolar material [7], low surface tension [8], and high self-diffusivity [6] of scCO₂, scCO₂ thus can convey the organic catalyst into confined spaces and carry it to go into the fabric while remains the substrate structure intact.

When it comes to the gas-sensing function, there are various fabrication methods to produce metal oxides (MO_x), which include high-temperature vapor deposition [9], polymer-mediated chemical reaction [10], hydrothermal-annealing procedure [11], and single-container electrolyte-based technique [12]. Among the fabrication techniques, cathodic deposition allows a facile and effective procedure for the fabrication of MO_x [13–16]. Furthermore, cathodic deposition can cooperate with lithography to allow further applications such as patterning, which is important for the MEMS fabrication process. The sensing material/metallization layer/elastic cloth fabric composite material was practiced by scCO₂-promoted EP and cathodic deposition toward applications in gas sensor in this study.

Even a slight uncomfotableness due to the rigid element in a WD can be annoying to the active users, and thus an elastic material is required in WDs. Silk fabric, a common clothing material, was selected due to its elasticity and stretchability in this study. A thin gold layer was selected as the electrically conductive layer. Furthermore, gold also shows great ductility [17], which is a critical prerequisite of WDs. There are many materials that can act as the sensing material in the hybrid material, such as titanium dioxide [18], copper (II) oxide [19], and zinc oxide [20]. Zinc oxide was deposited via cathodic deposition in this study as the sensing material due to its comprehensive applications, requirement of low fabrication temperature to have high crystallinity, and simple fabrication process.

On the other hand, co-EP technique was used in this study to equip the elastic silk fabric with electrically conductive NiP and sensing materials TiO₂ together by introducing TiO₂ particles into the NiP metallization electrolyte to form a suspension solution. Adhesive firmness can be enhanced by the included TiO₂ in the composite. There are several literature studied on the inclusion of TiO₂ in metal matrix via electrochemical methods such as electrodeposition and EP to enhance properties of the metal matrix. Gawad et al. [21] synthesized NiP-Al₂O₃ and NiP-TiO₂ composite layers on Cu substrate from alkaline hypophosphite gluconate baths and studied their properties. This study reported that inclusion of these oxide particles influences structure of the NiP matrix. Hardness, corrosion resistance, and coating brightness were enhanced with the TiO₂ inclusions. Thiemig and Bund [22] fabricated Ni-TiO₂ composite materials by electrocodeposition via an acidic sulfamate bath and an alkaline pyrophosphate electrolyte. Mechanical properties of the Ni-TiO₂ composite materials were enhanced while comparing to pure Ni electrodeposition in this literature. Parida et al. [23] investigated the ultrafine Ni-TiO₂ composite films by direct current electrodeposition technique on steel substrate from Watt's bath. With the inclusion of TiO₂ in the films, high microhardness and high wear resistance were realized while comparing to pure Ni electrodeposition. Benea et al. [24] worked on the electrocodeposition of Ni and TiO₂. The results showed high hardness and high wear resistance. Momenzadeh and Sanjabi [25]

studied the effect of TiO₂ concentration (conc.) in the electrolyte on the mechanical properties. They further introduced sodium dodecyl sulfate (SDS) surfactant into the electrolyte to increase the TiO₂ inclusion amount.

All the aforementioned literature worked on the mechanical properties such as wear resistance and hardness. In addition, all the composite materials were deposited on rigid substrates. However, flexibility is a critical requirement for gas sensing in WDs. There are merely limited literature working on decoration of metal-based composite on an elastic substrate and investigating its properties.

Here, we report a facile fabrication process in realization of an elastic and sensing material zinc oxide/gold/silk and TiO₂/NiP/silk-layered composite material, respectively, toward applications of gas sensor. Fundamental properties required for WDs such as electrical resistance, corrosion resistance, and adhesive firmness of the composite evaluations are demonstrated.

2. Silk/gold/zinc oxide hybrid structure

2.1 Activation of silk fabric via scCO₂ palladium (II) acetylacetonate cat.

Figure 1 shows OM images and X-ray diffraction patterns of the as-received silk and the catalyzed silk. The crossed-linked see-through bundles shown in **Figure 1(a)** imply the silk fabric, and the yellow flakes in **Figure 1(c)** specify the palladium (II) acetylacetonate catalyst. A broad peak at $2\theta = 20^\circ$ can be observed in **Figure 1(b)**, which reveals an amorphous structure of the silk fabric. On the other hand, diffraction peaks labeled by diamond symbols can be corresponded to palladium (II) acetylacetonate [26, 27], and the results suggested the catalysts were successfully inlaid into the substrate. As shown in the OM figures, silk fabric persisted after the cat. procedure due to the low surface tension, low viscosity, and nonacidic characters of scCO₂. The scCO₂-promoted cat. step confirmed a significant enhancement while compare to the CONV cat. process. Palladium (II)

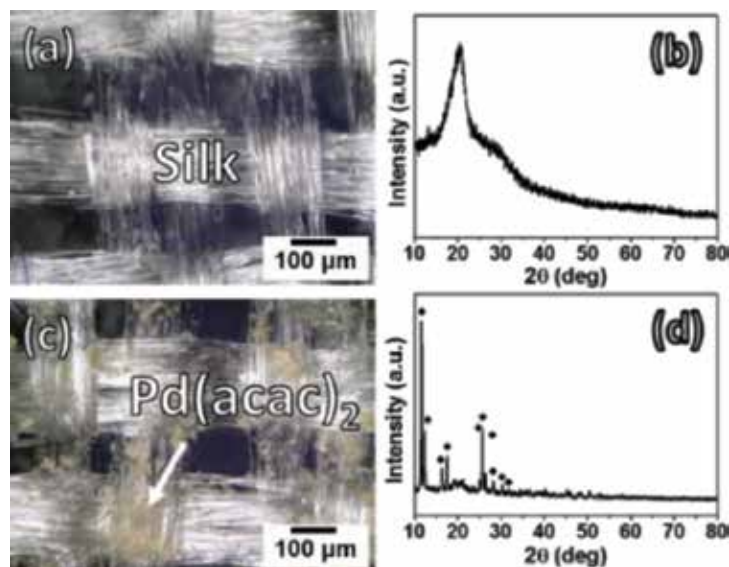


Figure 1. (a) OM image and (b) X-ray diffraction pattern of the as-received silk as well as (c) OM image and (d) X-ray diffraction pattern of the catalyzed silk (diamond symbol: Pd(acac)₂ catalysts).

acetylacetonate acts as an activation site after it was reduced to Pd metal by the reductant in the metallization solution. Pd metal can play the role of catalyst and activate the following metallization.

2.2 Morphology, composition, and structure of silk/gold

Development of the gold layer is shown in **Figure 2**. **Figure 2(a)** shows morphology of the specimen with the NiP metallization period at 4 min before the gold metallization. **Figure 2(b–d)** demonstrates the gold metallization period at 3, 5, and 80 min, respectively. At 3 min of the gold metallization (**Figure 2(b)**), part of the NiP layer was still not enclosed showing a gray luster. As the gold metallization period was extended to 5 min and longer (**Figure 2(c)** and **(d)**), the NiP layer was completely concealed by the gold layer.

The X-ray diffraction patterns at various gold metallization periods are shown in **Figure 3(a–c)**. Five apparent diffraction peaks shown in **Figure 3(a–c)** locate at $2\theta = 38.2, 44.4, 64.6, 77.6,$ and 81.7° can be indexed to (111), (200), (220), (311), and (222) planes, respectively, of the FCC structure for gold (JCPDS #65-2870). In **Figure 3(a)**, at 3 min of the gold metallization period, only a thin layer of gold was metallized on the silk, and the broad diffraction peak of silk at around 20° was still detectable. NiP diffraction peaks were not found in **Figure 3(a)**, because the NiP metallization layer is selected as the sacrificial metallization layer for thin gold metallization. Moreover, it performs amorphous structure, which the amorphous peaks are overlaid by the gold diffraction peaks with high intensity. As the gold metallization continued, no diffraction peaks of the silk fabric were detected in the X-ray diffraction patterns (**Figure 3(b)** and **(c)**) since the gold layer is thick enough to suppress the diffraction peaks from the silk. **Figure 3(d)** indicates the composition change with the gold metallization period. In the first place, owing to the inadequate thickness of gold, the thin NiP metallization layer was detected by EDX. On the other hand, thin NiP metallization layer was no longer found when the gold metallization period extended to 80 min. Phosphorus was not found due to the inadequate quantity.

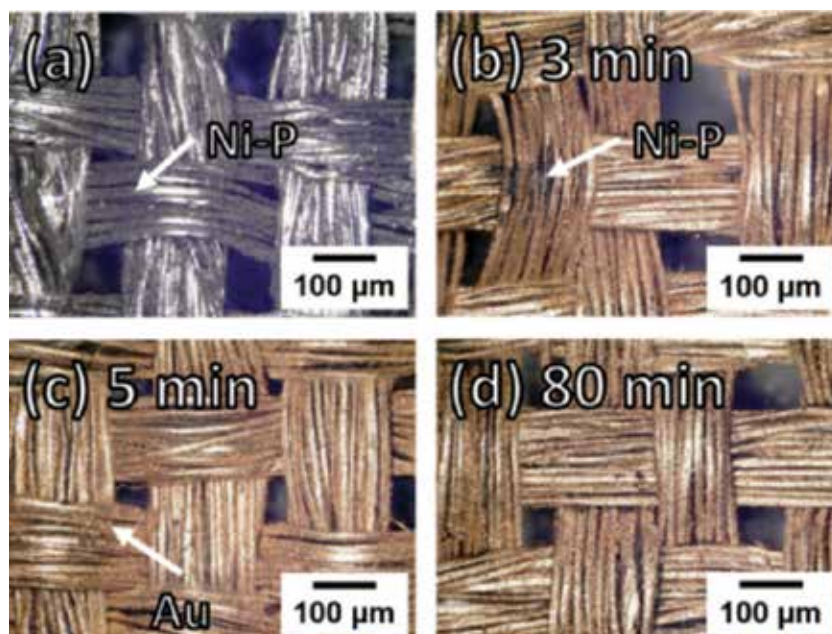


Figure 2. OM images of the (a) Ni-P metallized silk and the Au metallization at (b) 3 min, (c) 20 min, and (d) 80 min.

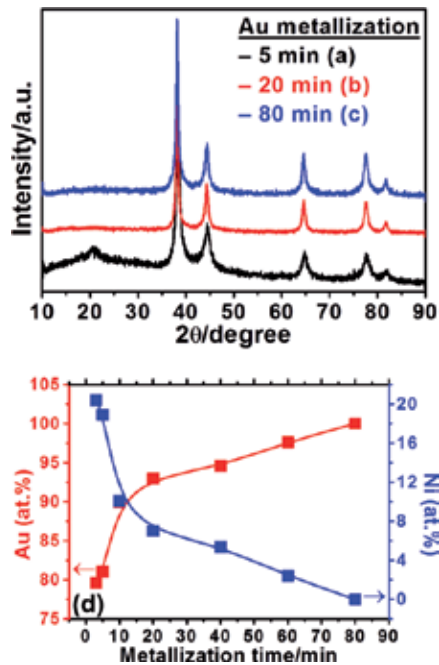


Figure 3. X-ray diffraction patterns of the Au metallization at (a) 5 min, (b) 20 min, and (c) 80 min and (d) the composition revolution with the Au metallization time.

Figure 4 illustrates growth of the gold layer thickness with the gold metallization period. There is no obvious partition of the NiP and gold layer shown in the inserted SEM image in **Figure 4**. A positive interrelationship was observed between thin gold metallization layer and the gold thickness showing the growth rate in average at 0.48 $\mu\text{m}/\text{h}$. The growth rate decreased marginally from 60 to 80 min of the gold metallization period due to the consumption and decline in concentration of the metal ion and reductant as the deposition continued.

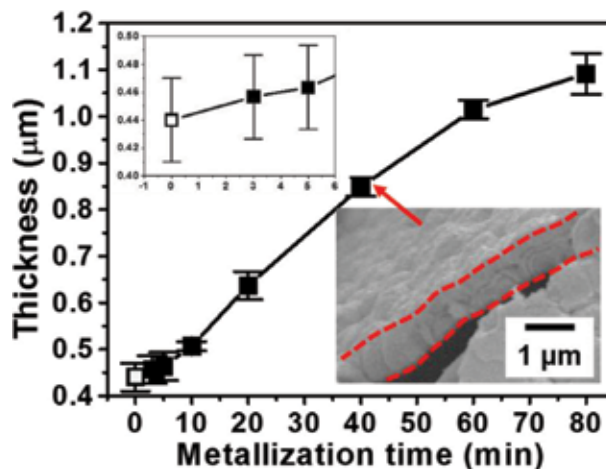


Figure 4. Plot of the Au metallization thickness versus the metallization time (hollow symbol: NiP metallization at 4 min and solid symbols: Au metallization thickness versus Au metallization time) (OM image of Au metallized at 40 min of the metallization time is inserted into bottom-right).

2.3 Electrical property of silk/gold

The electrical resistances at various gold metallization periods are shown in **Figure 5**. The electrical resistance dropped down in the early stage and increased after reaching a minimum point. Since the NiP layer is not fully covered by gold at 3 min of gold metallization period (solid symbol) (**Figure 2(a)**), it showed high electrical resistance close to the gold-free specimen at 0 min of gold metallization (hollow symbols) (**Figure 5(a)**). An inserted graph in **Figure 5(a)** shows results of the gold metallization period between 0 and 5 min.

The electrical resistances obtained from 0 to 5 min (the dash line shown in **Figure 5**) of the metallization period, which only showed a minor difference from the gold-free one, are categorized into the first stage. Full coverage was built as the gold metallization period reached 5 min, and the electrical resistance was enhanced consequently. The electrical resistance reached its minimum at the gold metallization period of 20 min due to the full coverage, smooth deposition, and adequate gold thickness (**Figure 5(b)**). From the beginning of the full coverage to the range near the lowest electrical resistance can be classified to the second stage (from the dash line at 5 min to the other one at 40 min). The electrical resistance increased marginally as the gold metallization period increased beyond the minimum point. The surface became rougher (indicated by the arrows in **Figure 5(c)**) with the lengthened metallization period, and the electrical resistances were worsened due to more scattering of electrons [28]. The section of deteriorated electrical resistance and rough deposition can be characterized into the third stage.

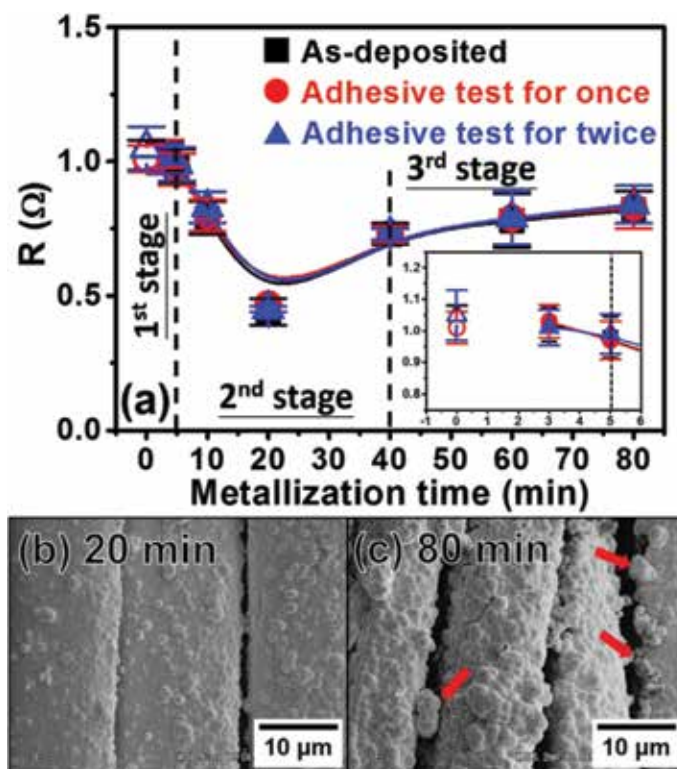


Figure 5.

(a) Electrical resistances of the Au-metallized silk at various metallization times and SEM images of the Au-metallized silk at (b) 20 min and (c) 80 min of the metallization time (hollow symbols: Au-free; solid symbols: Au metallized).

The electrical resistances with the adhesive treatments are also shown in **Figure 5(a)**. No substantial change was found in all stages because silk fabric was entirely deposited by the NiP and gold, and the adhesive property between the silk fabric and the NiP as well as between the NiP and the gold metallization layer both showed high adhesion.

2.4 Cathodic zinc oxide fabrication

Figure 6 shows SEM images (**Figure 6(a–d)**) and OM images (**Figure 6(e–h)**) of the pristine zinc oxide deposited with hydrogen peroxide concentration varied from 0 to 0.3 wt.%. Tower-like zinc oxide nanowires are observed in all of the SEM images (**Figure 6(a–d)**). Zinc oxide coverage on the gold metallization layer was conducted and calculated by a built-in software in OM. Zinc oxide coverages were at 63, 62, 41, and 32% for the samples fabricated with free hydrogen peroxide to 0.3 wt.% hydrogen peroxide. Structure of zinc oxide is often influenced by chloride ion in the electrolyte. The chloride ion acts as a capping agent adsorbing on the

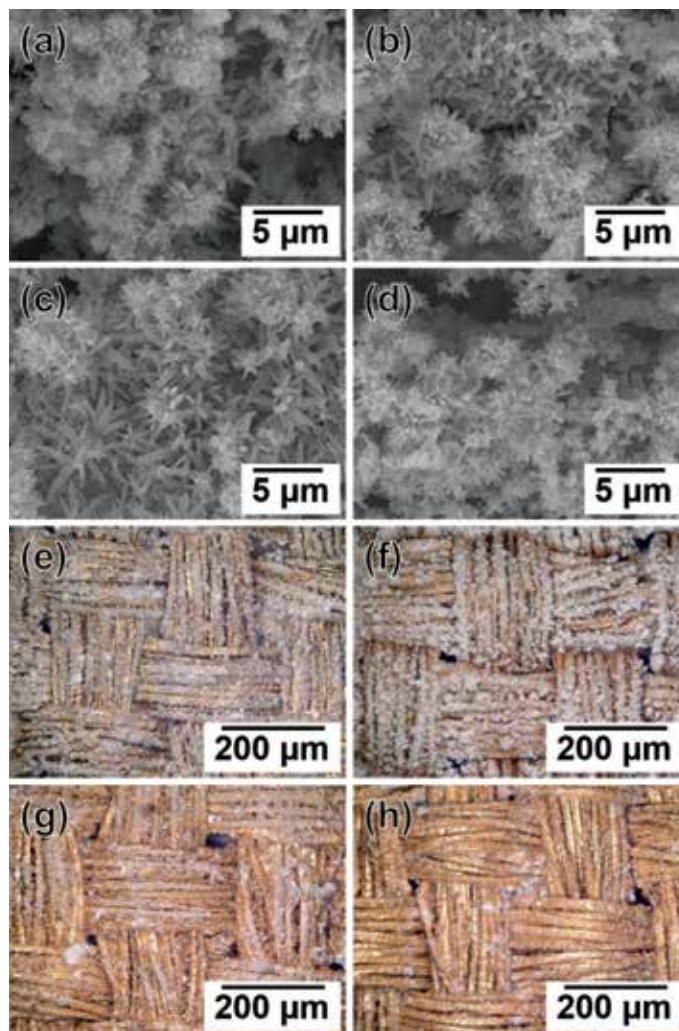
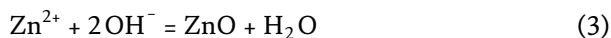
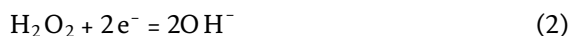
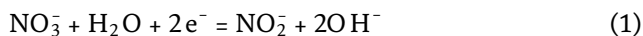


Figure 6. SEM images of the specimens deposited in (a) free of H_2O_2 , (b) 0.1 wt.%, (c) 0.2 wt.%, and (d) 0.3 wt.% H_2O_2 , and the OM images in (e) free of H_2O_2 , (f) 0.1 wt.%, (g) 0.2 wt.%, and (h) 0.3 wt.% H_2O_2 .

(0001) plan of zinc oxide to stabilize zinc oxide surface and results in development of nanorod-like morphologies. In contrast, when concentration of the chloride ion is low, tower-like morphologies rather than nanorod morphologies are developed [29]. Moreover, zinc oxide particle size increased as the hydrogen peroxide concentration increased from 0 to 0.2 wt.% as shown in the SEM images. Similar results on increase in the zinc oxide particle size as the hydrogen peroxide concentration increased were stated in a literature [30]. However, in **Figure 6(d)**, the particle size decreased when the hydrogen peroxide concentration went beyond 0.2 wt.%. Zinc oxide cathodic deposition reaction equations are as follows [31]:



OH^- formed on the electrode from Eqs. (1) and (2) is predicted to react with zinc ion in the solution to form zinc oxide on the electrode. As shown in Eq. (2), formation rate of the hydroxide ion is increased with high hydrogen peroxide concentration. Since the diffusivity of zinc ion in aqueous electrolyte is four times slower than that of hydrogen peroxide, zinc ion diffusion to the electrode surface cannot catch up with the formation of hydroxide ion as the hydrogen peroxide concentration increased [32]. As the amount of hydrogen peroxide was increased to 0.3 wt.%, formation rate of the hydroxide ion is too high and accumulates at the substrate surface.

A general scheme of the solute concentration profiles in the solution is shown in **Figure 7**. Hydroxide ions are formed on the electrode; hence, the concentration is progressively lowered toward the bulk electrolyte direction. Zinc ions diffuse from the bulk electrolyte to the electrode surface to react with hydroxide ions; therefore, the concentration decreases as it approaches the electrode surface. Depending on the hydroxide ion formation rate, local hydroxide ion concentration, or pH, on the electrode varies. Zinc oxide is deposited at a pH range of ca. 8–12, and zinc oxide dissolves away to form ZnO_2^{2-} or HZnO^{2-} as the pH goes beyond 12 [33, 34]. The region appropriate for the formation of zinc oxide is defined as region I, and the region results in dissolution of zinc oxide is classified as region II as shown in **Figure 7**.

The range near surface of the electrode is in region I when the hydrogen peroxide concentration was lower than 0.2 wt.%. Hence, an increase in the hydrogen peroxide concentration resulted in particle size increase (**Figure 6(a and b)**) and the high coverage (**Figure 6(e and f)**). As the hydrogen peroxide concentration was increased to 0.3 wt.%, both the zinc oxide particle size (**Figure 6(d)**) and the coverage (**Figure 6(h)**) were declined, which indicates the pH near electrode surface could be higher than 12. The results suggest the region near the electrode surface is in region II as the hydrogen peroxide concentration is higher than 0.3 wt.%.

Figure 8(a) shows X-ray diffraction patterns of the zinc oxide deposited with various hydrogen peroxide concentrations in the electrolyte. Only the diffraction peaks of gold (star symbol) and zinc oxide (hexagon symbol) were observed. No other phase was found in the X-ray diffraction patterns after the zinc oxide deposition. A comparative crystallinity of zinc oxide on the gold metallization was approximately estimated by calculating ratio of the gold (111) intensity to the zinc oxide (100) intensity with consideration of the zinc oxide coverage. The ratios were at 0.10, 0.11, 0.34, and 0.16 from free of hydrogen peroxide to 0.3 wt.% hydrogen

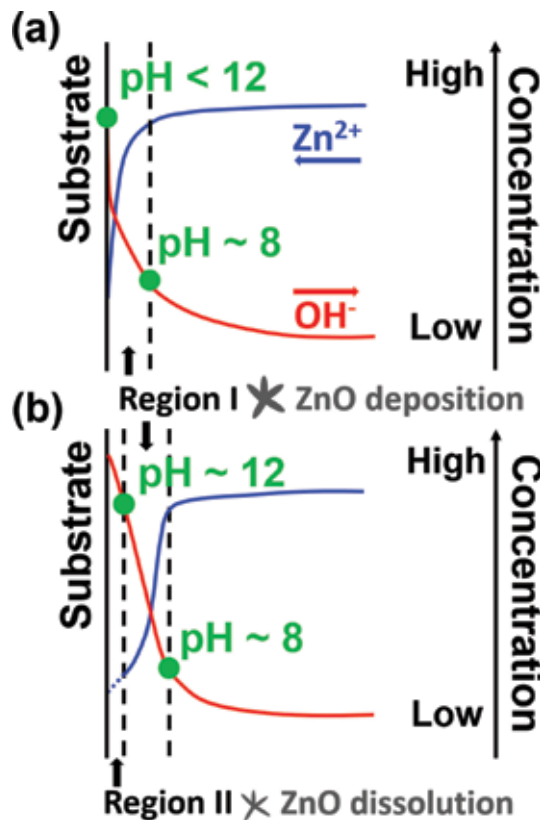


Figure 7. General scheme of the solute concentration profiles: (a) low OH⁻ concentration and (b) high OH⁻ concentration.

peroxide. The ratios suggested the solution containing 0.2 wt.% hydrogen peroxide deposited zinc oxide with the highest crystallinity, and the crystallinity became inferior when 0.3 wt.% hydrogen peroxide was used. Another explanation regarding to crystallinity of the zinc oxide is elaborated here. Crystallinity of the zinc oxide is known to be dependent on concentration of the zinc ion [35], which defects and worsened crystallinity are introduced to the zinc oxide when the zinc ion concentration is lowered. In this study, as the hydrogen peroxide concentration reached 0.3 wt.%, local concentration of hydroxide ion near the substrate surface is high, and high diffusion rate of hydroxide ion to the bulk electrolyte was constructed. Then, pH far away from the electrode surface became appropriate for deposition of zinc oxide and consumed high amount of the zinc ion. In this case, amount of the zinc ion diffused to the electrode surface was lowered and brought the low crystallinity.

Figure 8(b) shows the voltage-time plot in the zinc oxide cathodic deposition. When there is hydrogen peroxide in the solution, potential drop diminished as the hydrogen peroxide concentration increased. The potential drop here refers to the potential difference between the potential at ca. 0 s of the reaction time and the potential as the reaction steadily stabilized with deposition time. No obvious difference was detected in the specimens cathodically deposited with free of hydrogen peroxide and 0.1 wt.% hydrogen peroxide, which are in good agreement with the zinc oxide coverage in **Figure 6(e)** and **(f)** indicating that 0.1 wt.% hydrogen peroxide has only limited effect on the zinc oxide cathodic deposition. The potential oscillation became obvious with hydrogen peroxide concentration, which is because more N₂ gas is produced at high pH [36].

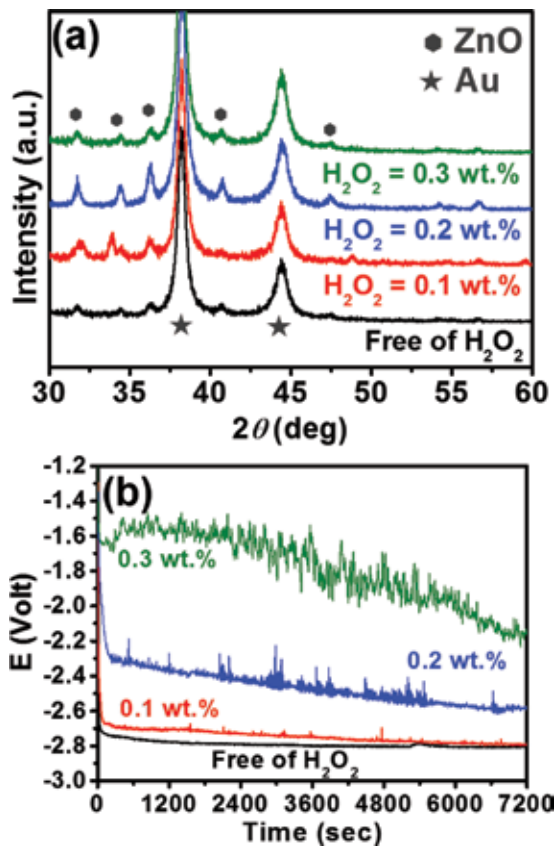


Figure 8. (a) X-ray diffraction patterns and (b) voltage-time plot of the specimens fabricated with electrolytes containing various H_2O_2 concentrations.

3. Silk/NiP/TiO₂ hybrid structure

3.1 Activation of silk fabric via scCO₂ palladium (II) acetylacetonate cat.

Figure 9 shows OM images and XRD patterns of the as-received silk and the scCO₂-catalyzed silk. The transparent interwoven bundles shown in **Figure 9(a)** indicate the silk fabric, and **Figure 9(b)** shows a broad peak at around $2\theta = 20^\circ$; this broad peak reveals an amorphous structure of the silk fabric. The light yellow flakes around the silk bundles in **Figure 9(c)** specify the palladium (II) acetylacetonate, and the diffraction peaks in **Figure 9(d)** labeled by triangle symbols can be indexed to palladium (II) acetylacetonate very well [26, 27], which indicated that the palladium (II) acetylacetonate organometallic compounds were successfully deposited on the silk substrate. As demonstrated in the **Figure 9(a)** and (c), the silk fabric remained undamaged after the 2 h scCO₂ cat. treatment due to the low surface tension, low viscosity, and noncorrosive properties to most of polymers of scCO₂ [37–39]. The scCO₂ cat. practiced a significant advancement when it is compared to the CONV cat. process [37].

3.2 NiP/TiO₂ codeposition

Surface conditions of the NiP/TiO₂-decorated silk fabrics prepared from the NiP electrolytes containing various TiO₂ concentrations (0, 10, 20, 30, 40, and 50 g/L) can

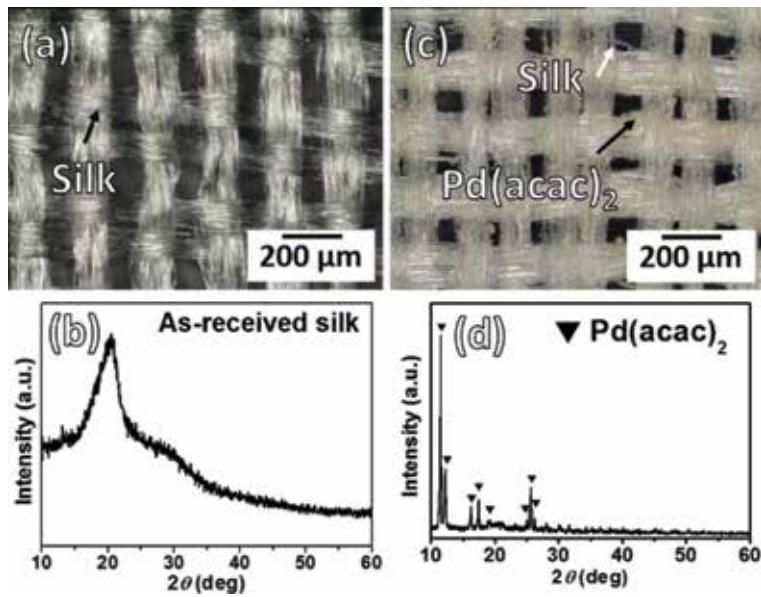


Figure 9. (a) OM image and (b) XRD pattern of the as-received silk, and (c) OM image and (d) XRD pattern of the $scCO_2$ catalyzed silk (triangle symbols: $Pd(acac)_2$).

be observed from SEM and OM images (inserted into top-left of each SEM images) shown in **Figure 10**. **Figure 10(a)** shows morphology of the specimen deposited without TiO_2 particles in the NiP electrolyte. It shows smooth surface while comparing to the other ones deposited with TiO_2 in the electrolyte (**Figure 10(b–f)**). The bright nano-sized protrusions shown in **Figure 10(b–f)** indicate the deposition of

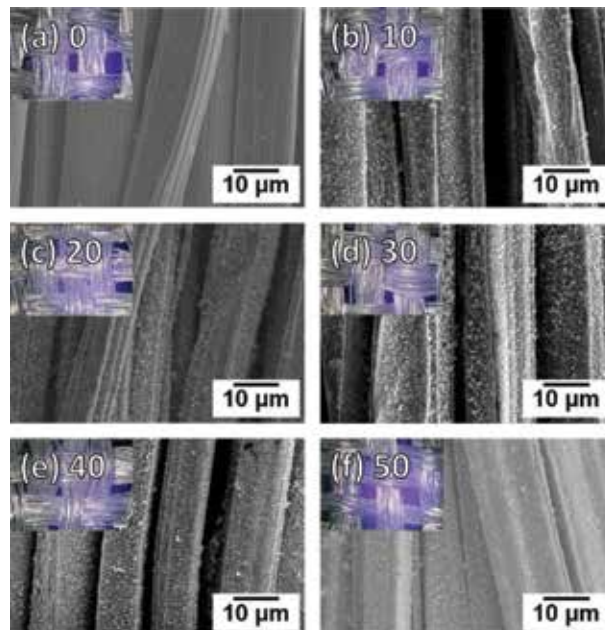


Figure 10. SEM images and OM images (inserted into top-left) of NiP/ TiO_2 deposition with various TiO_2 concentrations at (a) 0, (b) 10, (c) 20, (d) 30, (e) 40, and (f) 50 g/L, respectively.

TiO₂ which resulted in roughening of the surface. However, the surface roughness decreased when the TiO₂ concentration went beyond 30 g/L in NiP electrolyte.

The nanoscale TiO₂ particles in the electrolyte would aggregate to form large aggregate particles, and average size and size distribution of the aggregate particle are related to concentration of the oxide particles in the solution [40–45]. In this study, when the TiO₂ concentration is low (10 and 20 g/L), there is only slight aggregation of the TiO₂ particles in the NiP electrolyte. Average size of the aggregate particle size is small, and the distribution is narrow as illustrated in **Figure 11(a)**. Level of the aggregation gradually increases with an increase in concentration of the TiO₂, and average size of the aggregate particle becomes larger with a wider size distribution as shown in **Figure 11(b and c)**. Compositions of NiP/TiO₂ depositions are shown in **Table 1**.

The mechanism of the TiO₂ inclusion is illustrated in **Figure 12**. It is suggested that Ni ions would adsorb on surface of the TiO₂ aggregate particles suspending in the electrolyte to form Ni²⁺-TiO₂ complex particles, and the complex particles diffuse to the substrate; then, reduction of the Ni ions on surface of the complex particle occurred to engulf the TiO₂ aggregate particle into the NiP layer [24, 26]. When the TiO₂ concentration is low with a small aggregate particle size in the electrolyte, the TiO₂ aggregate particles are easily included into the NiP as shown in **Figures 11(a)** and **12(a)**. Because of the small aggregate particle size, a relatively smooth surface is obtained as exemplified by the specimen shown in **Figure 10(b and c)**. With an increase in the TiO₂ concentration, average size of aggregate particles included into the NiP gradually increases and leads to a roughened surface condition as illustrated in **Figure 12(b)**. **Figure 10(d)** demonstrates the result of the rough surface caused by the large aggregate particles in the moderate aggregate region (**Figure 11(b)**). The largest TiO₂ aggregate particle size was found at approximate 0.7 μm. When size of the TiO₂ aggregate (or the Ni²⁺-TiO₂ complex) particle reaches a critical size, a phenomenon named steric obstruction takes place to affect inclusion of the particles [46–53]. Steric obstruction is unfavorable for the inclusion as shown in **Figure 12(c)**. At first, removal of already-adsorbed oxide

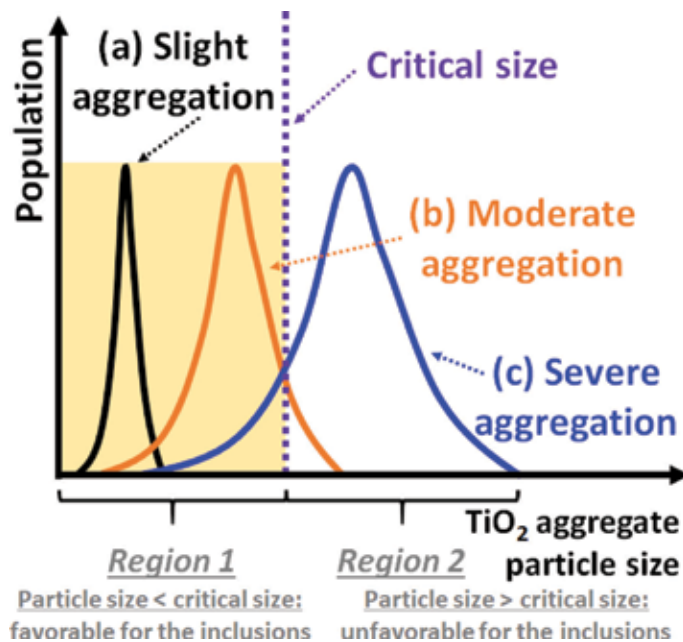


Figure 11. TiO₂ particle size distribution with different amount of TiO₂ in the electrolyte: (a) slight aggregation, (b) moderate aggregation, and (c) severe aggregation.

Atom	TiO ₂ (g/L)						
	0	10	20	30	40	50	60
P (at.%)	22.11	18.82	19.85	19.89	19.17	18.37	20.09
Ti (at.%)	0.00	4.62	5.95	10.16	6.15	5.32	4.76
Ni (at.%)	77.89	76.56	74.20	69.95	74.68	76.31	75.15
Sum	100.00	100.00	100.00	100.00	100.00	100.00	100.00

Table 1.
 Composition of as-deposited NiP/TiO₂ metallization layers on silk textiles.

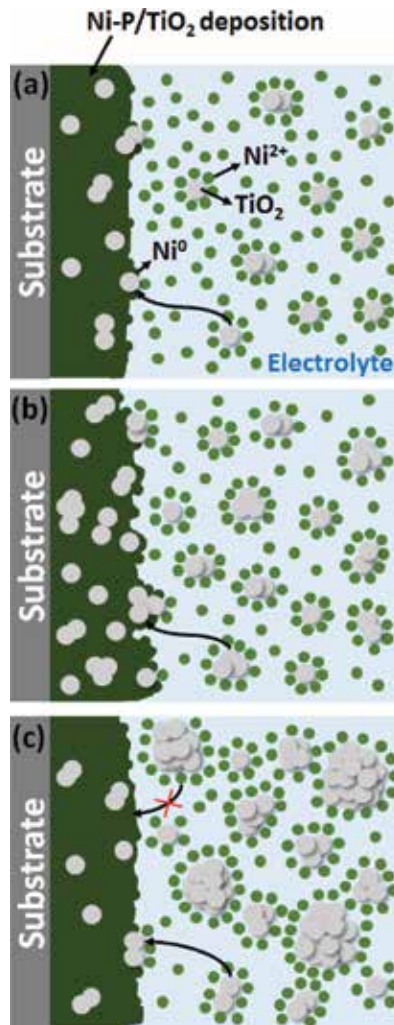


Figure 12.
 Mechanism of TiO₂ inclusion with (a) TiO₂ concentration less than critical amount, (b) TiO₂ concentration at critical amount, and (c) TiO₂ concentration more than critical amount.

particles and decrease in the number of new particles adhering to the substrate occur because of collisions between particles near the substrate [54]. Secondly, inclusion of the particles is dependent on reduction of Ni ions adsorbed on the aggregate TiO₂ particle surface. Surface-to-volume ratio of the aggregate particle is lowered with an increase in the aggregate TiO₂ particle size. When the aggregate TiO₂ particle size is

larger than the critical size, shortage of Ni ions adsorbed on surface of the particle makes it less likely to include the aggregate TiO_2 particle into the NiP before being removed away from the surface because of the collision [55]. In this study, average size of the aggregate TiO_2 particle is suggested to be close to the critical size causing the steric obstruction when the TiO_2 concentration is at 30 g/L (**Figures 10(d)** and **12(b)**), which is defined as the critical concentration resulting either maximum or minimum characteristics in the composite.

Figure 13 shows elemental mapping results of the NiP/ TiO_2 composite prepared with the electrolyte containing 30 g/L of TiO_2 . **Figure 13(a)** shows the rough surface condition of the composite layer deposited at the critical concentration. P, Ni, and Ti elements were homogeneously distributed on the surface indicating well-mixing of the electrolyte and homogeneous distribution of TiO_2 in the composite layer as indicated by results shown in **Figure 13(b)–(d)**. The compositions of NiP/ TiO_2 are shown in **Table 1**.

Figure 14 shows XRD patterns of the NiP/ TiO_2 -deposited silk fabrics at various TiO_2 concentrations in the electrolyte. A broad peak at around $2\theta = 45^\circ$ indicates amorphous structure of the NiP phase, while a sharp peak at around $2\theta = 25^\circ$ suggests anatase phase of the TiO_2 . All specimens show TiO_2 diffraction peak at $2\theta = 25^\circ$ except for the one without the introduction of TiO_2 (0 g/L) in **Figure 14(a)**. No impurity or third phase was found in the XRD pattern within the detection limitation. TiO_2 concentration was approximately compared by the ratio between intensities of the NiP and the TiO_2 major peaks to qualitatively estimate the TiO_2 concentration in the NiP metallization layer. The ratio increased as concentration of TiO_2 in the electrolyte increased until it reached 30 g/L, which implies an increase in concentration of TiO_2 in the composite layer. Then, the ratio decreased indicating a decrease in concentration of TiO_2 in the composite layer (**Figure 14e** and **f**). This observation confirmed 30 g/L of TiO_2 in the electrolyte being the critical concentration to give the highest TiO_2 inclusion in the composite and the effect of steric obstruction (**Figures 11** and **12**).

Figure 15 illustrates a positive correlation between the NiP/ TiO_2 composite layer thickness and the TiO_2 concentration in the electrolyte before reaching the critical concentration. A SEM image was inserted in the bottom-right corner of **Figure 15** to show cross-section of the silk/NiP/ TiO_2 composite layer deposited with 50 g/L TiO_2 in the electrolyte. The average growth rate was at 3.4 $\mu\text{m}/\text{h}$ before reaching the

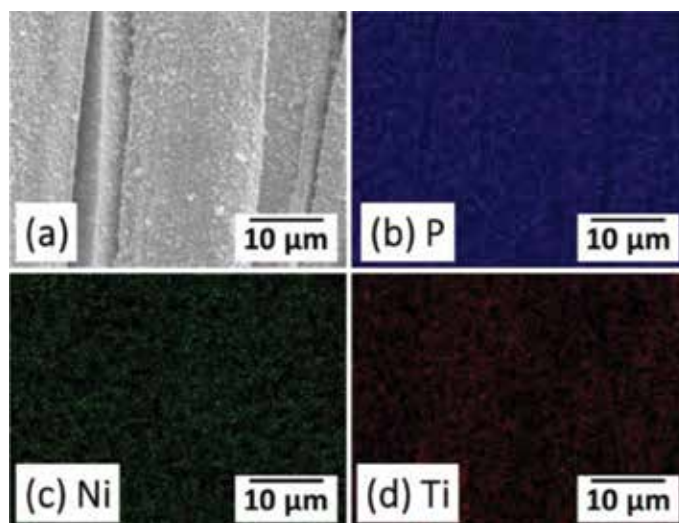


Figure 13.
Elemental mapping of NiP/ TiO_2 composite layer deposited with 30 g/L TiO_2 .

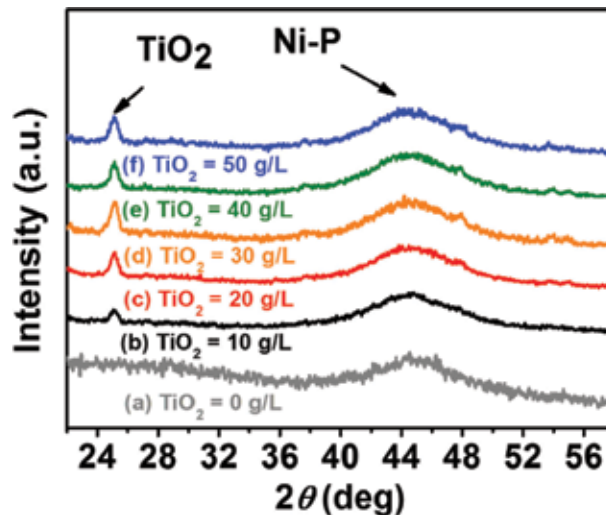


Figure 14. X-ray diffraction patterns of NiP/TiO₂ deposition with various TiO₂ concentrations at (a) 0, (b) 10, (c) 20, (d) 30, (e) 40, and (f) 50 g/L, respectively.

critical concentration. On the other hand, the thickness decreased slightly in the 40 and 50 g/L specimens since large TiO₂ aggregate particles were formed to cause the steric obstruction (Figures 11 and 12).

3.3 Electrical conductivity and adhesive tests

Electrical resistances of composite layers prepared at various TiO₂ concentrations in the NiP electrolyte are shown in Figure 16. Since TiO₂ is a semiconductor, it owns lower electrical conductivity than NiP. TiO₂ thus shows negative influence on the electrical conductivity in the NiP metallization layer. NiP metallization layer without TiO₂ inclusion performed the lowest electrical resistance. The electrical resistance increased monotonously with TiO₂ concentration in the electrolyte before reaching the critical concentration of TiO₂ (30 g/L) in the electrolyte. On the other hand, when the TiO₂ concentration in the electrolyte went beyond the critical concentration, the electrical resistance dropped owing to lower TiO₂ concentration in the NiP metallization layer. The inclusion trend of TiO₂ revealed by the electrical

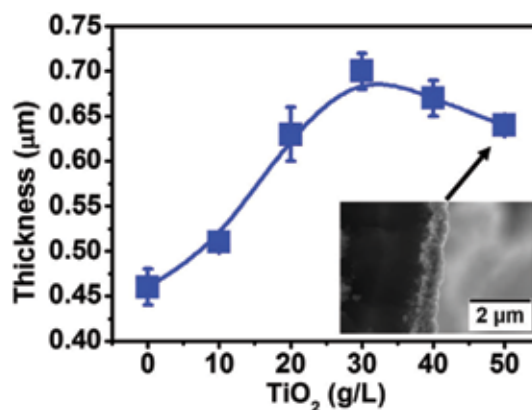


Figure 15. Relationship of NiP/TiO₂ thickness and TiO₂ concentration in the electrolyte.

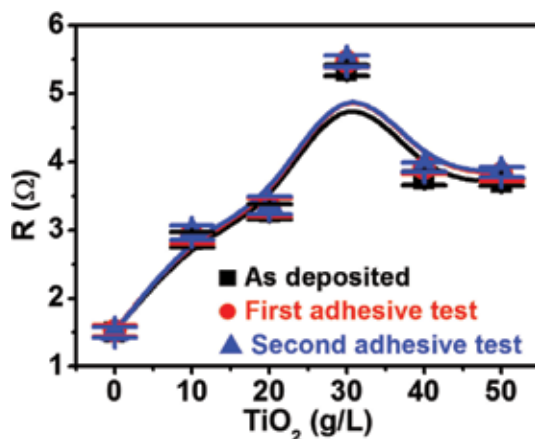


Figure 16. The influence of included TiO₂ concentration to the electrical resistance of the silk/NiP/TiO₂ composite material.

resistances is in accordance with the surface morphologies from SEM observations, the intensity ratios from XRD patterns, and the layer thickness results.

Adhesive test evaluations are also shown in **Figure 16**. Square symbol represents the as-deposited specimen, circle symbol depicts the first adhesive test, and the triangle one indicates the second adhesive test. Here, first adhesive test indicates one

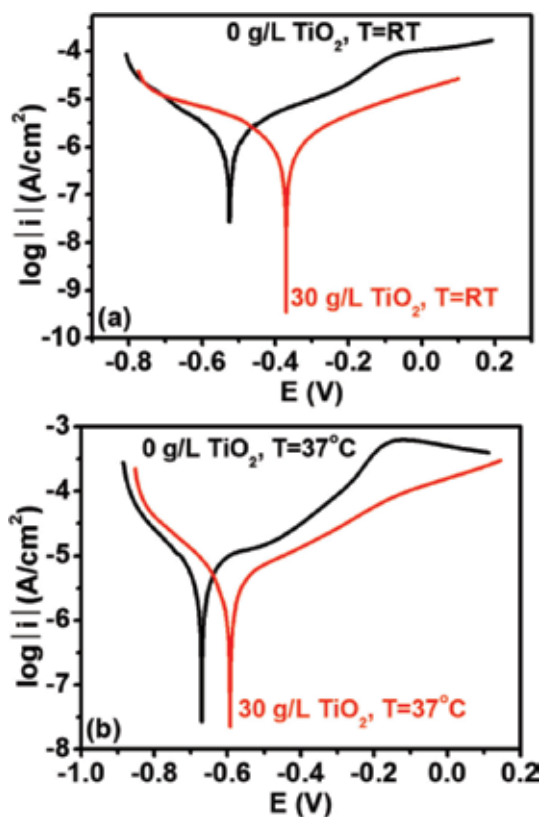


Figure 17. Polarization curves of pure NiP coating and NiP/TiO₂ (3 g/L TiO₂ in the electrolyte) deposition on silk textile at (a) room temperature and (b) 37°C (body temperature).

	E_{corr} (V)	I_{corr} (A/cm ²)
(a) Room temperature		
Silk/NiP	-0.53	6.00×10^{-7}
Silk/NiP/TiO ₂ (3 g/L)	-0.37	1.56×10^{-7}
(b) 37°C (body temperature)		
Silk/NiP	-0.67	3.79×10^{-6}
Silk/NiP/TiO ₂ (3 g/L)	-0.59	1.02×10^{-6}

Table 2.

Corrosion potentials and corrosion current densities of the silk/NiP and silk/NiP/TiO₂ composites in 3.5 wt.% NaCl at (a) room temperature and (b) 37°C (body temperature).

cycle of the adhesive treatment is performed. Accordingly, second adhesive test means two cycles of the test are conducted. The results show that the electrical resistances persisted after the second adhesive test. Moreover, no significant difference was found between the first and second adhesive tests, and thus no further adhesive tests were conducted. These results demonstrate the high reliability and the robustness of the silk/NiP/TiO₂ composite materials and indicate that it is practicable for WDs.

3.4 Corrosion resistance

Figure 17 shows the corrosion behaviors of the as-deposited silk/NiP composite and the silk/NiP/TiO₂ composite materials in 3.5 wt.% NaCl solution at both room temperature (**Figure 17(a)**) and 37°C (body temperature) (**Figure 17(b)**). The silk/NiP/TiO₂ composite fabricated with 30 g/L of TiO₂ in the electrolyte was chosen for the corrosion resistance evaluations. The corrosion potential (E_{corr}) and the corrosion current density (j_{corr}) are summarized in **Table 2**. These results show that the NiP/TiO₂ composites have excellent corrosion resistance when compared with the pure NiP coating at both room temperature and 37°C. According to the results, TiO₂ particles play an important role for the improvement of the corrosion resistance. TiO₂ particles act as inert physical barriers to the initiation and development of defect corrosion and modify microstructure of the NiP metallization layer to improve the corrosion resistance. On the other hand, the E_{corr} of silk/NiP/TiO₂ is more positive than the silk/NiP indicating that the silk/NiP/TiO₂ composite is more inert than the silk/NiP due to the inclusion of inert TiO₂ particles. This result demonstrates that the composite material can persist in salty human sweat at both room temperature and body temperature, which is promising for applications toward WDs.

4. Conclusions

Zinc oxide/gold-layered structure was successfully integrated on the silk fabric by scCO₂-promoted EP and cathodic deposition. Conventional problems encountered in the CONV EP were solved by the scCO₂-promoted technique. By the introduction of scCO₂, silk fabric was catalyzed without damages and the adhesion between silk fabric and the metallization layer was improved in the meanwhile. Surface coverage and thickness of gold metallization layer increased with the gold metallization period. The lowest electrical resistance was realized as the gold metallization period lengthened to 20 min. On the other hand, zinc oxide was fabricated on the gold-metallized silk fabric via the cathodic deposition technique. The depositions on the silk fabric have been detected to be metallic gold phase and zinc oxide wurtzite phase. Zinc

oxide deposited with 0.2 wt.% hydrogen peroxide performs the highest crystallinity showing the best photocurrent density. The zinc oxide-decorated specimen with 0.2 wt.% hydrogen peroxide performed 11.5 times improvement in the photocurrent density while compares to that of hydrogen peroxide-free one.

NiP/TiO₂ composite layer was successfully codeposited on silk fabric by scCO₂-assisted EP. Common difficulties encountered in the CONV EP were solved by the introduction of scCO₂, and the palladium (II) acetylacetonate organometallic compounds were embedded into the silk substrate. The composite layer on the silk was confirmed to be amorphous NiP phase and TiO₂ anatase phase. The composite showed the highest electrical resistance when the concentration of TiO₂ in the electrolyte was 30 g/L (critical concentration) since the highest TiO₂ concentration was included into the Ni-metallization layer. The largest TiO₂ aggregate particle size was found approximate 0.7 μm at the critical concentration. Highly adhesive property of this silk/NiP/TiO₂ composite was revealed by the adhesive tests and the electrical resistance. The NiP/TiO₂ showed higher corrosion resistance than that of NiP-metallized silk without TiO₂ particles at both room temperature and body temperature.

Acknowledgements

This work is supported by Japan Society for the Promotion of Science (JSPS) (17 J07395), the Grant-in-Aid for Scientific Research (B) (JSPS KAKENHI Grant Number 26282013), and JST CREST Grant Number JPMJCR1433.

Conflict of interest

We have no conflict of interest to declare.

Author details


Wan-Ting Chiu^{1*}, Chun-Yi Chen¹, Tso-Fu Mark Chang¹, Tomoko Hashimoto² and Hiromichi Kurosu²

¹ Institute of Innovative Research, Tokyo Institute of Technology, Yokohama, Japan

² Department of Clothing Environmental Science, Nara Women's University, Nara, Japan

*Address all correspondence to: chiu.w.aa@m.titech.ac.jp

IntechOpen

© 2018 The Author(s). Licensee IntechOpen. This chapter is distributed under the terms of the Creative Commons Attribution License (<http://creativecommons.org/licenses/by/3.0>), which permits unrestricted use, distribution, and reproduction in any medium, provided the original work is properly cited. 

References

- [1] Gozalvez J. 5G tests and demonstrations [mobile radio]. *IEEE Vehicular Technology Magazine*. 2015;**10**(2):16-25. DOI: 10.1109/MVT.2015.2414831
- [2] Sankapal BR, Gajare HB, Karade SS, Salunkhe RR, Dubal DP. Zinc oxide encapsulated carbon nanotube thin films for energy storage applications. *Electrochimica Acta*. 2016;**192**:377-384. DOI: 10.1016/j.electacta.2016.01.193
- [3] Mallory GO, Hajdu JB. EP: Fundamentals and Applications. New Jersey, USA: William Andrew; 1990. DOI: 10.1002/9783527616770.ch2
- [4] Adachi H, Taki K, Nagamine S, Yusa A, Ohshima M. Supercritical carbon dioxide assisted EP on thermoplastic polymers. *The Journal of Supercritical Fluids*. 2009;**49**(2):265-270. DOI: 10.1016/j.supflu.2013.11.012
- [5] Watkins JJ, McCarthy TJ. Polymer/metal nanocomposite synthesis in supercritical CO₂. *Chemistry of Materials*. 1995;**7**(11):1991-1994. DOI: 10.1021/cm00059a001
- [6] Brunner G. Gas Extraction: An Introduction to Fundamentals of Supercritical Fluids and the Application to Separation Processes. New York, USA: Springer Science & Business Media; 2013. DOI: 10.1002/bbpc.19961000668
- [7] Clifford A, Clifford T. Fundamentals of Supercritical Fluids. Oxford, UK: Oxford University Press; 1999
- [8] Sawan SP, Sawan SP. Supercritical Fluid Cleaning: Fundamentals, Technology and Applications. Amsterdam, Netherlands: Elsevier; 1998
- [9] Gorla C, Emanetoglu N, Liang S, Mayo W, Lu Y, Wraback M, et al. Structural, optical, and surface acoustic wave properties of epitaxial zinc oxide films grown on (0112) sapphire by metalorganic chemical vapor deposition. *Journal of Applied Physics*. 1999;**85**(5):2595-2602. DOI: 10.1063/1.369577
- [10] Panigrahy B, Aslam M, Misra D, Bahadur D. Polymer-mediated shape-selective synthesis of zinc oxide nanostructures using a single-step aqueous approach. *CrystEngComm*. 2009;**11**(9):1920-1925. DOI: 10.1039/B904833M
- [11] Ku C-H, Wu J-J. Aqueous solution route to high-aspect-ratio zinc oxide nanostructures on indium tin oxide substrates. *The Journal of Physical Chemistry B*. 2006;**110**(26):12981-12985. DOI: 10.1021/jp061458b
- [12] Zhang Q, Tian C, Wu A, Tan T, Sun L, Wang L, et al. A facile one-pot route for the controllable growth of small sized and well-dispersed zinc oxide particles on GO-derived graphene. *Journal of Materials Chemistry*. 2012;**22**(23):11778-11784. DOI: 10.1039/C2JM31401K
- [13] Peulon S, Lincot D. Mechanistic study of cathodic electrodeposition of zinc oxide and zinc hydroxychloride films from oxygenated aqueous zinc chloride solutions. *Journal of the Electrochemical Society*. 1998;**145**(3):864-874. DOI: 10.1149/1.1838359
- [14] Peulon S, Lincot D. Cathodic electrodeposition from aqueous solution of dense or open-structured zinc oxide films. *Advanced Materials*. 1996;**8**(2):166-170. DOI: 10.1002/adma.19960080216
- [15] Hu C-C, Hsu H-C, Chang K-H. Cathodic deposition of TiO₂: Effects of H₂O₂ and deposition modes. *Journal of the Electrochemical Society*.

- 2012;**159**(7):D418-DD24. DOI: 10.1149/2.026207jes
- [16] Chang T-FM, Sato T, Sone M. Fabrication of TiO₂ micro-structures by cathodic deposition. *Microelectronic Engineering*. 2014;**121**:80-82. DOI: 10.1016/j.mee.2014.03.033
- [17] Lee HM, Ge M, Sahu B, Tarakeshwar P, Kim KS. Geometrical and electronic structures of gold, silver, and gold–silver binary clusters: Origins of ductility of gold and gold–silver alloy formation. *The Journal of Physical Chemistry B*. 2003;**107**(37):9994-10005. DOI: 10.1021/jp034826+
- [18] Hsiao Y-C, Wu T-F, Wang Y-S, Hu C-C, Huang C. Evaluating the sensitizing effect on the photocatalytic decoloration of dyes using anatase-TiO₂. *Applied Catalysis B: Environmental*. 2014;**148**:250-257. DOI: 10.1016/j.apcatb.2013.11.014
- [19] Nakaoka K, Ueyama J, Ogura K. Photoelectrochemical behavior of electrodeposited CuO and Cu₂O thin films on conducting substrates. *Journal of the Electrochemical Society*. 2004;**151**(10):C661-C665. DOI: 10.1149/1.1789155
- [20] Lu X, Wang G, Xie S, Shi J, Li W, Tong Y, et al. Efficient photocatalytic hydrogen evolution over hydrogenated zinc oxide nanorod arrays. *Chemical Communications*. 2012;**48**(62): 7717-7719. DOI: 10.1039/C2CC31773G
- [21] Gawad SA, Baraka A, Morsi M, Eltoum MA. Development of electroless Ni–P–Al₂O₃ and Ni–P–TiO₂ composite coatings from alkaline hypophosphite gluconate baths and their properties. *International Journal of Electrochemical Science*. 2013;**8**:1722-1734
- [22] Thiemig D, Bund A. Characterization of electrodeposited Ni–TiO₂ nanocomposite coatings. *Surface and Coatings Technology*. 2008;**202**(13):2976-2984. DOI: 10.1016/j.surfcoat.2007.10.035
- [23] Parida G, Chaira D, Chopkar M, Basu A. Synthesis and characterization of Ni–TiO₂ composite coatings by electro-co-deposition. *Surface and Coatings Technology*. 2011;**205**(21-22):4871-4879. DOI: 10.1016/j.surfcoat.2011.04.102
- [24] Benea L, Danaila E, Celis J-P. Influence of electro-co-deposition parameters on nano-TiO₂ inclusion into nickel matrix and properties characterization of nanocomposite coatings obtained. *Materials Science and Engineering: A*. 2014;**610**:106-115. DOI: 10.1016/j.msea.2014.05.028
- [25] Momenzadeh M, Sanjabi S. The effect of TiO₂ nanoparticle codeposition on microstructure and corrosion resistance of electroless Ni–P coating. *Materials and Corrosion*. 2012;**63**(7):614-619. DOI: 10.1002/maco.201005985
- [26] Esken D, Zhang X, Lebedev OI, Schröder F, Fischer RA. Pd@MOF-5: Limitations of gas-phase infiltration and solution impregnation of [Zn₄O(bdc)₃] (MOF-5) with metal–organic palladium precursors for loading with Pd nanoparticles. *Journal of Materials Chemistry*. 2009;**19**(9):1314-1319. DOI: 10.1039/B815977G
- [27] Wang Y, Zheng H, Li Z, Xie K. Investigation of the interaction between Cu(acac)₂ and NH₄Y in the preparation of chlorine-free CuY catalysts for the oxidative carbonylation of methanol to a fuel additive. *RSC Advances*. 2015;**5**(124):102323-102331. DOI: 10.1039/C5RA19941G
- [28] Tang W, Xu K, Wang P, Li X. Surface roughness and resistivity of Au film on Si-(111) substrate. *Microelectronic Engineering*. 2003;**66**(1-4):445-450. DOI: 10.1016/S0167-9317(02)00909-7

- [29] Jiao S, Zhang K, Bai S, Li H, Gao S, Li H, et al. Controlled morphology evolution of zinc oxide nanostructures in the electrochemical deposition: From the point of view of chloride ions. *Electrochimica Acta*. 2013;**111**:64-70. DOI: 10.1016/j.electacta.2013.08.050
- [30] El Hichou A, Stein N, Boulanger C, Johann L. Structural and spectroscopic ellipsometry characterization for electrodeposited zinc oxide growth at different hydrogen peroxide concentration. *Thin Solid Films*. 2010;**518**(15):4150-4155. DOI: 10.1016/j.tsf.2009.11.070
- [31] Lin W-H, Chang T-FM, Lu Y-H, Sato T, Sone M, Wei K-H, et al. Supercritical CO₂-assisted electrochemical deposition of zinc oxide mesocrystals for practical Photoelectrochemical applications. *The Journal of Physical Chemistry C*. 2013;**117**(48):25596-25603. DOI: 10.1021/jp409607m
- [32] Pauporté T, Lincot D. Hydrogen peroxide oxygen precursor for zinc oxide electrodeposition II—Mechanistic aspects. *Journal of Electroanalytical Chemistry*. 2001;**517**(1):54-62. DOI: 10.1016/S0022-0728(01)00674-X
- [33] Bian S-W, Mudunkotuwa IA, Rupasinghe T, Grassian VH. Aggregation and dissolution of 4 nm zinc oxide nanoparticles in aqueous environments: Influence of pH, ionic strength, size, and adsorption of humic acid. *Langmuir*. 2011;**27**(10):6059-6068. DOI: 10.1021/la200570n
- [34] Wippermann K, Schultze J, Kessel R, Penninger J. The inhibition of zinc corrosion by bisaminotriazole and other triazole derivatives. *Corrosion Science*. 1991;**32**(2):205225-223230. DOI: 10.1016/0010-938X(91)90044-P
- [35] Tena-Zaera R, Elias J, Wang G, Lévy-Clément C. Role of chloride ions on electrochemical deposition of zinc oxide nanowire arrays from O₂ reduction. *The Journal of Physical Chemistry C*. 2007;**111**(45):16706-16711. DOI: 10.1021/jp073985g
- [36] Tekerlekopoulou AG, Pavlou S, Vayenas DV. Removal of ammonium, iron and manganese from potable water in biofiltration units: A review. *Journal of Chemical Technology and Biotechnology*. 2013;**88**(5):751-773. DOI: 10.1002/jctb.4031
- [37] Woo B-H, Sone M, Shibata A, Ishiyama C, Masuda K, Yamagata M, et al. Effects of ScCO₂ cat. in metallization on polymer by EP. *Surface and Coatings Technology*. 2009;**203**(14):1971-1978. DOI: 10.1016/j.surfcoat.2009.01.031
- [38] Tengsuwan S, Ohshima M. Electroless nickel plating on polypropylene via hydrophilic modification and supercritical carbon dioxide Pd-complex infusion. *The Journal of Supercritical Fluids*. 2012;**69**:117-123. DOI: 10.1016/j.supflu.2012.06.002
- [39] Sano M, Tahara Y, Chen C-Y, Chang T-FM, Hashimoto T, Kurosu H, et al. Application of supercritical carbon dioxide in cat. and Ni-P EP of nylon 6, 6 fabric. *Surface and Coatings Technology*. 2016;**302**:336-343. DOI: 10.1016/j.surfcoat.2016.06.037
- [40] Ns B, Sakai G, Miura N, Yamazoe N. Preparation of stabilized nanosized tin oxide particles by hydrothermal treatment. *Journal of the American Ceramic Society*. 2000;**83**(12):2983-2987. DOI: 10.1111/j.1151-2916.2000.tb01670.x
- [41] Korotcenkov G, Cho B. The role of the grain size on thermal stability of nanostructured SnO₂ and In₂O₃ metal oxides films aimed for gas sensor application. *Progress in Crystal Growth and Characterization of Materials*. 2012;**58**:167-208. DOI: 10.1016/j.pcrysgrow.2012.07.001

- [42] Abdel Hamid Z, Ghayad IM. Characteristics of electrodeposition of Ni-polyethylene composite coatings. *Materials Letters*. 2002;**53**(4):238-243. DOI: 10.1016/S0167-577X(01)00484-0
- [43] Müller C, Sarret M, Benballa M. ZnNi/SiC composites obtained from an alkaline bath. *Surface and Coatings Technology*. 2003;**162**(1):49-53. DOI: 10.1016/S0257-8972(02)00360-2
- [44] Krishnaveni K, Sankara Narayanan TSN, Seshadri SK. Electrodeposited Ni-B-Si₃N₄ composite coating: Preparation and evaluation of its characteristic properties. *Journal of Alloys and Compounds*. 2008;**466**(1):412-420. DOI: 10.1016/j.jallcom.2007.11.104
- [45] Liao C-W, Lee H-B, Hou K-H, Jian S-Y, Lu C-E, Ger M-D. Characterization of the Cr-C/Si₃N₄ composite coatings electroplated from a trivalent chromium bath. *Electrochimica Acta*. 2016;**209**:244-253. DOI: 10.1016/j.electacta.2016.05.084
- [46] Gutzeit G. Industrial nickel coating by chemical catalytic reduction. *Anti-Corrosion Methods and Materials*. 1956;**3**(6):208. DOI: 10.1108/eb019191
- [47] Cavallotti P, Salvago G. Studies on chemical reduction of nickel and cobalt by hypophosphite. Pt. 2. Characteristics of the process. *Electrochim Metallorum*. 1968;**3**(3):239-266
- [48] Salvago G, Cavallotti P. Characteristics of the chemical reduction of nickel alloys with hypophosphite. *Plating*. 1972;**59**(7):665-671
- [49] Rondin JP, Hintermann H. A calorimetric study of the electroless deposition of nickel. *Journal of the Electrochemical Society*. 1970;**117**(2):160-167. DOI: 10.1149/1.2408405
- [50] Mizuhashi S, Cordonier CEJ, Matsui H, Honma H, Takai O. Comparative study on physical and electrochemical characteristics of thin films deposited from electroless platinum plating baths. *Thin Solid Films*. 2016;**619**(Supplement C): 328-335. DOI: 10.1016/j.tsf.2016.10.040
- [51] Mizuhashi S, Cordonier CE, Honma H, Takai O. Stabilization of an electroless platinum plating bath using S-bearing additives. *Journal of the Electrochemical Society*. 2015;**162**(10):D497-D502. DOI: 10.1149/2.0081510jes
- [52] Rao CRK, Pushpavanam M. Electroless deposition of platinum on titanium substrates. *Materials Chemistry and Physics*. 2001;**68**(1):62-65. DOI: 10.1016/S0254-0584(00)00268-6
- [53] Pak JJ, Cha S-E, Ahn H-J, Lee S-K, editors. Fabrication of ionic polymer metal composites by EP of Pt. In: *Proc of the 32nd Intl Symp on Robotics*. 2001
- [54] Zahavi J, Hazan J. Electrodeposited nickel composites containing diamond particles. *Plating and Surface Finishing*. 1983;**70**(2):57-61
- [55] Lee W-H, Tang S-C, Chung K-C. Effects of direct current and pulse-plating on the co-deposition of nickel and nanometer diamond powder. *Surface and Coatings Technology*. 1999;**120**:607-611. DOI: 10.1016/S0257-8972(99)00445-4

Multi-Physics Simulation Platform and Multi-Layer Metal Technology for CMOS-MEMS Accelerometer with Gold Proof Mass

Katsuyuki Machida, Toshifumi Konishi, Daisuke Yamane, Hiroshi Toshiyoshi and Hiroyuki Ito

Abstract

This chapter describes technical features and solutions to realize a highly sensitive CMOS-MEMS accelerometer with gold proof mass. The multi-physics simulation platform for designing the CMOS-MEMS device has been developed to understand simultaneously both mechanical and electrical behaviors of MEMS stacked on LSI. MEMS accelerometer fabrication process is established by the multi-layer metal technology, which consists of the gold electroplating and the photo-sensitive polyimide film. The proposed MEMS accelerometers are fabricated and evaluated to verify the effectiveness of the proposed techniques regarding sub-1G MEMS and arrayed MEMS devices. The experimental results show that the Brownian noise of the sub-1G MEMS accelerometer can achieve $780 \text{ nG}/(\text{Hz})^{1/2}$ and the arrayed MEMS accelerometer has a wide detection, ranging from 1.0 to 20 G. Moreover, using the developed simulation platform, we demonstrate the proposed capacitive CMOS-MEMS accelerometer implemented by the multi-layer metal technology. In conclusion, it is confirmed that the multi-physics simulation platform and the multi-layer metal technology for the CMOS-MEMS device have a potential to realize a nano-gravity sensing technology.

Keywords: MEMS accelerometer, CMOS-MEMS, multi-physics simulation, gold proof mass, multi-layer metal technology

1. Introduction

Microelectromechanical systems (MEMS) capacitive accelerometers have been widely used in application fields such as mobile devices, air bag ignition for vehicles, and vital sign monitoring systems [1–10]. Also, in the progress of the attractive Internet of the Thing (IoT) technology, MEMS accelerometers have played an important role in key devices. Recently, for several applications such as activities monitoring or the integrated inertial measurement unit (IMU), the accurate sensing devices below 1 G ($G = 9.8 \text{ m/s}^2$) have been researched and developed regarding various types of MEMS capacitive accelerometer, while conventional MEMS accelerometers have an ability of sensing about 1 G or over several G's. The performance

of the MEMS capacitive accelerometer can be determined by Brownian noise (B_N) that is inversely proportional to the mass of the proof mass. **Figure 1** shows the transition of B_N of the reported MEMS accelerometers. In order to establish a micro-gravity sensing technology based on silicon bulk or surface micromachining technologies, various types of MEMS capacitive accelerometer and complementary metal-oxide semiconductor (CMOS)-MEMS accelerometer have been reported [11–22]. We have developed the MEMS accelerometer and also added the data of our miniaturized sub-1G MEMS capacitive accelerometer [23] to this figure. The proof mass area of our device is nearly one-tenth of a silicon proof mass area size. As a result, in terms of the technological trend, it is suggested that this research and development would be continuing toward a nano-gravity sensing.

On the other hand, the above applications require the devices, which have a wide detectable range of acceleration, small size, and low power consumption. In fact, there are many difficulties in making the devices because the large size of the proof mass makes the device size larger, and also the accelerometer chip is usually combined with the LSI chips on the assembly board. In order to overcome these technical barriers, we have proposed a CMOS-MEMS accelerometer that implements a MEMS on CMOS-LSI [24, 25]. **Figure 2** shows prospects and challenges of the CMOS-MEMS technology from the view point of CMOS-LSI. It indicates that this technology has a solution of the difficulties in developing high functional devices. Especially, digital micro mirror device (DMD) is well-known as a successful example of MEMS business. The technology has the features of high functionality, high accuracy, and mass production. Thus, we have developed the multi-layer metal technology that consists of gold electroplating and sacrificial layer formation using thick polyimide film. Its features include the suitability to realize the various MEMS structures and the post-CMOS processes, which does not degrade CMOS device because the process temperature is below 310°C. Using the multi-layer metal technology, MEMS devices on CMOS LSI have been fabricated [26, 27].

Moreover, to facilitate the design of the CMOS-MEMS devices, we have researched and proposed a multi-physics simulation technique to develop such CMOS-MEMS devices using an electrical circuit simulator with a Verilog-A compatible hardware description language (HDL) for equivalent circuit description

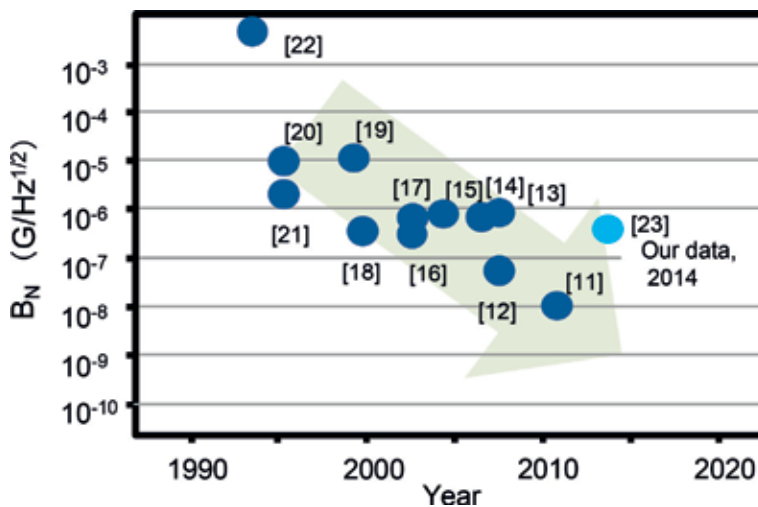


Figure 1. The transition of the B_N of the reported MEMS accelerometers.

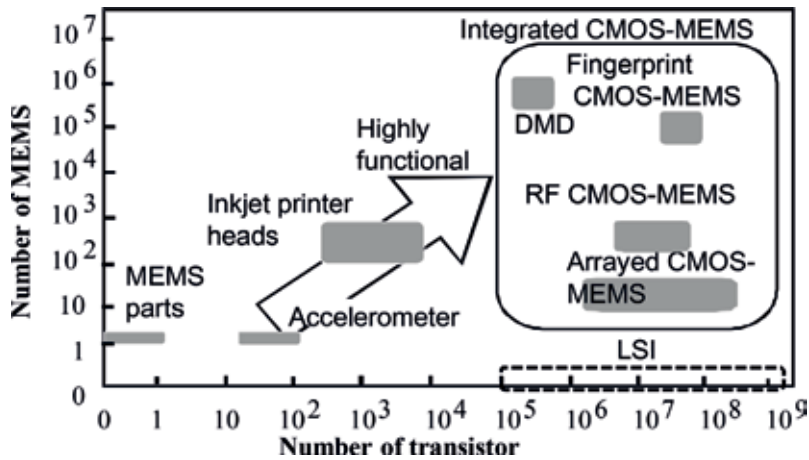


Figure 2. Business trend and correlation between the number of MEMS devices and transistors.

[28, 29]. Thus, we have developed a capacitive CMOS-MEMS sensor designed by our multi-physics simulation. The developed sensor shows that the capacitive MEMS device is implemented on the sensor LSI [30].

In this chapter, first, the multi-physics simulation platform for the CMOS-MEMS technology is presented. Next, we describe the newly developed sensor structure and the multi-layer metal technology, which can be compatible with post-CMOS process. Third, the sub-1G MEMS accelerometer is described. Fourth, the arrayed MEMS accelerometer for wide range detection is demonstrated. Fifth, we then show the proposed sensor circuit using our multi-physics simulation environment. Finally, we demonstrate the evaluation results of the fabricated CMOS-MEMS accelerometer by the multi-layer metal technology.

2. The multi-physics simulation

2.1 Analytical model for MEMS accelerometer

Figure 3 shows a diagram of an analytical model for the MEMS accelerometer. The electrostatic capacitive MEMS accelerometer basically consists of the upper electrode of a proof mass and the bottom plate of the fixed electrode. The upper plate is supported by the spring connected to the mechanical anchor. When the proof mass detects an input acceleration in the vertical direction, the electrical capacitance between the upper and the bottom plates is modulated. The fixed electrode is applied by the input voltage V to measure the capacitance change. The analytical model includes the capacitances of C_1 , C_2 , and C_{air} as shown in **Figure 3**. The capacitance of C_{total} can be obtained as the following equations:

$$C_1 = \frac{\epsilon_0 \epsilon_1 S_1}{t_1} \quad (1)$$

$$C_2 = \frac{\epsilon_0 \epsilon_2 S_1}{gini - x} \quad (2)$$

$$C_{air} = \frac{\epsilon_0 \epsilon_2 (S_2 - S_1)}{gini - x + t_i} \quad (3)$$

$$C_{total} = C_{air} + \left(\frac{1}{C_1} + \frac{1}{C_2} \right)^{-1} = \frac{\epsilon_2 \epsilon_0 (S_2 - S_1)}{gini - x + t_i} + \frac{\epsilon_0 S_1}{\frac{t_i}{\epsilon_1} + \frac{(gini - x)}{\epsilon_2}} \quad (4)$$

where ϵ_0 is the permittivity of vacuum, ϵ_1 is the relative permittivity of the SiO₂, ϵ_2 is the relative permittivity of the air, S_1 is the areas of the SiO₂ coverage, S_2 is the total areas of the movable electrode, t_i is the thickness of the SiO₂, $gini$ is the initial air gap, and x is the displacement of the proof mass.

The input force due to the acceleration F_{acc} , the mechanical viscoelastic force F_m , the electrostatic attractive force F_e , and the relationship of their contributions is expressed in the following equations:

$$F_{acc} = 9.8mG \quad (5)$$

$$F_s = kx + c\dot{x} \quad (6)$$

$$F_e = \frac{1}{2} \frac{\partial C}{\partial x} V^2 = \frac{V^2}{2} \left[\frac{\epsilon_2 \epsilon_0 (S_2 - S_1)}{(gini - x + t_i)^2} + \frac{\epsilon_0 S_1}{\epsilon_2 \left(\frac{t_i}{\epsilon_1} + \frac{gini - x}{\epsilon_2} \right)^2} \right] \quad (7)$$

$$F_{acc} + F_e + F_s = 0 \quad (8)$$

where m is the proof mass, G is the input acceleration value measured in gravitational acceleration, k is the spring constant, and c is the damping coefficient including the viscosity of the air.

2.2 Equivalent circuit model for MEMS accelerometer

Figure 4 shows the equivalent circuit for the MEMS accelerometer implemented in Cadence Virtuoso [31], which is widely used for LSI design.

According to the Eqs. (1)–(8), we have proposed equivalent circuit of five modules:

Module (I) represents the acceleration to provide an external force system.

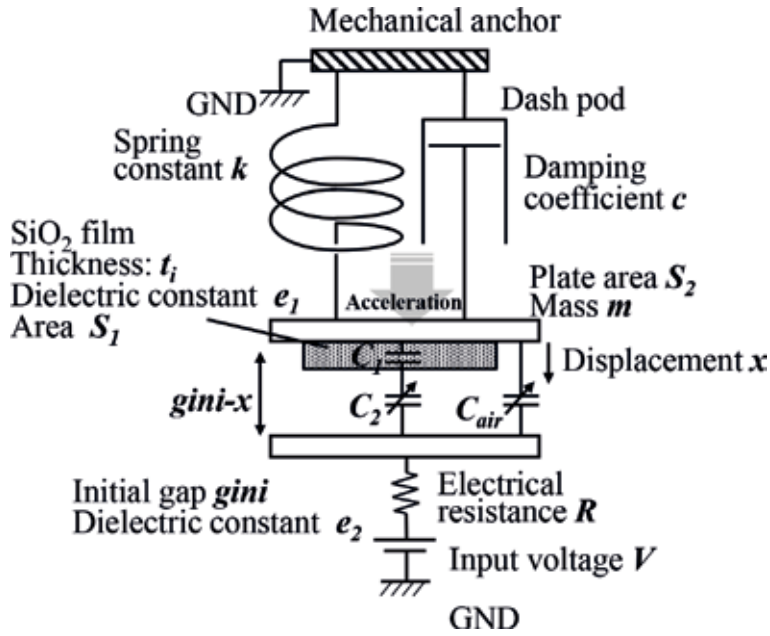


Figure 3.
 Analytical model for electrostatic MEMS accelerometer.

Module (II) is the parallel-plate electrostatic actuator to calculate the electrostatic attractive force and inductive charge as a function of the applied voltages.

Module (III) is the viscoelastic suspension module.

Module (IV) is the core of the equivalent circuit, where the equation of motion (EOM) is carried out under conditions of force applied to the mass m .

Module (V) represents the mechanical anchor.

These modules are described in a Verilog-A compatible HDL. We also have established modules (I) and (II) by extending our previous work reported elsewhere [29]; likewise, modules (III), (IV), and (V) are interpreted using Eqs. (6) and (8). Meandering suspensions are used in this chapter to lower the elastic rigidity in the direction normal to the chip surface.

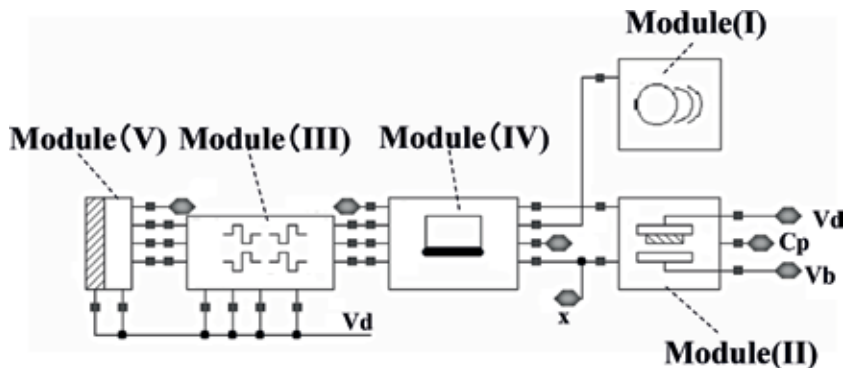


Figure 4.
 Schematic image of the proposed equivalent circuits for a single MEMS accelerometer.

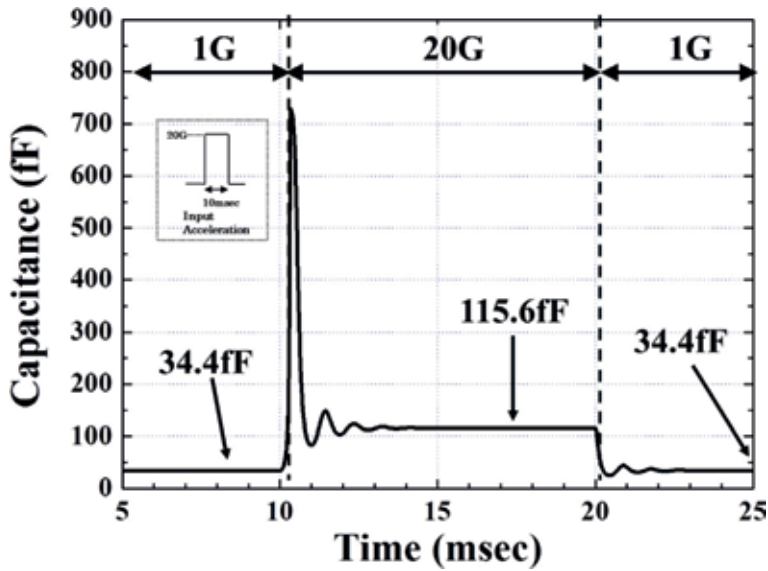


Figure 5. Simulation results of a single MEMS accelerometer.

For verification, we performed simulation. Thus, we applied the simulation to a single MEMS accelerometer to detect a 20 G using the above equivalent circuit. **Figure 5** shows the simulation results of a capacitance change of the MEMS accelerometer under the condition of 20 G at the period of 10 ms. The result suggests that the accelerometer can detect the capacitance change without stiction. From these results, it can be concluded that the equivalent circuit would quantitatively represent the device in this chapter.

3. MEMS accelerometer

3.1 Accelerometer structure

Figure 6 shows the concept of the proposed MEMS accelerometer structure, which is composed of the movable proof mass, the fixed bottom electrode, stopper, and suspension.

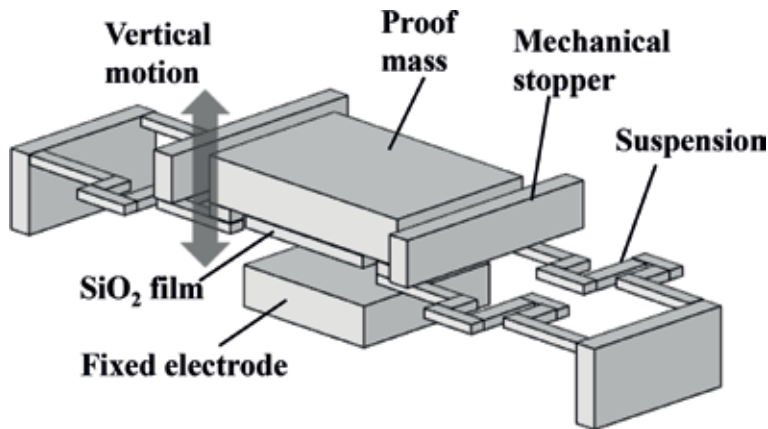


Figure 6. The conceptual image of the proposed MEMS sensor structure.

and suspension. The accelerometer structure has the following three features; (i) in order to facilitate flexibilities of design, we have utilized the multi-layer metal technology [12, 32–34]. The multi-layer metal technology can adjust the weight of the proof mass and the spring constant of mechanical suspensions, (ii) the stopper structure is built to prevent mechanical destruction from lateral and vertical over-swings of the proof mass, and (iii) the SiO₂ film is formed to prevent sticking and electrical short between the proof mass and the fixed electrode.

3.2 Proof mass material

The proof mass size should be substantially reduced while keeping adequate weight on it, we can then downscale the sensor area without compromising the sensitivity. The minimum detection sensitivity of the accelerometer is limited by Brownian noise (B_N) as described in the following equation [19]:

$$B_N = \frac{\sqrt{4k_B T b}}{m} \quad (9)$$

where T , b , k_B , and m are the absolute temperature, the viscous damping coefficient, the Boltzmann constant (1.38×10^{-23} J/K), the absolute temperature, and the proof mass of an accelerometer, respectively. We have searched the suitable materials for the proof mass to further minimize B_N . **Figure 7** shows the comparison of the Brownian noise on the proof masses made of different types of materials. Our target value of the B_N can be below $100 \mu\text{G}/(\text{Hz})^{1/2}$ to provide a sufficiently low Brownian noise [24, 25] for a practical use. Thus, gold could be a candidate material for small proof mass size. In addition, gold material should also be suitable for the fabrication process of the CMOS-MEMS accelerometer that gold electroplating has successfully stacked MEMS on an LSI circuit [26, 35, 36].

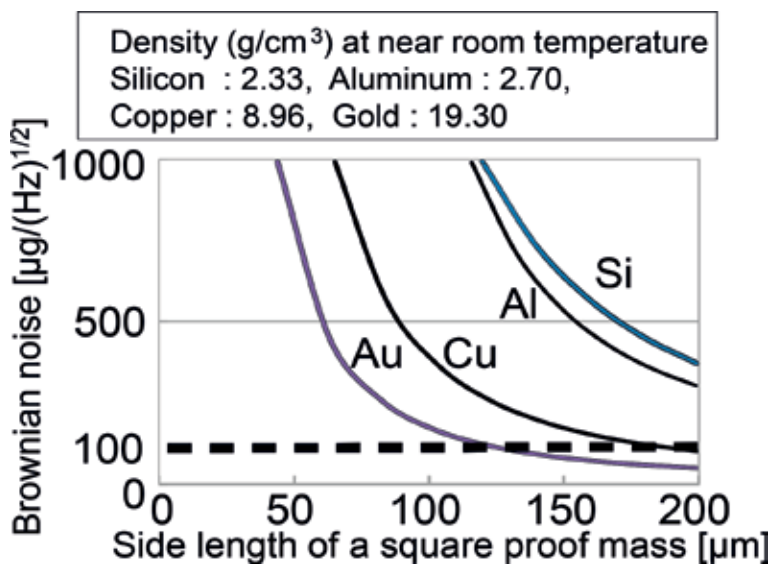


Figure 7.
 The comparison of the Brownian noise on the proof masses.

3.3 Fabrication process

Figure 8 shows the fabrication process flow for the designed MEMS accelerometer. Firstly, Ti/Au adhesion and seed layers were deposited by the vacuum evaporation on a thermal SiO₂ (**Figure 8a**). After forming the electrodes and interconnections using the patterning process, photo-sensitive polyimide film was then spin-coated and annealed at 310°C as a first sacrificial layer. The gold electroplating formed the bottom gold layer (**Figure 8b**); this metallization was applied in every metal layer process as described in the following. After depositing next sacrificial layer of photo-sensitive polyimide film supporting gold of the thickness of 3 μm (**Figure 8c**), contact holes for interconnections were made, and then a 0.5 μm thick SiO₂ was deposited by sputtering (**Figure 8d**). Finally, the proof mass and stopper structures 15 μm in thickness were formed on the uppermost gold (**Figure 8e**) followed by removing all sacrificial films by oxygen plasma etching (**Figure 8f**). Thus, this fabrication process is compatible with CMOS-LSI due to the control of the process temperature below 400°C.

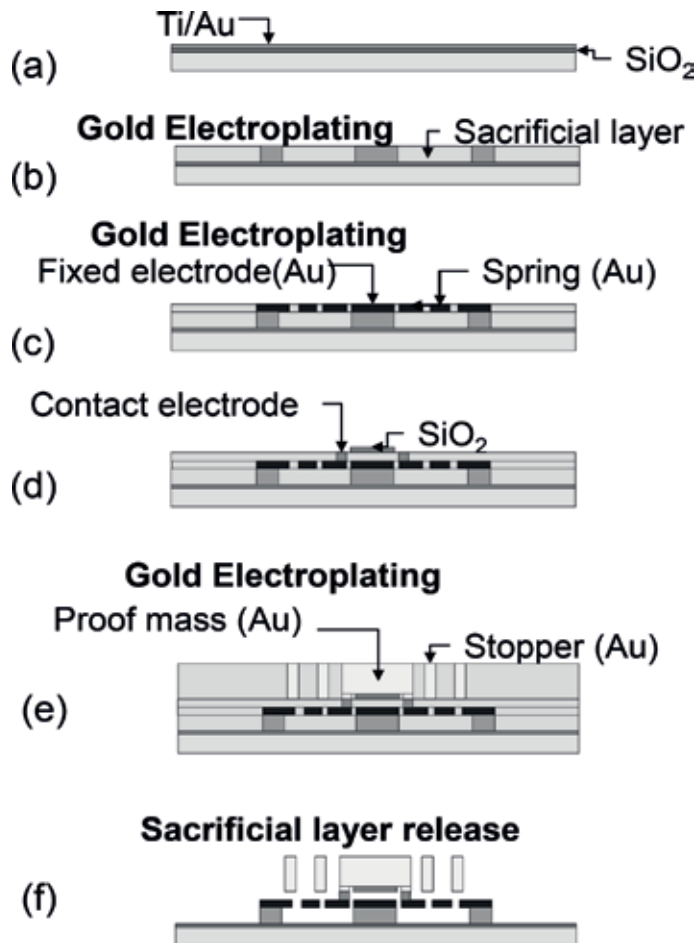


Figure 8. The micro-fabrication flow for the designed MEMS accelerometer. (a) adhesion and seed layers formation. (b) first metal and sacrificial film formation. (c) second metal formation. (d) contact metal and SiO₂ formation. (e) Proof mass and stopper formation. (f) Final process.

3.4 Experimental results of MEMS accelerometer

Figure 9 shows the SEM micrograph of the MEMS accelerometer, which has been successfully developed through the proposed fabrication process. We show the evaluation results of the measured characteristics of the developed MEMS accelerometer. **Figure 10** shows the capacitance vs. voltage characteristics were measured and plotted by applying a direct-current voltage between the movable proof mass and the fixed electrodes without applying acceleration. The initial capacitance C_0 at a voltage of 0 V, the electrostatic pull-in at a voltage of 6.4 V, and the release operation without stiction failure were observed from the hysteresis curve in **Figure 10**. The actual initial gap and spring constant have been estimated to be $4.3 \mu\text{m}$ and 0.26 N/m , respectively, in good agreement with the designed values. **Figure 11** shows the capacitance vs. frequency characteristics under the condition of a bias voltage of 2 V with 100 mV-amplitude oscillation. The measured

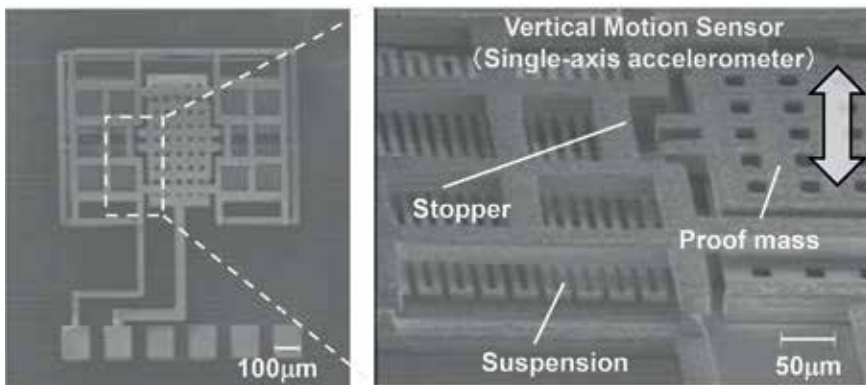


Figure 9.
The SEM micrograph of the MEMS accelerometer.

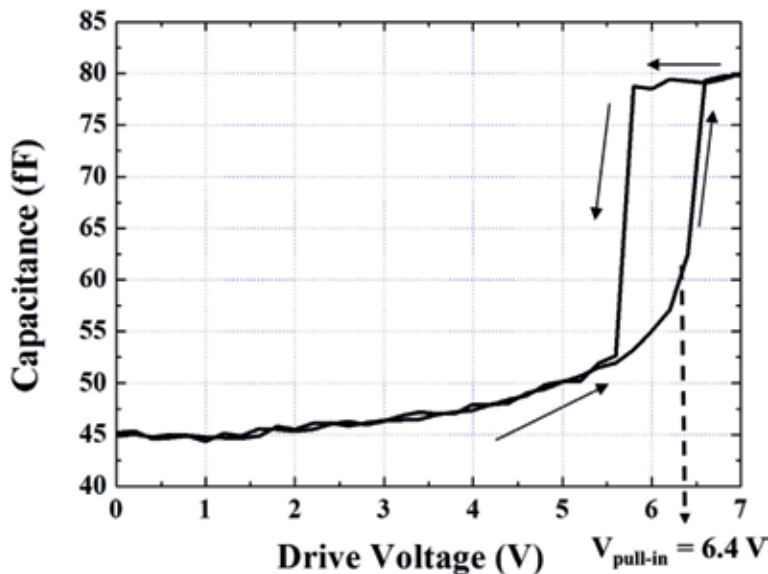


Figure 10.
The capacitance vs. voltage characteristics.

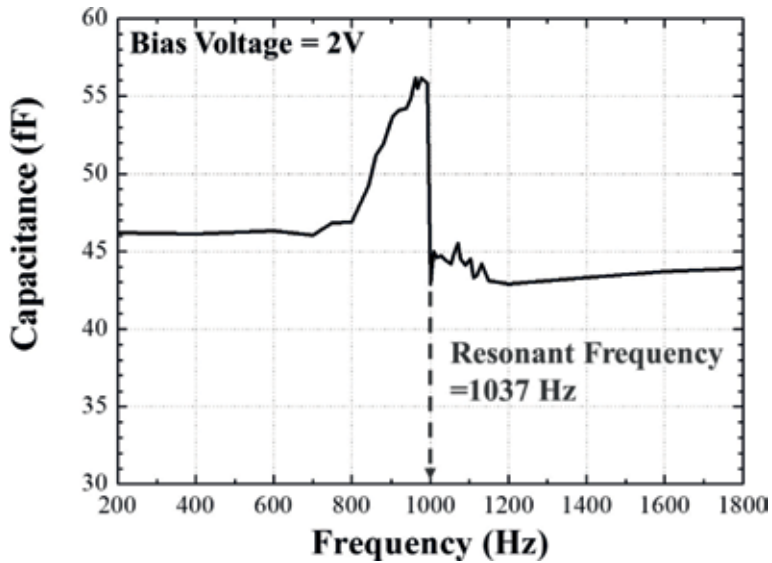


Figure 11.
The capacitance vs. frequency characteristics.

mechanical resonant frequency showed approximately 1037 Hz. The result suggested that it was higher than the designed value of 687 Hz due to the difference between the actual and the designed spring constants.

Figure 12 shows the capacitance vs. the applied acceleration characteristics. We measured the capacitance value at a bias voltage of 2 V with a frequency of 50 Hz. The measured results and the calculated data were square dots and the solid line, respectively. The calculated data used the actual proof mass of 6.12×10^{-9} kg. The designed proof mass was 1.07×10^{-8} kg. The result indicated that the experimental data was coincident with the calculated data.

Table 1 shows the comparison of the design and the obtained parameter values. The measured spring constant of 0.26 N/m is higher than the designed value of 0.2 N/m. The Brownian noise was measured to be $90.6 \mu\text{G}/(\text{Hz})^{1/2}$ for a proof mass

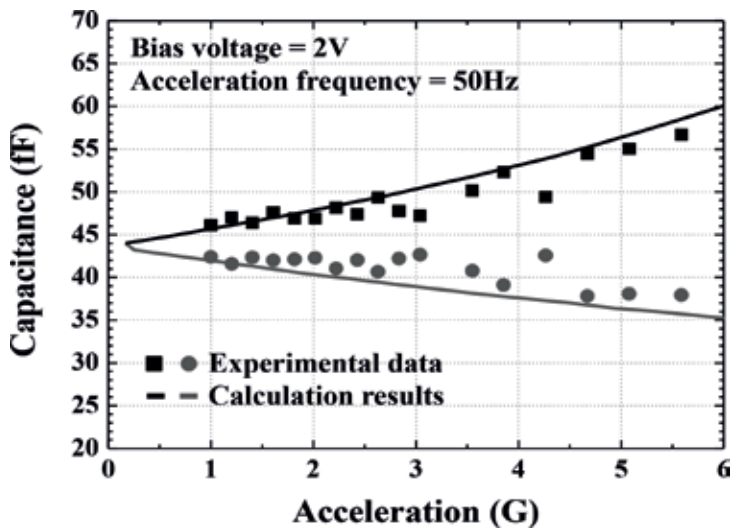


Figure 12.
The capacitance vs. the applied acceleration characteristics.

Parameter	Design Value	Measured	Unit
Initial Gap	5.0	4.3	μm
Pullin Voltage	6.0	6.4	V
Spring Constant	0.2	0.26	N/m
Mechanical Resonant Frequency	687	1037	Hz
Q factor	2.5	2.1	-
Brownian Noise	51.6	90.6	$\mu\text{G}/(\text{Hz})^{1/2}$
Detective Range	± 1.7	± 5.6	m/s^2

Table 1.
 The obtained parameter values.

with a size of $140 \times 140 \mu\text{m}^2$. Thus, this result attained the target value of less than $100 \mu\text{G}/(\text{Hz})^{1/2}$. Therefore, these evaluation results have verified the feasibility of our proposed structure and the multi-layer metal technology utilizing gold as a material for MEMS accelerometers.

4. Sub-1G MEMS accelerometer

4.1 Design of sub-1G MEMS accelerometer

This section shows a design approach of sub-1G detectable MEMS capacitive accelerometers for the miniaturization of CMOS-MEMS inertial sensors [23]. The minimum detectable acceleration can be determined by the Brownian noise B_N . Utilizing the high-density gold proof mass, the proof mass area of our device is nearly one-tenth of a silicon proof mass area size. The MEMS capacitive accelerometer for sub-1G sensing have been designed as follows: (i) a low B_N design below $10 \mu\text{G}/(\text{Hz})^{1/2}$, (ii) the mechanical resonant frequency of the accelerometer higher than the frequency of common environmental vibrations, which was mostly below 100 Hz [37, 38], and (iii) the multi-layer metal technology has been employed. Moreover, the feature size of the mechanical spring was designed to avoid physical contact between the proof mass and the fixed electrode. An SiO_2 film was used on the fixed electrode to avoid stiction as shown **Figure 6**.

We proposed a sub-1G detectable MEMS capacitive accelerometer with a proof mass made of gold. The proposed MEMS accelerometer has been developed by the multi-layer metal technology reported elsewhere [26, 27]. **Figure 13** shows the scanning electron microscope (SEM) micrographs of the fabricated accelerometer. The micrographs indicate the mechanical springs, the square proof mass with numbers of release holes, and mechanical stoppers. Thus, multi-layer gold has been successfully formed; the multi-layer metal structures have realized the decreased thickness of the mechanical springs to lower the vertical spring constant for the sub-1G sensing, while increasing the proof mass for a heavy mass. The proof mass was designed to be $1020 \mu\text{m} \times 1020 \mu\text{m}$ in area and $12 \mu\text{m}$ in thickness. From the designed result, we obtained the small value of $B_N = 120 \text{nG}/(\text{Hz})^{1/2}$. The value was considered to be sensitive to a sub-1G acceleration at the resolution of 1 mG.

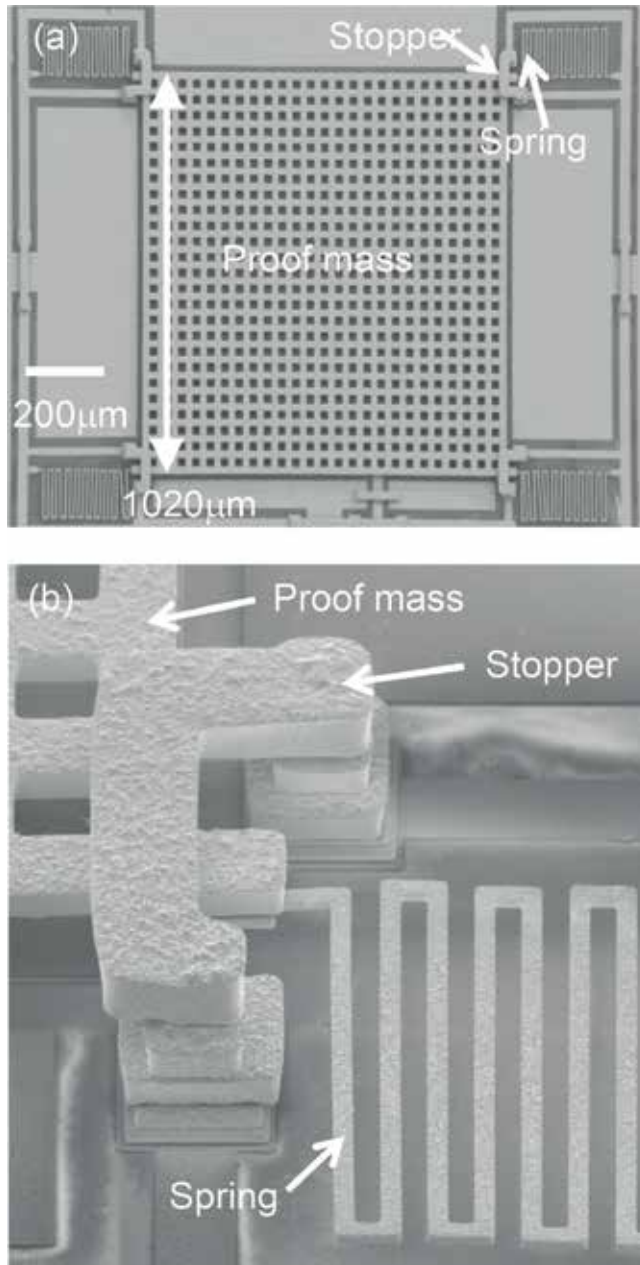


Figure 13. SEM micrographs of a MEMS accelerometer with the squared proof mass. (a) Chip view and (b) close-up image.

The resolution was presumed by considering the root-mean-square (rms) of the acceleration noise ($a_{n,rms}$). Assuming the single-pole roll-off characteristics, the equivalent noise bandwidth (Δf) is given by [39]:

$$\Delta f = 1.57 \times f_{-3dB} \quad (10)$$

where f_{-3dB} is the cutoff frequency, at which the output of the circuit falls -3 dB off the nominal passband level. The $a_{n,rms}$ is defined as [40]

$$a_{n,rms} = B_N \times \sqrt{\Delta f}. \quad (11)$$

For the Gaussian noise with a given rms value, the minimum detectable acceleration a_{min} can be statistically predicted by using $a_{min} = 6.6 \times a_{n,rms}$ [41]. The B_N value should satisfy the requirement of $a_{min} < 1$ mG is $B_N < 12 \mu\text{G}/(\text{Hz})^{1/2}$ for a typical f_{-3dB} of 100 Hz. Thus, we determined the target B_N to be lower than $10 \mu\text{G}/(\text{Hz})^{1/2}$ and designed a heavy proof mass with $B_N = 120 \text{ nG}/(\text{Hz})^{1/2}$ to allow for safety margin. **Figure 14** shows the capacitance vs. input acceleration (gravity) characteristics. The MEMS chip was set on a vibration exciter to apply vertical accelerations of 19.9 Hz with the DC bias voltage of 1.5 V. The result suggests the accelerometer's capability of sensing a sub-1G input acceleration with a 0.1-G step. **Figure 15** shows the capacitance vs. frequency characteristics. The measurement result indicates that the mechanical resonant frequency was measured to be 777 Hz and the resonant vibration of the proof mass was higher than the frequency of common environmental vibrations (<100 Hz). The quality factor (Q) of the device was 6.40 from the C-F characteristics by calculating the ratio between the real (Z_R) and imaginary (Z_I) parts of the electrical impedance at the resonant frequency; the Z_R and Z_I are 1.97×10^7 and -1.26×10^8 , respectively.

To estimate the actual value of B_N on the developed MEMS accelerometer, we use the following analytical models. The Q of a proof mass is expressed as [40]

$$Q = \frac{m\omega_{res}}{b}, \quad (12)$$

where ω_{res} is the resonant angular frequency. Using Eqs. (9) and (12), B_N can be given by

$$B_N = \sqrt{\frac{4k_B T \omega_{res}}{mQ}}. \quad (13)$$

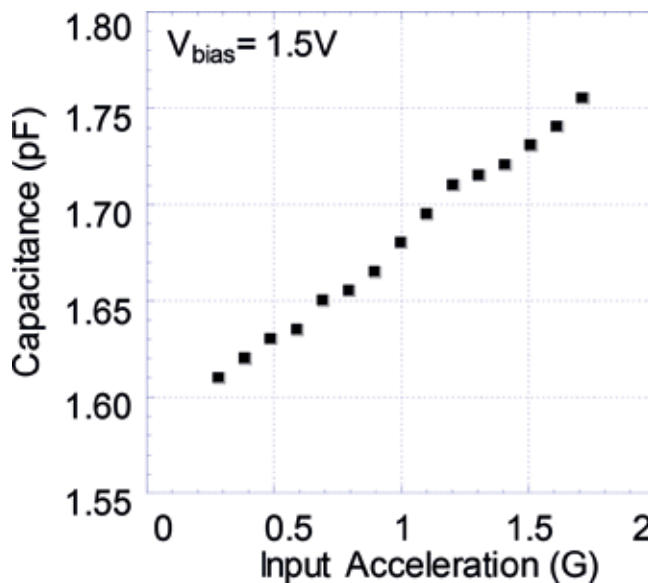


Figure 14. Capacitance as a function of acceleration.

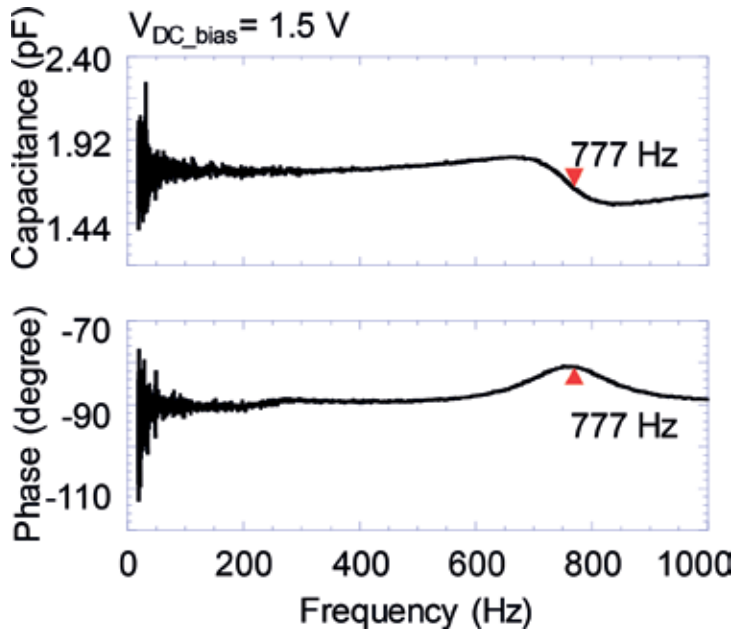


Figure 15. Measured capacitance and phase characteristics as a function of the frequency of sensing signal.

We can obtain the B_N value by the Eq. (13) and the experimentally obtained data, when it is difficult to explain the actual value of b due to the squeezed-film damping effect [41]. Measuring the area and height of the proof mass, and the m was obtained to be 2.17×10^{-7} kg. Thus, the actual B_N can be estimated to be $780\text{ nG}/(\text{Hz})^{1/2}$ at 300 K, which was below the target value of $10\text{ }\mu\text{G}/(\text{Hz})^{1/2}$.

Therefore, it is confirmed that the Brownian noise of the sub-1G MEMS accelerometer can achieve $780\text{ nG}/(\text{Hz})^{1/2}$ in spite of the small proof mass.

5. Arrayed MEMS accelerometer

5.1 Proposed MEMS accelerometer

Figure 16 shows that an arrayed CMOS MEMS accelerometer stacked on a single LSI chip [24]. In order to solve the issues on the conventional MEMS accelerometers, the proposed accelerometer has the following requirements: (i) the accelerometer should be in an arrayed type to detect a wide range of acceleration, (ii) the structure material for the accelerometer should be chosen to reduce the sensor size and the mechanical noise floor, and (iii) the accelerometer should be stacked on the single CMOS LSI. Proof masses of three different designs (areas 80×80 , 140×140 , and

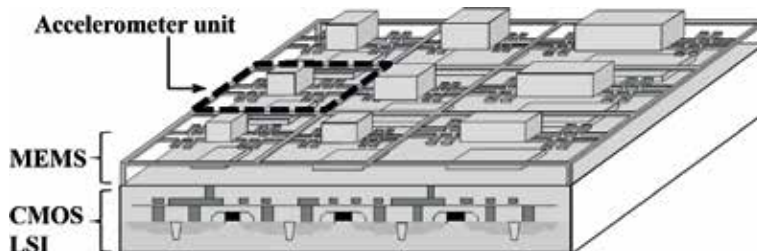


Figure 16. An integrated CMOS-MEMS accelerometer.

$200 \times 200 \mu\text{m}^2$) are combined with three types of different spring constants (0.2, 0.3, and 0.4 N/m) to detect the wide range of acceleration from 1 to 20 G. The total layout area is less than $4 \times 4 \text{mm}^2$, which is small enough for monolithically integration with CMOS circuits. **Figure 17** shows the calculated electrostatic capacitance as a function of the input acceleration by using the multi-physics simulation; a bias voltage of 1 V was applied to the sensing electrode for electrostatic capacitive readout. The acceleration was swept from 0 to ± 20 G in 10 s for each branch. The simulation results showed that the capacitance was changed by the input acceleration within the limited mechanical displacement range between the bottom electrode and the mechanical stopper. In the positive acceleration, the capacitance gradually increases by squeezing the air gap between the proof mass and the fixed electrode. Owing to the bias voltage of 1 V, the proof mass was brought into pull-in contact. In the opposite acceleration, the air gap is enlarged to decrease the capacitance. **Figure 17** also suggests that a wide range of acceleration between 1 and 20 G is covered by the arrayed accelerometers; for instance, any one of accelerometer #2, 3, 5, 6, 8, or 9 can detect an acceleration of 3 G or greater. For a range lower than 2 G, accelerometer #3 can be used.

5.2 Results and discussion of arrayed MEMS accelerometer

Figure 18 shows a scanning electron microscopy (SEM) image of the developed MEMS accelerometers in 3×3 formation. **Figure 19** shows the measured acceleration characteristics (dots) as a function of the capacitance change compared to the simulation results. The measurement was carried out under the condition of the acceleration frequency of 50 Hz and the bias voltage of 100 mV. The simulation results include the effect of the parasitic capacitance C_{pa} of the measurement system. The measured data of devices #1, 2, 4, 5, 7, and 8 exhibited good agreement with the simulation results. On the other hand, the data of devices #3, 6, and 9 showed the capacitance change smaller than the simulation. This is because these latter three devices used a proof mass of $200 \times 200 \mu\text{m}^2$ size so that the mismatch might be caused by a size effect such as warpage.

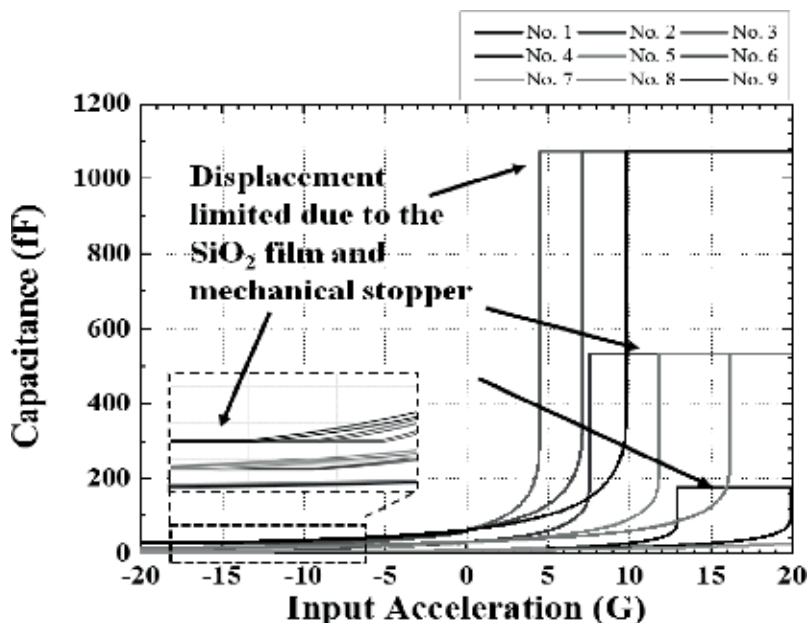


Figure 17. The calculated electrostatic capacitance as a function of the input acceleration by using the multi-physics simulation.

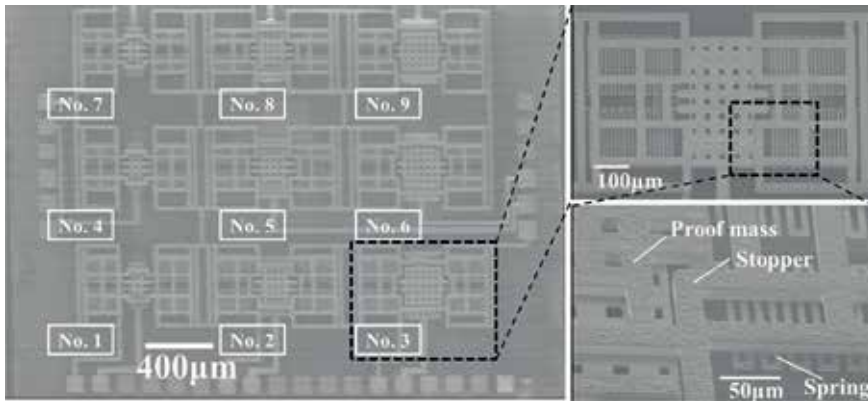


Figure 18.
A scanning electron microscopy (SEM) image of the developed MEMS accelerometers.

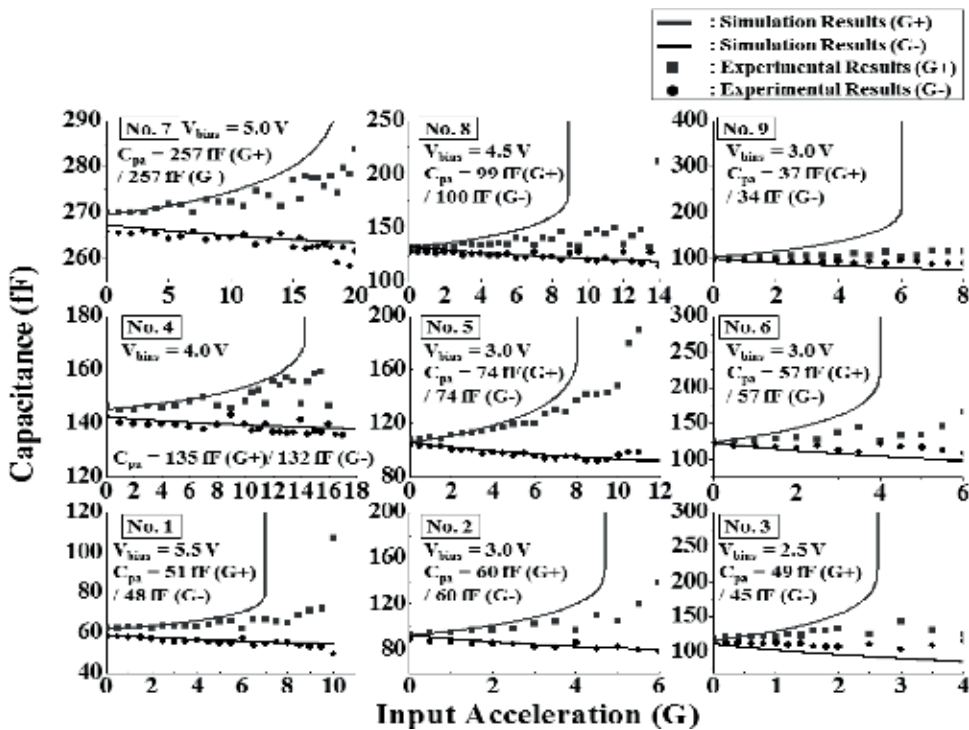


Figure 19.
The experimentally obtained acceleration characteristics.

Therefore, it is confirmed that the proposed arrayed MEMS accelerometer could detect a wide range of acceleration from 1 to 20 G.

6. CMOS-MEMS accelerometer

6.1 Capacitive CMOS sensor

In order to verify the validity of our CMOS-MEMS technology, we have developed a capacitive CMOS-MEMS accelerometer designed by our multi-physics

simulation. The developed accelerometer is composed of the capacitive sensor LSI circuit and the MEMS accelerometer. We propose the sensor circuit to detect the capacitance change of the MEMS device by comparing with the reference capacitor built-in LSI. The MEMS accelerometer and the proposed sensor circuit are simultaneously designed by the multi-physics simulation with a newly developed equivalent circuit of the capacitive MEMS sensor for CMOS-MEMS technology.

6.2 Sensor circuit

Figure 20 shows the comparison of our capacitive MEMS sensor circuit and the conventional MEMS sensor circuit. In conventional MEMS sensor circuits [42–44], capacitance change of the movable electrodes is differentially detected in response to the changes of another electrode pair within the identical MEMS chip such as the comb-drive devices. On the other hand, in our capacitive MEMS sensor circuit, it is needed to adopt other detection architecture different from the conventional sensor circuit as described above. It is because the electrode is only placed at the bottom side of the proof mass and also differential capacitance values are not produced.

In order to solve the above requirements, we propose the sensor circuit to detect a capacitance signal from a MEMS sensing element and compare it with a reference capacitor integrated within the sensor LSI. **Figure 20** shows the concept of our proposed sensor circuit. This circuit does not need other electrodes or structures for the differential capacitance. Thus, it is applicable to our capacitive CMOS-MEMS accelerometer. The circuit also has other features: (i) a reference capacitor in a MEMS chip is not needed, and hence the total device footprint is reduced, (ii) it is applicable and scalable to various types of capacitive MEMS devices including accelerometer in an arrayed format [24, 25], and (iii) calibration is simply proceeded as we can know the reference capacitor values at the stage of circuit design.

6.3 Capacitive CMOS-MEMS accelerometer design

To realize a capacitive CMOS-MEMS accelerometer, we utilized the multi-physics simulation platform based on our previous work [29]. **Figure 21** shows the proposed sensor circuit with an equivalent circuit of the capacitive MEMS accelerometer. The equivalent circuit consists of five modules. These modules are described by a Verilog-a compatible HDL, and designed to handle the multi-physics simulations in a single LSI design environment such as Cadence Virtuoso [31].

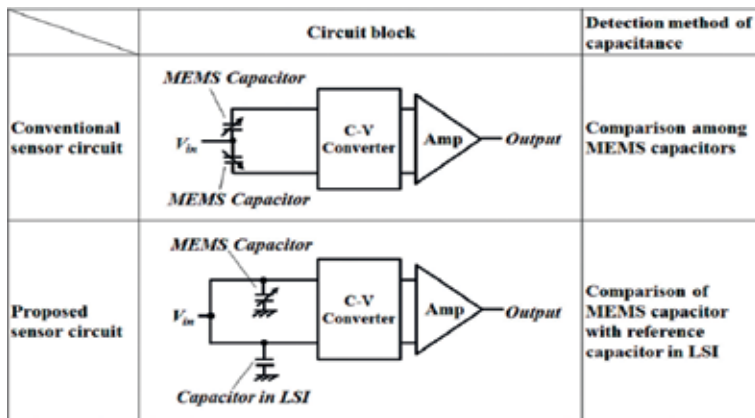


Figure 20.
 The comparison of the capacitive CMOS-MEMS sensor and the conventional MEMS sensor.

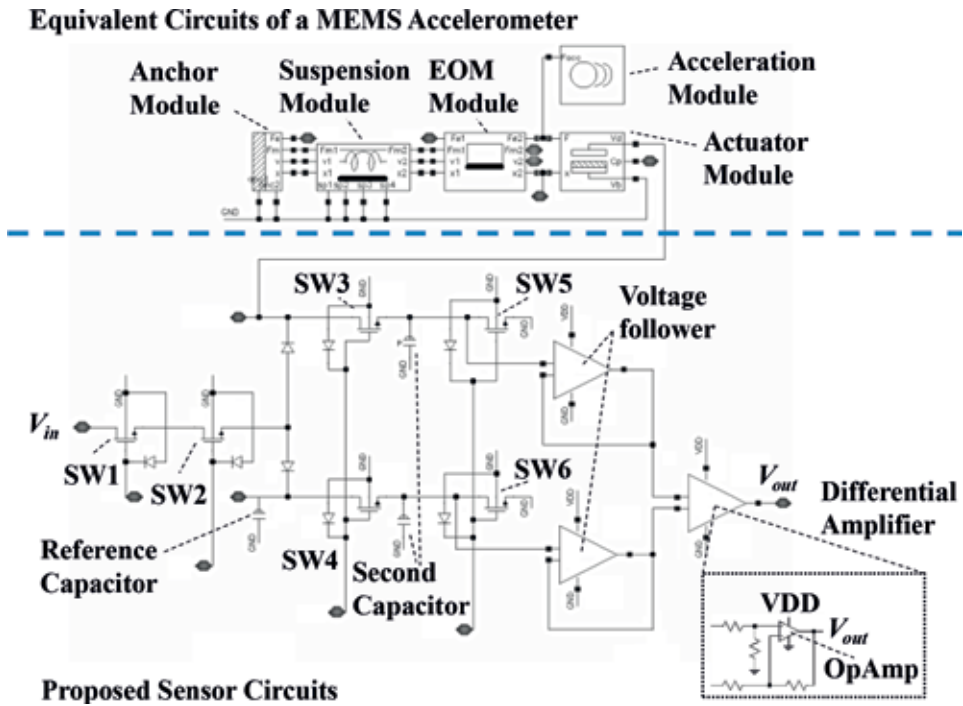


Figure 21. The schematic of the proposed sensor circuit with an equivalent circuit of the capacitive MEMS sensor as a MEMS accelerometer.

The behaviors of both LSI and MEMS should be simultaneously simulated to design the capacitive CMOS-MEMS accelerometer stacked on the sensor circuit. Capacitance values C_{tm} and C_{tr} of the capacitor are set to be 8 pF with the parasitic capacitance of 7 pF in the LSI and the measurement system. In these parameters, we performed a transient analysis for the acceleration of sinusoidal wave of 2 G_{in} at 49 Hz superposed onto a DC level acceleration of 1 G. **Figure 22** shows the simulation results of the output voltage from the proposed sensor circuit under given input acceleration. This result suggests that the output voltage has changed from 869.3 to 892.1 mV depending upon the input acceleration waveforms.

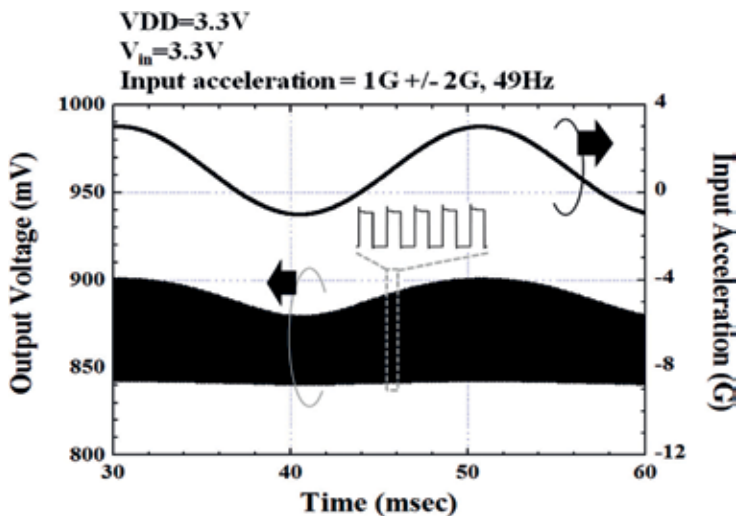


Figure 22. The simulation results of the output voltage from the proposed sensor circuit under given input acceleration.

As a result, it is confirmed that the proposed sensor circuit could detect the capacitance change of the MEMS device.

6.4 Experimental results of capacitive CMOS-MEMS accelerometer

Figure 23 shows a scanning electron microscopy (SEM) image and a close-up optical microscope view of the developed capacitive CMOS-MEMS accelerometer. It is clear that the MEMS structure interconnected to the LSI has been successfully fabricated by the micro fabrication process. **Figure 24** shows the output voltage as a function of the input acceleration obtained by both measurement and simulation.

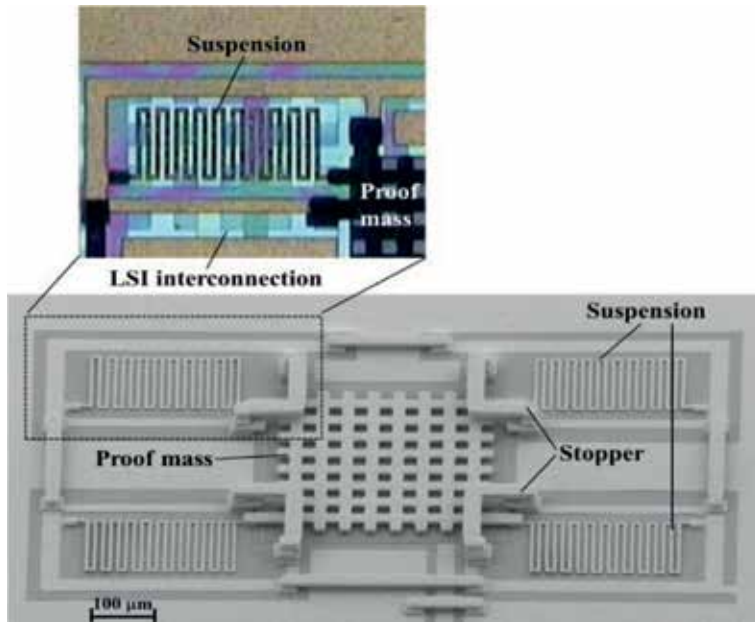


Figure 23.
A scanning electron microscopy (SEM) image.

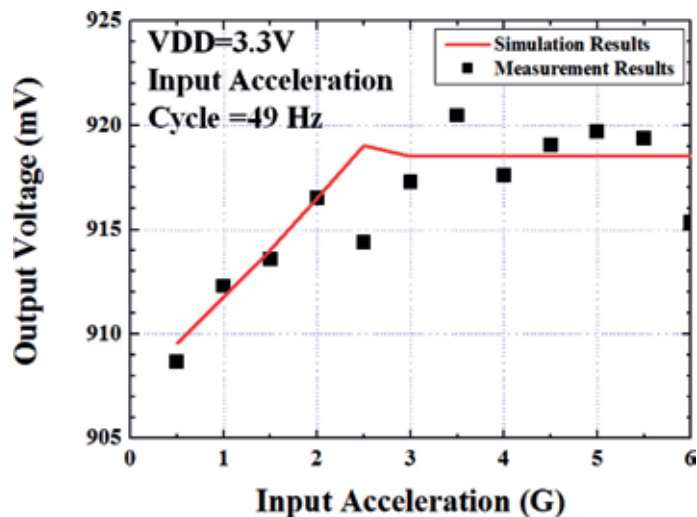


Figure 24.
The output voltage as a function of the input acceleration obtained by both experimental measurement and numerical simulation.

The simulation result was coincident with the experimental results for the input acceleration of 3 G or lower. For the input acceleration of 3 G or larger, notable deviations were observed in the experimental result possibly due to excess mechanical motion of the proof mass. The result suggested that fabricated capacitive CMOS-MEMS sensor can detect the capacitance change of a single-axis MEMS accelerometer.

Therefore, it is confirmed that the validity of the simultaneous design of both MEMS and sensor circuit using multi-physics simulation environment with an equivalent circuit of the MEMS accelerometer was verified.

7. Conclusions

This chapter presented technical features and solutions to realize a high sensitive CMOS-MEMS accelerometer with gold proof mass. The multi-physics simulation platform for the design of the CMOS-MEMS device was developed to understand simultaneously both the mechanical and electrical behaviors of MEMS stacked on LSI. An equivalent circuit for the accelerometer module was built by an electrical circuit simulator.

MEMS accelerometer fabrication process was formed by the multi-layer metal technology, which consists of the gold electroplating and the sacrificial layer formation using the photo-sensitive polyimide film. We proposed a sensor structure for MEMS accelerometers. The measured characteristics of the developed accelerometer were in good agreement with the designed values, and the actual Brownian noise was estimated to be below the target of $100 \mu\text{G}/(\text{Hz})^{1/2}$. Moreover, the experimental results showed that the Brownian noise of the sub-1G MEMS accelerometer could achieve $780 \text{ nG}/(\text{Hz})^{1/2}$. We also proposed an arrayed accelerometer device with a wide range of detection between 1 and 20 G. An arrayed accelerometer was successfully developed in a single chip of $4 \times 4 \text{ mm}^2$ in area by electroplated gold. The experimental results suggested that a wide detection range of acceleration has been achieved.

The proposed sensor LSI was fabricated by a $0.35\text{-}\mu\text{m}$ CMOS process and the MEMS accelerometer was implemented onto the LSI. The measured characteristics of the capacitive CMOS-MEMS accelerometer showed a good agreement with the simulation results. Thus, the validity of our multi-physics simulation was verified.

In conclusion, it is confirmed that the multi-physics simulation platform and the multi-layer metal technology for the CMOS-MEMS device will open the way to the future of nano-gravity sensing technology.

Acknowledgements

The authors would like to thank S. Iida, M. Yano, T. Safu, and K. Kudo with NTT-AT for technical discussions.

This work was supported by JST CREST Grant Number JPMJCR1433 and by the Grant-in-Aid for Scientific Research (B) (No. 23360149) of the Japan Society for the Promotion of Science (JSPS).

Conflicts of interest

I confirm there are no conflicts of interest.

Author details

Katsuyuki Machida^{1*}, Toshifumi Konishi², Daisuke Yamane¹, Hiroshi Toshiyoshi³
and Hiroyuki Ito¹


1 Tokyo Institute of Technology, Yokohama, Kanagawa, Japan

2 NTT Advanced Technology Corporation, Atsugi, Kanagawa, Japan

3 RCAST, The University of Tokyo, Tokyo, Japan

*Address all correspondence to: machida.k.ad@m.titech.ac.jp

IntechOpen

© 2018 The Author(s). Licensee IntechOpen. This chapter is distributed under the terms of the Creative Commons Attribution License (<http://creativecommons.org/licenses/by/3.0>), which permits unrestricted use, distribution, and reproduction in any medium, provided the original work is properly cited. 

References

- [1] Seidel H, Riedel H, Kolbeck R, Mück G, Kupke W, Königer M. Capacitive silicon accelerometer with highly symmetrical design. *Sensors and Actuators A*. 1990;**21**:312
- [2] Henrion W, DiSanza L, Lp M, Terry S, Jerman H. Wide dynamic range direct digital accelerometer. In: *IEEE 4th Solid-State Sensor and Actuator Workshop Technical Digest*. 1990. p. 153
- [3] Yun W, Howe T, Gray PR. Surface micromachined digitally force balanced accelerometer with integrated CMOS detection circuitry. In: *IEEE 5th Solid-State Sensor and Actuator Workshop Technical Digest*. 1992. p. 126
- [4] Ohtsuki Y, Fuda Y, Yoshida T. High-sensitivity accelerometer using multilayer piezoelectric ceramics. *Japanese Journal of Applied Physics*. 1993;**32**:4209
- [5] Ha B, Oh Y, Song C. A capacitive silicon microaccelerometer with force-balancing electrodes. *Japanese Journal of Applied Physics*. 1998;**37**:7052
- [6] Kim S, Yee Y, Kim H, Chun K, Hong I, Lee J. A complementary metal oxide semiconductor (CMOS) compatible capacitive silicon accelerometer with polysilicon rib-style flexures. *Japanese Journal of Applied Physics*. 1998;**37**:7093
- [7] Sim J-H, Lee J-H. A piezoresistive silicon accelerometer using porous silicon micromachining and flip-chip bonding. *Japanese Journal of Applied Physics*. 1999;**38**:1915
- [8] Lee KI, Takao H, Sawada K, Ishida M. Analysis of thermal drift of a constant temperature control type three-axis accelerometer for high temperatures. *IEEJ Transactions on Sensors and Micromachines*. 2003;**123**:583
- [9] Speller KE, Yu D. A low noise MEMS accelerometer for unattended ground sensor application. In: *Proceedings of the SPIE Unattended/Unmanned Ground, Ocean, and Air Sensor Technologies and Applications VI*. Vol. 5417. 2004. p. 63
- [10] Okada H, Kobayashi T, Masuda T, Itoh T. Ultra-low power event-driven wireless sensor node using piezoelectric accelerometer for health monitoring. *Japanese Journal of Applied Physics*. 2009;**48**:070222
- [11] Milligan D, Homeijer B, Walmsley R. An ultra-low noise MEMS accelerometer for seismic imaging. In: *Proceedings of IEEE Sensors 2011*; 28-31 October 2011; Limerick, Ireland. New Jersey: IEEE; 2012
- [12] Abdolvand R, Amini B, Ayazi F. Sub-micro-gravity in-plane accelerometers with reduced capacitive gaps and extra seismic mass. *Journal of Microelectromechanical Systems*. 2007; **16**:1036-1043. DOI: 10.1109/JMEMS.2007.900879
- [13] Dong Y, Kraft M, Redman-White W. Higher order noise-shaping filters for high-performance micromachined accelerometers. *IEEE Transactions on Instrumentation and Measurement*. 2007;**56**:1666-1674. DOI: 10.1109/TIM.2007.904477
- [14] Monajemi P, Ayazi F. Design optimization and implementation of a microgravity capacitive HARPSS accelerometer. *IEEE Sensors Journal*. 2006;**6**:39-46. DOI: 10.1109/JSEN.2005.854134
- [15] Chae J, Kulah H, Najafi K. An in-plane high-sensitivity, low-noise micro-g silicon accelerometer with CMOS readout circuitry. *Journal of Microelectromechanical Systems*. 2004;

13:628-635. DOI: 10.1109/
JMEMS.2004.832653

[16] Yazdi N, Najafi K, Salian A. A high-sensitivity silicon accelerometer with a folded-electrode structure. *Journal of Microelectromechanical Systems*. 2003; **12**:479-486. DOI: 10.1109/
JMEMS.2003.815837

[17] Kulah H, Chae J, Yazdi N, Najafi K. A multi-step electromechanical $\Sigma\Delta$ converter for micro-g capacitive accelerometers. In: *Proceedings of IEEE International Solid-State Circuits Conference 2013*; 13 February 2004; San Francisco, CA, USA. New Jersey: IEEE; 2004

[18] Yazdi Y, Najafi K. An all-silicon single-wafer micro-g accelerometer with a combined surface and bulk micromachining process. *Journal of Microelectromechanical Systems*. 2000; **9**:544-550. DOI: 10.1109/84.896777

[19] Lemkin M, Boser B. A three-axis micromachined accelerometer with a CMOS position-sense interface and digital offset-trim electronics. *IEEE Journal of Solid-State Circuits*. 1999; **34**: 456-468. DOI: 10.1109/4.753678

[20] Lu C, Lemkin M, Boser B. A monolithic surface micromachined accelerometer with digital output. *IEEE Journal of Solid-State Circuits*. 1995; **30**: 1367-1373. DOI: 10.1109/4.482163

[21] Smith T, Nys O, Chevroulet M, DeCoulon Y, Degrauwe M. A multi-step electromechanical $\Sigma\Delta$ converter for micro-g capacitive accelerometers. In: *Proceedings of IEEE International Solid-State Circuits Conference 1994*; 16-18 February 1994; San Francisco, CA, USA. New Jersey: IEEE; 2002. pp. 160-161

[22] Analog Devices, ADXL50 [Internet]. Available from: <http://www.analog.com/media/en/technical->

[documentation/obsolete-data-sheets/2044696ADXL50.pdf](#) [Accessed: 28-08-2018]

[23] Yamane D, Konishi T, Matsushima T, Machida K, Toshiyoshi H, Masu K. Design of sub-1g microelectromechanical systems accelerometers. *Applied Physics Letters*. 2014; **104**(7):074102. DOI: 10.1063/1.4865377

[24] Yamane D, Konishi T, Matsushima T, Motohashi G, Kagaya K, Ito H, et al. An arrayed MEMS accelerometer with a wide range of detection. In: *Transducers 2013*; Spain. 2013. p. 22

[25] Konishi T, Yamane D, Matsushima T, Motohashi G, Kagaya K, Ito H, et al. Novel sensor structure and its evaluation for integrated complementary metal oxide semiconductor microelectromechanical systems accelerometer. *Japanese Journal of Applied Physics*. 2013; **52**: 06GL04

[26] Machida K, Shigematsu S, Morimura H, Tanabe Y, Sato N, Shimoyama N, et al. A novel semiconductor capacitive sensor for a single-chip fingerprint sensor/identifier. *IEEE Transactions on Electron Devices*. 2001; **48**:2273

[27] Machida K, Morimura H. Integrated CMOS-MEMS technology and its application. In: *SSDM 2010*; 24 September 2010; Tokyo. 2010. p. 818

[28] Toshiyoshi H, Konishi T, Machida K, Masu K. A multi-physics simulation technique for integrated MEMS. In: *IEDM 2012*; USA. 2012. p. 6.3.1

[29] Konishi T, Machida K, Maruyama S, Mita M, Masu K, Toshiyoshi H. A single-platform simulation and design technique for CMOS-MEMS based on a circuit simulator with hardware description language. *IEEE/ASME*:

Journal of Microelectromechanical Systems. 2013;22(3):755

[30] Konishi T, Yamane D, Matsushima T, Maruyama S, Kagaya K, Ito H, et al. Novel sensor circuits design using multi-physics simulation for CMOS-MEMS technology. In: SSDM 2013; 24-27 September 2013; Fukuoka, Japan. 2013. p. 844

[31] Cadence Design Systems, Inc. Available from: <http://www.cadence.com/products/cic/pages/default.aspx>

[32] Qu H, Fnag D, Xie H. A monolithic CMOS-MEMS 3-axis accelerometer with a low-noise, low-power dual-chopper amplifier. IEEE Sensors Journal. 2008;8:1511

[33] Chen J-Y, Liao LP, Chien HT, Lin CS, Hsu YW. Issues in Path Toward Low Cost Three-Axis Accelerometer for Low-g Application. In: Proceedings of the 4th International Microsystems, Packaging, Assembly and Circuits Technology Conference. 2009. p. 263

[34] Comi C, Corigliano A, Langfelder G, Longoni A, Tocchio A, Simoni B. A resonant microaccelerometer with high sensitivity operating in an oscillating circuit. IEEE Journal of Microelectromechanical Systems. 2010; 19:1140

[35] Sato N, Morimura H, Shigematsu S, Yano M, Kudou K, Kamei T, et al. Force-sensing scheme for small mechanical signals in CMOS MEMS fingerprint sensor. Japanese Journal of Applied Physics. 2005;44:6481

[36] Kuwabara K, Urano M, Kodate J, Sato N, Morimura H, Sakata T, et al. Novel structure and fabrication process for integrated RF microelectromechanical-system technology. Japanese Journal of Applied Physics. 2006;45:6849

[37] Mitcheson PD, Yeatman EM, Rao GK, Holmes AS, Green TC. Energy harvesting from human and machine motion for wireless electronic devices. Proceedings of the IEEE. 2008;96:1457

[38] Kulahv H, Najafi K. Energy scavenging from low frequency vibrations by using frequency up conversion for wireless sensor applications. IEEE Sensors Journal. 2008;8(3):261-268

[39] Gray PR, Hurst PJ, Lewis SH, Meyer RG. Analysis and Design of Analog Integrated Circuits. 4th ed. New York: John Wiley & Sons, Inc.; 2001. p. 796

[40] Senturia SD. Microsystem Design. New York: Springer Science+Business Media, Inc.; 2001

[41] Jung WG. Op Amp Applications. Analog Devices, Inc; 2002. p. 1.83

[42] Kulah H, Chae J, Yazdi N, Najafi K. Noise analysis and characterization of a sigma-delta capacitive microaccelerometer. IEEE Journal of Solid-State Circuits. 2006;41(2):352-361

[43] Denison T, Consoer K, Santa W, Miesel K, Molnar G. A 2.2 microWatt, 95nV/rHz, chopper-stabilized instrumentation amplifier for chronic measurement of ECG and EEG. In: Proceedings of the Instrumentation and Measurement Technology Conference. 2007. p. 1

[44] Chen J, Ni X, Mo B. A low noise CMOS charge sensitive preamplifier for MEMS capacitive accelerometer readout. In: Proceedings of the 7th International Conference on ASIC. 2007. p. 490

Edited by Masato Sone and Kazuya Masu

Gold and noble metals have been attractive to humans from ancient times because of their beautiful features. In modern society, noble metals, especially gold, play important roles as components in electronic devices because of their high electrical conductivity, chemical stability, and density. In the field of MEMS devices, the demand for continuous miniaturization and sensitivity enhancement is always high. Especially for MEMS accelerometers, sensitivity is affected by Brownian noise, and components with sufficient mass are needed to suppress this noise. Therefore, it is difficult to reduce the dimensions of components to allow further miniaturization of the device. This book presents recent progress in noble metal electrodeposition and applications of gold-based materials in the realization of highly sensitive CMOS-MEMS accelerometers.

Published in London, UK

© 2019 IntechOpen
© Andrey_A / iStock

IntechOpen

